

**UCLA**

**UCLA Electronic Theses and Dissertations**

**Title**

Dilute Alloy Catalysts: Unraveling Enhanced Selectivity and Reactivity in (De)Hydrogenation Reactions through Theoretical Exploration

**Permalink**

<https://escholarship.org/uc/item/73z4b4ph>

**Author**

Ngan, Hio Tong

**Publication Date**

2024

Peer reviewed|Thesis/dissertation

UNIVERSITY OF CALIFORNIA

Los Angeles

Dilute Alloy Catalysts: Unraveling Enhanced Selectivity and Reactivity in (De)Hydrogenation  
Reactions through Theoretical Exploration

A dissertation submitted in partial satisfaction of the  
requirements for the degree Doctor of Philosophy in  
Chemical Engineering

by

Hio Tong Ngan

2024

© Copyright by

Hio Tong Ngan

2024

## ABSTRACT OF THE DISSERTATION

Dilute Alloy Catalysts: Unraveling Enhanced Selectivity and Reactivity in (De)Hydrogenation  
Reactions through Theoretical Exploration

by

Hio Tong Ngan

Doctor of Philosophy in Chemical Engineering

University of California, Los Angeles, 2024

Professor Philippe Sautet, Chair

Heterogeneous catalysis plays a crucial role in the production of industrially important chemicals. Conventional Pt-group metals have been widely used in various reactions for their high activity. However, these catalysts often favor undesired side-reactions, resulting in low reaction selectivity. To tackle this issue, a new class of catalytic materials named single-atom alloys (SAA) has been established in the past decade. Typically, SAAs are synthesized by dispersing a small amount of active elements into less reactive host metals, forming isolated dopant atoms on the surface. In this dissertation, we use density functional theory (DFT) and microkinetic modeling to unravel the reasons behind the improved activity and selectivity of the SAAs in different reactions.

DFT calculations and microkinetic modeling were first performed to investigate the selective hydrogenation of 1-hexyne to produce 1-hexene on dilute Pd-in-Au alloy catalysts. It is demonstrated that the high selectivity of isolated Pd atoms in Au(111) is attributed to the difficult H<sub>2</sub> dissociation and H-spillover steps, which help impede the supply of H atoms for further hydrogenation of 1-hexene. Although larger Pd ensembles could facilitate H<sub>2</sub> dissociation, and

hence supposedly enhance the reaction rates, they tend to be poisoned by the more strongly bound alkyne molecules, resulting in even lower reaction reactivity than isolated Pd atoms.

Besides alkyne hydrogenation, the challenging selective hydrogenation of  $\alpha,\beta$ -unsaturated aldehydes to form unsaturated alcohols was also addressed in this dissertation. In this work, mid-transition metals in Cu(111) appear to be the optimal systems for this reaction as they favor acrolein adsorption via the C=O bond but with a moderate binding strength, compatible with catalysis. In addition, there is a large barrier for reactant migration from the C=O to the C=C binding mode, which help impede C=C bond hydrogenation from happening and enhance the reaction selectivity.

Finally, the potential of Cu-based dilute alloys for alkane dehydrogenation was explored. Specifically, our results reveal that isolated Hf and Ir atoms in Cu(111) could selectively and reactively dehydrogenate propane. The former, in particular, even demonstrates higher reaction reactivity than the widely used Pt-based catalysts. It is shown in this study that for alkane dehydrogenation on single-atom alloys, C-H bond breaking might not be the sole rate-limiting step. The migration of H atoms away from the active sites, which has not been discussed in literature, is also somewhat rate-controlling.

The dissertation of Hio Tong Ngan is approved.

Anastassia N. Alexandrova

Boris Kozinsky

Dante A. Simonetti

Philippe Sautet, Committee Chair

University of California, Los Angeles

2024

Dedicated to my dad, my mom, and Huiheng

## Table of Contents

List of Figures .....	xi
List of Tables.....	xxix
Acknowledgements .....	xxxiii
Curriculum Vitae .....	xxxviii
Chapter 1 Research Background .....	1
1.1 Dilute Alloys in Heterogeneous Catalysis.....	1
1.2 Significance of Theoretical Modeling.....	5
1.3 Thesis Objectives.....	7
Chapter 2 Hydrogen Dissociation Controls 1-Hexyne Selective Hydrogenation on Dilute Pd-in-Au Catalysts.....	10
2.1 Introduction .....	10
2.2 Methods .....	13
2.2.1 DFT Calculations.....	13
2.2.2 Microkinetic Simulations .....	14
2.3 Results .....	16
2.3.1 Dissociation of H <sub>2</sub> .....	16
2.3.2 Hydrogenation of 1-Hexyne to 1-Hexene .....	18
2.3.3 Microkinetic Simulation of Catalytic Activity .....	22
2.3.4 Origin of Improved 1-Hexene Selectivity .....	29
2.4 Conclusion .....	32
Chapter 3 Unraveling 1-Hexene Hydrogenation over Dilute Pd-in-Au Alloys .....	35
3.1 Introduction .....	35

3.2 Methods .....	36
3.2.1 DFT Calculations.....	36
3.2.2 Microkinetic Simulations .....	36
3.3 Results .....	38
3.3.1 Isotopically Labeled 1-Hexene Hydrogenation Experiments.....	38
3.3.2 Adsorption, Isomerization, and Hydrogenation Energies from First-Principles Calculations.....	40
3.3.3 Microkinetic Simulations of 1-Hexene Hydrogenation.....	42
3.3.4 Theoretical Assessment of H/D Exchange in 1-Hexene Hydrogenation .....	45
3.4 Conclusion .....	48
Chapter 4 Influence of Pd Concentration in Au-Pd Nanoparticles for the Hydrogenation of Alkynes .....	49
4.1 Introduction .....	49
4.2 Methods .....	51
4.2.1 DFT Calculations.....	51
4.2.2 Microkinetic Simulations .....	51
4.3 Results .....	54
4.3.1 Binding Strengths of Surface Species.....	54
4.3.2 Microkinetic Simulations of Catalytic Performance .....	55
4.4 Conclusion .....	65
Chapter 5 Tuning the Hydrogenation Selectivity of an Unsaturated Aldehyde via Single-Atom Alloy Catalysts.....	66
5.1 Introduction .....	66

5.2 Methods .....	71
5.2.1 DFT Calculations.....	71
5.2.2 Microkinetic Modeling.....	72
5.3 Results .....	75
5.3.1 Dopant Segregation and Aggregation.....	75
5.3.2 Binding Modes of Acrolein.....	76
5.3.3 Early-Transition Metals in Cu(111) .....	78
5.3.4 Mid-Transition Metals in Cu(111).....	80
5.3.5 Late-Transition Metals in Cu(111).....	90
5.3.6 Chemical Bonding Analysis .....	91
5.4 Conclusion .....	92
Chapter 6 Cu-Based Atom Alloys as Tunable Catalysts for Selective Propane Dehydrogenation	
.....	95
6.1 Introduction .....	95
6.2 Methods .....	98
6.2.1 DFT Calculations.....	98
6.2.2 Microkinetic Modeling.....	100
6.3 Results .....	102
6.3.1 Dopant Segregation and Aggregation.....	102
6.3.2 Propane Activation.....	103
6.3.3 H-H Recombination .....	107
6.3.4 Transition State Energy Comparison .....	109
6.3.5 Microkinetic Simulation of Catalytic Activity and Selectivity.....	112

6.3.6 Catalyst Stability under Reaction Conditions .....	118
6.3.7 Origin of Catalytic Activity .....	119
6.4 Conclusion .....	122
Chapter 7 Conclusion .....	125
Appendix A Supplementary Information for Chapter 2 .....	132
A.1 Supplementary Energetics and Adsorption Configurations .....	132
A.2 Detailed Description of the Microkinetic Model .....	135
A.3 1-Hexyne Hydrogenation Reactivity and Selectivity at Higher Conversion .....	137
A.4 Reaction Pathway Selectivity in 1-Hexyne Hydrogenation .....	138
A.5 Degree of Rate Control of Intermediate States in the Reaction Network .....	139
A.6 Chemical Potentials .....	139
A.7 Electronic Structure of Pd(111) and Pd <sub>1</sub> Au(111) .....	140
Appendix B Supplementary Information for Chapter 3 .....	141
B.1 Experimental Results .....	141
B.2 Supplementary Adsorption Configurations .....	142
B.3 Detailed Description of Microkinetic Model .....	142
B.4 Degree of Selectivity Control .....	145
B.5 Additional Microkinetic Simulations .....	146
B.6 Binding Strengths of Carbonaceous Species .....	147
Appendix C Supplementary Information for Chapter 4 .....	148
C.1 Detailed Description of Microkinetic Model .....	148
C.2 Supplementary Energetics and Adsorption Configurations .....	151
C.3 Catalyst Surface Coverage .....	161

C.4 Degree of Rate Control of Surface Intermediates and Apparent Activation Energies ·	162
C.5 Reaction Network of Acetylene Hydrogenation on Pd <sub>3</sub> ·····	165
C.6 Ensemble Size Distribution in Pd-Au Catalyst·····	166
Appendix D Supplementary Information for Chapter 5 ·····	167
D.1 Detailed Description of Microkinetic Model ·····	167
D.2 Supplementary Energetics and Adsorption Configurations ·····	168
D.3 Degree of Rate and Selectivity Controls ·····	173
D.4 Additional Microkinetic Simulations ·····	176
D.5 Magnetization of Dopants in Cu(111) ·····	177
Appendix E Supplementary Information for Chapter 6·····	178
E.1 Detailed Description of Microkinetic Model ·····	178
E.2 Supplementary Energetics and Adsorption Configurations·····	181
E.3 Additional Microkinetic Simulations ·····	191
Bibliography ·····	192

## List of Figures

- Figure 1.1. Schematic representation of the formation of a single-atom alloy catalyst. .... 2
- Figure 2.1. Schematic representation of the course of 1-hexyne hydrogenation. The bottommost pathway shows  $H_2$  dissociation and subsequent migration to supply H atoms for 1-hexyne hydrogenation on another  $Pd_1Au(111)$  site. 1-Hexyne can be hydrogenated either by fully hydrogenating one of the two unsaturated carbon atoms followed by the remaining one (left) or by alternately hydrogenating the two carbon atoms (right). The former is detrimental to selectivity as it skips 1-hexene formation and produces hexyls directly through 1-hexylidene. Double-headed and single-headed arrows indicate reversibility and irreversibility, respectively, based on experiments and theory in this chapter. .... 12
- Figure 2.2. (a) Enthalpy and (b) free energy profiles for hydrogen dissociation and migration on the  $Pd_1$ -in-Au(111) surface. All species are chemisorbed, unless indicated by (g) for gas phase species. (c) Structure of each intermediate and transition state along the energy profiles. Conditions used for the free energy calculations are  $T = 363$  K and  $P(H_2) = 0.2$  bar.  $H_2$ : molecular adsorption mode of  $H_2$ ; TS-Dis:  $H_2$  dissociation transition state; 2H: dissociated  $H_2$  into two H atoms adsorbed in  $Pd_1$ -Au<sub>2</sub> fcc hollow sites; TS-M: transition state for migration of one H atom toward the Au region; H(Pd,Au): adsorption of one H atom in the  $Pd_1$ -Au<sub>2</sub> fcc hollow site and one in the Au fcc hollow site. .... 16
- Figure 2.3. Free energy diagram for 1-hexyne hydrogenation to form 1-hexene on the  $Pd_1Au(111)$  surface. The butyl group attached to  $C\equiv C$  bond is abbreviated as R. All species are chemisorbed, unless indicated by (g) for gas phase species.  $H_2$  dissociation occurs on another Pd site, with migration of one H over the Au toward the Pd site where the 1-hexyne is adsorbed. This process is lumped into one effective activation barrier of 0.86 eV labeled as  $H_2$ -Diss. The green and red

pathways represent the hydrogenation of the terminal carbon atom ( $C_1$ ) and the carbon atom attached to the butyl group ( $C_2$ ), respectively, in the first reaction step, followed by the hydrogenation of the remaining carbon atom. The newly added H atoms are indicated in red or green. Reaction conditions are  $T = 363$  K,  $P(H_2) = 0.2$  bar,  $P(C_6H_{10}) = 0.01$  bar,  $P(C_6H_{12}) = P(C_6H_{14}) = 0.001$  bar. .... 18

Figure 2.4. Microkinetic simulations of 1-hexyne hydrogenation to 1-hexene and n-hexane under a typical experimental reaction environment corresponding to low ( $< 20\%$ ) conversion:  $P(H_2) = 0.2$  bar,  $P(1\text{-hexyne}) = 0.01$  bar,  $P(1\text{-hexene}) = P(n\text{-hexane}) = 0.001$  bar. (a) rate ( $s^{-1}$ ) for the conversion of 1-hexyne (blue line) and selectivity for the formation of 1-hexene and n-hexane (red lines) as a function of temperature. The selectivity for 1-hexene was found to be above 98% through the temperature range  $T = 313 - 413$  K. (b) Steady-state fraction of reactive intermediates on  $Pd_1Au(111)$  as a function of temperature: adsorbed 1-hexyne (orange line) and 1-hexene (purple line) were found to be the most abundant reactive intermediates until 353 K. (c) Schematics of structures in panel (b). .... 23

Figure 2.5. Analysis of the kinetics for hydrogenation of 1-hexyne shows  $H_2$  dissociation to be the rate-controlling step. (a) Apparent activation enthalpy (blue line) and kinetic orders of  $H_2$  (black solid line), 1-hexyne (dot-dashed line), and 1-hexene (dashed line) for the hydrogenation of 1-hexyne as a function of temperature. The apparent activation enthalpy of the reaction progressively decreases in the temperature range  $T = 313 - 413$  K, while the orders of 1-hexyne and 1-hexene increase. (b) Degree of rate control (DRC) of various transition states as a function of temperature. The transition state for  $H_2$  dissociation is the main rate-controlling transition state (red line), while the migration of H from the Pd single atom to the Au substrate (orange line) is second in importance. Importantly, C-H bond formation steps (green and purple lines) do not appear to be rate-controlling.

(c) Schematics of the four elementary steps shown in panel (b). ..... 25

Figure 2.6. Destabilization of hydrocarbon intermediates and transition states energy by 0.2 eV enables an improved agreement with the experiment for the kinetic order of 1-hexyne and the apparent activation enthalpy. (a) Apparent activation enthalpy (eV) of 1-hexyne hydrogenation as a function of temperature without (full line) and with (dashed line) destabilization of surface  $C_6H_x$  intermediates and transition states. The experimental value (+0.39 eV, reported in ref 64) is shown as a green horizontal bar. (b) Orders of reaction of  $H_2$  (blue) and 1-hexyne (red) as a function of temperature without (full line) and with (dashed line) destabilization of surface  $C_6H_x$  intermediates and transition states. Experimental values (order of  $H_2$ : 0.94, order of 1-hexyne: -0.08, reported in ref 64) are shown as triangles. .... 28

Figure 2.7. Degree of selectivity control (DSC), evaluated at  $T = 373$  K,  $P(H_2) = 0.2$  bar,  $P(1\text{-hexyne}) = 0.01$  bar,  $P(1\text{-hexene}) = 0.001$  bar, of the TS for  $H_2$  dissociation over  $Pd_1$  ( $DSC = -2.75 \times 10^{-3}$ ), 1-hexyne hydrogenation to 1-hexenyl ( $DSC = 8.24 \times 10^{-3}$ ), and 1-hexyl hydrogenation to n-hexane ( $DSC = -2.46 \times 10^{-3}$ ). The values were multiplied by 100 in the figure. Decreasing the free energy barrier for 1-hexyne hydrogenation to 1-hexenyl increases the selectivity for 1-hexene, while decreasing the free energy barrier of  $H_2$  dissociation and 1-hexyl hydrogenation to n-hexane decreases the selectivity for 1-hexene. .... 29

Figure 3.1. Free-energy profiles for (a) 1-hexene hydrogenation and (b) isomerization to 2-hexene calculated using DFT. The abbreviation R represents the butyl group attached to the C=C bond. Two different hydrogenation pathways are shown in (a): the green pathway first hydrogenates the terminal carbon atom of 1-hexene to form 2-hexyl while the red pathway first hydrogenates the carbon atom which is attached to the butyl group R to form 1-hexyl. Both pathways finish by hydrogenating the remaining unsaturated carbon atom in the hexyl intermediates. The H atoms

newly added to the unsaturated hydrocarbons are denoted in red or green. Reaction conditions are  $T = 363 \text{ K}$ ,  $P(\text{H}_2) = 0.2 \text{ bar}$ ,  $P(1\text{-hexene}) = 0.01 \text{ bar}$ ,  $P(2\text{-hexene}) = 0.001 \text{ bar}$ , and  $P(\text{n-hexane}) = 0.001 \text{ bar}$ . ..... 40

Figure 3.2. 1-Hexene consumption rate, product selectivity, and degrees of rate control (DRC) of transition states for 1-hexene consumption evaluated for the  $\text{Pd}_1\text{Au}(111)$  model catalyst at fixed partial pressures. Microkinetic model of the 1-hexene reaction with  $\text{H}_2$  evaluated at  $P(\text{H}_2) = 0.2 \text{ bar}$ ,  $P(1\text{-Hexene}) = 0.01 \text{ bar}$ , and  $P(2\text{-Hexene}) = P(\text{n-Hexane}) = 0.001 \text{ bar}$ . (a) Rate of 1-hexene consumption, (b) selectivity of 2-hexene and n-hexane formation, and (c) main rate-controlling transition states (TS) and their DRC for 1-hexene consumption as functions of temperature. (d) Schematic representations of the elementary steps corresponding to the transition states in panel (c). The reaction was found to start at  $\sim 350 \text{ K}$  with 2-hexene as the minority product and  $\text{H}_2$  dissociation as the main rate-controlling TS. .... 43

Figure 3.3. Product and isotope selectivity of 1-hexene deuteration and isomerization, with the barriers of  $\text{H}_2$  dissociation and H-spillover increased by  $0.1 \text{ eV}$ . (a) 1-Hexene conversion and (b) selectivity of 2-hexene and n-hexane as functions of reactor temperature. (c) 1-Hexene isotope distribution, (d) 2-hexene isotope distribution, and (e) n-hexane isotope distribution as functions of 1-hexene conversion. The PFR, with  $200 \text{ mg}$  of catalyst loading, was assumed to operate at constant temperature and pressure ( $1 \text{ bar}$ ). The 1-hexene conversion and product/isotope selectivity were evaluated under an inlet flow of  $50 \text{ standard mL/min}$  (corresponding to the standard condition of  $T = 273.15 \text{ K}$  and  $P = 1 \text{ atm}$ ), consisting of  $1 \text{ vol } \% 1\text{-hexene}$  and  $20 \text{ vol } \% \text{D}_2$  with an inert balance. .... 46

Figure 4.1. Measurements of the rate of 1-hexyne conversion (bars) and selectivity (gray diamonds) for 1-hexene production. An optimum in the rate of 1-hexyne conversion is achieved for

Au<sub>0.96</sub>Pd<sub>0.04</sub>. Reproduced from ref 64. Copyright 2020 American Chemical Society. .... 49

Figure 4.2. Schematic representation of the regular pathway, where acetylene adsorbs on one Pd<sub>n</sub> site, H<sub>2</sub> adsorbs and dissociates on another Pd<sub>n</sub> site, and H migrates over Au to reach the adsorbed acetylene and perform the successive hydrogenation steps; the no-migration pathway where for Pd<sub>3</sub> acetylene adsorbs on one Pd<sub>3</sub> site and H<sub>2</sub> subsequently adsorbs and dissociates on the same Pd<sub>3</sub> – C<sub>2</sub>H<sub>2</sub>\* site; the special pathway where acetylene adsorbs on a Pd<sub>3</sub> site occupied by one H adatom (noted ([H<sup>3</sup> – Pd<sub>3</sub>])). For simplicity, only the first half of the hydrogenation reaction (C<sub>2</sub>H<sub>2</sub> → C<sub>2</sub>H<sub>4</sub>) is shown in the latter two pathways as the second half (C<sub>2</sub>H<sub>4</sub> → C<sub>2</sub>H<sub>6</sub>) follows the same pattern. An asterisk indicates the surface species. .... 55

Figure 4.3. Reaction rates (a-c) and degree of rate controls (DRCs) of transition states (d-f) for acetylene hydrogenation on Pd<sub>1</sub> (a, d), Pd<sub>2</sub> (b, e), and Pd<sub>3</sub> (c, f) calculated using microkinetic simulations. Hydrocarbon co-adsorbing with an H atom on a Pd ensemble in the regular pathway is denoted as [C<sub>2</sub>H<sub>x</sub>(H) – Pd<sub>y</sub>]. Note that [H – C<sub>2</sub>H<sub>3</sub> – Pd<sub>3</sub>] also represents the co-adsorption of C<sub>2</sub>H<sub>3</sub> with an H atom, but its configuration differs from that in the regular pathway (see Figure C.6, C.7, and C.13). The number superscripted next to H in (e) is the coordination number of the H atom with the Pd atoms in the absence of any hydrocarbon. Only elementary steps with significant DRCs are shown in (d-f). The calculations were performed at P(C<sub>2</sub>H<sub>2</sub>) = 0.01 bar, P(H<sub>2</sub>) = 0.2 bar, P(C<sub>2</sub>H<sub>4</sub>) = 0.001 bar, and P(C<sub>2</sub>H<sub>6</sub>) = 0.001 bar. .... 57

Figure 4.4. Degree of selectivity controls (DSCs) of transition states for acetylene hydrogenation on (a) Pd<sub>1</sub>, (b) Pd<sub>2</sub>, and (c) Pd<sub>3</sub> calculated using microkinetic simulations. On Pd<sub>3</sub>, steps with positive DSCs include C<sub>2</sub>H<sub>4(g)</sub> + [H<sup>3</sup> – Pd<sub>3</sub>] ⇌ [C<sub>2</sub>H<sub>4</sub>(H) – Pd<sub>3</sub> – SP] (blue square), C<sub>2</sub>H<sub>4(g)</sub> + [Pd<sub>3</sub>] ⇌ [C<sub>2</sub>H<sub>4</sub> – Pd<sub>3</sub>] (blue circle), and [C<sub>2</sub>H<sub>2</sub>(H) – Pd<sub>3</sub>] ⇌ [C<sub>2</sub>H<sub>3</sub> – Pd<sub>3</sub>] (red curve). Steps with negative DSCs, on the other hand, include [H<sub>2</sub> – C<sub>2</sub>H<sub>2</sub> – Pd<sub>3</sub>] ⇌ [H – H – C<sub>2</sub>H<sub>2</sub> – Pd<sub>3</sub>] (black triangle up),

$[H_2 - C_2H_4 - Pd_3] \rightleftharpoons [H - H - C_2H_4 - Pd_3]$  (black triangle down),  $[C_2H_4(H) - Pd_3] \rightleftharpoons [C_2H_5 - Pd_3]$  (dark red circle),  $[C_2H_4(H) - Pd_3 - SP] \rightleftharpoons [C_2H_5 - Pd_3]$  (dark red square), and  $[H - H - C_2H_4 - Pd_3] \rightleftharpoons [C_2H_5(H) - Pd_3]$  (dark red triangle up). Note that the curves of  $H_2$  dissociation in the presence of ethylene (black triangle down) and the subsequent C-H bond formation (dark red triangle up) overlap in (c). For simplicity, elementary steps with negligible DSCs are excluded in the results. The calculation was evaluated at:  $P(C_2H_2) = 0.01$  bar,  $P(H_2) = 0.2$  bar,  $P(C_2H_4) = 0.001$  bar, and  $P(C_2H_6) = 0.001$  bar. .... 62

Figure 5.1. Schematic diagram demonstrating the C=O and C=C binding modes of acrolein on a single-atom alloy catalyst. .... 67

Figure 5.2. Schematic diagram showing the processes of segregation and aggregation of dopants in dilute alloy catalysts. Segregation is used to bring the dopant atom from the subsurface layer to the surface layer, and aggregation is used to bring two isolated surface dopant atoms (monomers) together to form a dimer. .... 68

Figure 5.3. Segregation (tan) and aggregation (green) energies of various transition metals in Cu(111). Negative segregation energies indicate that segregation is favorable, while positive aggregation energies imply that aggregation is unfavorable. .... 75

Figure 5.4. Adsorption electronic energies of acrolein on early-, mid-, and late-transition metals in Cu(111) with the C=O (blue, C=O binding mode) and C=C (red, C=C binding mode) bonds on top of the dopant atom. No adsorption energy is reported for the C=C binding mode on early transition metals, as this configuration is not a metastable state on them and transforms into the C=O binding mode. .... 76

Figure 5.5. Free energy profile for acrolein hydrogenation on  $CuTi_1$  (green),  $CuZr_1$  (blue), and  $CuHf_1$  (red). (b) Corresponding reaction configurations on  $CuTi_1$ . Transition states are omitted in

this study for simplicity. Reaction conditions are  $T = 375$  K,  $P(\text{acrolein}) = 0.1$  bar,  $P(\text{H}_2) = 300$  bar, and  $P(\text{propenol}) = P(\text{propanal}) = 0.01$  bar. .... 78

Figure 5.6. (a) Free energy profile for hydrogenation of the C=O bond (blue) and C=C bond (red) in acrolein on CuCr<sub>1</sub>. (b) Configurations of the corresponding reaction intermediates and transition states along the energy profile. Reaction conditions are  $T = 375$  K,  $P(\text{acrolein}) = 0.1$  bar,  $P(\text{H}_2) = 300$  bar,  $P(\text{propanal}) = 0.01$  bar, and  $P(\text{propenol}) = 0.01$  bar. .... 80

Figure 5.7. Selectivity for propenol formation on CuCr<sub>1</sub> as a function of temperature. Reaction conditions are  $P(\text{acrolein}) = 0.1$  bar,  $P(\text{H}_2) = 300$  bar,  $P(\text{propanal}) = 0.01$  bar, and  $P(\text{propenol}) = 0.01$  bar. .... 84

Figure 5.8. Electronic energies and the corresponding configurations of the transition states for C=O (blue) and C=C (red) hydrogenation on CuNi<sub>1</sub>. .... 90

Figure 5.9. Crystal Orbital Hamilton Population (COHP) curves of the interactions between the O atom in acrolein and the three different dopant elements in Cu(111): Hf, Cr, and Ni. .... 91

Figure 6.1. (a) Free energy profile and (b,c) corresponding adsorption configurations for propane dehydrogenation on CuHf<sub>1</sub>. Side view of the transition states is provided in Figure S1. Red and blue sections along the pathway indicate dehydrogenation at the terminal or central carbon atoms as the first step, respectively. For better visibility, the H atoms that are being detached in the transition states are colored in red or blue, accordingly, and in black for further dehydrogenation beyond propene. Reaction conditions are:  $T = 773$  K,  $P(\text{C}_3\text{H}_8) = 0.64$  bar,  $P(\text{H}_2) = 0.36$  bar, and  $P(\text{C}_3\text{H}_6) = 0.11$  bar. .... 104

Figure 6.2. (a) Free energy profile and (b) corresponding adsorption configurations for H atoms recombination on CuHf<sub>1</sub>. Reaction conditions are:  $T = 773$  K and  $P(\text{H}_2) = 0.36$  bar. .... 107

Figure 6.3. (a) Free energies of the transition states for the steps of initial C-H bond cleavage and subsequent H-migration away from the active ensembles. Note that H-migration steps are not considered for Pt(111) due to the homogeneous nature of the surface. The free energies of the H-migration transition states were obtained by adding the activation barriers, which are the energy differences between “C<sub>3</sub>H<sub>7</sub> + TS-M (in the absence of the H residing on the active ensemble)” and “C<sub>3</sub>H<sub>7</sub> + H”, to “C<sub>3</sub>H<sub>7</sub> + H”, to “C<sub>3</sub>H<sub>7</sub> + H”. A schematic diagram for this process is provided in Figure E.7. (b) Corresponding adsorption configurations of the transition states for the initial C-H bond cleavage steps on the four catalyst surfaces, along with the lengths of the C-H bonds that are being cleaved listed. Side view of these transition states can be found in Figures S1, S3, S5 and S6. Blue and red colors for bars and frames represent the pathways in which the central or terminal carbon atoms of propane are dehydrogenated as the first step, respectively. The H atoms that are being detached are highlighted in blue or red accordingly. Reaction conditions are: T = 773 K, P(C<sub>3</sub>H<sub>8</sub>) = 0.64 bar, P(H<sub>2</sub>) = 0.36 bar, and P(C<sub>3</sub>H<sub>6</sub>) = 0.11 bar. .... 109

Figure 6.4. Degree of rate control of the transition states for the steps of initial C-H bond cleavage and subsequent H-migration away from the active ensembles. Note that H-migration steps are not considered for Pt(111) due to the homogeneous nature of the surface. Reaction conditions are: T = 773 K, P(C<sub>3</sub>H<sub>8</sub>) = 0.64 bar, P(H<sub>2</sub>) = 0.36 bar, and P(C<sub>3</sub>H<sub>6</sub>) = 0.11 bar. .... 112

Figure 6.5. Steady-state surface coverage of reaction intermediates on (a) CuHf<sub>1</sub> and (b) CuIr<sub>1</sub> as a function of temperature. Reaction conditions are: P(C<sub>3</sub>H<sub>8</sub>) = 0.64 bar, P(H<sub>2</sub>) = 0.36 bar, and P(C<sub>3</sub>H<sub>6</sub>) = 0.11 bar. .... 115

Figure 6.6. Steady-state rate of propylene production on the four catalyst surfaces. Blue represents the production rate at a lower temperature of 723 K and brown is at a higher temperature of 773 K. Pressures of reactants and products are: P(C<sub>3</sub>H<sub>8</sub>) = 0.64 bar, P(H<sub>2</sub>) = 0.36 bar, and P(C<sub>3</sub>H<sub>6</sub>) =

0.11 bar..... 116

Figure 6.7. Energy of interaction (absolute value, green) between propane and the surface in the geometry of the transition states for initial C-H bond cleavage, and energy of deformation (brown) of propane in the same transition state geometry. .... 119

Figure 6.8. Crystal Orbital Hamilton Population (COHP) for the interactions between the dopants (Hf and Rh) alloyed in Cu(111) and the C (blue) or H (red) atoms in the transition states associated with the first C-H bond cleavage producing  $\text{CH}_3\text{CHCH}_3$ . .... 121

Figure A.1. Adsorption configuration of the carbonaceous intermediates on  $\text{Pd}_1\text{Au}(111)$  for (a) the hydrogenation of the terminal carbon atom ( $\text{C}_1$ ) in the first reaction step, followed by the hydrogenation of the carbon atom attached to the butyl group ( $\text{C}_2$ ) and for (b) the hydrogenation of  $\text{C}_2$  in the first step, followed by the hydrogenation of  $\text{C}_1$ ..... 132

Figure A.2. Free energy diagram of 1-hexyl formation via 1-hexylidene on the  $\text{Pd}_1\text{Au}(111)$  surface. The  $\text{C}_2$  atom was chosen in the first place for the over-hydrogenation as there is electron donation from the carbon chain to help stabilize the transition state. The barrier for the forward hydrogenation of 1-hexylidene ( $\text{RHHCCCH}$ ) is 0.33 eV higher than the reverse barrier. In addition, this side-pathway has an overall free energy barrier (1.09 eV) that is at least 0.26 eV higher than that of the regular pathway to form 1-hexyl via 1-hexene (0.83 eV). Hence, this pathway is energetically unfavorable and is unlikely to deteriorate the selectivity for 1-hexene formation. Conditions are:  $T = 363 \text{ K}$ ,  $P(\text{H}_2) = 0.2 \text{ bar}$ ,  $P(\text{C}_6\text{H}_{10}) = 0.01 \text{ bar}$ ,  $P(\text{C}_6\text{H}_{12}) = P(\text{C}_6\text{H}_{14}) = 0.001 \text{ bar}$ . .... 133

Figure A.3. (a) Free energy diagram and (b) the corresponding configurations of 1-hexyne hydrogenation to form 1-hexene on  $\text{Pd}(111)$ . The butyl group attached to  $\text{C}\equiv\text{C}$  bond is abbreviated as R. For simplicity, only the first hydrogenation step is detailed. Reaction conditions are:  $T = 363$

K,  $P(\text{H}_2) = 0.2$  bar,  $P(\text{C}_6\text{H}_{10}) = 0.01$  bar,  $P(\text{C}_6\text{H}_{12}) = P(\text{C}_6\text{H}_{14}) = 0.001$  bar. All species are chemisorbed, unless indicated by (g) for gas phase species. .... 135

Figure A.4. Microkinetic simulations performed in the temperature range of 323-373 K at a constant inlet flow rate (50 SCCM, 20%  $\text{H}_2$ , 1% 1-Hexyne, balance inert) and catalyst loading (20 mg). (a) 1-Hexyne conversion (black circles, full line), 1-hexene selectivity (blue triangles, dashed line), and 1-hexyne selectivity (blue squares, dashed line) as a function of reactor temperature. (b) 1-Hexene selectivity plotted against 1-hexyne conversion. .... 137

Figure A.5. Pathway selectivity for (a) the formation of 1-hexene through the hydrogenation of adsorbed 1-hexyne to 1-hexenyl ( $r_9$ , blue) and through the hydrogenation of adsorbed 1-hexyne to 2-hexenyl ( $r_{14}$ , orange), and (b) the formation of n-hexane through the hydrogenation of adsorbed 1-hexene to 1-hexyl ( $r_{16}$ , blue), through the hydrogenation of adsorbed 1-hexene to 1-hexyl ( $r_{23}$ , orange), and through the hydrogenation of 1-hexenyl to 1-hexylidene and then 1-hexyl ( $r_{27}$ , green). .... 138

Figure A.6. The degrees of rate control of key intermediate states in the hydrogenation of 1-hexyne to 1-hexene. Adsorbed 1-hexyne (orange line) and 1-hexene (purple line) are the main rate-controlling intermediates until 353 K, largely mirroring the influence of temperature on coverages. .... 139

Figure A.7. The chemical potentials of 1-hexyne (blue) and 1-hexene (red) as functions of temperature at fixed pressures (1 kPa for both 1-hexyne and 1-hexene), compared to their adsorption enthalpies measured by TPD (dashed lines) and their adsorption energies calculated by the optPBE XC functional (dots). .... 139

Figure A.8. Projected density of states (DOS) onto the Pd 4d orbitals of a single Pd atom on the surface of (a) Pd(111) and (b) Pd<sub>1</sub>Au(111). The first moment of the Pd 4d states (d band center) in

two situations is not very different. ....	140
Figure B.1. Deuterium incorporation in the hexene isomers and n-hexane for the Pd <sub>4</sub> Au <sub>96</sub> and Pd catalysts. Product selectivity to (a) 1-hexene d <sub>0</sub> and d <sub>1</sub> , and (b) n-hexane d <sub>0</sub> – d <sub>3</sub> . The catalytic data were measured under steady-state conditions at 373 K (Pd <sub>4</sub> Au <sub>96</sub> ) and 320 K (Pd) in 1 vol % 1-hexene and 20 vol % D <sub>2</sub> in Ar, with a total flow of 50 mL/min using a catalyst bed of 20 mg of 4.2 wt % Pd <sub>4</sub> Au <sub>96</sub> and 2 mg of 0.6 wt % Pd. ....	141
Figure B.2. Adsorption configurations of the reactant, the intermediates, and the products on Pd <sub>1</sub> Au(111) for the hydrogenation of 1-hexene to n-hexane via the 1-hexyl (a) and 2-hexyl (b) intermediates, and (c) isomerization of the 2-hexyl intermediate to 2-hexene. ....	142
Figure B.3. Degree of selectivity control (DSC) of selected TS for 2-hexene formation evaluated at fixed partial pressures. DSC for 2-hexene formation evaluated at T = 373 K, P(H <sub>2</sub> ) = 0.2 bar, P(1-hexene) = 0.01 bar, and P(2-hexene) = P(n-hexane) = 0.001 bar. The TS of H <sub>2</sub> dissociation (DSC = -0.57) and H spillover to 2-hexyl (DSC = -0.57) have the most negative impact on the selectivity of 2-hexene, while the TS of the hydrogenation of 1-hexene to 2-hexyl (DSC = 0.93) and the dehydrogenation of 2-hexyl to 2-hexene (DSC = 0.69) have the most positive impact on the selectivity of 2-hexene. ....	145
Figure B.4. 1-Hexene consumption rate and product selectivity evaluated at fixed partial pressures after increasing the barriers of H <sub>2</sub> dissociation and H spillover by 0.1 eV. Microkinetic model of 1-hexene reaction with H <sub>2</sub> evaluated at P(H <sub>2</sub> ) = 0.2 bar, P(1-hexene) = 0.01 bar, and P(2-hexene) = P(n-hexane) = 0.001 bar. (a) Rate of 1-hexene consumption, (b) selectivity of 2-hexene and n-hexane. ....	146
Figure B.5. Plug flow reactor (PFR) simulations of product and isotope selectivity of 1-hexene deuteration and isomerization without shifts to the barrier of H <sub>2</sub> dissociation and spillover. (a) 1-	

Hexene conversion and (b) selectivity of 2-hexene and n-hexane as functions of reactor temperature. (c) 1-Hexene isotope distribution, (d) 2-hexene isotope distribution, and (e) n-hexane isotope distribution as functions of 1-hexene conversion. .... 146

Figure C.1. (a) Free energy profile and (b) corresponding adsorption configurations of  $H_2$  dissociation and migration on  $Pd_1$  evaluated at  $T = 363$  K and under the standard-state pressures of the gaseous species. TS-D and TS-M stand for the transition states for dissociation and migration, respectively.  $H-Pd_1$  indicates that the H atom is singly-coordinated to Pd. Color codes: Green (Pd), Gold (Au), and White (H). .... 152

Figure C.2. (a) Free energy profile and (b) corresponding adsorption configurations of acetylene hydrogenation on  $Pd_1$  evaluated at  $T = 363$  K and under the standard-state pressures of the gaseous species. Color codes: Green (Pd), Gold (Au), Dark Brown (C), and White (H). .... 153

Figure C.3. (a) Free energy profile and (b) corresponding adsorption configurations of  $H_2$  dissociation and migration on  $Pd_2$  evaluated at  $T = 363$  K and under the standard-state pressures of the gaseous species. TS-D and TS-M stand for the transition states for dissociation and migration, respectively.  $H^2-Pd_2$  and  $H^1-Pd_2$  mean that the H atom is doubly and singly-coordinated to Pd. Color codes: Green (Pd), Gold (Au), and White (H). .... 154

Figure C.4. (a) Free energy profile and (b) corresponding adsorption configurations of acetylene hydrogenation on  $Pd_2$  evaluated at  $T = 363$  K and under the standard-state pressures of gaseous species. Color codes: Green (Pd), Gold (Au), Dark Brown (C), and White (H). .... 155

Figure C.5. (a) Free energy profile and (b) corresponding adsorption configurations of  $H_2$  dissociation and migration on  $Pd_3$  evaluated at  $T = 363$  K and under the standard-state pressures of gaseous species. TS-D and TS-M stand for the transition states for dissociation and migration, respectively.  $H^3-Pd_3$  and  $H^1-Pd_3$  mean that the H atom is triply and singly-coordinated to Pd. The

migration barrier of the triply-coordinated H atom toward the Au site is large with the value being 0.77 eV. Color codes: Green (Pd), Gold (Au), and White (H). ..... 156

Figure C.6. (a) Free energy profile and (b) corresponding adsorption configurations of acetylene hydrogenation on Pd<sub>3</sub> evaluated at T = 363 K and under the standard-state pressures of the gaseous species. The inset in (a) is the special pathway when an ethylene molecule adsorbs onto a Pd<sub>3</sub> ensemble in the presence of a triply-coordinated H atom. Subsequent hydrogenation would eventually lead this pathway to the C<sub>2</sub>H<sub>5</sub> state in the regular pathway. Color codes: Green (Pd), Gold (Au), Dark Brown (C), and White (H). ..... 157

Figure C.7. (a) Free energy profile and (b) corresponding adsorption configurations of acetylene hydrogenation on Pd<sub>3</sub> evaluated at T = 363 K and under the standard-state pressures of gaseous species. This is the no-migration pathway which considers the dissociation of H<sub>2</sub> (transition state for dissociation is represented as TS-D) on the same Pd<sub>3</sub> ensemble on which an acetylene or ethylene molecule already resides. The inset shows the special pathway in which an acetylene molecule adsorbs onto a Pd<sub>3</sub> ensemble in the presence of a triply-coordinated H atom. This special pathway ultimately leads to the [C<sub>2</sub>H<sub>3</sub> + H (2)] state in the no-migration pathway. Color codes: Green (Pd), Gold (Au), Dark Brown (C), and White (H). ..... 159

Figure C.8. (a) Free energy profile and (b) corresponding adsorption configurations of ethylenyl hydrogenation to form ethyl via ethylidyne on Pd<sub>3</sub> evaluated at T = 363 K and under the standard-state pressures of gaseous species. Note that this reaction pathway was not included in the microkinetic modeling as it is significantly less favorable than the regular pathway to form C<sub>2</sub>H<sub>5</sub>. ..... 160

Figure C.9. Surface coverage of the active sites of the dilute Pd-in-Au alloy catalyst at steady states as a function of temperature. The study was performed under the following conditions: P(H<sub>2</sub>) =

0.2 bar,  $P(\text{C}_2\text{H}_2) = 0.01$  bar,  $P(\text{C}_2\text{H}_4) = 0.001$  bar and  $P(\text{C}_2\text{H}_6) = 0.001$  bar. .... 161

Figure C.10. (a) Degree of rate control of surface intermediates and (b) apparent activation energy for acetylene hydrogenation on  $\text{Pd}_1$  calculated using microkinetic simulations. The calculations were performed at  $P(\text{C}_2\text{H}_2) = 0.01$  bar,  $P(\text{H}_2) = 0.2$  bar,  $P(\text{C}_2\text{H}_4) = 0.001$  bar, and  $P(\text{C}_2\text{H}_6) = 0.001$  bar. .... 162

Figure C.11. (a) Degree of rate control of surface intermediates and (b) apparent activation energy for acetylene hydrogenation on  $\text{Pd}_2$  calculated using microkinetic simulations. The calculations were performed at  $P(\text{C}_2\text{H}_2) = 0.01$  bar,  $P(\text{H}_2) = 0.2$  bar,  $P(\text{C}_2\text{H}_4) = 0.001$  bar, and  $P(\text{C}_2\text{H}_6) = 0.001$  bar. .... 163

Figure C.12. (a) Degree of rate control of surface intermediates and (b) apparent activation energy for acetylene hydrogenation on  $\text{Pd}_3$  calculated using microkinetic simulations. The calculations were performed at  $P(\text{C}_2\text{H}_2) = 0.01$  bar,  $P(\text{H}_2) = 0.2$  bar,  $P(\text{C}_2\text{H}_4) = 0.001$  bar, and  $P(\text{C}_2\text{H}_6) = 0.001$  bar. .... 164

Figure C.13. Simplified reaction network of acetylene hydrogenation on  $\text{Pd}_3$ , with the special pathway on top, regular pathway in the middle, and no-migration pathway at the bottom. The thickness of the arrows indicates the magnitude of the reaction rate of each elementary step. Elementary steps with negligible reaction rates are omitted from this reaction network. .... 165

Figure D.1. Reaction configurations for acrolein hydrogenation on (a)  $\text{CuZr}_1$  and (b)  $\text{CuHf}_1$ . · 168

Figure D.2. (a) Free energy profile and (b) corresponding reaction configurations for  $\text{H}_2$  activation on  $\text{CuCr}_1$ . The notations used are defined as:  $\text{H}_2$  – molecular adsorption of hydrogen, TS-Dis – transition state for dissociation,  $2\text{H}$  – co-adsorption of two H atoms on the same  $\text{Cr}_1$  ensemble, TS-M – transition state for migration of one H atom away from the  $\text{Cr}_1$  ensemble, and  $\text{H}(\text{Cr}, \text{Cu})$  – adsorption of one H atom on the  $\text{Cr}_1$  ensemble and the other one on the  $\text{Cu}(111)$  surface. Reaction

conditions are $T = 375$ K and $P(\text{H}_2) = 300$ bar. ....	169
Figure D.3. (a) Free energy profile and (b) corresponding reaction configurations for hydrogenation of the C=O bond (blue) and C=C bond (red) in acrolein on $\text{CuMn}_1$ . Reaction conditions are $T = 375$ K, $P(\text{Acrolein}) = 0.1$ bar, $P(\text{H}_2) = 300$ bar, $P(\text{Propanal}) = P(\text{Propenol}) = 0.01$ bar. ....	170
Figure D.4. (a) Free energy profile and (b) corresponding reaction configurations for $\text{H}_2$ activation on $\text{CuMn}_1$ . The notations used are defined as: $\text{H}_2$ – molecular adsorption of hydrogen, TS-Dis – transition state for dissociation, 2H – co-adsorption of two H atoms on the same $\text{Mn}_1$ ensemble, TS-M – transition state for migration of one H atom away from the $\text{Mn}_1$ ensemble, and H(Mn, Cu) – adsorption of one H atom on the $\text{Mn}_1$ ensemble and the other one on the Cu(111) surface. Reaction conditions are $T = 375$ K and $P(\text{H}_2) = 300$ bar. ....	171
Figure D.5. (a) Free energy profile and (b) corresponding reaction configurations for hydrogenation of the C=O bond (blue) and C=C bond (red) in acrolein on $\text{AuFe}_1$ . Reaction conditions are $T = 375$ K, $P(\text{Acrolein}) = 0.1$ bar, $P(\text{H}_2) = 300$ bar, $P(\text{Propanal}) = P(\text{Propenol}) = 0.01$ bar. ....	172
Figure D.6. Degree of selectivity control (DSC) of the transition states in the reaction network. For simplicity, only the transition states with significant DSC values are shown. Steps in the hydrogenation of the C=O bond and C=C bond of the acrolein molecule are represented in blue and red, respectively. Reaction conditions are: $T = 375$ K, $P(\text{Acrolein}) = 0.1$ bar, $P(\text{H}_2) = 300$ bar, $P(\text{Propanal}) = 0.01$ bar, and $P(\text{Propenol}) = 0.01$ bar. ....	173
Figure D.7. Degree of rate control (DRC) of transition states at (a) $T = 375$ K and (b) $T = 475$ K on $\text{CuCr}_1$ . Steps in the hydrogenation of the C=O bond and C=C bond of the acrolein molecule are represented in blue and red, respectively, whereas the step of $\text{H}_2$ dissociation on Cu(111) is	

represented in brown. The most rate-controlling transition state under both conditions is acrolein adsorption, with the DRC values being close to 1 (0.98 at  $T = 375$  K and 1.00 at  $T = 475$  K). It is omitted in this study to demonstrate the differences between the other steps. Reaction conditions are:  $P(\text{Acrolein}) = 0.1$  bar,  $P(\text{H}_2) = 300$  bar,  $P(\text{Propanal}) = 0.01$  bar, and  $P(\text{Propenol}) = 0.01$  bar. ·

..... 174

Figure D.8. Degree of rate control (DRC; red) of the “2H” state on the Cr active sites and the surface coverage (blue) of H atoms on the catalyst surface. “2H” corresponds to H-adsorption on the Cr active sites and H(Cu) corresponds to the adsorption on the Cu(111) surface. Surface coverage is normalized with respect to the total number of active sites and Cu sites. Reaction conditions are:  $P(\text{Acrolein}) = 0.1$  bar,  $P(\text{H}_2) = 300$  bar,  $P(\text{Propanal}) = 0.01$  bar, and  $P(\text{Propenol}) = 0.01$  bar..... 175

Figure D.9. Calculated selectivity for propenol formation on  $\text{CuCr}_1$  after (a) increasing the diffusion transition state energy by 0.1 eV and (b) lowering the transition state energy for O-H bond formation by 0.1 eV. Reaction conditions are:  $P(\text{Acrolein}) = 0.1$  bar,  $P(\text{H}_2) = 300$  bar,  $P(\text{Propanal}) = 0.01$  bar, and  $P(\text{Propenol}) = 0.01$  bar..... 176

Figure D.10. Magnetization of the dopants (Cr and Mn) in Cu(111) when the surface is bare (orange), and in the presence of acrolein (teal) and mono-hydrogenated intermediate (maroon). Acrolein adopts the C=O binding configuration for this magnetization calculation, and the mono-hydrogenated intermediate reported here is the one formed after hydrogenating the C atom in the C=O bond..... 177

Figure E.1. Side view of the adsorption configurations of the transition states for C-H bond cleavage on  $\text{CuHf}_1$ . The H atoms that are being detached are colored in blue and red..... 181

Figure E.2. (a) Free energy profile and (b) corresponding adsorption configurations for H atoms

recombination on CuIr<sub>1</sub>. Reaction conditions are: T = 773 K, P(H<sub>2</sub>) = 0.36 bar. .... 182

Figure E.3. (a) Free energy profile and (b,c,d) corresponding adsorption configurations for propane dehydrogenation on CuIr<sub>1</sub>. A side view is specifically provided in (c) for transition states to facilitate the visualization of the C-H bonds that are being cleaved. Red and blue sections along the pathway indicate dehydrogenation at the terminal or central carbon atoms as the first step, respectively. H atoms that are being detached in the transition states are colored in red or blue, accordingly, and in black for further dehydrogenation beyond propene. Reaction conditions are: T = 773 K, P(C<sub>3</sub>H<sub>8</sub>) = 0.64 bar, P(H<sub>2</sub>) = 0.36 bar, and P(C<sub>3</sub>H<sub>6</sub>) = 0.11 bar. .... 184

Figure E.4. (a) Free energy profile and (b) corresponding adsorption configurations for H atoms recombination on CuRh<sub>1</sub>. Reaction conditions are: T = 773 K, P(H<sub>2</sub>) = 0.36 bar. .... 185

Figure E.5. (a) Free energy profile and (b,c,d) corresponding adsorption configurations for propane dehydrogenation on CuRh<sub>1</sub>. A side view is specifically provided in (c) for transition states to facilitate the visualization of the C-H bonds that are being cleaved. Red and blue sections along the pathway indicate dehydrogenation at the terminal or central carbon atoms as the first step, respectively. H atoms that are being detached in the transition states are colored in red or blue, accordingly, and in black for further dehydrogenation beyond propene. Reaction conditions are: T = 773 K, P(C<sub>3</sub>H<sub>8</sub>) = 0.64 bar, P(H<sub>2</sub>) = 0.36 bar, and P(C<sub>3</sub>H<sub>6</sub>) = 0.11 bar. .... 187

Figure E.6. (a) Free energy profile and (b,c,d) corresponding adsorption configurations for propane dehydrogenation on Pt(111). A side view is specifically provided in (c) for transition states to facilitate the visualization of the C-H bonds that are being cleaved. Red and blue sections along the pathway indicate dehydrogenation at the terminal or central carbon atoms as the first step, respectively. H atoms that are being detached in the transition states are colored in red or blue, accordingly, and in black for further dehydrogenation beyond propene. Reaction conditions are: T

= 773 K, $P(\text{C}_3\text{H}_8) = 0.64$ bar, $P(\text{H}_2) = 0.36$ bar, and $P(\text{C}_3\text{H}_6) = 0.11$ bar. ....	189
Figure E.7. A schematic representation of the calculation of activation barriers for H-migration away from the mono-dehydrogenated intermediate. Note that a bare slab is needed to balance the number of atoms in the calculation. ....	190
Figure E.8. Free energies relative to gaseous propane and corresponding adsorption configurations of the transition states for dehydrogenating propyls in the presence of an H atom. The H atoms that are being detached are marked in red and blue. Reaction conditions are: $T = 773$ K, $P(\text{C}_3\text{H}_8) = 0.64$ bar, $P(\text{H}_2) = 0.36$ bar, and $P(\text{C}_3\text{H}_6) = 0.11$ bar. ....	190
Figure E.9. Steady-state surface coverage of reaction intermediates on (a) $\text{CuRh}_1$ and (b) $\text{Pt}(111)$ as a function of temperature. Reaction conditions are: $P(\text{C}_3\text{H}_8) = 0.64$ bar, $P(\text{H}_2) = 0.36$ bar, and $P(\text{C}_3\text{H}_6) = 0.11$ bar. ....	191

## List of Tables

Table 4.1. Adsorption and Reaction Free Energies of Various Species on Pd <sub>1</sub> , Pd <sub>2</sub> , and Pd <sub>3</sub> at T = 363 K, P(H <sub>2</sub> ) = 0.2 bar, P(C <sub>2</sub> H <sub>2</sub> ) = 0.01 bar, and P(C <sub>2</sub> H <sub>4</sub> ) = P(C <sub>2</sub> H <sub>6</sub> ) = 0.001 bar. ....	54
Table A.1. Free energy values for 1-hexene hydrogenation to form hexane. The same reference for 1-hexyne hydrogenation was used, i.e. 1-hexyne and H <sub>2</sub> in the gas phase. Conditions are: T = 363 K, P(H <sub>2</sub> ) = 0.2 bar, P(C <sub>6</sub> H <sub>10</sub> ) = 0.01 bar, P(C <sub>6</sub> H <sub>12</sub> ) = P(C <sub>6</sub> H <sub>14</sub> ) = 0.001 bar. ....	133
Table A.2. Kinetic parameters, Gibbs free energies of reaction and activation derived from DFT-computed electronic energies evaluated at 363 K and standard pressure (1 bar). The n-butyl tail of gaseous and adsorbed C <sub>6</sub> species is denoted as “R”. Hydrogen atoms co-adsorbed with carbonaceous intermediates are indicated as (H). ....	135
Table B.1. Kinetic rate constants, Gibbs free energies of reaction and of activation derived from DFT-computed electronic energies and evaluated at 373.15 K and standard pressure (1 bar). The n-propyl tail of gaseous and adsorbed C <sub>6</sub> species is denoted as “R”. Steps in bold indicated those not involving deuterium. No shift was applied to the barriers of H <sub>2</sub> /D <sub>2</sub> /HD dissociation or H/D spillover steps. ....	142
Table B.2. Adsorption Internal Energies of 1- and 2-Hexene on a Monometallic Pd(111) and Single Pd Atom on the Au(Pd <sub>1</sub> Au, 111) Surface. The values were computed using density functional theory (DFT) calculations. ....	147
Table C.1. Elementary steps included in the microkinetic simulation of acetylene hydrogenation on Pd <sub>1</sub> in Au(111). For microkinetic simulation of acetylene hydrogenation on Pd <sub>1</sub> , a total of 15 elementary steps were considered. Steps 1, 5, 10, and 15 represent the adsorption/desorption processes while the others are the surface reaction steps. Note that surface species are shown in brackets. [H – Pd <sub>1</sub> ] and [C <sub>2</sub> H <sub>x</sub> – Pd <sub>1</sub> ] stand for the H atom and the hydrocarbon intermediate	

binding to a Pd<sub>1</sub> active site while [H – Au] is that binding to the Au surface. [C<sub>2</sub>H<sub>x</sub>(H) – Pd<sub>1</sub>], on the other hand, corresponds to the co-adsorption of a H atom and a hydrocarbon intermediate C<sub>2</sub>H<sub>x</sub> on the same Pd<sub>1</sub> active site. .... 148

Table C.2. Elementary steps included in the microkinetic simulation of acetylene hydrogenation on Pd<sub>2</sub> in Au(111). A total of 15 elementary steps were considered in the microkinetic simulation of acetylene hydrogenation on Pd<sub>2</sub>. The notations used in Table C.2 are similar to those in Table C.1 except that the surface species are now binding to a Pd<sub>2</sub> ensemble. Note that one of the two H atoms formed after dissociation is doubly-coordinated to Pd while the remaining one is singly-coordinated. The former and the latter are shown as [H<sup>2</sup> – Pd<sub>2</sub>] and [H<sup>1</sup> – Pd<sub>2</sub>], respectively. [H<sup>2</sup> – Pd<sub>2</sub> – H<sup>1</sup>] represents the co-adsorption of the two H atoms on the same Pd<sub>2</sub> site. Note that [Pd<sub>2</sub>] represents a full dimer, not an individual Pd atom in the dimer. .... 149

Table C.3. Elementary steps included in the microkinetic simulation of acetylene hydrogenation on Pd<sub>3</sub> in Au(111). A total of 34 elementary steps were considered for acetylene hydrogenation on Pd<sub>3</sub>. The notations used are similar to the ones used on Pd<sub>1</sub> and Pd<sub>2</sub>. [H – H – C<sub>2</sub>H<sub>2</sub> – Pd<sub>3</sub>] and [H – H – C<sub>2</sub>H<sub>4</sub> – Pd<sub>3</sub>] represent the co-adsorption of two H atoms with acetylene and ethylene on the same Pd<sub>3</sub> ensemble. [H – C<sub>2</sub>H<sub>2</sub> – Pd<sub>3</sub>]/[H – C<sub>2</sub>H<sub>3</sub> – Pd<sub>3</sub>] is also the co-adsorption of an H atom with C<sub>2</sub>H<sub>2</sub>/C<sub>2</sub>H<sub>3</sub>, but it adopts a different configuration from [C<sub>2</sub>H<sub>2</sub>(H) – Pd<sub>3</sub>]/[C<sub>2</sub>H<sub>3</sub>(H) – Pd<sub>3</sub>]. The abbreviations used in the step numbering are: R for the regular pathway, SP for the special pathway, NM for the no-migration pathway and C for the configurational transformation. Note that [Pd<sub>3</sub>] represents a full trimer, not an individual Pd atom in the trimer. .... 150

Table C.4. Probability of Finding Pd as Monomers, Dimers, and Trimers Based on the Binomial Distribution for the Surface Atoms, Assuming a Uniform Distribution of Pd. .... 166

Table D.1. Elementary steps considered in the microkinetic modeling of acrolein hydrogenation

on CuCr<sub>1</sub>. Co-adsorption of a reaction intermediate with a H atom is denoted as [X(H) – Cr<sub>1</sub>] or [(H)X – Cr<sub>1</sub>], where X is the reaction intermediate. The suffixes “OB” and “PB” represent the C=O and C=C binding modes, respectively. A total of 17 elementary steps were considered, where step 1 is the dissociative adsorption of H<sub>2</sub> on Cu(111), steps 2 – 5 are H<sub>2</sub> activation on Cr<sub>1</sub> and subsequent migration towards the Cu surface, steps 6 – 11 represent the hydrogenation of the C=O bond in acrolein, and steps 12 – 17 illustrate the hydrogenation of the C=C bond in the same molecule. .... 167

Table E.1. Elementary steps considered in the microkinetic modeling of propane dehydrogenation on CuHf<sub>1</sub>. Co-adsorption of a reaction intermediate with a H atom is denoted as [X(H) – Hf<sub>1</sub>], where X is the reaction intermediate. A total of 17 elementary steps were considered, where step 1 is the recombination of H atoms on the Cu(111) surface, steps 2-5 are the same process on the active ensemble, step 6 is the adsorption of the propane molecule, steps 7-9 (dehydrogenate central C atom first) and 10-12 (dehydrogenate terminal C atom first) correspond to the two different pathways for propane activation, steps 13-14 are H-migration away from propylene adsorption site, followed by propylene desorption, and steps 15-17 are further dehydrogenation of propylene. 178

Table E.2. Elementary steps considered in the microkinetic modeling of propane dehydrogenation on CuIr<sub>1</sub>. Co-adsorption of a reaction intermediate with a H atom is denoted as [X(H) – Ir<sub>1</sub>], where X is the reaction intermediate. A total of 14 elementary steps were considered, where step 1 is the recombination of H atoms on the Cu(111) surface, steps 2-4 are the same process on the active ensemble, steps 5-7 (dehydrogenate central C atom first) and 8-10 (dehydrogenate terminal C atom first) correspond to the two different pathways for propane activation, steps 11-12 are H-migration away from propylene adsorption site, followed by propylene desorption, and steps 13-14 are further dehydrogenation of propylene. .... 179

Table E.3. Elementary steps considered in the microkinetic modeling of propane dehydrogenation on CuRh<sub>1</sub>. Co-adsorption of a reaction intermediate with a H atom is denoted as [X(H) – Rh<sub>1</sub>], where X is the reaction intermediate. A total of 15 elementary steps were considered, where step 1 is the recombination of H atoms on the Cu(111) surface, steps 2-5 are the same process on the active ensemble, steps 6-8 (dehydrogenate central C atom first) and 9-11 (dehydrogenate terminal C atom first) correspond to the two different pathways for propane activation, steps 12-13 are H-migration away from propylene adsorption site, followed by propylene desorption, and steps 14-15 are further dehydrogenation of propylene. .... 180

Table E.4. Elementary steps considered in the microkinetic modeling of propane dehydrogenation on Pt(111). A total of 8 elementary steps were considered, where step 1 is the recombination of H atoms on the Pt(111) surface, step 2 is the adsorption of the propane molecule, steps 3-4 (dehydrogenate central C atom first) and 5-6 (dehydrogenate terminal C atom first) correspond to the two different pathways for propane activation, step 7 is propylene desorption, and step 8 is the further dehydrogenation of propylene. .... 181

## Acknowledgements

To begin with, I would like to convey my sincerest appreciation to my esteemed advisor, Philippe Sautet, whose direction and steadfast support have been indispensable over the last five years. Philippe's mentorship has been nothing short of invaluable, encompassing not only his exceptional expertise but also his commitment to my academic and personal growth. His profound dedication and encouragement have served as the cornerstone of my journey, consistently steering me towards scholarly excellence. I am very grateful for Philippe's unparalleled mentorship, which has played an integral role in molding me into the researcher I am today.

In addition, I would like to express my gratitude to Geng Sun and Kaining Duanmu for their guidance on conducting DFT simulations on dilute alloys, and to George Yan for his assistance on performing microkinetic modeling. I am also grateful to my experimental collaborators, both domestically and internationally, for their valuable contributions to our joint research efforts.

My heartfelt appreciation also goes to Anastassia Alexandrova, Boris Kozinsky, and Dante Simonetti of my dissertation committee for their dedicated effort, unwavering support, and invaluable guidance throughout every step of my research journey. Additionally, I wish to thank my colleagues for their assistance, both in personal matters and research endeavors. I am especially grateful to Celine Tesvara, Simran Kumari, Dongfang Cheng, and Robert Michael Kowalski for the insightful dialogue, which has significantly contributed to the depth and breadth of my scholarly exploration.

Lastly, I would like to express my profound gratitude to my parents, who have made immense sacrifices and worked tirelessly to support me as I journeyed into adulthood. They have nurtured me with boundless love, and it will forever be ingrained in my heart. In addition to my

parents, I am sincerely thankful to my wife, Huiheng, for her company through triumphs and trials. Her persistent support has been an invaluable source of strength to me. I am very happy to have all of you in my life.

Several chapters in this dissertation contain materials adapted from published and submitted manuscripts with multiple contributing authors, as noted in the following.

Chapter 2 includes figures and text adapted from the article “Hydrogen Dissociation Controls 1-Hexyne Selective Hydrogenation on Dilute Pd-in-Au Catalysts” by Hio Tong Ngan, George Yan, Jessi E. S. van der Hoeven, Robert J. Madix, Cynthia M. Friend, and Philippe Sautet, with permission from the American Chemical Society, *ACS Catal.* **2022**, *12* (21), 13321-13333, <https://doi.org/10.1021/acscatal.2c03560>. P.S., C.M.F., and R.J.M. guided the research. H.T.N. performed the DFT calculations, advised by P.S. G.Y. performed the microkinetic modeling. J.v.d.H. prepared the catalysts and conducted the catalysis experiments. All authors participated in discussions and have approved the final version of the manuscript. This work was supported as part of the Integrated Mesoscale Architectures for Sustainable Catalysis (IMASC), an Energy Frontier Research Center funded by the U.S. Department of Energy, Office of Science, Basic Energy Sciences under Award #DE-SC0012573. The DFT calculations in this work used computational and storage services associated with the Hoffman2 cluster at the UCLA Institute for Digital Research and Education (IDRE), the National Energy Research Scientific Computing Center (NERSC) of the U.S. Department of Energy, and the Bridges-2 cluster through the allocation TG-CHE170060 at the Pittsburgh Supercomputing Center (supported by National Science Foundation award number ACI-1928147) through the Extreme Science and Engineering Discovery Environment (supported by National Science Foundation grant number ACI-1548562).

Chapter 3 includes figures and text adapted from the article “Unraveling 1-Hexene Hydrogenation over Dilute Pd-in-Au Alloys” by Jessi E. S. van der Hoeven, Hio Tong Ngan, George Yan, Joanna Aizenberg, Robert J. Madix, Philippe Sautet, and Cynthia M. Friend, with permission from the American Chemical Society, *J. Phys. Chem. C* **2022**, *126* (37), 15710-15723, <https://doi.org/10.1021/acs.jpcc.2c04982>. C.M.F., P.S., and R.J.M. guided the research. J.E.S.v.d.H. prepared and characterized the catalysts, as advised by J.A., conducted the catalysis experiments, and developed the quantitative data analysis. H.T.N. performed the DFT calculations. G.Y. performed the microkinetic modeling. All authors participated in discussions and the interpretation of the data. J.E.S.v.d.H. wrote the manuscript, with contributions from all authors. This work was supported as part of the Integrated Mesoscale Architectures for Sustainable Catalysis (IMASC), an Energy Frontier Research Center funded by the U.S. Department of Energy, Office of Science, Basic Energy Sciences under award no. DE-SC0012573. The DFT calculations in this work used computational and storage services associated with the Hoffman2 cluster at the UCLA Institute for Digital Research and Education (IDRE), the National Energy Research Scientific Computing Center (NERSC) of the U.S. Department of Energy, and the Bridges-2 cluster at the Pittsburgh Supercomputing Center (supported by National Science Foundation award number ACI-1928147) through the Extreme Science and Engineering Discovery Environment (supported by National Science Foundation grant number ACI-1548562) grant TG-CHE170060. The authors thank Dr. M. Luneau and D. Verbart for their initial 1-hexene hydrogenation work, Dr. S. Dussi for writing the Python code to deconvolute the GC-MS spectra, and Dr. M. Aizenberg for critically reading the manuscript.

Chapter 4 includes figures and text adapted from the article “Influence of Pd Concentration in Au-Pd Nanoparticles for the Hydrogenation of Alkynes” by Alexandre C. Foucher, Hio Tong

Ngan, Tanya Shirman, Amanda Filie, Kaining Duanmu, Michael Aizenberg, Robert J. Madix, Cynthia M. Friend, Joanna Aizenberg, Philippe Sautet, and Eric A. Stach, with permission from the American Chemical Society, *ACS Appl. Nano Mater.* **2023**, *6* (24), 22927-22938, <https://doi.org/10.1021/acsnm.3c04278>. E.A.S. and P.S. guided and supervised the work in the article. A.C.F. and H.T.N. contributed equally to this work. This work was supported as part of the Integrated Mesoscale Architectures for Sustainable Catalysis (IMASC), an Energy Frontier Research Center funded by the U.S. Department of Energy, Office of Science, Basic Energy Sciences under Award #DE-SC0012573. Experiments were also carried out at the Singh Center for Nanotechnology at the University of Pennsylvania, supported by the National Science Foundation (NSF) National Nanotechnology Coordinated Infrastructure Program grant NNCI-1542153. Additional support to the Nanoscale Characterization Facility at the Singh Center has been provided by the Laboratory for Research on the Structure of Matter (MRSEC) supported by the National Science Foundation (DMR-1720530). The DFT calculations used computational and storage services associated with the Hoffman2 cluster at the UCLA Institute for Digital Research and Education (IDRE), the National Energy Research Scientific Computing Center (NERSC) of the U.S. Department of Energy, and the Bridges-2 cluster at the Pittsburgh Supercomputing Center. The authors thank Dr. George Yan for helpful discussions.

Chapter 5 includes figures and text adapted from the article “Tuning the Hydrogenation Selectivity of an Unsaturated Aldehyde via Single-Atom Alloy Catalysts” by Hio Tong Ngan and Philippe Sautet, with permission from the American Chemical Society, *J. Am. Chem. Soc.* **2024**, *146* (4), 2556-2567, <https://doi.org/10.1021/jacs.3c10994>. P.S. guided and supervised the work in the article. H.T.N. performed the DFT calculations, microkinetic modeling, and wrote the manuscript. This work was supported as part of the Integrated Mesoscale Architectures for

Sustainable Catalysis (IMASC), an Energy Frontier Research Center funded by the U.S. Department of Energy, Office of Science, Basic Energy Sciences under Award No. DE-SC0012573. DFT calculations reported in this work used computational and storage resources on the Hoffman2 cluster at the UCLA Institute for Digital Research and Education (IDRE), the National Energy Research Scientific Computing Center (NERSC) of the U.S. Department of Energy, and the Bridges-2 cluster through the allocation CHE170060 at the Pittsburgh Supercomputing Center through ACCESS.

Chapter 6 includes figures and text adapted from the manuscript “Cu-Based Single Atom Alloys as Tunable Catalysts for Selective Propane Dehydrogenation” by Hio Tong Ngan and Philippe Sautet, which was recently submitted to the American Chemical Society. P.S. guided and supervised the research. H.T.N. performed the DFT calculations, microkinetic modeling, and wrote the manuscript. This work was supported as part of the Integrated Mesoscale Architectures for Sustainable Catalysis (IMASC), an Energy Frontier Research Center funded by the U.S. Department of Energy, Office of Science, Basic Energy Sciences under Award No. DE-SC0012573. DFT calculations reported in this work used computational and storage resources on the Hoffman2 cluster at the UCLA Institute for Digital Research and Education (IDRE), the National Energy Research Scientific Computing Center (NERSC) of the U.S. Department of Energy, and the Bridges-2 cluster through the allocation CHE170060 at the Pittsburgh Supercomputing Center through ACCESS.

## Curriculum Vitae

2018 B.S. in Chemical Engineering, University of California, Berkeley, Berkeley, California

### Awards

2023 UCLA Dissertation Fellowship

### Publications at UCLA

1. **Ngan, H. T.**; Sautet, P. Tuning the Hydrogenation Selectivity of an Unsaturated Aldehyde via Single-Atom Alloy Catalysts. *J. Am. Chem. Soc.* **2024**, *146* (4), 2556-2567.
2. **Ngan, H. T.**; Yan, G.; van der Hoeven, J. E. S.; Madix, R. J.; Friend, C. M.; Sautet, P. Hydrogen Dissociation Controls 1-Hexyne Selective Hydrogenation on Dilute Pd-in-Au Catalysts. *ACS Catal.* **2022**, *12* (21), 13321-13333.
3. Shi, J.; **Ngan, H. T.\***; Sautet, P.; Weaver, J. F. High Selectivity and Activity of Ti-Cu(111) Dilute Alloys for the Deoxygenation of Ethanol to Ethylene. *ACS Catal.* **2023**, *13* (17), 11244–11255.
4. Foucher, A. C.; **Ngan, H. T.\***; Shirman, T.; Filie, A.; Duanmu, K.; Aizenberg, M.; Madix, R. J.; Friend, C. M.; Aizenberg, J.; Sautet, P.; Stach, E. A. Influence of Pd Concentration in Au-Pd Nanoparticles for the Hydrogenation of Alkynes. *ACS Appl. Nano Mater.* **2023**, *6* (24), 22927-22938.
5. van der Hoeven, J. E. S.; **Ngan, H. T.**; Taylor, A.; Eagan, N. M.; Aizenberg, J.; Sautet, P.; Madix, R. J.; Friend, C. M. Entropic Control of HD Exchange Rates over Dilute Pd-in-Au Alloy Nanoparticle Catalysts. *ACS Catal.* **2021**, *11* (12), 6971–6981.
6. Zhou, C.; **Ngan, H. T.**; Lim, J. S.; Darbari, Z.; Lewandowski, A.; Stacchiola, D. J.; Kozinsky, B.; Sautet, P.; Boscoboinik, J. A. Dynamical Study of Adsorbate-Induced Restructuring Kinetics in Bimetallic Catalysts Using the PdAu(111) Model System. *J. Am. Chem. Soc.* **2022**,

- 144 (33), 15132–15142.
7. Karatok, M.; **Ngan, H. T.**; Jia, X.; O'Connor, C. R.; Boscoboinik, J. A.; Stacchiola, D. J.; Sautet, P.; Madix, R. J. Achieving Ultra-High Selectivity to Hydrogen Production from Formic Acid on Pd–Ag Alloys. *J. Am. Chem. Soc.* **2023**, *145* (9), 5114–5124.
  8. van der Hoeven, J. E. S.; **Ngan, H. T.**; Yan, G.; Aizenberg, J.; Madix, R. J.; Sautet, P.; Friend, C. M. Unraveling 1-Hexene Hydrogenation over Dilute Pd-in-Au Alloys. *J. Phys. Chem. C* **2022**, *126* (37), 15710–15723.
  9. Shi, J.; Owen, C. J.; **Ngan, H. T.**; Qin, S.; Mehar, V.; Sautet, P.; Weaver, J. F. Formation of a Ti–Cu(111) Single Atom Alloy: Structure and CO Binding. *J. Chem. Phys.* **2021**, *154* (23), 234703.
  10. Giannakakis, G.; Kress, P.; Duanmu, K.; **Ngan, H. T.**; Yan, G.; Hoffman, A. S.; Qi, Z.; Trimpalis, A.; Annamalai, L.; Ouyang, M.; Liu, J.; Eagan, N.; Biener, J.; Sokaras, D.; Flytzani-Stephanopoulos, M.; Bare, S. R.; Sautet, P.; Sykes, E. C. H. Mechanistic and Electronic Insights into a Working NiAu Single-Atom Alloy Ethanol Dehydrogenation Catalyst. *J. Am. Chem. Soc.* **2021**, *143* (51), 21567–21579.
  11. Lee, J. D.; Qi, Z.; Foucher, A. C.; **Ngan, H. T.**; Dennis, K.; Cui, J.; Sadykov, I. I.; Crumlin, E. J.; Sautet, P.; Stach, E. A.; Friend, C. M.; Madix, R. J.; Biener, J. Facilitating Hydrogen Dissociation over Dilute Nanoporous Ti–Cu Catalysts. *J. Am. Chem. Soc.* **2022**, *144* (37), 16778–16791.
  12. Patel, D. A.; Giannakakis, G.; Yan, G.; **Ngan, H. T.**; Yu, P.; Hannagan, R. T.; Kress, P. L.; Shan, J.; Deshlahra, P.; Sautet, P.; Sykes, E. C. H. Mechanistic Insights into Nonoxidative Ethanol Dehydrogenation on NiCu Single-Atom Alloys. *ACS Catal.* **2023**, *13* (7), 4290–4303.
- \*: equal contribution

# Chapter 1 Research Background

## 1.1 Dilute Alloys in Heterogeneous Catalysis

Heterogeneous catalysis plays a significant role in various aspects of our daily lives, often without us realizing it. One common example is in the automotive industry, where catalytic converters transform harmful pollutants emitted from vehicle exhausts, such as carbon monoxide, into less harmful substances like carbon dioxide. Catalytic processes also hold promises in the manufacture of numerous consumer goods and industrial products, including fine chemicals and petrochemicals.<sup>1-6</sup> In light of its significance, researchers consistently seek to enhance efficiency and reduce the costs associated with these processes.

Pt-group metals have long been favored in heterogeneous catalysis due to their remarkable reactivity, making them indispensable in various industrial processes.<sup>7-13</sup> Nevertheless, despite their effectiveness, these metals commonly confront selectivity-related hurdles. Alkane activation on Pt-based metals, for example, often leads to over-dehydrogenation and C-C bond cleavage under reaction conditions, resulting in lower product selectivity as well as coking.<sup>14,15</sup> On the other hand, the Lindlar catalyst, which consists of a high concentration of Pd, also tends to over-hydrogenate alkyne to produce alkane, leading to an insufficient selectivity for alkene formation.<sup>16,17</sup> Consequently, while Pt-group metals offer unparalleled reactivity, their inclination towards over-(de)hydrogenation emphasizes the critical necessity for continuous research and development endeavors, which aimed at refining their performance and broadening their applicability across diverse catalytic contexts.

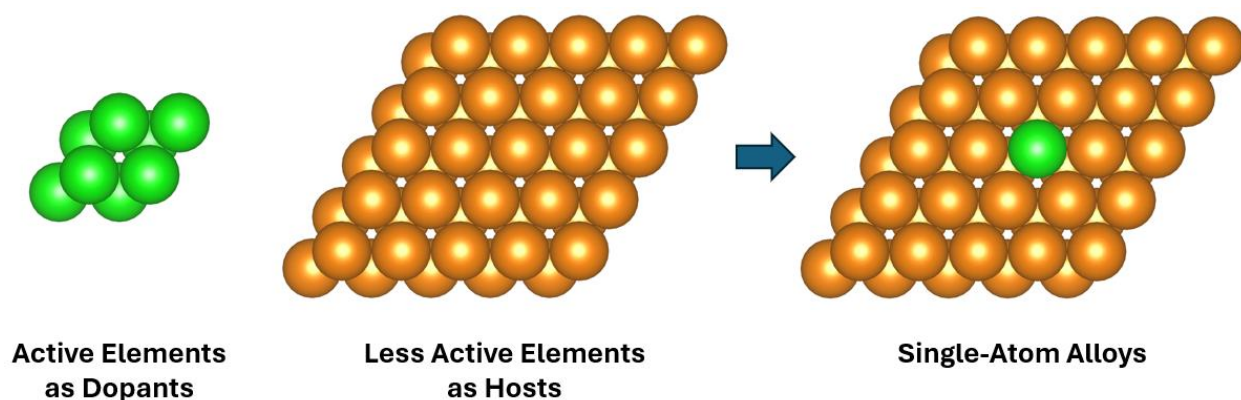


Figure 1.1. Schematic representation of the formation of a single-atom alloy catalyst.

Single-atom alloys (SAAs; Figure 1.1), which are formed by dispersing a highly dilute amount of an active element (e.g. Pd, Pt, Ni, Rh, and Ru) into a less reactive metal host (e.g. Au, Ag, and Cu),<sup>18–22</sup> could be a promising class of catalytic materials for attaining both high reaction selectivity and reactivity. These reactions include ethanol dehydrogenation, hydrogenolysis of biomass type molecules, alkyne hydrogenation, and formic acid decomposition, etc.<sup>23–29</sup> Despite the long-standing investigation of bimetallics, which may or may not feature isolated sites, in the catalysis field, it was the research conducted by Sykes and Flytzani-Stephanopoulos in 2012 that recognized SAAs as a catalyst class and triggered recent interest.<sup>18,30–33</sup>

SAAs achieve remarkable selectivity and reactivity concurrently owing to their distinctive dual functionality. In this type of catalysts, a highly reactive minority metal plays a pivotal role in initiating the catalytic cycle, whereas the less reactive metal host enhances selectivity by offering a different environment, coordination, and electronic properties to the active element.<sup>18,20,34–39</sup> To elaborate further, via dilute dispersion, the metal host could effectively transform the extended surfaces of the active elements into isolated atoms, and this geometric modification prevents unwanted side-reactions that require larger active sites from happening. As an illustration, in propane activation, dilute Pt-in-Cu catalysts can effectively reduce over-dehydrogenation and

coking, phenomena that would otherwise occur readily on Pt-based metals.<sup>40,41</sup> Similar event is also observed in the non-oxidative dehydrogenation of ethanol, where undesired C-C bond scission is restrained on Ni-single atoms in Au(111), but becomes more pronounced as the Ni ensembles increase in size.<sup>42</sup> It is worth noting that upon alloying, the electronic structures of the active dopants are also modified, in addition to the geometry. Typically, the d-states of the active dopants would become narrower in the alloys, and this narrowing is attributed to the weak orbital mixing between the two different elements.<sup>43,44</sup> By diluting early-, mid-, and late-transition metals in noble metals, the relative energy position of the dopants' d-states could also be adjusted. The modulation of d-states enables control over the interaction between the dopant and a specific functional group within a multi-functional-group molecule, making subsequent selective hydrogenation possible. Mid-transition metals in Cu(111), for example, have been found to interact more strongly with the C=O bond than the C=C bond in acrolein, which renders the hydrogenation of the C=O bond more favorable. Conversely, late-transition metals on the Cu(111) surface exhibit a preference for the adsorption of acrolein through its C=C bond, thereby facilitating the undesired C=C bond hydrogenation.<sup>45</sup>

Despite the improved selectivity, concern is often raised regarding the stability of the single-atom alloys, especially under reaction conditions. Depending on the alloy combinations, it might be thermodynamically more favorable for dopant atoms to stay in the subsurface layer (i.e. anti-segregation) of the metal host than the surface layer. Catalyst surfaces like this are akin to having only the inert metal host, meaning low reactivity, and should be avoided. Nevertheless, alloy combinations that do not demonstrate a strong tendency towards anti-segregation can be pretreated under CO or O<sub>2</sub> pressures to bring the dopant atoms to the surface layer and function in this metastable state throughout the course of the hydrogenation reaction. Segregation of Pd in Au(111)

(Pd in the subsurface layer is 0.31 eV more stable than in the surface layer of Au(111)), for example, has been previously shown to be promoted in the presence of CO.<sup>46</sup> Additionally, the presence of intermediates on the alloy catalysts during reactions can also facilitate the retention of dopants at the surface, an observation attributed to the adsorbate-dopant interaction.<sup>47,48</sup> Besides anti-segregation, aggregation of surface dopant atoms into larger active ensembles should also be circumvented in the synthesis of single-atom alloys. This scenario, however, can be easily suppressed by strictly controlling the amount of active dopants that one is going to put into the less reactive metal host. Put simply, maintaining a low dopant concentration reduces the probability of aggregate formation, while higher concentrations increase the likelihood.<sup>49</sup>

Catalyst sintering, a phenomenon in which catalyst particles agglomerate or coalesce over time due to elevated temperature or other environmental factors, frequently results in catalyst deactivation. For example, monometallic Cu-based catalysts, which are commonly used in the non-oxidative dehydrogenation of ethanol to produce acetaldehyde and hydrogen, often experience rapid deactivation due to copper particle sintering.<sup>50-53</sup> Nevertheless, Shan et al. and Hannagan et al. managed to discover that the incorporation of trace amounts of Ni and Rh into Cu (forming highly dilute alloys) could significantly inhibit sintering of Cu nanoparticles, thereby preserving the catalytic activity of the metals over extended reaction periods.<sup>54,55</sup> Hence, not only do SAAs enhance reaction selectivity, but they also effectively mitigate catalyst deactivation issues.

In summary, single-atom alloys are a promising category of catalysts with the power to enhance reaction selectivity, while maintaining reactivity. The systematic and thorough exploration of a wide array of alloy combinations reveals a strategic pathway to precisely adjust and tailor the desired catalytic properties based on specific requirements, and provides the researchers with a robust and versatile framework. Despite not previously mentioned in this dissertation, the

utilization of SAAs also holds the promise of cost reduction, as only a minimal amount of precious metals is required within the metal host. This aspect is particularly pertinent in the context of industrial catalysis. Overall, the substantial impact of SAAs observed emphasizes the necessity of ongoing research endeavors aimed at delving deeper into their potential capabilities and refining their applicability.

## 1.2 Significance of Theoretical Modeling

Density functional theory (DFT), a quantum mechanics-based computational method, is indispensable in investigating heterogeneous reactions on dilute alloys. Particularly suited for understanding materials at atomic and molecular levels, DFT offers a theoretical framework for predicting properties and behaviors of materials with high accuracy. Instead of solving the many-body Schrödinger equation directly, DFT approximates the electronic density of a system, making it a more efficient approach for calculating electronic properties such as energy, structure, bonding, and reactivity. Despite potential uncertainties that might originate from these approximations, especially from the exchange-correlation functionals, DFT remains one of the most accurate computational tools for studying heterogeneous catalysis, typically demonstrating an error margin of approximately  $\pm 0.1$  eV. This computational method holds significant importance as it offers a potent means to elucidate experimental findings, and provides a time-efficient and cost-effective alternative to conventional experimentation. Additionally, the use of DFT also helps eliminate potential hazards associated with laboratory work, including the exposure to radiation and the handling of poisonous substances etc.

In experiments, researchers may frequently encounter challenges in fully grasping the underlying reasons behind a given experimental observation. For example, while typical experimentation like reactor studies and temperature programmed desorption can be useful in

identifying reactive and selective catalysts, unraveling the specific factors contributing to the superior performance can be complex. In such instances, DFT, when combined with microkinetic modeling, can offer fundamental insights into the critical steps in the reaction mechanism that lead to the phenomena observed, and provide guidance for the rational design of other novel catalysts.<sup>29,56,57</sup> Additionally, when different types of active sites (e.g. monomers, dimers, and trimers etc.) are simultaneously present in dilute alloys, determining the origin of the observed reactivity solely through experiments becomes difficult. DFT, however, is capable of investigating the reactivity of these various types of active sites independently, thereby offering comprehensive insights at the atomic level and enriching the understanding of the experimental observations.<sup>49</sup> Hence, DFT plays a crucial role in supporting and complementing experimental techniques in scientific research, which help facilitate a thorough understanding of heterogeneous catalysis on dilute alloys.

Aside from complementing experimental findings, DFT also provides a time-efficient and cost-effective method for screening a list of catalysts to identify those with promising properties, thus expediting the selection process. It is noteworthy that obtaining the complete reaction energy profiles on a specific catalyst is not necessary to determine its reactivity or selectivity. Through DFT calculations, mean-field microkinetic modeling, and scaling relations, activity and selectivity maps could be constructed such that for future predictions, researchers only need to calculate the adsorption energies of certain reaction intermediates on the surface. Wang et al., for example, has reported these maps for the reaction of propane dehydrogenation using the binding energies of  $\text{CH}_3\text{CHCH}_2$  and  $\text{CH}_3\text{CH}_2\text{CH}$  as descriptors.<sup>58</sup> We also adopted similar strategy in our study on selective hydrogenation of  $\alpha,\beta$ -unsaturated aldehydes, which will be further discussed in Chapter 5. In short, for this reaction, the initial binding of the unsaturated aldehydes via the C=O and C=C

bonds could possibly determine the selectivity; hence, researchers can rapidly assess the potential selectivity by determining which adsorption configuration is more favorable. In addition to accelerating the discovery of novel catalysts, it should be emphasized that the observed trends within the catalyst set also offer valuable insights into the essential characteristics necessary for future catalyst development.

### 1.3 Thesis Objectives

In this dissertation, we seek to elucidate the mechanisms underlying the efficacy of dilute alloys, especially single-atom alloys, as reactive and selective catalysts in (de)hydrogenation reactions using state-of-the-art periodic DFT calculations, atomistic thermodynamics, and microkinetic modeling.

Chapters 2, 3 and 4 focus on the alkyne hydrogenation on dilute Pd-in-Au alloy catalysts. In this work, 1-hexyne hydrogenation to 1-hexene on isolated Pd atoms on Au(111) is found to be irreversible due to the highly exergonic nature of this process. In contrast to Pd(111), the rate of this reaction on AuPd<sub>1</sub> is primarily governed by the steps of H<sub>2</sub> dissociation and subsequent H-spillover, while on Pd(111), it is limited by C-H bond formations. Despite being rate-limiting, the challenging dissociation and spillover steps help prevent 1-hexene from being over-hydrogenated, as there are fewer H atoms readily available on the surface for the reaction. It is worth noting that even if 1-hexene hydrogenation takes place, hexyl can still be transformed back to hexene isomers. This is supported by the non-exergonic nature of the reaction and the significant forward barriers for H<sub>2</sub> dissociation and H-spillover, which are crucial steps in providing H atoms for hexane formation. The study was further extended to larger Pd ensembles, namely Pd dimers (Pd<sub>2</sub>) and triangular Pd trimers (Pd<sub>3</sub>). Although larger Pd ensembles could effectively lower down the H<sub>2</sub> activation barrier, they are found to be less reactive than isolated Pd atoms. This observation is

attributed to the fact that the Pd<sub>2</sub> and Pd<sub>3</sub> active sites are poisoned by the strongly bound acetylene molecule, rendering H<sub>2</sub> activation even more challenging.

Chapter 5 focuses on the selective hydrogenation of  $\alpha,\beta$ -unsaturated aldehydes on Cu-based single-atom alloys. In this work, we explore, on the basis of first-principles simulations, single-atom alloy (SAA) catalysts on copper as a class of catalytic materials to enhance the selectivity for C=O bond hydrogenation in unsaturated aldehydes by controlling the binding strength of the C=C and C=O bonds. We demonstrate that although early-transition metals in Cu(111) favor the C=O binding mode of the reactant, the binding is too strong such that subsequent hydrogenation and desorption steps are highly endergonic in nature. On late-transition metals, on the other hand, the C=C binding mode and subsequent C=C hydrogenation is preferred, thereby producing the undesired saturated aldehydes. Mid-transition metals in Cu(111) are the most promising candidates to selectively hydrogenate the C=O bond in unsaturated aldehydes as they favor the reactant adsorption via the C=O bond and with a moderate binding strength, compatible with catalysis. Additionally, acrolein migration from the C=O to the C=C binding mode is hampered by the large barrier for this process, which further enhances the reaction selectivity towards unsaturated alcohols.

Chapter 6 explores the selective dehydrogenation of propane to produce propylene. Pt-based catalysts, which have been widely used in the industry for this reaction, often suffer from various issues including deep-dehydrogenation, coking, and sintering. In this work, we utilize first-principles simulations to investigate the potential of Cu-based single-atom alloys (SAAs) as a promising class of catalytic materials for enhancing the reactivity and selectivity for propylene formation. Particularly, we show that SAAs formed by dispersing Ir and Hf into Cu(111) are capable of serving these functions. The former is demonstrated to possess comparable reactivity

to pure Pt and the previously identified CuRh<sub>1</sub> catalysts. Additionally, it does not promote over-dehydrogenation beyond propylene for the presence of a large activation barrier. Despite over-dehydrogenation could take place on CuHf<sub>1</sub>, which partially covers the catalyst surface with CH<sub>2</sub>CHCH<sub>2</sub>, further dehydrogenation beyond this intermediate is very unlikely. Moreover, a high propylene production rate, exceeding that on the monometallic Pt catalysts by an order of magnitude, is also observed on CuHf<sub>1</sub>. As evidenced by our chemical bonding analysis, the anti-bonding orbitals between Hf and the two atoms (C and H) in the most rate-limiting transition state (i.e. first C-H bond cleavage in propane) in the entire reaction network on CuHf<sub>1</sub> is depleted. This depletion hence leads to the strong stabilization of this transition state, which results in the lower activation barrier and the higher propylene production rate observed.

## Chapter 2 Hydrogen Dissociation Controls 1-Hexyne Selective

### Hydrogenation on Dilute Pd-in-Au Catalysts

#### 2.1 Introduction

Selective hydrogenation holds significant importance in both the fine chemicals and petrochemical industries. Selectively hydrogenating particular functional groups such as  $-C\equiv C$ ,  $-C=O$ ,  $-NO_2$ , and  $-COOH(R)$ , for example, is often required for fine chemicals production.<sup>59</sup> Additionally, selective hydrogenation is a vital process for eliminating alkynes, which can act as catalyst poisons for downstream polymerization in the petrochemical industry.<sup>60</sup>

Achieving high conversion and selectivity in the partial hydrogenation of alkynes to selectively produce alkenes is a persistent challenge in heterogeneous catalysis. Ideally, the goal is to achieve 100% conversion with 100% selectivity for alkene formation. The Lindlar catalyst, known for its high concentration of Pd and support on  $CaCO_3$  (5 w/w % Pd/ $CaCO_3$ ), is commonly employed for alkyne hydrogenation;<sup>17</sup> however, its selectivity for alkene formation remains inadequate. For instance, the selectivity of converting 2-hexyne to 2-hexene on the Lindlar catalyst is only ~88% at around 25% conversion.<sup>16</sup> Alkynes exhibit stronger binding to the Pd catalyst surface compared to alkenes;<sup>61-63</sup> thus, when conversion rates are low, most active sites of the catalyst are occupied by the alkyne molecules.<sup>64</sup> This strong adsorption of alkynes removes the alkene molecules from the catalyst surface, preventing over-hydrogenation and thereby enhancing selectivity.<sup>65</sup> However, when the conversion is high, the selectivity deteriorates. To address this issue, quinoline and lead are often added to the Lindlar catalyst to enhance both its activity and selectivity.<sup>16</sup> Since lead is extremely toxic, there is a necessity to develop a more selective and environmentally friendly catalyst for alkyne hydrogenation.

An alternative approach to enhancing selectivity involves utilizing dilute alloy catalysts,

where an active element like Pd is diluted in a less active metal, such as Au, Ag, and Cu.<sup>19–21,33</sup> The idea is that the active metal will initiate the catalytic cycle (e.g. H<sub>2</sub> dissociation in the case of hydrogenation), while the majority, less reactive metal brings in selectivity by electronically modifying the dispersed dopant compared to its bulk state. At the single-atom limit, the reactive dopant element Pd on the surface layer of Au(111) or Ag(111) exhibits a narrow d-band due to the poor orbital mixing between the two different species.<sup>43,66</sup> This distinct electronic structure reduces the covalent binding strength of molecules on the catalyst surface,<sup>44,67</sup> which helps facilitate alkene desorption over further reaction for selective alkyne hydrogenation. Side reactions like oligomerization require a larger ensemble of active metals and can also be deterred with the utilization of dilute alloy catalysts.<sup>68</sup> Therefore, by careful tuning, dilute alloys have the potential to improve catalytic performance if these diverse factors can be comprehended and linked to alterations in activity and selectivity.

Formerly, dilute alloys formed by incorporating Pd into Cu, Ag, or Au were employed to enhance selectivity in the partial hydrogenation of alkynes.<sup>33,69–72</sup> This work is motivated by the previous research on dilute Pd-in-Au RCT SiO<sub>2</sub> catalysts, which demonstrated high selectivity for 1-hexene formation even at high conversion. In contrast, the selectivity notably deteriorated at high conversion for pure Pd. Luneau et al. suggested that the high selectivity for the dilute Pd-in-Au alloy arises from the relatively weak binding of half-hydrogenated 1-hexene (hexyl) to Pd single atoms on the dilute alloy, compared to that of the half-hydrogenated 1-hexyne (1-hexenyl), leading to the favored  $\beta$ -C-H bond cleavage to regenerate one of the hexene isomers.<sup>64</sup> The rate-limiting step of the 1-hexyne hydrogenation was proposed to be the second hydrogenation step of 1-hexyne.

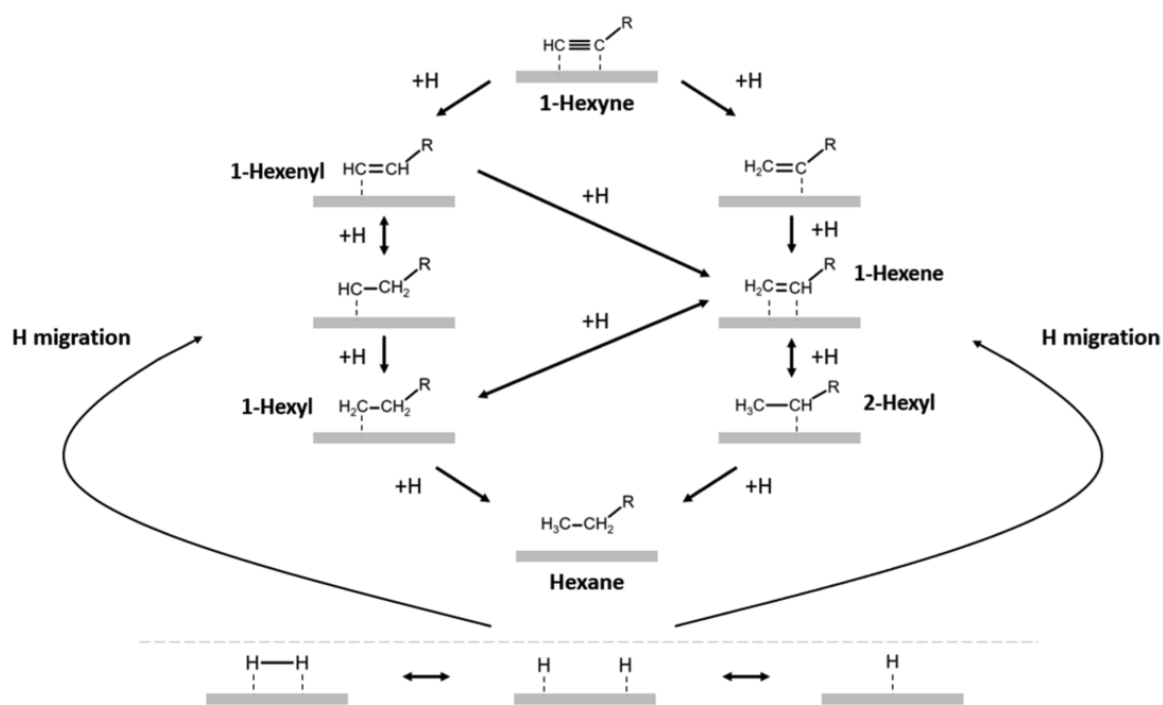


Figure 2.1. Schematic representation of the course of 1-hexyne hydrogenation. The bottommost pathway shows  $\text{H}_2$  dissociation and subsequent migration to supply H atoms for 1-hexyne hydrogenation on another  $\text{Pd}_1\text{Au}(111)$  site. 1-Hexyne can be hydrogenated either by fully hydrogenating one of the two unsaturated carbon atoms followed by the remaining one (left) or by alternately hydrogenating the two carbon atoms (right). The former is detrimental to selectivity as it skips 1-hexene formation and produces hexyls directly through 1-hexylidene. Double-headed and single-headed arrows indicate reversibility and irreversibility, respectively, based on experiments and theory in this chapter.

In this study, the underlying factors contributing to the high selectivity at high conversion of 1-hexyne hydrogenation catalyzed by a dilute Pd-in-Au catalyst were investigated (Figure 2.1). A combination of theoretical modeling using density functional theory (DFT) and microkinetic modeling, and results from isotopic exchange experiments was employed to establish that the rate of alkyne hydrogenation on Pd single atoms embedded in Au is primarily governed by  $\text{H}_2$

dissociation, whereas C-H bond formation, on the other hand, is commonly believed to be the rate-determining step on pure Pd.<sup>73</sup> The significant barrier for H<sub>2</sub> dissociation and small barrier for the hydrogenation of 1-hexyne compared to that of 1-hexene control the selectivity in 1-hexene, allowing for high selectivity even at high conversion. Experiments and theory show that hydrogenation of 1-hexyne is irreversible. The DFT calculations additionally suggest that hydrocarbon adsorption (1-hexyne and 1-hexene) is notably weaker on the dilute Pd-in-Au alloy compared to Pd(111), and the unwanted pathway for forming 1-hexylidene is not favored, consistent with earlier findings.<sup>64,74</sup> These results illustrate a powerful methodology for the rational design of new catalysts for selective alkyne hydrogenation using the synergy between advanced theory and meticulously crafted experiments.

## 2.2 Methods

### 2.2.1 DFT Calculations

All DFT calculations were performed using the Vienna ab initio simulation package (VASP).<sup>75,76</sup> The Pd<sub>1</sub>Au(111) surface for 1-hexyne hydrogenation was modeled with a six-layer slab and a (4 × 4) unit cell, and a Monkhorst-Pack<sup>77</sup> generated 7 × 7 × 1 K-points grid was employed for this unit cell size. Among different exchange-correlation functionals, optPBE-vdw shows the best agreement with the low energy recoil scattering and nuclear micro-analysis experiments regarding the adsorption energies of H atoms.<sup>78–83</sup> The same also applies to the adsorption energy of 1-hexyne when compared with the TPD results. Hence, this functional, along with a plane wave basis set with a cutoff energy of 400 eV, was employed for all calculations reported. During geometric optimization, the bottom four layers of the metal slab were fixed in the bulk Au position, while the upper two layers and the surface adsorbates were allowed to relax until the convergence threshold of < 0.03 eV/Å was reached. Transition states were located using both the dimer

method<sup>84</sup> and the quasi-Newton method. All atomic structures reported in this chapter are visualized using VESTA.<sup>85</sup>

For simplicity, free energy calculations only take into consideration the translational and rotational entropies of the gaseous species, and zero-point energies (ZPE) and vibrational entropies were neglected for all species. Since the ZPEs of gaseous H<sub>2</sub> and the transition state for H<sub>2</sub> dissociation, which is the most rate-controlling in the reaction network as will be discussed, are both 0.27 eV, the effect of ZPE inclusion would cancel out. Hence, omitting the ZPEs in free energy calculations would not affect the overall reaction kinetics.<sup>86</sup>

## 2.2.2 Microkinetic Simulations

Microkinetic modeling was performed using the DFT energies as input parameters to compare the theoretically proposed reaction pathway to experimental measurements. In this modeling, the rate constants for adsorption ( $k_{ads,i}$ )/desorption ( $k_{des,i}$ ) (Eqs 2.1 and 2.2) and surface reaction steps ( $k_i$ ) were computed using the collision theory and transition state theory (Eq 2.3), respectively:<sup>87</sup>

$$k_{ads,i} = \frac{\sigma A_{site} P^o}{\sqrt{2\pi m_i k_B T}} \quad (2.1)$$

$$k_{des,i} = k_{ads,i} * \exp\left(\frac{\Delta G_{ads,i}^o}{k_B T}\right) \quad (2.2)$$

$$k_i = \frac{k_B T}{h} * \exp\left(\frac{-\Delta G_{act}^o}{k_B T}\right) \quad (2.3)$$

where  $\sigma$  is the sticking coefficient (assumed to be 1),  $A_{site}$  is the area of the active site,  $P^o$  is the standard state pressure,  $m_i$  is the mass of the adsorbate, and  $k_B$  is the Boltzmann's constant,  $T$  is the temperature,  $\Delta G_{ads,i}^o$  is the adsorption free energy of the adsorbate under standard state pressure,  $h$  is the Planck's constant, and  $\Delta G_{act}^o$  is the free energy of the activation barrier under

standard state pressure.

The rate of elementary step  $j$  was computed using the following equation:

$$r_j = k_j^{fwd} \prod_i \alpha_{i,IS}^{v_{ij}^{fwd}} \prod_i \alpha_{i,gas}^{v_{ij}^{fwd}} - k_j^{rev} \prod_i \alpha_{i,IS}^{v_{ij}^{rev}} \prod_i \alpha_{i,gas}^{v_{ij}^{rev}} \quad (2.4)$$

where  $k_j^{fwd}$  and  $k_j^{rev}$  are the forward and reverse rate constants, and  $v_{ij}^{fwd}$  and  $v_{ij}^{rev}$  are the stoichiometric coefficients of reactant  $i$  in the forward and reverse directions, respectively. The activity  $\alpha_i$  was assumed to be the surface coverage fraction  $\theta_i$  for surface intermediates (including bare sites) and as the ratio of the partial pressure to the standard pressure,  $P_i/P^0$ , for gaseous species.<sup>88</sup>

The time-dependent coverages of surface intermediates are obtained as the steady-state solution of the following system of ordinary differential equations:

$$\frac{d\theta_i}{dt} = - \sum_j v_{ij}^{fwd} r_j + \sum_j v_{ij}^{rev} r_j \quad (2.5)$$

Following Wang et al., the steady-state solution is achieved in two steps.<sup>89</sup> Starting from a bare surface, the equations are first integrated over 500 s until they have approximately reached a steady state. The resulting coverages are then used as an initial guess for the numerical solution as follows:

$$0 = - \sum_j v_{ij}^{fwd} r_j + \sum_j v_{ij}^{rev} r_j \quad (2.6)$$

$$\theta_{Pd}(t = 0) = \sum_i \theta_{Pd,i} \quad (2.7)$$

$$1 = \sum_i \theta_{Pd,i} + \sum_i \theta_{Au,i} \quad (2.8)$$

where  $\theta_{Pd,i}$  and  $\theta_{Au,i}$  are the surface coverages of species  $i$  on Pd and Au sites, respectively.

## 2.3 Results

### 2.3.1 Dissociation of H<sub>2</sub>

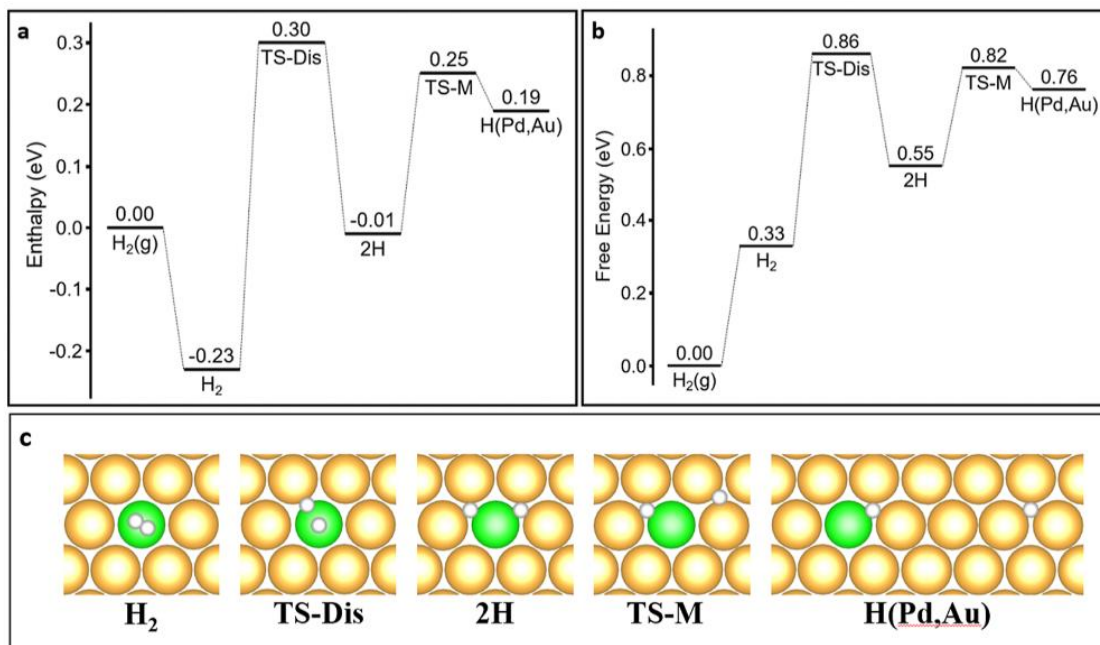


Figure 2.2. (a) Enthalpy and (b) free energy profiles for hydrogen dissociation and migration on the Pd<sub>1</sub>-in-Au(111) surface. All species are chemisorbed, unless indicated by (g) for gas phase species. (c) Structure of each intermediate and transition state along the energy profiles. Conditions used for the free energy calculations are  $T = 363$  K and  $P(\text{H}_2) = 0.2$  bar. H<sub>2</sub>: molecular adsorption mode of H<sub>2</sub>; TS-Dis: H<sub>2</sub> dissociation transition state; 2H: dissociated H<sub>2</sub> into two H atoms adsorbed in Pd<sub>1</sub>-Au<sub>2</sub> fcc hollow sites; TS-M: transition state for migration of one H atom toward the Au region; H(Pd,Au): adsorption of one H atom in the Pd<sub>1</sub>-Au<sub>2</sub> fcc hollow site and one in the Au fcc hollow site.

Alkyne hydrogenation requires the dissociation of molecular hydrogen, which takes place on both single Pd atoms and small Pd ensembles on the surface, as described previously.<sup>90</sup> The

calculations included here exclusively focus on Pd monomers embedded in the surface layer of Au(111) (known as Pd<sub>1</sub>Au(111)), for their predominant existence on the Pd<sub>4</sub>Au<sub>96</sub> catalyst investigated experimentally.<sup>71</sup> The reaction begins with H<sub>2</sub> molecular adsorption [H<sub>2</sub>], followed by the transition state of dissociation [TS-Dis] to form two separated H atoms [2H] (Figure 2.2), a state that is seen to be metastable with respect to the gaseous H<sub>2</sub> molecules. The free energy and the corresponding enthalpy barriers associated with H<sub>2</sub> dissociation are 0.86 eV and 0.30 eV, respectively, under the studied conditions. Subsequent to H<sub>2</sub> dissociation, one of the H atoms in the hollow site neighboring the Pd atom can migrate to the Au surface by going through the transition state for migration [TS-M], resulting in the adsorption of one H atom next to the Pd monomer, and one on a pure Au region [H(Pd,Au)]. It is worth noting that the H-migration process is also activated. However, the free energy of the transition state for this step (TS-M; G = 0.82 eV) is lower than that for H<sub>2</sub> dissociation (G = 0.86 eV). Hence, the latter is considered to be the overall rate-limiting step for the entire H<sub>2</sub> activation process on the alloy surface.<sup>90</sup>

In the subsequent hydrogenation pathways of 1-hexyne, the steps involving H<sub>2</sub> dissociation and H-migration will be combined into a single process, characterized by an effective enthalpy barrier of 0.30 eV and an effective Gibbs free energy barrier of 0.86 eV. The large barrier for H<sub>2</sub> dissociation and the metastable H-H co-adsorption state [2H] are significantly different from that on the extended Pd(111) surface, on which there is no enthalpy barrier for H<sub>2</sub> dissociation and the adsorption of H atoms are stable versus gas phase H<sub>2</sub> in similar conditions.<sup>33</sup> The significant barrier for H<sub>2</sub> dissociation on Pd<sub>1</sub>Au(111) will be demonstrated to contribute to the enhanced selectivity of the alloy catalyst for alkyne hydrogenation. Given the metastable state of H on the surface, it is assumed in the presentation of the reaction pathways that one of the two H atoms formed from dissociation will diffuse and react with 1-hexyne adsorbed on another Pd<sub>1</sub>Au(111) site, while the

remaining one will recombine with another surface H atom and desorb as H<sub>2</sub> molecules. Therefore, one H<sub>2</sub> molecule dissociation event is needed every time an H atom is required to form a C-H bond in the model underlying the free energy profiles. This limitation is removed in the subsequent microkinetic simulations, where all elementary reaction steps are permitted to occur simultaneously.

### 2.3.2 Hydrogenation of 1-Hexyne to 1-Hexene

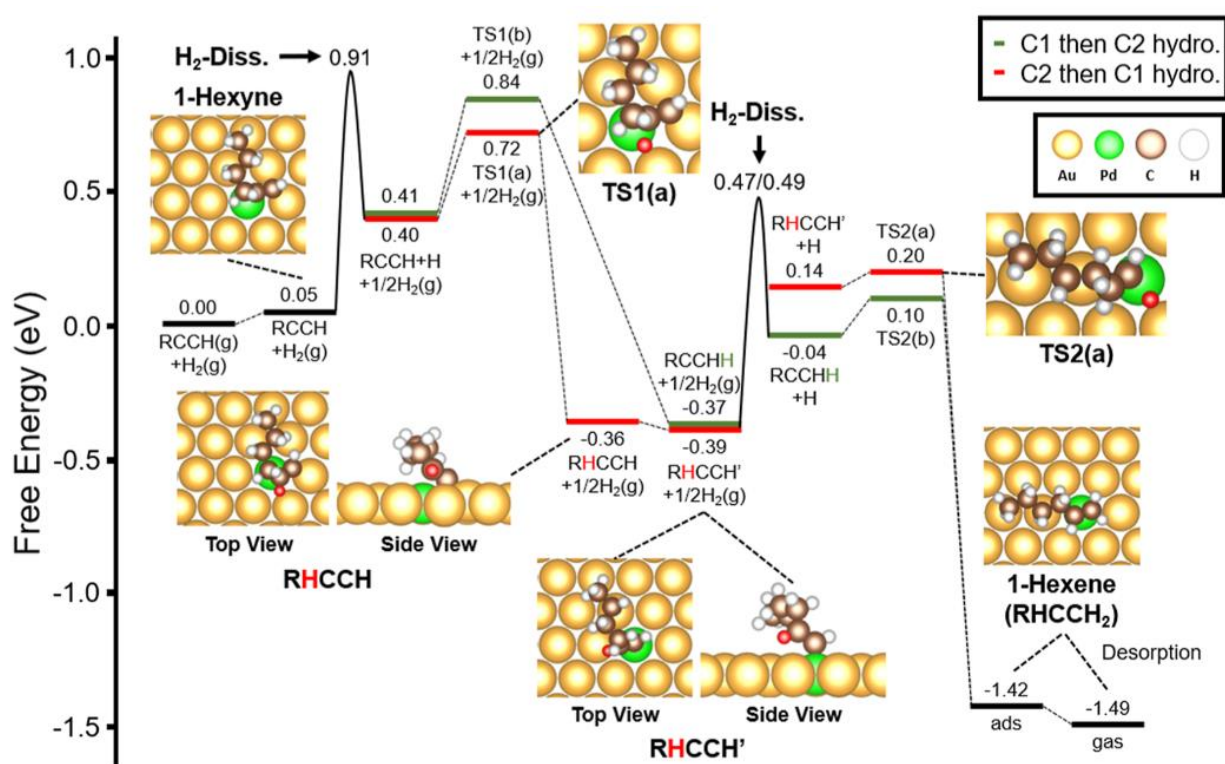


Figure 2.3. Free energy diagram for 1-hexyne hydrogenation to form 1-hexene on the Pd<sub>1</sub>Au(111) surface. The butyl group attached to C≡C bond is abbreviated as R. All species are chemisorbed, unless indicated by (g) for gas phase species. H<sub>2</sub> dissociation occurs on another Pd site, with migration of one H over the Au toward the Pd site where the 1-hexyne is adsorbed. This process is lumped into one effective activation barrier of 0.86 eV labeled as H<sub>2</sub>-Diss. The green and red pathways represent the hydrogenation of the terminal carbon atom (C<sub>1</sub>) and the carbon atom

attached to the butyl group ( $C_2$ ), respectively, in the first reaction step, followed by the hydrogenation of the remaining carbon atom. The newly added H atoms are indicated in red or green. Reaction conditions are  $T = 363$  K,  $P(H_2) = 0.2$  bar,  $P(C_6H_{10}) = 0.01$  bar,  $P(C_6H_{12}) = P(C_6H_{14}) = 0.001$  bar.

1-Hexyne hydrogenation to form 1-hexene on  $Pd_1Au(111)$  is irreversible and is limited by  $H_2$  dissociation (Figure 2.3 and A.1). The initial step involves the favorable adsorption of 1-hexyne on the  $Pd_1Au(111)$  site, with an enthalpy change of  $-1.16$  eV, resulting in a slightly positive Gibbs free energy of adsorption of  $+0.05$  eV due to the entropy loss of the molecule. Hence, only part of the  $Pd_1Au(111)$  active sites are covered by 1-hexyne, leaving some sites vacant for  $H_2$  activation. Following the  $H_2$  activation process as previously described, an H atom is brought to the 1-hexyne adsorption site before the reaction occurs, resulting in the co-adsorption of the two species ( $RCCH + H$ ) on the same  $Pd_1Au(111)$  site. It is worth noting that  $H_2$  dissociation into two separated H atoms on a  $Pd_1Au(111)$  site where a 1-hexyne molecule already resides is less energetically favored compared to that on a bare  $Pd_1Au(111)$  site ( $\Delta G_{ads} = 0.77$  eV for the former and  $\Delta G_{ads} = 0.55$  eV for the latter). This implies that  $H_2$  dissociation scarcely takes place on  $Pd_1Au(111)$  sites occupied by a 1-hexyne molecule.

Two pathways exist for the initial hydrogenation of 1-hexyne: addition of hydrogen to the terminal carbon ( $C_1$ , green pathway) and to the second carbon atom ( $C_2$ , red pathway in Figure 2.3) of the  $C\equiv C$  bond. The Gibbs free energy barriers for these initial steps are low –  $0.43$  eV and  $0.32$  eV for H addition to the  $C_1$  and  $C_2$  positions, respectively. The variances in these barriers stem from the heightened electron donation from the long carbon chain to  $C_2$ . Consequently, the transition state for  $C_2$  hydrogenation [TS1(a)] exhibits a free energy that is  $0.12$  eV lower than that of the transition state for  $C_1$  hydrogenation [TS1(b)].

The resulting partially hydrogenated surface species demonstrate similar stability irrespective of whether hydrogenation takes place at the C<sub>1</sub> or C<sub>2</sub> position. Two distinct adsorption structures exist for the intermediates formed from C<sub>2</sub> hydrogenation:  $\eta^2$  (RHCCH) and  $\eta^1$  (RHCCH') binding modes (Figure 2.3). On the other hand, only one adsorption configuration is found for the intermediate formed from C<sub>1</sub> hydrogenation, which is RCCHH and is in an  $\eta^1$  binding mode. Due to steric hindrance, the same intermediate in the  $\eta^2$  binding mode is seen to be unstable.

The hydrogenation of the partially hydrogenated intermediates (RHCCH' and RCCHH) is preferred over the reverse reaction leading to the regeneration of 1-hexyne on Pd<sub>1</sub>Au(111) (Figure 2.3). Dehydrogenation has Gibbs free energy barriers ranging from 1.08 to 1.21 eV, surpassing the 0.86 eV barrier for the dissociation of a second H<sub>2</sub> molecule. Upon co-adsorption of an H atom with the partially hydrogenated intermediates (RHCCH' + H and RCCHH + H), C-H bond formation proceeds with remarkably low activation barriers, measured at 0.06 and 0.14 eV, respectively. Hence, the H<sub>2</sub> dissociation and migration steps are once again rate-limiting in this second part of the reaction. Notably, 1-hexene irreversible forms, based on the high reverse barrier of at least 1.52 eV. The adsorption of the product 1-hexene is moderate ( $\Delta H = -1.22$  eV,  $\Delta G = +0.07$  eV), so that in reaction conditions, desorption of 1-hexene is slightly exergonic ( $\Delta G_{\text{des}} = -0.07$  eV) and 1-hexene coverage on the catalyst should be low. However, it is important to note that the adsorption energies of both 1-hexyne and 1-hexene are closely alike. As a result, hydrogenation selectivity is not governed by the competitive adsorption between the two species, as is the case on bulk Pd catalysts. The observed selectivity enhancement will be further discussed in the microkinetic modeling section.

The irreversible hydrogenation of 1-hexyne and the rate-limiting step being H<sub>2</sub> dissociation on Pd<sub>1</sub>Au(111) present a marked contrast with pure Pd catalysts. On pure Pd catalysts, H<sub>2</sub>

dissociation lacks an enthalpy barrier, and the reaction is instead limited by the C-H bond formation steps.<sup>33,73</sup> Another distinctive feature is the rather weak 1-hexyne adsorption on Pd<sub>1</sub>Au(111), with the adsorption enthalpy being -1.16 eV, versus -2.33 eV on Pd(111). On the other hand, 1-hexene shows a similar adsorption enthalpy (-1.22 eV) as 1-hexyne on Pd<sub>1</sub>Au(111), while its adsorption on Pd(111) (-1.46 eV) is much weaker than that of 1-hexyne. This suggests that the selectivity is not controlled by competitive adsorption on Pd<sub>1</sub>Au(111), whereas it typically plays a role in controlling the selectivity on Pd(111).

Experiments of running the reaction in D<sub>2</sub> over a dilute Pd-in-Au nanoparticle catalyst confirmed the irreversible conversion of 1-hexyne to 1-hexene. The catalyst used was the so-called raspberry colloid-templated material (RCT) containing  $4.9 \pm 0.9$  nm nanoparticles with 4 atm % Pd supported on a microporous silica support (4.2 wt % total metal loading). The reactor study shows that no significant formation of deuterated 1-hexyne and HD was formed, verifying the irreversibility of the reaction. Additionally, the decrease in the conversion levels from 10.6 to 4.6 % when switching from H<sub>2</sub> to D<sub>2</sub> further supports the claim that H<sub>2</sub> (or D<sub>2</sub>) is the rate-limiting step. These results demonstrate a strong agreement between theory and empirical observations.

Further hydrogenation of 1-hexene to 1-hexyl, 2-hexyl, and hexane proceeds with a similar mechanism, although the reaction is much less exergonic, with a DFT-calculated reaction free energy of -1.07 eV in the conditions shown in Figure 2.3, versus -1.49 eV for 1-hexyne to 1-hexene (Table A.1). Due to the smaller exothermicity of the reaction, the intermediates connecting the reactant and the product lie higher in free energy in the case of 1-hexene hydrogenation. Hence, they encounter barriers of similar magnitude in both the forward and reverse direction, and the hydrogenation reaction of 1-hexene is reversible (Table A.1). For completeness, a possible side reaction from the mono-hydrogenated 1-hexyne intermediate RHCCH has also been considered

by hydrogenating the C<sub>2</sub> atom again to form RH<sub>2</sub>CCH (1-hexylidene), followed by hydrogenation of C<sub>1</sub> to form 1-hexyl (Figure A.2). That path would be detrimental to the selectivity of the alloy catalyst because it skips the formation of the desired 1-hexene and produces hexyls directly. However, it presents an overall free energy barrier of 1.09 eV on Pd<sub>1</sub>Au(111) under the considered conditions, which is at least 0.26 eV higher than that of the pathway to form 1-hexyl via 1-hexene. Hence, this pathway is energetically unfavorable and is unlikely to affect the selectivity for 1-hexene formation. More details regarding 1-hexene hydrogenation can be found in Chapter 3.

### 2.3.3 Microkinetic Simulation of Catalytic Activity

Microkinetic simulations were employed to identify the factors governing the activity and selectivity of the reaction. Briefly, the elementary steps considered in this microkinetic modeling include 1-hexyne hydrogenation on one Pd<sub>1</sub>Au(111) site, and H<sub>2</sub> activation on another Pd<sub>1</sub>Au(111) site. Prior to each bond-formation event, an H atom is drawn to the 1-hexyne/intermediate adsorption site via the Au surface for the reaction to take place. The details of the reaction network are summarized in Appendix A (Table A.2).

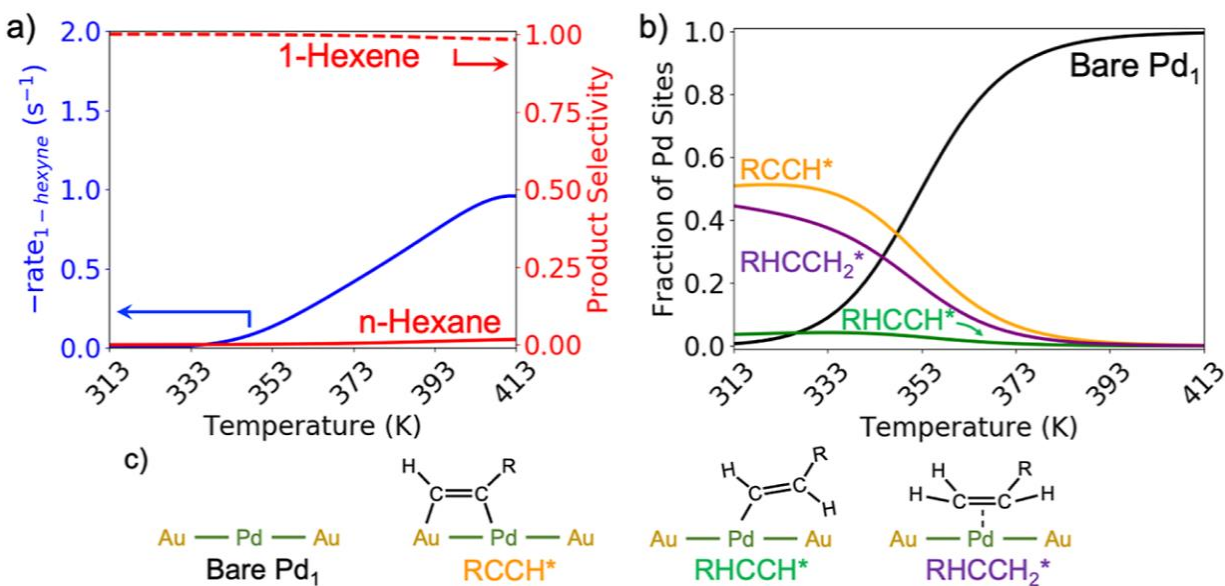


Figure 2.4. Microkinetic simulations of 1-hexyne hydrogenation to 1-hexene and n-hexane under a typical experimental reaction environment corresponding to low (< 20%) conversion:  $P(\text{H}_2) = 0.2$  bar,  $P(1\text{-hexyne}) = 0.01$  bar,  $P(1\text{-hexene}) = P(\text{n-hexane}) = 0.001$  bar. (a) rate ( $\text{s}^{-1}$ ) for the conversion of 1-hexyne (blue line) and selectivity for the formation of 1-hexene and n-hexane (red lines) as a function of temperature. The selectivity for 1-hexene was found to be above 98% through the temperature range  $T = 313 - 413$  K. (b) Steady-state fraction of reactive intermediates on  $\text{Pd}_1\text{Au}(111)$  as a function of temperature: adsorbed 1-hexyne (orange line) and 1-hexene (purple line) were found to be the most abundant reactive intermediates until 353 K. (c) Schematics of structures in panel (b).

The rate of 1-hexyne hydrogenation was evaluated under a typical experimental reaction environment at low conversion [ $T = 313 - 413$  K,  $P(\text{H}_2) = 0.2$  bar,  $P(1\text{-hexyne}) = 0.01$  bar,  $P(1\text{-hexene}) = P(\text{n-hexane}) = 0.001$  bar]. 1-Hexyne starts to react at 333 K, a temperature at which vacant sites begin to become available. At 373 K, the rate of selective hydrogenation to 1-hexene stands at  $0.42 \text{ s}^{-1}$ , in contrast to the rate of complete hydrogenation to n-hexane, which is  $0.0021 \text{ s}^{-1}$  (Figure 2.4a). Overall, in the temperature range of  $T = 313 - 413$  K and low 1-hexyne conversion, the selectivity for the formation of 1-hexene was found to be consistently above 98%. The selectivity towards 1-hexene remains high (> 70%) even if the conversion is as high as 90%, an observation that highly aligns with the experimental findings (Figure A.4).<sup>64</sup> Before closing up, it is important to note that the  $\text{Pd}_1\text{Au}(111)$  active sites were found to be largely covered by adsorbed 1-hexyne and 1-hexene below 353 K, but becomes mostly bare above this temperature. Vacating these active sites creates more space for hydrogenation to occur, leading to a noticeable surge in the reaction rate (Figure 2.4b).

Microkinetic modeling further dictates that in the process of forming 1-hexene from 1-hexyne,

the C<sub>2</sub> atom was seen to be hydrogenated first, consistent with the analysis based on Gibbs free energy (Figure A.5a). The formation of 1-hexenyl and 1-hexene was both exothermic and irreversible. The reversibility factor, defined as the ratio between the reverse and forward rates of an elementary step with a positive rate ( $r_{\text{rev}}/r_{\text{fwd}}$ ), is below  $10^{-4}$  across the entire temperature range considered.<sup>91</sup> The formation of 1-hexyl, on the other hand, was found to be partially reversible in the same temperature range, with the reversibility factors being  $\sim 1$  at 313 K and 0.46 at 413 K. Furthermore, the creation of the 1-hexylidene intermediate followed by the formation of hexyl and hexane was determined to be unfavorable across all temperatures (Figure A.5b). Details of 1-hexene hydrogenation can be found in Chapter 3 of this dissertation.

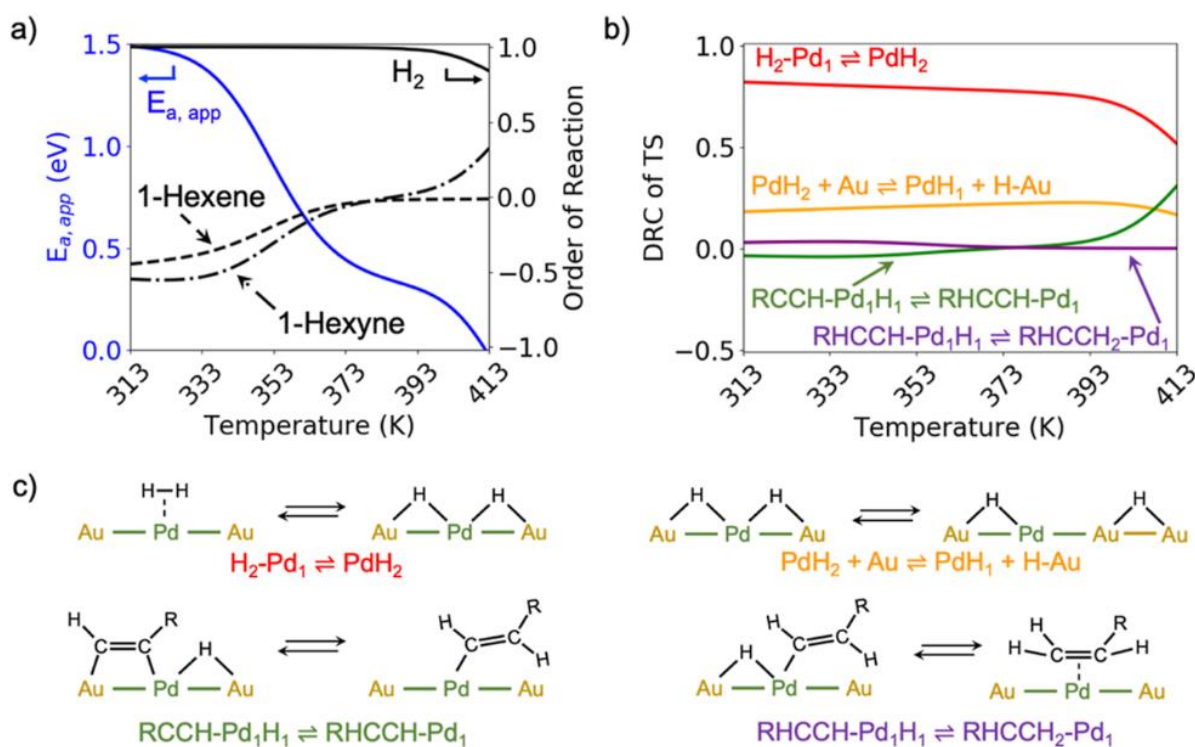


Figure 2.5. Analysis of the kinetics for hydrogenation of 1-hexyne shows  $H_2$  dissociation to be the rate-controlling step. (a) Apparent activation enthalpy (blue line) and kinetic orders of  $H_2$  (black solid line), 1-hexyne (dot-dashed line), and 1-hexene (dashed line) for the hydrogenation of 1-

hexyne as a function of temperature. The apparent activation enthalpy of the reaction progressively decreases in the temperature range  $T = 313 - 413$  K, while the orders of 1-hexyne and 1-hexene increase. (b) Degree of rate control (DRC) of various transition states as a function of temperature. The transition state for  $H_2$  dissociation is the main rate-controlling transition state (red line), while the migration of H from the Pd single atom to the Au substrate (orange line) is second in importance. Importantly, C-H bond formation steps (green and purple lines) do not appear to be rate-controlling. (c) Schematics of the four elementary steps shown in panel (b).

The apparent activation enthalpy and kinetic orders of  $H_2$ , 1-hexyne, and 1-hexene for the consumption of 1-hexyne were next computed. Under an  $H_2$ -rich reaction environment and low reaction conversion [ $P(H_2) = 0.2$  bar,  $P(1\text{-Hexyne}) = 0.01$  bar,  $P(1\text{-Hexene}) = 0.001$  bar] along the rise of temperature from 313 to 373 K, the apparent activation enthalpy for 1-hexyne hydrogenation was observed to decrease from 1.49 to 0.44 eV. The orders of 1-hexyne and 1-hexene, on the other hand, were found to increase from  $\sim -0.5$  to  $\sim 0$ , and the order of  $H_2$  remained roughly constant at 1 (Figure 2.5a). The decline in apparent activation enthalpy and the increase in kinetic orders of 1-hexyne and 1-hexene accompany a notable surge in the rate of 1-hexyne hydrogenation without compromising the selectivity (Figure 2.4). At a reaction temperature of 373 K, the apparent activation enthalpy, order of  $H_2$ , and order of 1-hexyne were found to be 0.44 eV, 1, and -0.04, respectively.

The kinetics of the semi-hydrogenation of 1-hexyne catalyzed by dilute Pd-in-Au alloys have been investigated by two different research groups. For the gas-phase hydrogenation of 1-hexyne to 1-hexene at 313 K, Luneau et al. discovered that the rate of 1-hexyne hydrogenation over  $Pd_4Au_96$  nanoparticles supported on RCT-SiO<sub>2</sub> predominantly depends on the partial pressure of  $H_2$  (with an order of 0.94) but exhibits weak dependence on the partial pressure of 1-hexyne (with

an order of -0.08).<sup>64</sup> The apparent activation enthalpy was found to be 0.39 eV between 303 and 343 K. Since the orders of H<sub>2</sub> and 1-hexyne over Pd<sub>4</sub>Au<sub>96</sub> (0.94 for H<sub>2</sub> and -0.08 for 1-hexyne) are similar to those over pure Pd (0.99 for H<sub>2</sub> and -0.20 for 1-hexyne), the authors proposed that the rate-controlling step over Pd<sub>4</sub>Au<sub>96</sub> should be the hydrogenation of 1-hexenyl to 1-hexene.<sup>64</sup>

In the liquid-phase hydrogenation of 1-hexyne to 1-hexene, Liu et al. observed similar reaction orders as Luneau et al. At 298 K, the authors noted that the reaction rate exhibited a linear dependence on the pressure of H<sub>2</sub> but showed no dependence on the concentration of 1-hexyne, implying an order of approximately 1 for H<sub>2</sub> and 0 for 1-hexyne.<sup>74</sup> In the temperature range of 273-318 K, the authors determined the apparent activation enthalpy of the reaction to be 0.43 eV. They suggested that because of the similarity of this apparent activation enthalpy to that of the H/D exchange reaction [H<sub>2</sub> + D<sub>2</sub> → 2HD, E<sub>a,app</sub> = 0.43 eV] over the same catalyst, the activation of H<sub>2</sub> should be the rate-limiting step.<sup>74</sup>

At first glance, the calculated apparent activation enthalpy and reaction orders in this study align with those measured by Luneau et al., albeit at a higher temperature, shifted by approximately 60 K. The reason behind this shift will be explored in more detail later.

Degree of rate control (DRC) analysis was carried out to identify the surface intermediates and transition states that have a significant impact on the rate of 1-hexyne hydrogenation (Figure 2.5b and A.6).<sup>92</sup> Across the temperature range of 313 – 353 K, the catalyst surface is found to be mostly populated by 1-hexyne and 1-hexene. Above 353 K, however, more than half of the Pd sites become bare (Figure 2.4b). This depletion of the surface C<sub>6</sub> intermediates is reflected in the calculated DRCs of reactive intermediates, where the DRCs of surface intermediates gradually move to 0 in this temperature range, while the bare surface becomes the rate-limiting intermediate (Figure A.6). The decline in surface C<sub>6</sub> intermediates is associated with both a decrease in apparent

activation enthalpy and an increase in  $C_6$  reaction orders within this temperature range. On the other hand,  $H_2$  dissociation remains the primary rate-controlling transition state for the reaction across the entire temperature range. The calculated apparent activation enthalpy and reaction orders can be explained through the DRCs. Building on Mao and Campbell's work, the apparent activation enthalpy can be interpreted as roughly the difference between the enthalpic barrier for  $H_2$  dissociation relative to  $H_2$  gas and the enthalpies of adsorption of 1-hexyne and 1-hexene weighed by the DRCs of their adsorbed states.<sup>93</sup> These analyses revealed that the transition state for  $H_2$  dissociation is the primary rate-controlling step for the hydrogenation of 1-hexyne to 1-hexene, aligning with the qualitative analysis derived from reaction pathways.

The difference between the calculated apparent activation enthalpy and reaction orders and those measured by Luneau et al. could be attributed to the computed adsorption enthalpies of 1-hexyne and 1-hexene. In our calculations, the desorption enthalpies of 1-hexyne and 1-hexene were calculated to be 1.16 and 1.22 eV, respectively, at 363 K. These values, however, seem to be overestimated when compared with the TPD experiments of Liu et al.<sup>74</sup> In relation to the gas-phase chemical potentials of 1-hexyne and 1-hexene (Figure A.7), the over-estimation of the desorption enthalpies would lead to higher calculated coverage of  $C_6$  intermediates at typical reaction temperatures, namely 298 – 343 K.

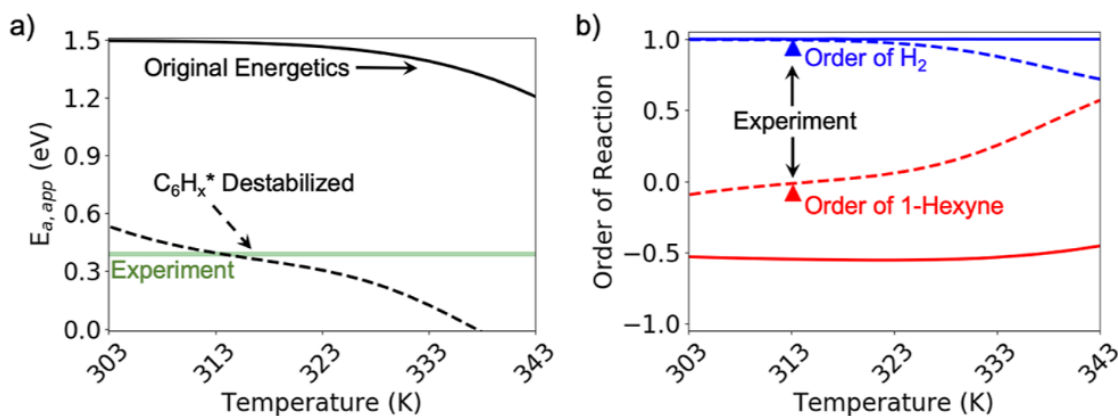


Figure 2.6. Destabilization of hydrocarbon intermediates and transition states energy by 0.2 eV enables an improved agreement with the experiment for the kinetic order of 1-hexyne and the apparent activation enthalpy. (a) Apparent activation enthalpy (eV) of 1-hexyne hydrogenation as a function of temperature without (full line) and with (dashed line) destabilization of surface  $C_6H_x$  intermediates and transition states. The experimental value (+0.39 eV, reported in ref 64) is shown as a green horizontal bar. (b) Orders of reaction of  $H_2$  (blue) and 1-hexyne (red) as a function of temperature without (full line) and with (dashed line) destabilization of surface  $C_6H_x$  intermediates and transition states. Experimental values (order of  $H_2$ : 0.94, order of 1-hexyne: -0.08, reported in ref 64) are shown as triangles.

To qualitatively address the variances, a modified microkinetic model was devised, where surface intermediate states and transition states containing adsorbed carbonaceous species were destabilized by 0.20 eV (Figure 2.6). After modification, the apparent activation enthalpy and the order of 1-hexyne were found to be 0.39 eV and -0.01, respectively, at 313 K, which compare much more favorably with the experimental measurements by Luneau et al. (apparent activation enthalpy: +0.39 eV, order of 1-hexyne: -0.08) and Liu et al. (apparent activation enthalpy: +0.43 eV, order of 1-hexyne:  $\sim 0$ ). It is noteworthy that even after the modification,  $H_2$  dissociation remains the most rate-limiting transition state in the reaction network.

### 2.3.4 Origin of Improved 1-Hexene Selectivity

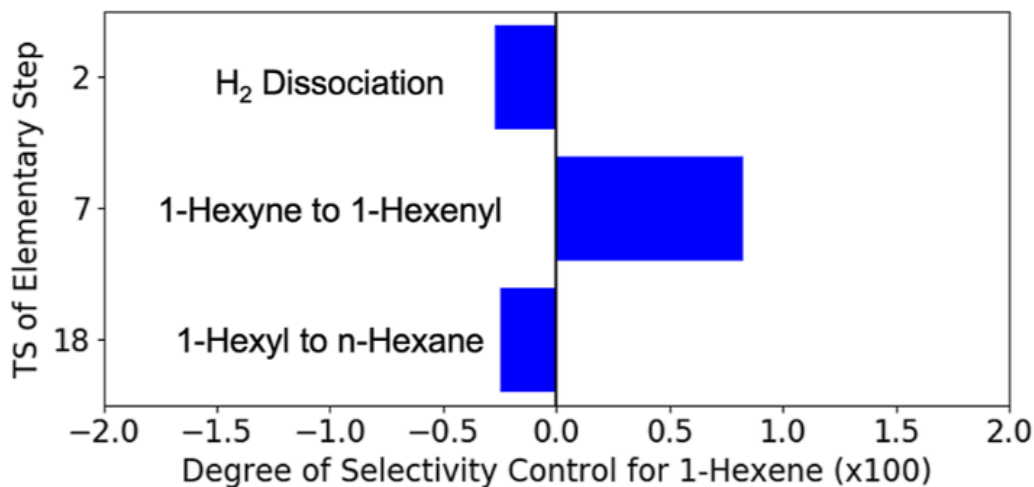


Figure 2.7. Degree of selectivity control (DSC), evaluated at  $T = 373$  K,  $P(\text{H}_2) = 0.2$  bar,  $P(1\text{-hexyne}) = 0.01$  bar,  $P(1\text{-hexene}) = 0.001$  bar, of the TS for  $\text{H}_2$  dissociation over  $\text{Pd}_1$  ( $\text{DSC} = -2.75 \times 10^{-3}$ ), 1-hexyne hydrogenation to 1-hexenyl ( $\text{DSC} = 8.24 \times 10^{-3}$ ), and 1-hexyl hydrogenation to n-hexane ( $\text{DSC} = -2.46 \times 10^{-3}$ ). The values were multiplied by 100 in the figure. Decreasing the free energy barrier for 1-hexyne hydrogenation to 1-hexenyl increases the selectivity for 1-hexene, while decreasing the free energy barrier of  $\text{H}_2$  dissociation and 1-hexyl hydrogenation to n-hexane decreases the selectivity for 1-hexene.

The degree of selectivity controls (DSC)<sup>92</sup> was calculated for all surface intermediates and transition states under typical low-conversion experimental reaction conditions [ $T = 373$  K,  $P(\text{H}_2) = 0.2$  bar,  $P(1\text{-hexyne}) = 0.01$  bar,  $P(1\text{-hexene}) = 0.001$  bar] to quantitatively evaluate how the elementary steps in the reaction network influence the selectivity towards 1-hexene. The negative DSCs of the transition states for  $\text{H}_2$  dissociation on  $\text{Pd}_1$  and for 1-hexyl hydrogenation to produce n-hexane (Figure 2.7) suggest that lowering the free energy of either transition state would decrease the selectivity for 1-hexene formation. The former is justified by the fact that atomic H

would become more readily available for 1-hexene hydrogenation when the H<sub>2</sub> dissociation barrier shrinks. The latter is even more intuitive, as it directly influences the formation of the undesired product n-hexane. Conversely, the transition state with the largest positive DSC corresponds to the hydrogenation of 1-hexyne to form 1-hexenyl (Figure 2.7). Given that the initial hydrogenation step of 1-hexyne features a higher activation barrier than the subsequent step, lowering the free energy of this transition state could considerably enhance the yield of 1-hexene and consequently, the selectivity. It is noted that the DSC analysis is carried out at a condition under which only 11% of all surface Pd sites are occupied by carbonaceous intermediates; thus, the influence of site-competition is negligible (Figure 2.4b).

At low conversion, Pd catalysts achieve high selectivity via competitive binding: strong binding of 1-hexyne expels the relatively weakly bound 1-hexene from the catalyst surface. This competitive binding, however, would be lost when conversion becomes higher. The high selectivity of the dilute Pd-in-Au catalyst at high conversion, on the other hand, does not depend on competitive binding, as evident from the comparable adsorption energies of 1-hexyne and 1-hexene. Rather, the selectivity is predominantly influenced by the difference in the rate constants of hydrogenation between 1-hexyne and 1-hexene, as demonstrated by the DSC analysis. One important factor to slow down 1-hexyn hydrogenations is the high H<sub>2</sub> dissociation barrier, which encourages hexyls to proceed in the reverse direction to form hexenes, as also shown by van der Hoeven et al. in the case of hexene hydrogenation on the same catalyst.<sup>57</sup> Notably, this sizable barrier is lacking on the Pd catalysts.<sup>33</sup> Since the H<sub>2</sub> dissociation barrier is unaffected by reaction conversion, the selectivity for hexene formation can be preserved even at high conversion. The production of hexyls via hexylidene, which undermines selectivity by bypassing the formation of 1-hexene, is also energetically unfavorable on the alloy catalyst (Figure A.2). Collectively, these

features contribute to the significantly enhanced selectivity of the Pd<sub>1</sub>Au(111) catalyst.

One can delve further into the distinctions between the Pd<sub>1</sub>Au(111) and bulk Pd(111) catalysts regarding 1-hexyne hydrogenation. The hydrogenation energy profiles differ in that surface intermediates and transition states exhibit much weaker adsorption on Pd<sub>1</sub>Au(111). Compared to Pd(111), adsorbed 1-hexyne is destabilized in free energy by 1.37 eV on Pd<sub>1</sub>Au(111), and the first C-H bond formation TS1(a) by a similar amount of 1.33 eV (Figure A.3). Hydrogen adsorption is also weakened, experiencing a destabilization of 0.49 eV/H atom.<sup>94</sup> The co-adsorbed state, where both 1-hexyne and H are interacting with Pd<sub>1</sub>, is destabilized by 1.87 eV and hence roughly cumulates the two effects. As a result, for the elementary C-H bond formation process, the reactant state experiences greater destabilization than the transition state, resulting in the activation energy being reduced from 0.86 eV on Pd(111) to 0.32 eV on Pd<sub>1</sub>Au(111). The destabilizations observed on the single atom alloy<sup>48,64,95,96</sup> primarily arise from reduced active ensemble effects. For instance, on Pd(111), 1-hexyne binds to three Pd atoms, whereas it binds to one Pd and two Au atoms on Pd<sub>1</sub>Au(111). Au's d-states are lower in energy, fully occupied, and have limited interaction with the adsorbate.<sup>97</sup> Electronic effects are also present as the electronic states on Pd for the single-atom alloy are less dispersed in energy than for a surface atom of Pd(111).<sup>98</sup> Note, however, that the d-band center for the surface Pd atom has a very similar value [-1.69 eV for Pd(111) and -1.65 eV for Pd<sub>1</sub>Au(111), Figure A.8], so that electronic effects should remain moderate. The significant destabilization along the energy profile results in large H<sub>2</sub> dissociation activation energy and small C-H bond formation activation energy on Pd<sub>1</sub>Au(111), with strong positive consequences on the 1-hexyne hydrogenation selectivity, as shown from our kinetic analysis. Considering the dominance of ensemble effects, it is reasonable to anticipate that the phenomenon depicted here would apply across a broad spectrum of single-atom alloys.

The insights gleaned from this study offer valuable guidance for crafting selective catalysts. A critical factor to consider is the energy barrier associated with H<sub>2</sub> dissociation, where we encounter a trade-off between activity and selectivity. Increasing further the barrier for H<sub>2</sub> dissociation could diminish activity (as it is the main rate-limiting process), while excessively reducing it may compromise selectivity. However, we can play within a range of favorable barrier values to identify an optimal scenario. This could involve keeping Pd as the active metal while transitioning the host to Ag or Cu.<sup>95</sup> Another option is to substitute the active metal with Ni. Replacing the active metal with Pt may not be advisable, as the H<sub>2</sub> dissociation barrier is considerably lower on Pt SAAs in Au, Ag, and Cu.<sup>95</sup> Increasing the ensemble size of Pd or Ni, such as forming dimers or trimers, would also significantly reduce the H<sub>2</sub> dissociation barrier, at the expense of selectivity, and should not be an efficient direction of design.

## 2.4 Conclusion

In this work, our combined theoretical and experimental study reveals that over dilute Pd-in-Au alloy catalysts, the H<sub>2</sub> dissociation step, with a sizable free energy barrier of 0.86 eV at 363 K and 0.2 bar of H<sub>2</sub>, plays a major role in controlling the activity and selectivity of 1-hexyne hydrogenation. Specifically, our Gibbs free energy-based analysis and first-principles microkinetic simulations demonstrate that H<sub>2</sub> dissociation acts as the rate-limiting process for 1-hexyne hydrogenation on Pd<sub>1</sub>Au(111), while the C-H bond formation steps proceed with lower barriers. Somewhat more surprisingly, the sizable H<sub>2</sub> dissociation barrier also positively influences the selectivity for the partial hydrogenation to 1-hexene by mitigating the unwanted over-hydrogenation to hexane. This is confirmed by our DSC analysis, which reveals that a reduction in the free energy barrier for H<sub>2</sub> dissociation decreases the selectivity for 1-hexene formation. Additionally, other elementary steps also play crucial roles in determining the selectivity. For

example, decreasing the barrier for 1-hexyl hydrogenation to n-hexane also decreases the selectivity for 1-hexene, while decreasing the barrier for 1-hexyne hydrogenation to 1-hexenyl increases it.

The major role of H<sub>2</sub> dissociation in the kinetic control of 1-hexyne hydrogenation on dilute Pd-in-Au catalysts starkly differs from the previously studied extended Pd catalysts. For the latter, the addition of atomic H to the adsorbed alkyne or alkenyl is acknowledged as the rate-determining step, with selectivity being governed by the competitive adsorption of alkyne and alkene. On dilute Pd-in-Au catalysts, the selectivity is instead regulated by the competition of the hydrogenation rates of alkyne and alkene, which maintains a high selectivity even at high conversion. Consequently, the energetics and kinetics of the 1-hexyne hydrogenation mechanism over dilute Pd-in-Au alloy are distinct with respect to bulk Pd catalysts. Our reaction profiles derived from first-principles calculations and microkinetic modeling also indicate that 1-hexyne hydrogenation to 1-hexene is an irreversible process due to the strongly exothermic nature of the reaction. This assertion is confirmed by the isotopic exchange hydrogenation experiment carried out on Pd<sub>0.04</sub>Au<sub>0.96</sub> embedded in RCT-SiO<sub>2</sub>.

Another key property of dilute Pd-in-Au alloys is that the adsorption energy of hydrocarbon species is moderate, so that the coverage of Pd sites by these hydrocarbon intermediates is low, enabling access and activation of H<sub>2</sub> and preventing poisoning and coking of the catalysts. Once more, this is different from extended Pd catalysts, on which hydrocarbon species exhibit strong binding and have the potential to form coke at high coverage, thus deactivating the catalyst. The apparent activation enthalpies and reaction orders for dilute Pd-in-Au obtained from our microkinetic modeling align well with previous experiments, despite a temperature shift of approximately 60 K. This temperature variation is attributed to the slight overestimation of the

adsorption energies of surface species when the xc-functional optPBE-vdW is used. In summary, this study remarkably illustrates that the enhanced selectivity of the dilute Pd-in-Au alloy catalyst arises from two key factors: the significant barrier for H<sub>2</sub> dissociation and the small barrier for C-H bond formation from 1-hexyne to 1-hexenyl (which is smaller than that for C-H bond formation from 1-hexene to 1-hexyl). The formation of dilute active species in a less active host metal can therefore be seen as a way to tune the binding energy of reactants, alter reaction profiles, and induce distinct kinetic behaviors for an optimal catalytic activity and selectivity. This concept of dilute alloy catalyst is hence a versatile approach to design highly selective heterogeneous catalysts.

## Chapter 3 Unraveling 1-Hexene Hydrogenation over Dilute Pd-in-Au Alloys

### 3.1 Introduction

Selective hydrogenation is of considerable importance in both the fine chemicals and petrochemical sectors.<sup>59,60</sup> It also serves as a critical process in purifying alkene feedstocks for polymer manufacturing, as even minute traces of alkynes and diene impurities in the monoalkene feeds can substantially poison the catalysts downstream.<sup>60</sup> Partial hydrogenation of these impurities to monoalkenes is typically used to solve this problem. Although Pd-based catalysts (e.g. Lindlar catalyst) have been the state-of-the-art catalysts for this process due to their remarkable catalytic activity at low temperatures, they still lack the desired selectivity for alkene formation.<sup>16,17</sup> Nevertheless, previous studies show that alloying Pd with a less reactive but more selective second metal (e.g. Au, Ag, and Cu) could effectively prevent over-hydrogenation of alkenes to produce alkanes, and we aim to understand the reasoning behind this improved selectivity.<sup>33,59,64,70,74,99–102</sup>

This work is a continuation of Chapter 2, which primarily focuses on the hydrogenation of 1-hexyne to produce 1-hexene. Herein, a combined experimental and theoretical approach is employed to elucidate the reaction mechanisms and the rate- and selectivity-controlling steps of 1-hexene hydrogenation/isomerization over the same dilute Pd-in-Au alloy nanoparticle catalyst as in Chapter 2. The primary goal is to comprehend the favorable selectivity of dilute alloys for hexene isomerization and their capability to inhibit the hydrogenation to hexane. Isotopic labeling experiments, in conjunction with density functional theory calculations and microkinetic modeling, provided understanding regarding the reaction mechanism, energy barriers, and processes governing rates and selectivity. This study also highlighted the key distinctions between dilute Pd-in-Au alloy catalysts and monometallic Pd nanoparticle catalysts.

## 3.2 Methods

### 3.2.1 DFT Calculations

All density functional theory (DFT) calculations were performed using the Vienna ab initio simulation package (VASP).<sup>75,76</sup> The Pd<sub>1</sub>Au(111) surface for hexene hydrogenation/isomerization was constructed using a six-layer slab and a (4 × 4) unit cell, and a Monkhorst-Pack generated 7 × 7 × 1 K-points grid was employed for this unit cell size.<sup>77</sup> For all calculations, a plane wave basis set with a cutoff energy of 400 eV and the optPBE-vdW functional were employed.<sup>78-80</sup> During geometric optimizations, the bottom four layers of the slab model were fixed in the bulk Au position, while the upper two layers and the surface adsorbates were allowed to relax until the convergence threshold of < 0.03 eV/Å was reached. Transition states were located using both the dimer method and the quasi-Newton method.<sup>84</sup> All atomic structures reported in this Chapter are visualized using VESTA.<sup>85</sup>

For simplicity, free energy calculations only take into consideration the translational and rotational entropies of the gaseous species, and zero-point energies (ZPE) and vibrational entropies were neglected for all species. It is emphasized that omitting the ZPEs in free energy calculations does not have a substantial impact on the overall reaction kinetics, as discussed in Chapter 2.

### 3.2.2 Microkinetic Simulations

Microkinetic modeling, which utilized DFT energies as input parameters, was performed to compare the theoretically proposed reaction pathway to experimental observations. In this modeling, the rate constants for adsorption ( $k_{\text{ads},i}$ )/desorption ( $k_{\text{des},i}$ ) (Eqs 3.1 and 3.2) and surface reaction steps ( $k_i$ ) were computed using the collision theory and transition state theory (Eq 3.3), respectively.<sup>87</sup>

$$k_{ads,i} = \frac{\sigma A_{site} P^o}{\sqrt{2\pi m_i k_B T}} \quad (3.1)$$

$$k_{des,i} = k_{ads,i} * \exp\left(\frac{\Delta G_{ads,i}^o}{k_B T}\right) \quad (3.2)$$

$$k_i = \frac{k_B T}{h} * \exp\left(\frac{-\Delta G_{act}^o}{k_B T}\right) \quad (3.3)$$

where  $\sigma$  is the sticking coefficient (assumed to be 1),  $A_{site}$  is the area of the active site,  $P^o$  is the standard state pressure,  $m_i$  is the mass of the adsorbate, and  $k_B$  is the Boltzmann's constant,  $T$  is the temperature,  $\Delta G_{ads,i}^o$  is the adsorption free energy of the adsorbate under standard state pressure,  $h$  is the Planck's constant, and  $\Delta G_{act}^o$  is the free energy of the activation barrier under standard state pressure.

The rate of elementary step  $j$  was computed using the following equation:

$$r_j = k_j^{fwd} \prod_i \alpha_{i,IS}^{v_{ij}^{fwd}} \prod_i \alpha_{i,gas}^{v_{ij}^{fwd}} - k_j^{rev} \prod_i \alpha_{i,IS}^{v_{ij}^{rev}} \prod_i \alpha_{i,gas}^{v_{ij}^{rev}} \quad (3.4)$$

where  $k_j^{fwd}$  and  $k_j^{rev}$  are the forward and reverse rate constants, and  $v_{ij}^{fwd}$  and  $v_{ij}^{rev}$  are the stoichiometric coefficients of reactant  $i$  in the forward and reverse directions, respectively. The activity  $\alpha_i$  was assumed to be the surface coverage fraction  $\theta_i$  for surface intermediates (including bare sites) and as the ratio of the partial pressure to the standard pressure,  $P_i/P^o$ , for gaseous species.<sup>88</sup>

The time-dependent coverages of surface intermediates are obtained as the steady-state solution of the following system of ordinary differential equations:

$$\frac{d\theta_i}{dt} = - \sum_j v_{ij}^{fwd} r_j + \sum_j v_{ij}^{rev} r_j \quad (3.5)$$

Following Wang et al., the steady-state solution is achieved in two steps.<sup>86,89</sup> Starting from a bare surface, the equations are first integrated over 500 s until they have approximately reached a steady state. The resulting coverages are then used as an initial guess for the numerical solution as follows:

$$0 = - \sum_j v_{ij}^{fwd} r_j + \sum_j v_{ij}^{rev} r_j \quad (3.6)$$

$$\theta_{Pd}(t = 0) = \sum_i \theta_{Pd,i} \quad (3.7)$$

$$1 = \sum_i \theta_{Pd,i} + \sum_i \theta_{Au,i} \quad (3.8)$$

where  $\theta_{Pd,i}$  and  $\theta_{Au,i}$  are the surface coverages of species  $i$  on Pd and Au sites, respectively.

In order to assess the degree of H/D exchange in 1-hexene, 2-hexene, and n-hexane as a function of 1-hexene conversion, the microkinetic model described above was embedded in an isothermal and isobaric plug-flow reactor (PFR). The catalyst was assumed to contain a 4.2 wt% of metal. Each Pd-in-Au nanoparticle within the catalyst was assumed to be a sphere with a diameter of 4.9 nm, with 5% of all atoms in each particle being Pd.

### 3.3 Results

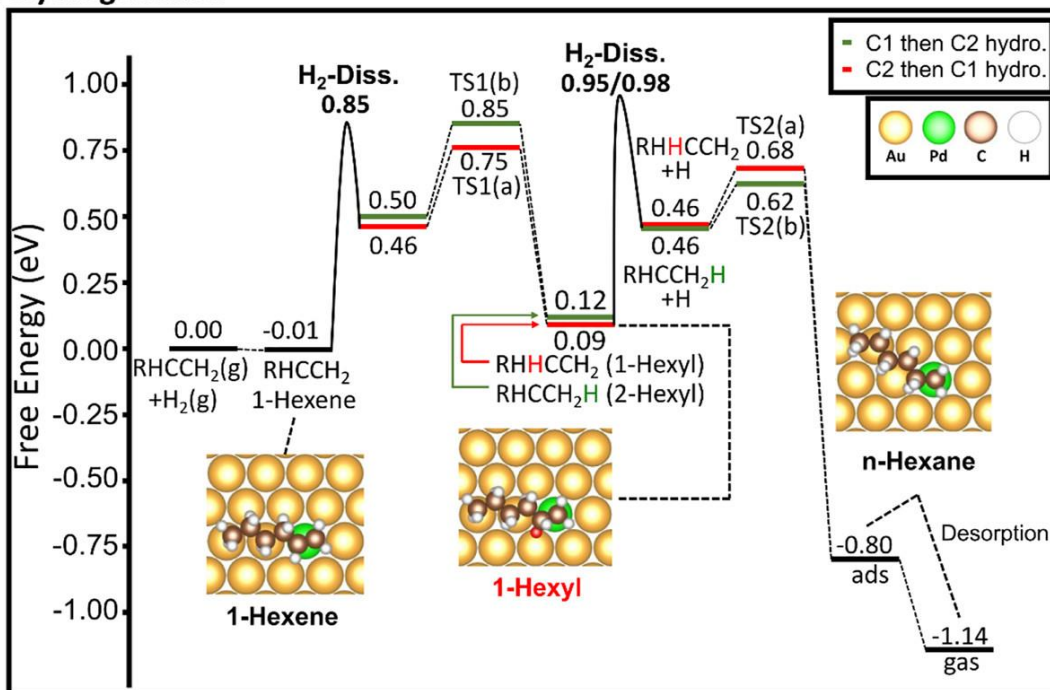
#### 3.3.1 Isotopically Labeled 1-Hexene Hydrogenation Experiments

The isotope-exchange hydrogenation experiments were performed on the Pd<sub>4</sub>Au<sub>96</sub> and Pd RCT catalysts, and the synthesis of which is described by van der Hoeven et al.<sup>90</sup> These experiments first demonstrate that the selectivity towards n-hexane is higher on the monometallic catalyst than that on the dilute alloy catalyst, regardless of whether the reaction was run in H<sub>2</sub> or D<sub>2</sub>. Upon running the reaction in D<sub>2</sub> at T = 373 K, the fraction of 1-hexene d<sub>1</sub> is seen to be lower

for the Pd catalyst (Figure B.1), which implies that the probability of forming 1-hexene from the 1-, or 2-hexyl intermediate is lower on a Pd than on a Pd<sub>4</sub>Au<sub>96</sub> surface. Additionally, the number of deuterium atoms incorporated in n-hexane is higher for the Pd compared to the Pd<sub>4</sub>Au<sub>96</sub> catalyst (Figure B.1), indicating a higher concentration of adsorbed deuterium atoms on the Pd surface and/or a higher probability for hydrogenation vs. isomerization to occur. These observations are in good agreement with the computational results as will be discussed.

### 3.3.2 Adsorption, Isomerization, and Hydrogenation Energies from First-Principles Calculations

#### a Hydrogenation



#### b Isomerization

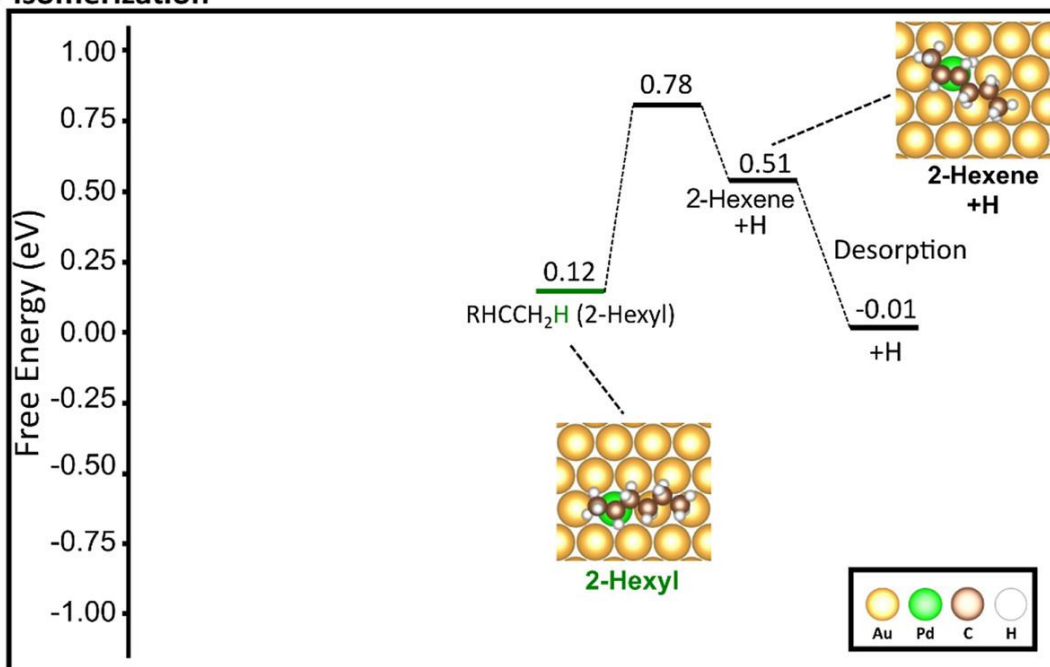


Figure 3.1. Free-energy profiles for (a) 1-hexene hydrogenation and (b) isomerization to 2-hexene calculated using DFT. The abbreviation R represents the butyl group attached to the C=C bond. Two different hydrogenation pathways are shown in (a): the green pathway first hydrogenates the terminal carbon atom of 1-hexene to form 2-hexyl while the red pathway first hydrogenates the carbon atom which is attached to the butyl group R to form 1-hexyl. Both pathways finish by hydrogenating the remaining unsaturated carbon atom in the hexyl intermediates. The H atoms newly added to the unsaturated hydrocarbons are denoted in red or green. Reaction conditions are  $T = 363 \text{ K}$ ,  $P(\text{H}_2) = 0.2 \text{ bar}$ ,  $P(1\text{-hexene}) = 0.01 \text{ bar}$ ,  $P(2\text{-hexene}) = 0.001 \text{ bar}$ , and  $P(\text{n-hexane}) = 0.001 \text{ bar}$ .

Free-energy profiles for 1-hexene hydrogenation to n-hexane and for isomerization to 2-hexene were first constructed to study the reaction mechanisms in detail (Figure 3.1). The full set of adsorption configurations of the reactants, intermediates, and products corresponding to the states in the energy profiles is provided in Figure B.2. These energy profiles begin with the adsorption of 1-hexene on the Pd<sub>1</sub> site, which is thermoneutral under the studied conditions. This is followed by hydrogen dissociation on a second Pd active site and the migration of an H atom to the Pd site where the 1-hexene molecule already resides. As discussed in Chapter 2, the associated overall barrier for these processes is 0.86 eV. The H atoms could subsequently be attached to either the first or second carbon atoms of the hexene molecule, leading to the formation of the 2-hexyl (green) and 1-hexyl (red) intermediates, respectively. Next, the hexyl intermediates can be hydrogenated by the spillover of another H atom to the Pd site and adding a H atom to the remaining carbon radical/remaining unsaturated carbon of the hexyl intermediate to form n-hexane. Once again, the effective free-energy barrier for this second part of the reaction is 0.86 eV (H<sub>2</sub> dissociation). Alternatively, the reverse process from the hexyl intermediates to 1-hexene via

reductive H-elimination can occur, and the effective barrier for this process is 0.67 – 0.73 eV (for 1-hexyl to TS1(a) and 2-hexyl to TS1(b), respectively), which is lower than that for hydrogenation to n-hexane. The barrier for isomerization to 2-hexene is even slightly lower, 0.66 eV, suggesting that the formation of both 1- and 2-hexene is more favorable than the formation of n-hexane. Hence, the DFT calculations suggest that on the Pd<sub>1</sub>Au surface, backward dehydrogenation leading to the formation of a hexene isomer is favored over hydrogenation to n-hexane, and isomerization to 2-hexene is preferred over the regeneration of 1-hexene.

### 3.3.3 Microkinetic Simulations of 1-Hexene Hydrogenation

The reactivity and product selectivity of the calculated reaction mechanism for Pd<sub>1</sub>Au(111) were evaluated under the operating temperature and pressure using microkinetic models, which were parameterized using DFT-calculated reaction energies and barriers from Figure 3.1. In brief, the microkinetic model of 1-hexene hydrogenation/isomerization consists of four groups of reactions: (i) the dissociation of H<sub>2</sub> on a vacant Pd site and the exchange of atomic H between Pd sites, eventually also occupied by the hydrocarbon intermediate, via spillover on Au, (ii) the hydrogenation of 1-hexene to n-hexane through either the 1-hexyl or (iii) 2-hexyl intermediate, and (iv) the isomerization of 1- to 2-hexene through the 2-hexyl intermediate. The hydrogenation of hydrocarbon intermediates was assumed to take place only after hydrogen exchange. Table B.1 summarizes all elementary steps, their kinetic rate constants, the Gibbs free energies of reaction, and the activation energies.

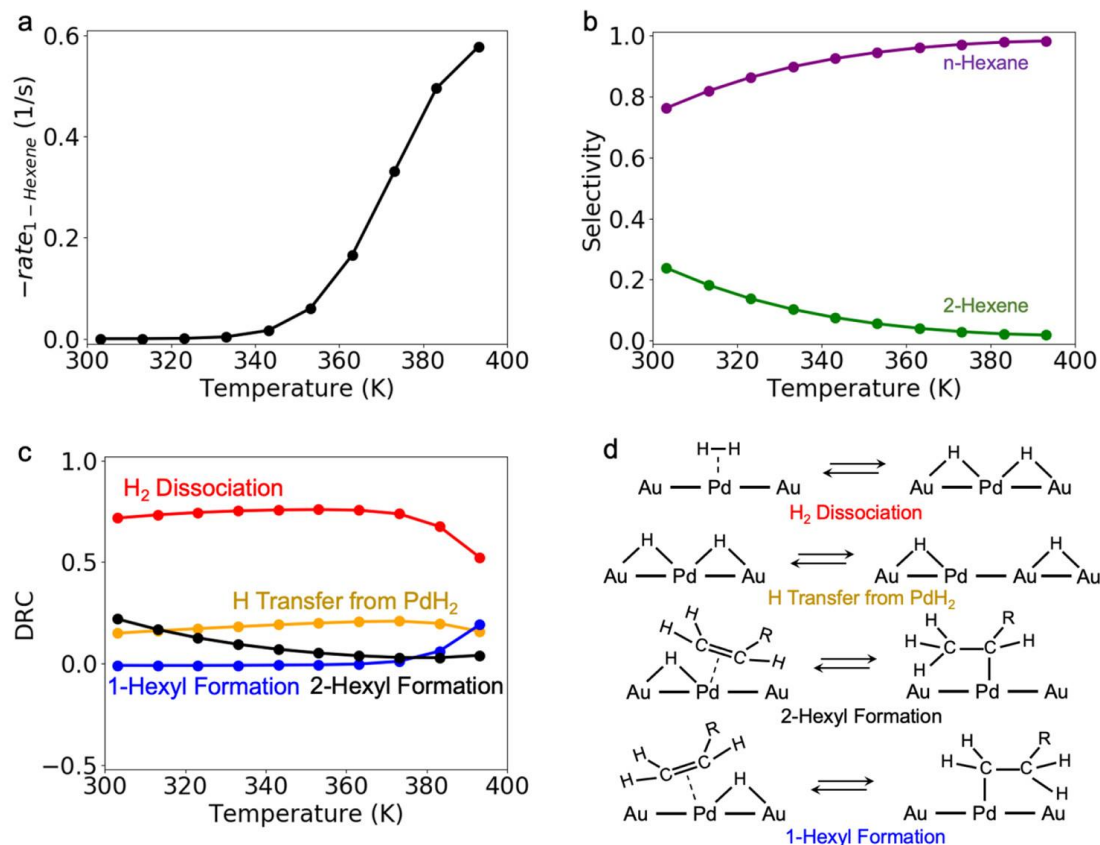


Figure 3.2. 1-Hexene consumption rate, product selectivity, and degrees of rate control (DRC) of transition states for 1-hexene consumption evaluated for the Pd<sub>1</sub>Au(111) model catalyst at fixed partial pressures. Microkinetic model of the 1-hexene reaction with H<sub>2</sub> evaluated at P(H<sub>2</sub>) = 0.2 bar, P(1-Hexene) = 0.01 bar, and P(2-Hexene) = P(n-Hexane) = 0.001 bar. (a) Rate of 1-hexene consumption, (b) selectivity of 2-hexene and n-hexane formation, and (c) main rate-controlling transition states (TS) and their DRC for 1-hexene consumption as functions of temperature. (d) Schematic representations of the elementary steps corresponding to the transition states in panel (c). The reaction was found to start at ~350 K with 2-hexene as the minority product and H<sub>2</sub> dissociation as the main rate-controlling TS.

Microkinetic modeling indicates that at low 1-hexene conversion (fixed partial pressures of P(H<sub>2</sub>) = 0.2 bar, P(1-Hexene) = 0.01 bar, and P(2-Hexene) = P(n-Hexane) = 0.001 bar), the

transformation of 1-hexene commenced at  $T = 333$  K. The reaction rate reaches  $0.331 \text{ s}^{-1}$  at  $T = 373$  K (Figure 3.2a), with 3% of the 1-hexene being isomerized to 2-hexene and the rest hydrogenated to n-hexane (Figure 3.2b). 93% of the produced n-hexane formed through the 1-hexyl intermediate, while the rest proceeded through the 2-hexyl intermediate. The discrepancy between the calculated product selectivity to preferential n-hexane formation and the experimental product selectivity to 2-hexene will be addressed in subsequent discussion.

The degree of rate control (DRC) and degree of selectivity control (DSC) of transition states were carried out to identify the steps that significantly influence the consumption rates of 1-hexene and the selectivity for 2-hexene formation in a quantitative manner.<sup>92</sup> The calculated DRC of transition states (Figure 3.2c,d) for 1-hexene consumption at  $T = 373$  K and partial pressures corresponding to low 1-hexene conversion indicate that  $\text{H}_2$  dissociation (DRC = 0.74) is the main rate-controlling TS, similar to that of 1-hexyne hydrogenation as discussed in Chapter 2. The transition state of H transfer from the  $\text{PdH}_2$  species onto the Au support is also partially rate-controlling (DRC = 0.21), whereas the transition state of C-H bond formation has only a very minor influence on the overall rate: DRC = 0.01 and 0.03 for the formation of 1-hexyl and 2-hexyl, respectively. The DSC showed that under the same conditions [ $T = 373$  K,  $P(\text{H}_2) = 0.2$  bar,  $P(1\text{-Hexene}) = 0.01$  bar, and  $P(2\text{-Hexene}) = P(\text{n-Hexane}) = 0.001$  bar], the selectivity for 2-hexene formation is most negatively impacted by the transition state of  $\text{H}_2$  dissociation and that of H transfer to 2-hexyl (Figure B.3, DSC = -0.57 for both), which could eventually lead to hexane formation. On the other hand, the transition state of 1-hexene hydrogenation to 2-hexyl (DSC = +0.93) and that of 2-hexyl dehydrogenation to 2-hexene (DSC = +0.69) are found to positively influence the selectivity for 2-hexene formation (decreasing the energy of these transition states favors the selectivity to 2-hexene).

The calculated DSCs and DRCs unambiguously show that the free-energy barriers of H<sub>2</sub> dissociation and H-spillover are critical in controlling the overall reactivity and selectivity of the catalyst. This aligns with the rate-determining step observed in the partial hydrogenation of 1-hexyne over Pd<sub>1</sub>/Au, where high H<sub>2</sub> dissociation and H-spillover free-energy barriers lead to the reversible formation of hexyls on Pd<sub>1</sub> sites, enhancing the catalyst's selectivity for 1-hexene by impeding the further hydrogenation of hexyls (Chapter 2). Here, the large H<sub>2</sub> dissociation and H-transfer barriers impact the selectivity in a similar way: 1-hexene isomerization becomes favored when further hydrogenation of hexyl intermediates is hindered by large H<sub>2</sub> dissociation barriers. To test the importance of the barriers beyond a local derivative in the DRCs and DSCs, the rates of 1-hexene conversion and product selectivity were recalculated after increasing the barrier of the H<sub>2</sub> dissociation and H-spillover steps by 0.1 eV, which is within the error bar of DFT calculations (Figure B.4). The recalculated 2-hexene selectivity is in much better agreement with experimental observations, where 2-hexene was found to be the majority product, and this will be further discussed.

### 3.3.4 Theoretical Assessment of H/D Exchange in 1-Hexene Hydrogenation

To further strengthen the argument that large H<sub>2</sub> dissociation and H-spillover barriers are accountable for the high selectivity to 2-hexene, the microkinetic models were extended to include D<sub>2</sub>/HD adsorption, D exchange between Pd/Au sites, and the deuteration of hydrocarbon intermediates (Table B.1). For 1- and 2-hexene, one H atom was allowed to be exchanged for D, while for n-hexane, up to two H atoms were allowed to be exchanged for D. The microkinetic model was embedded in an isothermal and isobaric plug flow reactor (PFR) with 200 mg of catalyst loading to assess the degree of H/D exchange in the hexenes and n-hexane as a function of temperature and 1-hexene conversion. The inlet flow rate to the reactor was assumed to be 50

standard mL/min (corresponding to the standard condition of  $T = 273.15$  K and  $P = 1$  atm), consisting of 1 vol % 1-hexene and 20 vol %  $D_2$  with an inert balance. These simulations were first carried out without any changes in the  $H_2$  dissociation and H-spillover barriers (Figure B.5). Following the 1-hexene consumption rates and 2-hexene selectivity evaluated at fixed partial pressures (Figure 3.2), n-hexane was found to be the major product. Marked H/D exchange was observed in the hydrocarbon species, with n-hexane  $d_1$  as the most prevalent product at 10% 1-hexene conversion.

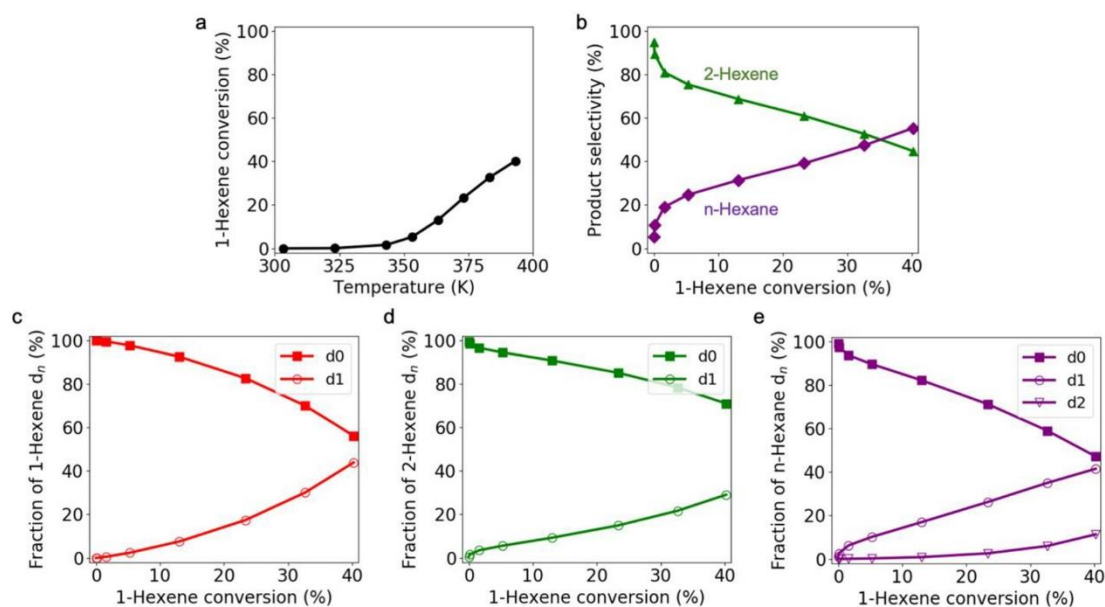


Figure 3.3. Product and isotope selectivity of 1-hexene deuteration and isomerization, with the barriers of  $H_2$  dissociation and H-spillover increased by 0.1 eV. (a) 1-Hexene conversion and (b) selectivity of 2-hexene and n-hexane as functions of reactor temperature. (c) 1-Hexene isotope distribution, (d) 2-hexene isotope distribution, and (e) n-hexane isotope distribution as functions of 1-hexene conversion. The PFR, with 200 mg of catalyst loading, was assumed to operate at constant temperature and pressure (1 bar). The 1-hexene conversion and product/isotope selectivity were evaluated under an inlet flow of 50 standard mL/min (corresponding to the

standard condition of  $T = 273.15$  K and  $P = 1$  atm), consisting of 1 vol % 1-hexene and 20 vol %  $D_2$  with an inert balance.

The simulated product selectivity qualitatively agrees with experimental observations after increasing the barriers of  $H_2/D_2/HD$  dissociation and H/D-spillover by 0.1 eV (Figure 3.3). The conversion of 1-hexene commenced at 343 K, reaching an overall conversion of 40.2% at 393 K (Figure 3.3a). In the temperature range of 303 to 383 K, 2-hexene emerged as the predominant product across most temperatures (Figure 3.3b), which is in agreement with experimental observation. At 373 K, the conversion of 1-hexene was 23.3%, with a 60.9% selectivity for 2-hexene. The calculated degree of H/D exchange (Figure 3.3c-e) also followed the trend observed in the experiment. The quantity of deuterated hexenes and n-hexane rose from 303 to 393 K but never surpassed the amount of non-deuterated carbonaceous species. Similar to the experimental findings, the microkinetic modeling results at 373 K indicate that the majority of all carbonaceous species in the reactor outlet remained  $d_0$ : 82.6% 1-hexene  $d_0$ , 85.1% 2-hexene  $d_0$ , and 71.2% n-hexane  $d_0$ .

Prior to concluding, it is important to discuss the origin of the improved selectivity to hexenes in detail. Our combined DFT and microkinetic modeling approach revealed that the preferential hexene isomerization of the  $Pd_4Au_96$  catalysts is likely caused by  $H_2$  dissociation and H-spillover being rate-limiting on the  $Pd_1Au(111)$  alloy surface. With high  $H_2$  dissociation and H-spillover barriers, fewer H atoms will be available for hydrogenation at the adsorption sites of the reaction intermediates, leading to lower hexane formation. Weaker alkene adsorption is often invoked to explain the improved alkene selectivity of dilute alloy systems. Indeed, our DFT calculations support a lower alkene adsorption energy on dilute alloy surfaces than on pure Pd surfaces (Table B.2), which aligns well with previous experimental findings where the ethylene adsorption energy

decreased when diluting Pd in Au and when lower coverages of ethylene were measured with microcalorimetry.<sup>71</sup> However, the free-energy profiles and our microkinetic simulations show that this is not the main reason for the improved selectivity of dilute alloys.

### 3.4 Conclusion

In this study, new mechanistic insight was presented to unravel the enhanced alkene selectivity of dilute alloy catalysts and their ability to impede 1-hexene hydrogenation under hydrogen. By combining isotope-exchange experiments, DFT calculations, and microkinetic modeling, hexene isomerization and hydrogenation on a dilute Pd-in-Au alloy catalyst is shown to take place via the same Horiuti-Polanyi mechanism as on a monometallic Pd surface. H<sub>2</sub> dissociation and H-spillover onto the Au host are also demonstrated to be the rate- and selectivity-limiting elementary steps in the reaction mechanism, which hinders the hydrogenation reaction. Once more, this is distinct from the common assumption that the enhanced alkene selectivity of Pd alloys originates from the weakening of the alkene adsorption energies. It is emphasized that hexene adsorption and H<sub>2</sub> dissociation cannot occur on the same Pd site, thus H-migration is a key step in hexene conversion on the dilute alloys. Our results help shed light on the future design of more efficient alloy catalysts for alkyne and alkene hydrogenation.

# Chapter 4 Influence of Pd Concentration in Au-Pd Nanoparticles for the Hydrogenation of Alkynes

## 4.1 Introduction

AuPd systems are commonly applied in the hydrogenation of alkynes ( $C\equiv C$ ) into alkenes ( $C=C$ ).<sup>64,69,103,104</sup> As discussed in Chapter 2 and 3, catalysts consisting of Pd single atoms on Au(111), which correspond to the  $Pd_{0.04}Au_{0.96}$  particles in experiments, have been shown to reactively and selectively convert 1-hexyne into hexene isomers. It was observed that the high selectivity for alkene formation is attributed to the sizable  $H_2$  dissociation and H-spillover barriers. Although these barriers help enhance selectivity, they also lead to lower catalytic reactivity. In this Chapter, we aim to explore larger Pd ensembles on Au(111) to determine if they could achieve higher reactivity by lowering the aforementioned barriers while preserving the desired selectivity for alkene formation.

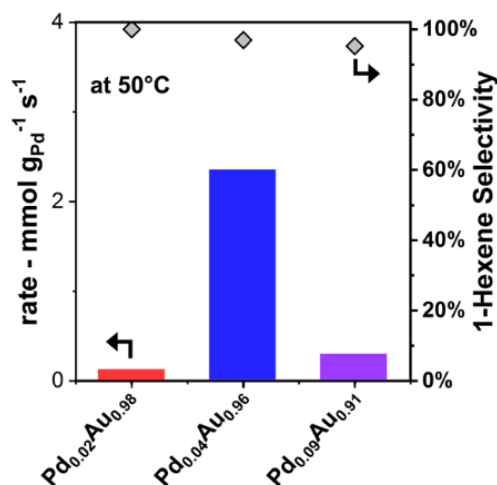


Figure 4.1. Measurements of the rate of 1-hexyne conversion (bars) and selectivity (gray diamonds) for 1-hexene production. An optimum in the rate of 1-hexyne conversion is achieved for  $Au_{0.96}Pd_{0.04}$ . Reproduced from ref 64. Copyright 2020 American Chemical Society.

Former experimental studies have demonstrated that 1-hexyne conversion rate is higher on the Pd<sub>0.04</sub>Au<sub>0.96</sub> catalyst than the Pd<sub>0.09</sub>Au<sub>0.91</sub> and the Pd<sub>0.02</sub>Au<sub>0.98</sub> catalysts (Figure 4.1).<sup>64,105</sup> It is understood that the spatial distribution of Pd in Au-Pd would change with Pd concentration. To elaborate, an increase in Pd concentration should lead to greater segregation of Pd atoms towards the surface layer of Au, and simultaneously increase the likelihood of the formation of Pd-rich islands.<sup>106</sup> Contrary to expectations, Pd<sub>0.09</sub>Au<sub>0.91</sub>, which is anticipated to have higher reactivity due to the presence of more surface Pd atoms and the potential formation of Pd-rich islands, exhibits lower reactivity than Pd<sub>0.04</sub>Au<sub>0.96</sub>.<sup>64</sup> Nevertheless, these catalysts all demonstrate high selectivity (> 90%) for 1-hexene formation based on previous experimental investigations.<sup>64</sup> The origin of these observations has not been fully comprehended, and this work aims to provide answers to these seeming contradictions.

Herein, a comprehensive experimental and theoretical methodology was employed to elucidate the relationship between reaction reactivity and catalyst surface configuration. We demonstrated that Au-Pd particles with higher Pd concentration (in the considered regime, where Pd is diluted) show substantial segregation of Pd to the surface. DFT analysis further presents that the activity of isolated Pd atoms in Au(111) is higher than Pd dimers and triangular Pd trimers, as the small Pd aggregates are poisoned by the strongly bound alkyne molecule. The optimal Pd concentration should hence be characterized by a high concentration of Pd monomers along with an enhanced segregation of Pd atoms towards the surface, and this explains the high reactivity observed for the Pd<sub>0.04</sub>Au<sub>0.96</sub> catalyst.

## 4.2 Methods

### 4.2.1 DFT Calculations

All DFT calculations were performed with the Vienna ab initio simulation package (VASP).<sup>75,76</sup> The surfaces of Pd/Au(111) for acetylene hydrogenation were modeled using a 6-layer slab and a (3 × 3) unit cell. The dDsC-dispersion-corrected PBE functional,<sup>107,108</sup> a cutoff energy of 400 eV, and a Monkhorst-Pack-generated 7 × 7 × 1 K-points mesh were employed for all calculations.<sup>77</sup> During structural optimization, the bottom four layers of the slab were fixed at the bulk Au lattice parameters, while the upper two layers and the adsorbates were allowed to relax until convergence thresholds of 10<sup>-5</sup> eV for energies and 0.03 eV/Å for forces were reached. A stricter energy convergence criterion of 10<sup>-7</sup> eV was set for the transition states. Transition states were located using both the climbing image nudged elastic band (CI-NEB) and the dimer method.<sup>84,109</sup> For simplicity, free energy calculations neglect zero-point energies and vibrational entropies of both the surface and gaseous species. All atomic configurations reported were visualized using VESTA.<sup>85</sup>

### 4.2.2 Microkinetic Simulations

Microkinetic simulations were performed by using the energetics obtained from DFT calculations. Collision theory (Eqs 4.1 and 4.2) and transition state theory (Eq 4.3) were used to compute the rate constants for adsorption ( $k_{ads,i}$ )/desorption ( $k_{des,i}$ ) and surface reactions ( $k_j$ ), respectively:<sup>87</sup>

$$k_{ads,i} = \frac{A_{st}}{\sqrt{2\pi m_i k_B T}} \quad (4.1)$$

$$k_{des,i} = k_{ads,i} P^o \exp\left(\frac{\Delta G_{ads,i}^o}{k_B T}\right) \quad (4.2)$$

$$k_j = \frac{k_B T}{h} \exp\left(-\frac{\Delta H^\ddagger}{k_B T}\right) \exp\left(\frac{T \Delta S^\ddagger}{k_B T}\right) \quad (4.3)$$

where  $A_{st}$  is the area of the adsorption site,  $m_i$  is the mass of the adsorbing species  $i$ ,  $k_B$  is the Boltzmann's constant,  $T$  is the temperature,  $P^\circ$  is the standard state pressure,  $G_{ads,i}^o$  is the adsorption free energy of species  $i$  under standard state pressure,  $h$  is the Planck's constant, and  $\Delta H^\ddagger$  and  $\Delta S^\ddagger$  are, respectively, the enthalpy and entropy difference between the initial state and the transition state in elementary step  $j$ .

In the microkinetic simulations, species rate equation  $i$  was obtained from the combination of the rate equation of each elementary step  $j$ :

$$\frac{d\theta_i}{dt} = \sum_j v_{ij} r_j \quad (4.4)$$

where  $\theta_i$  is the surface coverage of species  $i$ ,  $t$  is time,  $v_{ij}$  is the stoichiometric coefficient of species  $i$  in step  $j$ , and  $r_j$  is the reaction rate of elementary step  $j$ .

The catalyst surface is set to be bare initially. Solutions are then obtained from the set of differential equations (see Tables C.1, C.2, and C.3) when the system reaches steady state (i.e.  $\frac{d\theta_i}{dt} = 0$ ), which is safely assumed to occur before  $t = 50$  s.

The degree of rate and selectivity controls (DRCs and DSCs, respectively) measure the extent of an increase in the net reaction rate and the selectivity with an increase in the rate constants of a specific elementary step, which could be reflected in the free energy of the transition state.<sup>92</sup> In such calculations, the free energies of all the other transition states and surface intermediates are kept constant. Mathematically, DRCs and DSCs are defined as

$$DRC = \left( \frac{\partial \ln(r)}{\partial \left( \frac{-G_j^{o,TS}}{k_B T} \right)} \right)_{G_{j \neq k}^{o,TS}, G_{im}^o} \quad (4.5)$$

$$DSC = \left( \frac{\partial \ln(S)}{\partial \left( \frac{-G_j^{o,TS}}{k_B T} \right)} \right)_{G_{j \neq k}^{o,TS}, G_{im}^o} \quad (4.6)$$

where  $r$  is the net reaction rate,  $S$  is the selectivity defined as the ratio of ethylene formation rate to acetylene consumption rate,  $G_j^{o,TS}$  is the standard state free energy of the transition state of the elementary step  $j$ , and  $G_{im}^o$  is the standard state free energy of all surface intermediates.

## 4.3 Results

### 4.3.1 Binding Strengths of Surface Species

Table 4.1. Adsorption and Reaction Free Energies of Various Species on Pd<sub>1</sub>, Pd<sub>2</sub>, and Pd<sub>3</sub> at T = 363 K, P(H<sub>2</sub>) = 0.2 bar, P(C<sub>2</sub>H<sub>2</sub>) = 0.01 bar, and P(C<sub>2</sub>H<sub>4</sub>) = P(C<sub>2</sub>H<sub>6</sub>) = 0.001 bar.

	Pd <sub>1</sub>	Pd <sub>2</sub>	Pd <sub>3</sub>
G <sub>ads</sub> (C <sub>2</sub> H <sub>2</sub> )	-0.05 eV	-0.37 eV	-1.03 eV
G <sub>ads</sub> (C <sub>2</sub> H <sub>4</sub> )	0.19 eV	0.09 eV	-0.06 eV
G <sub>ads</sub> (2H)	0.35 eV	0.11 eV	-0.24 eV
G <sub>ads</sub> (C <sub>2</sub> H <sub>3</sub> )	-0.50 eV	-0.81 eV	-1.20 eV
G <sub>ads</sub> (C <sub>2</sub> H <sub>5</sub> )	-1.74 eV	-1.93 eV	-2.04 eV

Binding strengths of surface species on dilute alloys increase significantly with increasing Pd ensemble sizes (Table 4.1). On Pd<sub>1</sub>, the adsorption free energy of acetylene is the smallest among the three different Pd ensembles, with the value being -0.05 eV under the studied condition. This small magnitude prevents the catalyst surface from being completely covered by acetylene and leaves a portion of the active sites vacant for H<sub>2</sub> activation, as has been seen in 1-hexyne hydrogenation in Chapter 2. Since the binding strength of acetylene generally outcompetes that of atomic H, the blocking of the active sites would only make H<sub>2</sub> activation more difficult on larger Pd ensembles, despite the stronger binding of atomic H and hence a smaller H<sub>2</sub> dissociation barrier on them. The adsorption free energies of ethylene also follow this identical pattern, with the binding strength being the weakest on Pd<sub>1</sub> and the strongest on Pd<sub>3</sub> (Table 4.1). On Pd<sub>1</sub> and Pd<sub>2</sub>, the adsorption free energies of ethylene are positive, indicating the tendency to desorb. However,

desorption of ethylene is slightly unfavorable on Pd<sub>3</sub> as designated by the negative value, which would hamper ethylene production. The free energy values of the reaction intermediates additionally mirror the same trend. Complete free energy profiles constructed under standard-state pressures for the three ensembles are provided in Figure C.1 – C.8, and the effect of the binding strength will be explored in more detail in the microkinetic simulations.

### 4.3.2 Microkinetic Simulations of Catalytic Performance

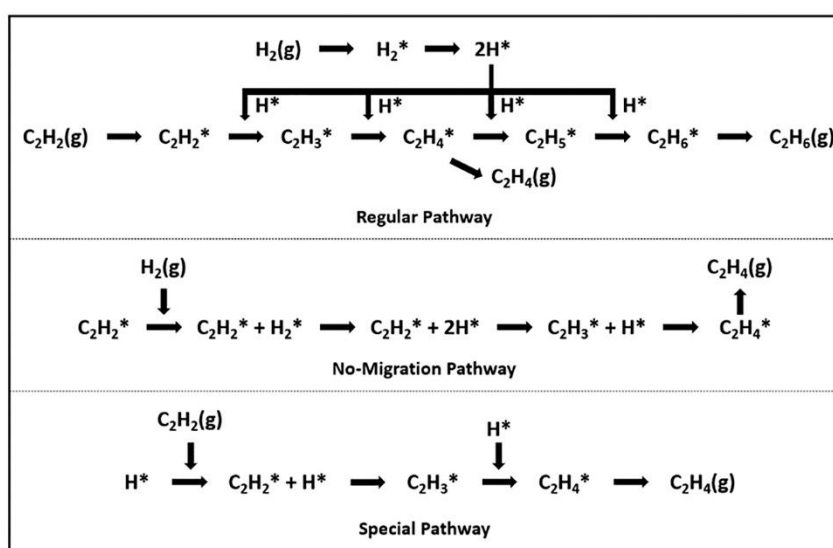


Figure 4.2. Schematic representation of the regular pathway, where acetylene adsorbs on one Pd<sub>n</sub> site, H<sub>2</sub> adsorbs and dissociates on another Pd<sub>n</sub> site, and H migrates over Au to reach the adsorbed acetylene and perform the successive hydrogenation steps; the no-migration pathway where for Pd<sub>3</sub> acetylene adsorbs on one Pd<sub>3</sub> site and H<sub>2</sub> subsequently adsorbs and dissociates on the same Pd<sub>3</sub> – C<sub>2</sub>H<sub>2</sub><sup>\*</sup> site; the special pathway where acetylene adsorbs on a Pd<sub>3</sub> site occupied by one H adatom (noted ([H<sup>3</sup> – Pd<sub>3</sub>])). For simplicity, only the first half of the hydrogenation reaction (C<sub>2</sub>H<sub>2</sub> → C<sub>2</sub>H<sub>4</sub>) is shown in the latter two pathways as the second half (C<sub>2</sub>H<sub>4</sub> → C<sub>2</sub>H<sub>6</sub>) follows the same pattern. An asterisk indicates the surface species.

Microkinetic simulations were performed to shed light on the reaction rates and the rate- and selectivity-determining steps in the convoluted reaction mechanisms. The hydrogenation pathway starts with acetylene adsorption on one vacant  $\text{Pd}_n$  active site and  $\text{H}_2$  activation on another  $\text{Pd}_n$  active site of the alloy surface. Following the  $\text{H}_2$  dissociation, one of the H atoms will migrate to the acetylene adsorption site and hydrogenate the molecule to chemisorbed ethylenyl ( $\text{C}_2\text{H}_3^*$ ). Subsequent hydrogenation steps occur similarly, and the H-migration event is assumed to take place every time a C-H bond is formed.  $\text{C}_2\text{H}_4^*$  can desorb or be further hydrogenated. This reaction pathway is termed the regular pathway (Figure 4.2). In addition, two more reaction pathways were included exclusively for  $\text{Pd}_3$ , considering its larger ensemble size: (1)  $\text{H}_2$  dissociation on the acetylene/ethylene adsorption site followed by C-H bond formation (no-migration pathway) and (2) adsorption of an acetylene/ethylene molecule on the  $\text{Pd}_3$  ensemble where a H atom already resides on the  $\text{Pd}_3$  fcc hollow site ( $[\text{H}^3 - \text{Pd}_3]$ ) and, subsequently, hydrogenation takes place (special pathway) (Figure 4.2).

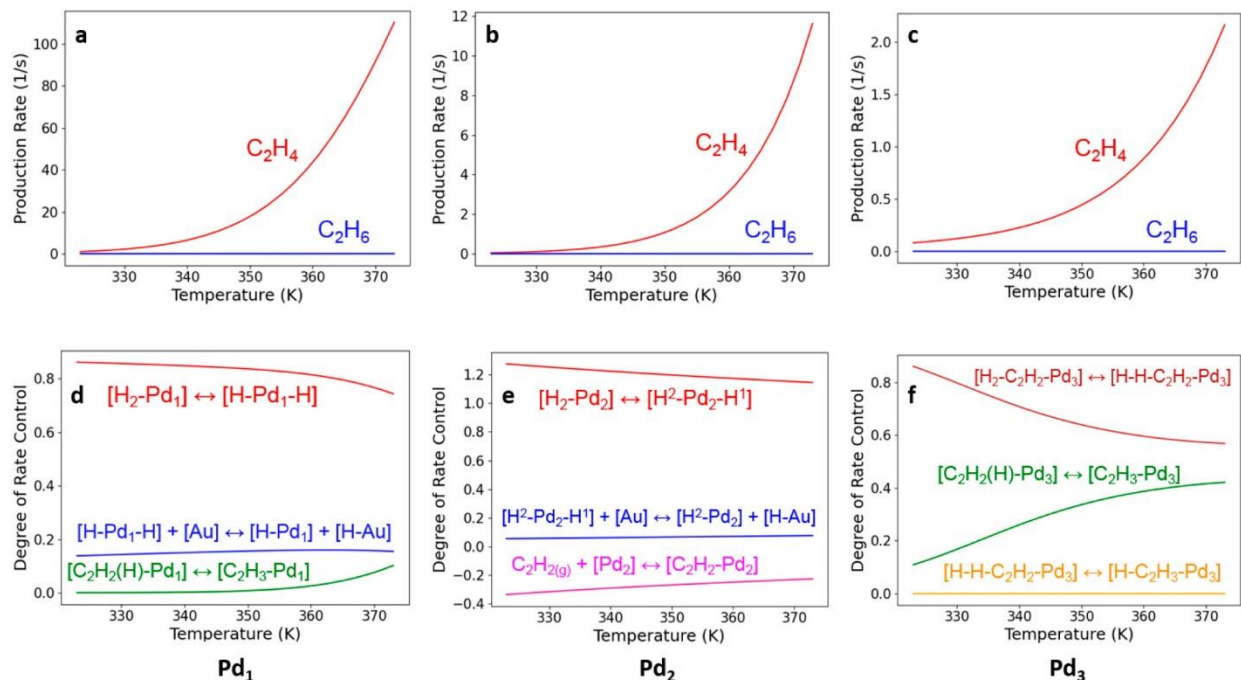


Figure 4.3. Reaction rates (a-c) and degree of rate controls (DRCs) of transition states (d-f) for acetylene hydrogenation on Pd<sub>1</sub> (a, d), Pd<sub>2</sub> (b, e), and Pd<sub>3</sub> (c, f) calculated using microkinetic simulations. Hydrocarbon co-adsorbing with an H atom on a Pd ensemble in the regular pathway is denoted as [C<sub>2</sub>H<sub>x</sub>(H) – Pd<sub>y</sub>]. Note that [H – C<sub>2</sub>H<sub>3</sub> – Pd<sub>3</sub>] also represents the co-adsorption of C<sub>2</sub>H<sub>3</sub> with an H atom, but its configuration differs from that in the regular pathway (see Figure C.6, C.7, and C.13). The number superscripted next to H in (e) is the coordination number of the H atom with the Pd atoms in the absence of any hydrocarbon. Only elementary steps with significant DRCs are shown in (d-f). The calculations were performed at P(C<sub>2</sub>H<sub>2</sub>) = 0.01 bar, P(H<sub>2</sub>) = 0.2 bar, P(C<sub>2</sub>H<sub>4</sub>) = 0.001 bar, and P(C<sub>2</sub>H<sub>6</sub>) = 0.001 bar.

Then, the reaction rates and degree of rate controls (DRCs) were calculated and are listed in Figure 4.3. The rate of acetylene hydrogenation on Pd monomers (Pd<sub>1</sub>) is much higher than those on larger Pd ensembles (Figure 4.3a-c). The difference in the reaction rates among the three Pd ensembles is a consequence of the different adsorbate binding strengths. On Pd monomers, the

binding of the reactant, acetylene, is weak with the adsorption free energy being  $-0.05$  eV at  $T = 363$  K (Table 4.1). As mentioned, this weak binding results in the active sites being only partially occupied by acetylene, which leaves some  $\text{Pd}_1$  sites vacant for  $\text{H}_2$  activation. Indeed, microkinetic simulation shows that acetylene coverage starts to decrease at  $T = 323$  K due to the entropy penalty, rendering the catalyst surface partly bare (Figure C.9). Notably, the production rate of ethylene also begins to increase at the same temperature. To better understand the rate-limiting steps in acetylene hydrogenation on  $\text{Pd}_1$ , degree of rate control (DRC) calculations of the transition states were performed (Figure 4.3d-f). Similar to 1-hexyne hydrogenation on the same catalyst (Chapter 2), it is seen that  $\text{H}_2$  dissociation is the most rate-controlling step with a minor contribution from atomic H migration. The observation that  $\text{H}_2$  molecular dissociation is the most rate-controlling step is also consistent with the weak binding of H species on  $\text{Pd}_1$ . For weak binding, the transition state for  $\text{H}_2$  dissociation is not well-stabilized, resulting in a large free energy barrier of  $0.62$  eV. It is important to emphasize that the difference between this barrier of  $0.62$  eV and that found in Chapter 2 ( $0.86$  eV) is attributed to the different functionals used. The dDsC-corrected-PBE functional used in this Chapter is known to slightly over-estimate the binding strength of H atoms, resulting in the smaller free energy barrier observed.<sup>81</sup>

The apparent activation energy for acetylene hydrogenation on  $\text{Pd}_1$  drops from approximately  $1.06$  eV at  $T = 323$  K to  $0.73$  eV at  $T = 373$  K (Figure C.10). According to Mao and Campbell, the apparent activation energy ( $E_{\text{app}}$ ) can be interpreted as the sum of the enthalpies of all transition states and surface intermediates weighed by their respective DRCs.<sup>93</sup> Hence, the decrease in  $E_{\text{app}}$  observed here is attributed to the lower DRC of the  $\text{H}_2$  dissociation transition state (which has a positive enthalpy value) and the higher DRCs of the transition state for acetylene hydrogenation and the surface intermediate  $\text{C}_2\text{H}_2$  across this temperature range (both of which possess negative

enthalpy values) (see Figure 4.3 and Figure C.10).

Microkinetic simulations demonstrate that the reaction rate on Pd<sub>2</sub> is approximately one-tenth of that on Pd<sub>1</sub> (Figure 4.3b). This low reaction rate is a direct consequence of the strong binding of acetylene, of which the adsorption free energy is -0.37 eV at T = 363 K (Table 4.1). This strong binding expels any H<sub>2</sub> molecules from the Pd active sites, rendering H<sub>2</sub> activation either impossible on occupied Pd ensembles or difficult on Au domains. Evidence from surface coverage and DRC analysis support this claim and are consistent with the free-energy-based analysis. It is shown that all the Pd<sub>2</sub> active sites are solely occupied by acetylene in the entire temperature range studied (Figure C.9b). Acetylene adsorption is also demonstrated to be negatively rate-controlling, meaning that if acetylene adsorption becomes more stabilizing, then the reaction rate would be even lower (Figure 4.3e). From an alternative perspective, since all active Pd sites are occupied by acetylene, H<sub>2</sub> dissociation becomes very positively rate-determining on Pd<sub>2</sub>. Additionally, the apparent activation energy for this hydrogenation reaction on Pd<sub>2</sub> remains constant at 1.16 eV (Figure C.11). This value is very consistent with the enthalpy value of C<sub>2</sub>H<sub>2</sub> on the catalyst surface weighed by its DRC of -1 (Figure C.11), which further supports the claim that C<sub>2</sub>H<sub>2</sub> poisons the active sites and renders the catalyst less active. Note that, although the transition state of H<sub>2</sub> dissociation has a large and positive DRC value, it has no impact on the E<sub>app</sub> calculation, as the relative enthalpy value of this transition state is roughly equal to 0.

Pd<sub>3</sub> has the lowest reactivity for acetylene hydrogenation among the three Pd ensembles, with the reaction rate being approximately 2% that of Pd<sub>1</sub> (Figure 4.3c). Among all elementary steps, the most-rate-controlling one is found to be the dissociation of H<sub>2</sub> on the same Pd<sub>3</sub> site, where an acetylene molecule already resides. Additionally, the hydrogenation of acetylene to form ethylenyl is also somewhat rate-controlled (Figure 4.3f). DRC of surface intermediates and apparent

activation energy for acetylene hydrogenation on Pd<sub>3</sub> calculated using microkinetic simulations are provided in Figure C.12. Since the reaction network on Pd<sub>3</sub> is convoluted, building a reaction scheme would be necessary to gain insight into these observations.

Acetylene hydrogenation on Pd<sub>3</sub> involves three parallel pathways, as shown in Figure C.13. At steady state, instead of adsorbing acetylene on a bare Pd<sub>3</sub> site, the reaction starts with acetylene adsorption on [H<sup>3</sup> – Pd<sub>3</sub>]. Given that C<sub>2</sub>H<sub>2</sub> on the Pd<sub>3</sub> hollow site is more stable than the H atom on the same site, the surface species undergo a configurational transformation to reach this new adsorption state [C<sub>2</sub>H<sub>2</sub>(H) – Pd<sub>3</sub>]. The reaction then proceeds via a regular pathway in which an H atom is drawn to the hydrocarbon each time a C-H bond is created. Once ethylene is formed on the catalyst surface, most of it will desorb into the gas phase directly under the studied condition. The rest will participate in the regular pathway again to reach the state of ethylene co-adsorbing with another H atom [C<sub>2</sub>H<sub>4</sub>(H) – Pd<sub>3</sub>]. It is more stable to put the H atom on the Pd<sub>3</sub> hollow site and C<sub>2</sub>H<sub>4</sub> on the Pd<sub>1</sub> top site (as in the special pathway [C<sub>2</sub>H<sub>4</sub>(H) – Pd<sub>3</sub> – SP]) than to put the configuration where C<sub>2</sub>H<sub>4</sub> is on the Pd – Pd bridge site and the H atom is on the Au<sub>1</sub> – Pd<sub>2</sub> hollow site (as in the regular pathway [C<sub>2</sub>H<sub>4</sub>(H) – Pd<sub>3</sub>]). Additionally, [C<sub>2</sub>H<sub>4</sub>(H) – Pd<sub>3</sub> – SP] also lies lower in free energy than ethyl. Hence, [C<sub>2</sub>H<sub>4</sub>(H) – Pd<sub>3</sub>] in the regular pathway will transform into the special pathway configuration [C<sub>2</sub>H<sub>4</sub>(H) – Pd<sub>3</sub> – SP]. Ethylene desorption could subsequently occur, leaving the H atom on the Pd<sub>3</sub> hollow site.

However, the dissociation of H<sub>2</sub> in the presence of acetylene as in the no-migration pathway is the most rate-controlling step on Pd<sub>3</sub> (Figure 4.3f). The no-migration pathway begins with the H<sub>2</sub> adsorption on [C<sub>2</sub>H<sub>2</sub> – Pd<sub>3</sub>], followed by dissociation to reach the state where C<sub>2</sub>H<sub>2</sub> co-adsorbs with two H atoms. Since the Pd<sub>3</sub> hollow site is occupied by the acetylene molecule, the dissociation must take place on the Au<sub>2</sub> – Pd<sub>1</sub> hollow site. Hence, the H<sub>2</sub> dissociation free energy barrier in the

no-migration pathway is much higher than that on a bare active site (0.85 eV for the former and 0.16 eV for the latter under standard-state pressures). Following the dissociation, one of the two H atoms can either attach to the acetylene molecule to form  $C_2H_3$  or migrate away from the  $Pd_3$  ensemble for hydrogenation on a second active site. Microkinetic simulations demonstrate that migration is more favorable, and the surface species left behind would transform into the co-adsorption configuration in the regular pathway. The no-migration pathway is not the most active pathway in acetylene hydrogenation on  $Pd_3$  as indicated by its reaction rate of  $0.31\text{ s}^{-1}$  at  $T = 363\text{ K}$ , which is lower than the overall reaction rate of  $1.1\text{ s}^{-1}$  at the same temperature. Yet, this pathway possesses the greatest positive degree of rate control. In other words, the overall reaction rate is most severely impacted by this elementary step of  $H_2$  dissociation in the no-migration pathway. This pathway acts as an amplifier in the coupled reaction mechanism for enhancing the reaction rate.

Now, one can interpret the reaction rates for  $Pd_1$ ,  $Pd_2$ , and  $Pd_3$  to explain the changes in activity shown in Figure 4.1.  $Pd_1$  sites are more active than  $Pd_2$  sites, which are more active than  $Pd_3$  sites.  $Au_{0.91}Pd_{0.09}$  has more  $Pd_2$  and  $Pd_3$  sites than  $Au_{0.96}Pd_{0.04}$  and fewer  $Pd_1$  sites, based on the binomial distribution, as shown in Table C.4. This explains why  $Au_{0.91}Pd_{0.09}$  is less active than  $Au_{0.96}Pd_{0.04}$  per gram of Pd. However, there seems to be a contradiction for the low activity of  $Au_{0.98}Pd_{0.02}$  (rich in  $Pd_1$ ) compared to  $Au_{0.96}Pd_{0.04}$ . We hypothesize that Pd can more easily segregate on the surface of Au-Pd particles if the Pd concentration is high. Adding more Pd atoms to the Au particles increases the number of defects and voids that can facilitate the segregation of Pd to the surface after calcination. Thus,  $Au_{0.96}Pd_{0.04}$  appears to benefit from two factors: A high concentration of active  $Pd_1$  sites was combined with Pd segregation to the surface. These two factors cannot be found together in  $Au_{0.98}Pd_{0.02}$  and  $Au_{0.91}Pd_{0.09}$ .

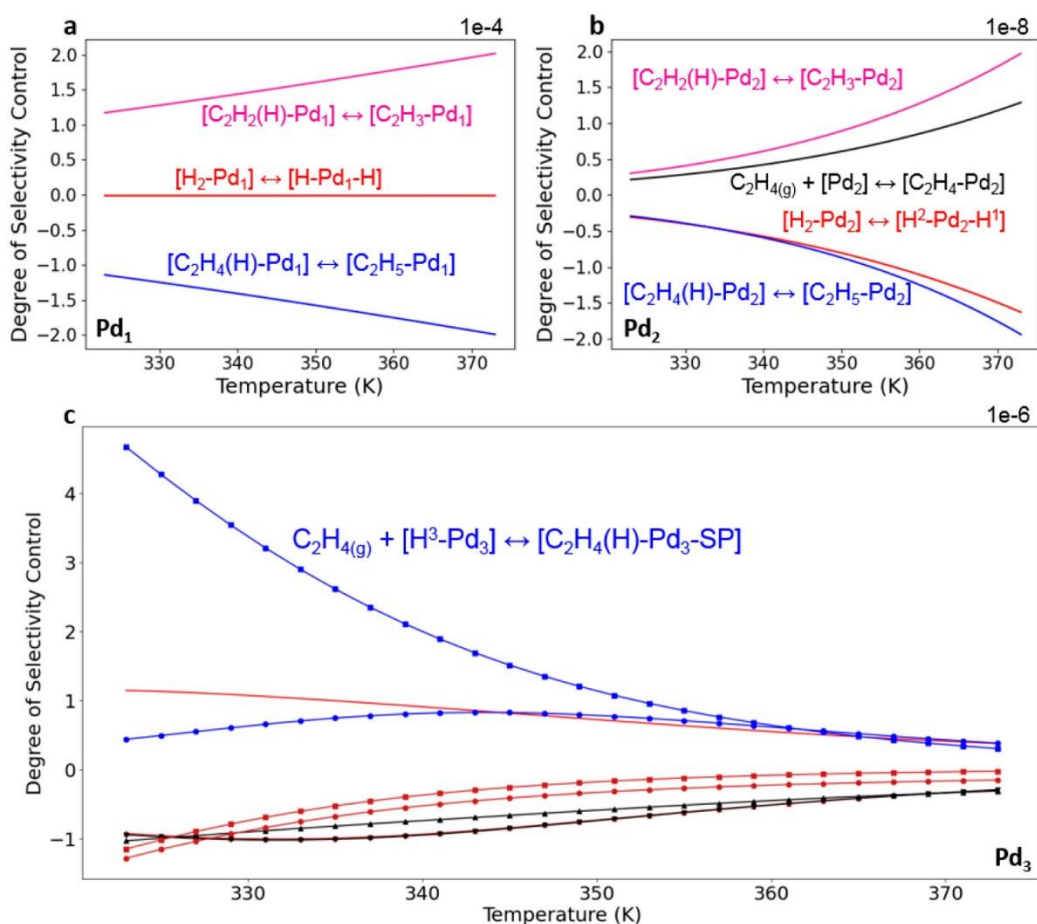


Figure 4.4. Degree of selectivity controls (DSCs) of transition states for acetylene hydrogenation on (a) Pd<sub>1</sub>, (b) Pd<sub>2</sub>, and (c) Pd<sub>3</sub> calculated using microkinetic simulations. On Pd<sub>3</sub>, steps with positive DSCs include  $C_2H_{4(g)} + [H^3 - Pd_3] \rightleftharpoons [C_2H_4(H) - Pd_3 - SP]$  (blue square),  $C_2H_{4(g)} + [Pd_3] \rightleftharpoons [C_2H_4 - Pd_3]$  (blue circle), and  $[C_2H_2(H) - Pd_3] \rightleftharpoons [C_2H_3 - Pd_3]$  (red curve). Steps with negative DSCs, on the other hand, include  $[H_2 - C_2H_2 - Pd_3] \rightleftharpoons [H - H - C_2H_2 - Pd_3]$  (black triangle up),  $[H_2 - C_2H_4 - Pd_3] \rightleftharpoons [H - H - C_2H_4 - Pd_3]$  (black triangle down),  $[C_2H_4(H) - Pd_3] \rightleftharpoons [C_2H_5 - Pd_3]$  (dark red circle),  $[C_2H_4(H) - Pd_3 - SP] \rightleftharpoons [C_2H_5 - Pd_3]$  (dark red square), and  $[H - H - C_2H_4 - Pd_3] \rightleftharpoons [C_2H_5(H) - Pd_3]$  (dark red triangle up). Note that the curves of H<sub>2</sub> dissociation in the presence of ethylene (black triangle down) and the subsequent C-H bond formation (dark red triangle up) overlap in (c). For simplicity, elementary steps with negligible DSCs are excluded in the results.

The calculation was evaluated at:  $P(\text{C}_2\text{H}_2) = 0.01$  bar,  $P(\text{H}_2) = 0.2$  bar,  $P(\text{C}_2\text{H}_4) = 0.001$  bar, and  $P(\text{C}_2\text{H}_6) = 0.001$  bar.

Despite the difference in reaction activity, these dilute Pd-in-Au catalysts all exhibit 100% selectivity for the formation of ethylene, which is the desired product, in the temperature range studied. To investigate the reasons behind this high selectivity, degree of selectivity control (DSC) calculations of the transition states were carried out (Figure 4.4). The selectivity here is defined as the ratio of the ethylene formation rate to the acetylene consumption rate. It is broadly accepted that easy desorption of the partially hydrogenated product is the key to enhancing selectivity. However, in the case of Pd<sub>1</sub>, the high selectivity is mainly attributed to the easy hydrogenation of acetylene to form ethylenyl. If more ethylenyl is formed, then more ethylene could subsequently be formed, too, especially when the second hydrogenation step has a smaller free energy barrier. Ethylene hydrogenation, on the other hand, has a negative degree of selectivity control. The negative value is easily understood by the fact that more of the desired product will be consumed if this ethylene hydrogenation step is made easier, which would shrink the numerator in the definition aforementioned and hence the selectivity. In contrast to the influence observed in the hydrogenation of 1-hexyne, where H<sub>2</sub> dissociation transition state plays a role in determining the selectivity (Chapter 2), its impact appears to be negligible in this study. This discrepancy is ascribed to the utilization of the PBE-dDsC functional, renowned for its tendency to over-estimate H atom binding and yield a reduced H<sub>2</sub> dissociation barrier.<sup>81</sup> Nonetheless, this research effectively delineates the unique characteristics among the three Pd ensembles, despite the effects of over-estimation.

In the case of Pd<sub>2</sub>, the high selectivity is a consequence of the ethylene desorption in addition to the first acetylene hydrogenation step. The reasoning behind ethylene desorption to enhance

selectivity is straightforward, as once desorbed, ethylene would not stay on the catalyst surface for further hydrogenation to form the undesired product ethane. On the same catalyst surface,  $H_2$  dissociation is found to negatively impact the selectivity for ethylene formation, in addition to ethylene hydrogenation. When  $H_2$  dissociation is made easier, atomic H would become more readily available. These H atoms could subsequently hydrogenate more ethylene molecules, which in turn, reduces the ethylene formation and selectivity.

On  $Pd_3$ , the selectivity for ethylene formation is controlled by several elementary steps. Among them, the DSC of  $C_2H_4$  desorption from the catalyst surface with an H atom on the  $Pd_3$  hollow site (blue square in Figure 4.4c, special pathway) is the most positive. This positivity suggests that, if  $C_2H_4$  desorption is made easier, the selectivity would be enhanced, as there are fewer ethylene molecules on the surface for further hydrogenation. The same also applies to the desorption of  $C_2H_4$  in the absence of the H atom (blue circle in Figure 4.4c, regular pathway), which has a positive DSC but a smaller magnitude. In addition, hydrogenation of  $C_2H_2$  to form  $C_2H_3$  in the regular pathway also has a positive DSC as it will augment the production of ethylene and hence increase the selectivity. On the other hand, steps with negative DSCs include the hydrogenation of  $C_2H_4$  in the regular pathway (dark red circle in Figure 4.4c), special pathway (dark red square in Figure 4.4c), and the no-migration pathway (dark red triangle up in Figure 4.4c). These elementary steps consume the desired product  $C_2H_4$  and encourage unwanted  $C_2H_6$  generation. The selectivity for ethylene formation will hence decrease if these steps are able to proceed with lower free energy barriers. Additionally,  $H_2$  dissociation in the presence of  $C_2H_2$  and  $C_2H_4$  as in the no-migration pathway also has a negative DSC (black curves in Figure 4.4c). This is justified by the fact that, if  $H_2$  dissociation becomes more facile, atomic H will become more readily available, which could participate in the over-hydrogenation reaction to form the undesired

product ethane.

## 4.4 Conclusion

To summarize, this work offers important insights into the remarkable reactivity observed during alkyne hydrogenation using the  $\text{Au}_{0.96}\text{Pd}_{0.04}$  catalyst. Our DFT calculations reveal that isolated Pd atoms in Au(111) exhibit notably higher reactivity when compared to larger Pd ensembles (i.e.  $\text{Pd}_2$  and  $\text{Pd}_3$ ) on the same Au surface. The diminished reactivity of  $\text{Pd}_2$  and  $\text{Pd}_3$  is attributed to surface poisoning by the strongly bound acetylene molecule, resulting in challenging and highly rate-limiting  $\text{H}_2$  dissociation to provide H atoms for the reaction. Conversely,  $\text{Pd}_1$  demonstrates a moderate binding strength for acetylene, allowing for the presence of vacant active sites for H-atom generation. Hence, in experiments, an optimum Pd concentration in Au should strike a balance between a high concentration of Pd monomers and a high segregation of Pd atoms to the surface. The  $\text{Au}_{0.96}\text{Pd}_{0.04}$  catalyst appears to achieve this balance; its higher Pd concentration compared to  $\text{Au}_{0.98}\text{Pd}_{0.02}$  promotes the segregation of Pd atoms to the surface, while the concentration is still low enough to inhibit the significant formation of larger Pd ensembles, as is the case in  $\text{Au}_{0.91}\text{Pd}_{0.09}$ .

# Chapter 5 Tuning the Hydrogenation Selectivity of an Unsaturated Aldehyde via Single-Atom Alloy Catalysts

## 5.1 Introduction

Selective hydrogenation of  $\alpha,\beta$ -unsaturated aldehydes to produce unsaturated alcohols is an essential process in the fine chemicals and pharmaceutical industries.<sup>110</sup> However, this reaction remains a challenge in catalysis as thermodynamically, it is easier (by about 35 kJ/mol) to hydrogenate the C=C bond of the unsaturated aldehydes, forming the saturated aldehydes, than to hydrogenate the C=O bond.<sup>111</sup> Hence, selective hydrogenation of the C=O bond to produce unsaturated alcohols is a kinetically controlled process and requires a specific catalyst for attainment. Common active hydrogenation catalysts such as the Pt-group metals, however, have been previously shown to favor the C=C bond hydrogenation over the C=O bond hydrogenation.<sup>112–114</sup> Other studies by Laref et al. and Loffreda et al. demonstrate that the unsaturated alcohol could be formed by hydrogenation of acrolein on the Pt(111) surface but that desorption of this product is difficult, therefore favoring the gas phase formation of saturated aldehyde.<sup>115,116</sup> Although some alloy catalysts, such as Pd<sub>0.001</sub>Ag<sub>0.999</sub>/SiO<sub>2</sub>, Sn<sub>0.32</sub>Rh<sub>0.68</sub>/SiO<sub>2</sub>, Pt<sub>0.005</sub>Cu<sub>0.995</sub>/SBA-15, and Ir<sub>0.13</sub>Au<sub>0.87</sub>/TiO<sub>2</sub>, have been reported to be more selective and reactive than their monometallic counterparts in the literature, they either still possess considerably low selectivity values or demonstrate efficacy exclusively for larger and bulkier unsaturated aldehydes.<sup>35,117–120</sup> Therefore, there exists a pressing necessity to resolve the selectivity issue through the development of innovative catalysts, especially for small unsaturated aldehydes that do not benefit from the destabilization of the C=C bond by the substituents.

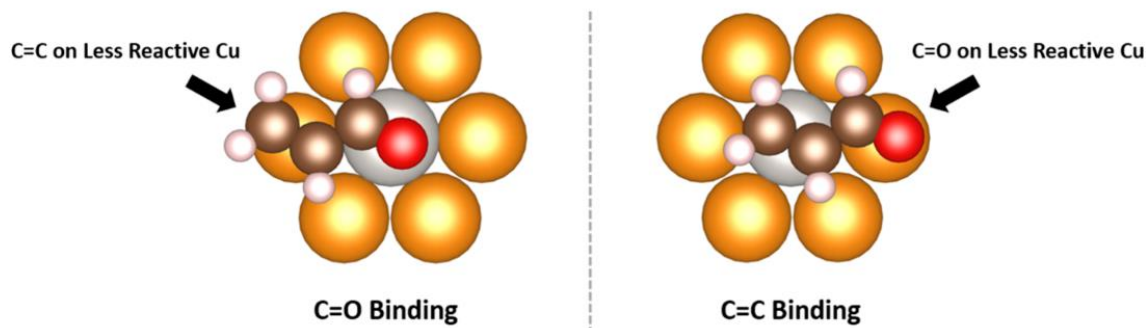


Figure 5.1. Schematic diagram demonstrating the C=O and C=C binding modes of acrolein on a single-atom alloy catalyst.

Single-atom alloys, which are formed by dispersing a small amount of active elements in less active metals (e.g. Au, Ag, and Cu), could be a promising class of catalytic materials to enhance the selectivity for C=O bond hydrogenation in unsaturated aldehydes.<sup>18–22,121</sup> The concept is that in addition to H<sub>2</sub> activation, a well-chosen dopant element could favor the C=O binding mode and its subsequent hydrogenation, while the C=C bond will sit on a rather less reactive part of the surface (Figure 5.1 left). The binding strength of the C=C and C=O bonds on the dopant element depends largely on their interaction with the dopant's d-states. Typically, when an active dopant is diluted in an inert metal host, it tends to have d-states narrow in energy due to the weak orbital mixing between the two elements.<sup>43,44</sup> By diluting early-, mid-, and late-transition metals in noble metals, the relative energy position of the dopant's d-states could be adjusted and the optimal interaction between the two functional groups in unsaturated aldehydes and the dopant atoms could be achieved.

Single-atom alloy catalysts comprising dilute Pd in Au have been demonstrated to effectively enhance the semi-hydrogenation selectivity of alkynes, and to provide different rate and selectivity controlling steps compared to monometallic catalysts due to geometric constraint.<sup>29,64</sup> Dilute Pt in Cu catalysts were shown to selectively promote the hydrogenation of C=O bonds in unsaturated

aldehydes; however, surface spectroscopy revealed that the surface is covered by a thin layer of Cu oxide so that the origin of the observed selectivity is not fully understood.<sup>35</sup> Monometallic Ag has been demonstrated to possess high selectivity for allyl alcohol formation, although challenging H<sub>2</sub> activation on it often results in low reaction activity. Highly dilute Pd in Ag catalytic nanoparticles on SiO<sub>2</sub> (~1 Pd for 800 Ag), however, provided a selectivity for acrolein hydrogenation to propenol (31%) close to that on Ag nanoparticles, but with an improvement in the activity.<sup>119</sup> Pd on Ag(111) SA alloys were further studied for the same reaction of acrolein hydrogenation with temperature-programmed desorption.<sup>122</sup> Compared to that of Ag(111), adding Pd SAs increased the conversion of acrolein but decreased the selectivity to propenol. In a different investigation of selective hydrogenation on alloys, it was discovered that adding Sn to Pt significantly increased the selectivity for allyl alcohol formation from 1.6% to 27.5%.<sup>112</sup> Using density functional theory, it was proposed by some of us that the charge transfer from Sn (to form Sn<sup>+</sup>) to Pt facilitates the binding of the acrolein molecule through its aldehyde functionality. This mechanism could potentially elucidate the enhanced selectivity observed if this adsorption configuration leads to C=O bond hydrogenation.<sup>123</sup>

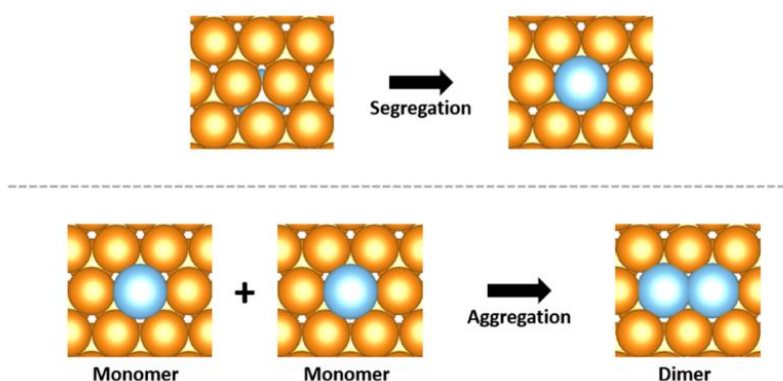


Figure 5.2. Schematic diagram showing the processes of segregation and aggregation of dopants in dilute alloy catalysts. Segregation is used to bring the dopant atom from the subsurface layer to

the surface layer, and aggregation is used to bring two isolated surface dopant atoms (monomers) together to form a dimer.

While the category of single-atom alloy catalysts hold promise for enhanced selectivity, concern is often raised regarding the dopant's segregation and aggregation for optimal catalytic performance (Figure 5.2). Ideally, active dopants should stay in the surface layer (favorable surface segregation) as isolated atoms in the metal host, avoiding segregation into larger metal ensembles at the surface. Nevertheless, alloy combinations showing slight tendencies toward anti-segregation and aggregation can still be employed, provided they undergo adequate pretreatment. For instance, pretreatment under CO or O<sub>2</sub> pressures prior to reactions can enable one to disperse and position the dopant atoms in the surface layer in a metastable situation.<sup>46</sup> A previous computational study proposed that dilute Fe-in-Au alloy catalysts could be a promising candidate for selective hydrogenation of unsaturated aldehydes, and it was shown that the calculated product selectivity is consistent with the crotonaldehyde initial adsorption configurations in cases that the authors have tested.<sup>121</sup> Using this conclusion as a starting point, other alloy combinations are explored in detail in the present work and a combination with kinetic simulations enables us to excavate potential catalysts for this reaction.

Herein, trends in early-, mid-, and late-transition metals dispersed in the less reactive metal Cu were investigated by using theoretical modeling to provide insights into the rational design of novel catalysts for the selective hydrogenation of unsaturated aldehydes into unsaturated alcohols. Acrolein, being the smallest possible unsaturated aldehyde, was chosen as the model reactant for this purpose. Selectivity to unsaturated alcohols is expected to be higher for larger unsaturated aldehydes with a functional group attached to the C=C bond (e.g. crotonaldehyde and cinnamaldehyde) than for acrolein as the extra functional group could destabilize the transition

states for C=C bond hydrogenation. In addition, the presence of the extra substituents is also anticipated to reduce the binding strength of the unsaturated alcohols formed and to facilitate desorption, as demonstrated by a former study on Pt(111) by Laref et al.<sup>116</sup> Therefore, if acrolein is selectively hydrogenated on a specific catalyst and can readily desorb, the same should also apply to other larger unsaturated aldehydes. However, it is important to note that the substituent effect is not the sole factor influencing selectivity, as will be further elaborated. In this study, it is demonstrated that on SAA of early transition metals such as Ti, Zr, and Hf, the C=O binding mode of acrolein (and subsequent mono-hydrogenated intermediate) is much more stable when compared with the C=C binding mode. However, the binding is too strong such that subsequent hydrogenation and desorption steps are highly endergonic in nature. Conversely, on SAAs of late-transition metals, the C=C binding mode of acrolein and subsequent C=C bond hydrogenation are more favorable, resulting in the production of the undesired saturated aldehydes. Mid-transition metals (Cr, Mn) in Cu(111) are the most promising choices, as they offer moderate binding strength and facilitate acrolein adsorption via the C=O bond. Specifically, the barrier that impedes acrolein migration from its more stable configuration in the C=O binding mode to the less stable but more reactive and unselective C=C binding mode, along with the barrier for H-migration to that C=C binding acrolein, helps enhance the selectivity. This improvement arises because these transition states (acrolein diffusion and H-migration) exhibit free energy comparable to that of the rate-limiting transition state in the C=O hydrogenation pathway. Collectively, these findings demonstrate that by carefully adjusting the interaction between the catalyst surface and the two functional groups in acrolein, single-atom alloy catalysts could create new avenues for selective hydrogenation of  $\alpha,\beta$ -unsaturated aldehydes.

## 5.2 Methods

### 5.2.1 DFT Calculations

All density functional theory (DFT) calculations were performed using the Vienna Ab initio Simulation Package (VASP).<sup>75,76</sup> The (111) surfaces of the various bimetallic catalysts were modeled using a four-layer slab and a  $(3 \times 3)$  unit cell, and a Monkhorst-Pack-generated<sup>77</sup>  $5 \times 5 \times 1$  K-point grid was employed for this unit cell size. Increasing the K-point grid further to  $7 \times 7 \times 1$  is demonstrated to have negligible impact ( $\Delta E < 0.02$  eV) on the total energy obtained for the CuTi<sub>1</sub> slab, let alone the adsorption energies in which the differences could be canceled out in the calculations. During structural optimization, the bottom two layers of the slab were constrained in the bulk Cu position while the upper two layers and the surface adsorbates were allowed to relax until the force convergence threshold of 0.02 eV/Å was reached. A plane-wave basis set with a cutoff energy of 450 eV and the dDsC-dispersion-corrected PBE functional were used, and spin polarization was included for all calculations.<sup>107,108</sup> The second-order Methfessel-Paxton smearing method with the width of smearing set to 0.2 eV was also employed for these calculations.<sup>124</sup> Standard PAW pseudopotentials were utilized for all elements except for the early transition metals Ti, Zr, and Hf. For these early transition metals, the versions “Ti\_sv” with 12 valence electrons, “Zr\_sv” with 12 valence electrons, and “Hf\_pv” with 10 valence electrons were used instead.<sup>125,126</sup> Transition states were located using both the climbing image nudged elastic band (CI-NEB) and the dimer methods.<sup>84,109,127</sup> Crystal Orbital Hamilton Populations (COHP) analysis was made feasible using the Local Orbital Basis Suite Toward Electronic Structure Reconstruction (LOBSTER).<sup>128</sup> All structural configurations reported in this study are visualized using VESTA.<sup>85</sup>

The segregation energy reported in this study is defined as the energy gain/loss to bring a dopant atom from the subsurface layer of the metal slab to the surface layer, and hence is calculated

as:

$$E_{seg} = E_{surf} - E_{subsurf} \quad (5.1)$$

where  $E_{seg}$  is the segregation energy,  $E_{surf}$  is the DFT energy of the metal slab when the dopant is in the surface layer, and  $E_{subsurf}$  is the DFT energy when the dopant is in the subsurface layer.

Aggregation energy, on the other hand, is defined as the energy gain/loss to bring two separated surface dopant atoms together, and is calculated as:

$$E_{agg} = E_{dimer} + E_{Cu} - 2 * E_{monomer} \quad (5.2)$$

where  $E_{agg}$  is the aggregation energy,  $E_{dimer}$  is the DFT energy of the metal slab when two surface dopant atoms are brought together,  $E_{Cu}$  is the energy of a pure Cu slab for balancing the number of atoms, and  $E_{monomer}$  is the energy when there is only one dopant atom in the surface layer of the slab.

For simplicity, free energy calculations consider only the translational and rotational entropies of the gaseous species. Zero-point energies (ZPEs) and vibrational contributions of the entropies of all species were neglected.

## 5.2.2 Microkinetic Modeling

Microkinetic modeling was performed by using the DFT energies as input parameters to study the reaction selectivity. In this modeling, the rate constants for adsorption ( $k_{ads,i}$ )/desorption ( $k_{des,i}$ ) and surface reaction steps ( $k_j$ ) were computed using the collision theory (Eqs 5.3 and 5.4) and transition state theory (Eq 5.5), respectively.<sup>87</sup>

$$k_{ads,i} = \frac{A_{st}}{\sqrt{2\pi m_i k_B T}} \quad (5.3)$$

$$k_{des,i} = k_{ads,i} P^o \exp\left(\frac{\Delta G_{ads,i}^o}{k_B T}\right) \quad (5.4)$$

$$k_j = \frac{k_B T}{h} \exp\left(-\frac{\Delta H^{\ddagger,o}}{k_B T}\right) \exp\left(\frac{\Delta S^{\ddagger,o}}{k_B}\right) \quad (5.5)$$

where  $A_{st}$  is the effective area of the adsorption site,  $m_i$  is the mass of the adsorbing species  $i$ ,  $k_B$  is the Boltzmann's constant,  $T$  is the temperature,  $P^o$  is the standard state pressure,  $\Delta G_{ads,i}^o$  is the adsorption free energy of species  $i$  under standard state pressure,  $h$  is the Planck's constant, and  $\Delta H^{\ddagger,o}$  and  $\Delta S^{\ddagger,o}$  are respectively the standard-state enthalpy and entropy differences between the initial state and the transition state in elementary step  $j$ .

Surface species coverages were used to calculate the acrolein consumption and propenol production rates, as manifested in their elementary step rate equations. To solve the surface species coverages, a set of ordinary differential equations (O.D.E.s) were constructed based on the reaction network considered (see Table D.1 and Eq 5.6):

$$\frac{d\theta_i}{dt} = \sum_j v_{ij} r_j \quad (5.6)$$

where  $\theta_i$  is the surface coverage of species  $i$ ,  $t$  is time,  $v_{ij}$  is the stoichiometric coefficient of species  $i$  in step  $j$ , and  $r_j$  is the reaction rate of elementary step  $j$ . These O.D.E.s were solved by assuming the surface was initially bare. Once the surface species coverages and hence the steady-state reaction rates were obtained, the selectivity ( $S$ ) for propenol formation was calculated as follows:

$$S = \frac{\text{propenol formation rate}}{\text{acrolein consumption rate}} \quad (5.7)$$

Degree of selectivity control (DSC) analysis<sup>92</sup> was also carried out to identify the elementary

steps that have a significant impact on the reaction selectivity. DSC was calculated as:

$$DSC = \left( \frac{\partial \ln S}{\partial \left( -\frac{G_i^o}{k_B T} \right)} \right)_{G_j^o \neq i} \quad (5.8)$$

where  $G_i^o$  is the standard-state free energy of species  $i$ . The partial derivative in Eq 5.8 is taken such that the standard-state free energies of all other species are kept constant. The degree of rate control (DRC) was calculated in a similar way, except that selectivity should be replaced by the acrolein consumption rate in Eq 5.8. By definition, a positive DRC/DSC value suggests that the rate/selectivity would be improved with a decrease in the standard-state free energy of species  $i$ , and vice versa.

## 5.3 Results

### 5.3.1 Dopant Segregation and Aggregation

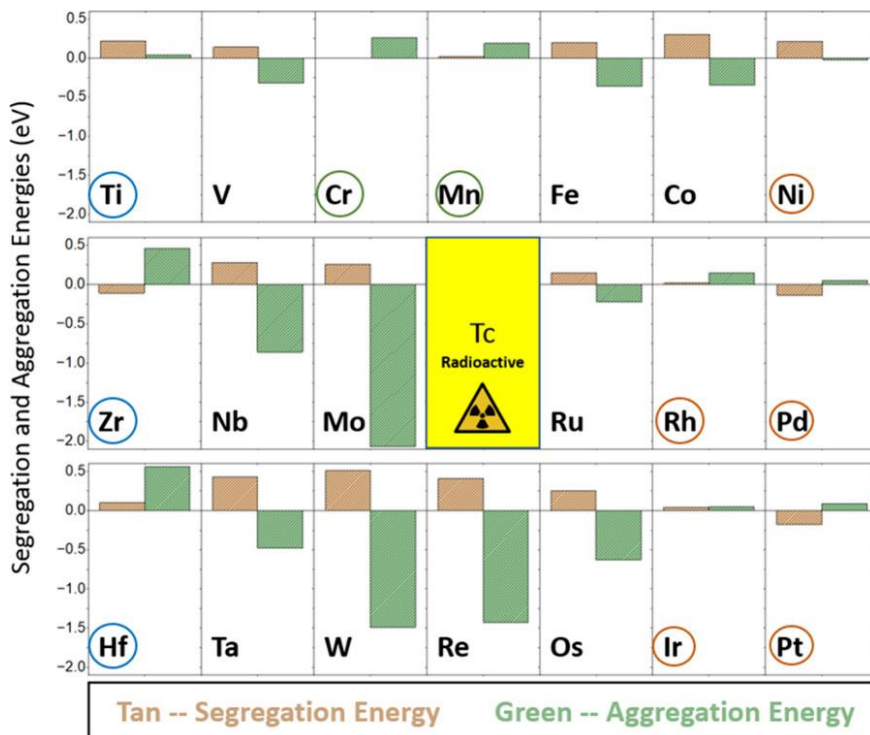


Figure 5.3. Segregation (tan) and aggregation (green) energies of various transition metals in Cu(111). Negative segregation energies indicate that segregation is favorable, while positive aggregation energies imply that aggregation is unfavorable.

In a single-atom alloy catalyst, the active dopant should exist within the surface layer of the less reactive metal host as an isolated atom. To assess the feasibility of creating such catalysts experimentally, segregation and aggregation energies were evaluated for all transition metals of groups 4 to 10 (excluding Tc) in the Cu host (Figure 5.3). Ideally, negative segregation and positive aggregation energies are preferred for the stability of the single-atom alloy catalysts. However, catalysts with slightly positive segregation energies are still acceptable, as they can undergo pretreatment before reactions to position the active metal on the surface layer and function as

metastable states.<sup>46</sup> Among the diverse alloy combinations, early-transition metals Ti, Zr, and Hf, mid-transition metals Cr and Mn, and late-transition metals Rh, Ir, Ni, Pd, and Pt exhibit segregation and aggregation energies within acceptable ranges, making them feasible for realization. Ti in Cu(111) is the one that has the most positive segregation energy value in these 10 alloy candidates, but its magnitude is only 0.22 eV, which is small enough for pretreatment to bring it up to the surface layer, where it could stay during the course of the reaction. In particular, Ti has been previously shown to exist as isolated atoms in the Cu(111) surface in experiment.<sup>129</sup> Additionally, unlike other alloy combinations, these 10 candidates do not exhibit a strong tendency to aggregate, rendering them viable for experimental creation as single-atom alloys.

### 5.3.2 Binding Modes of Acrolein

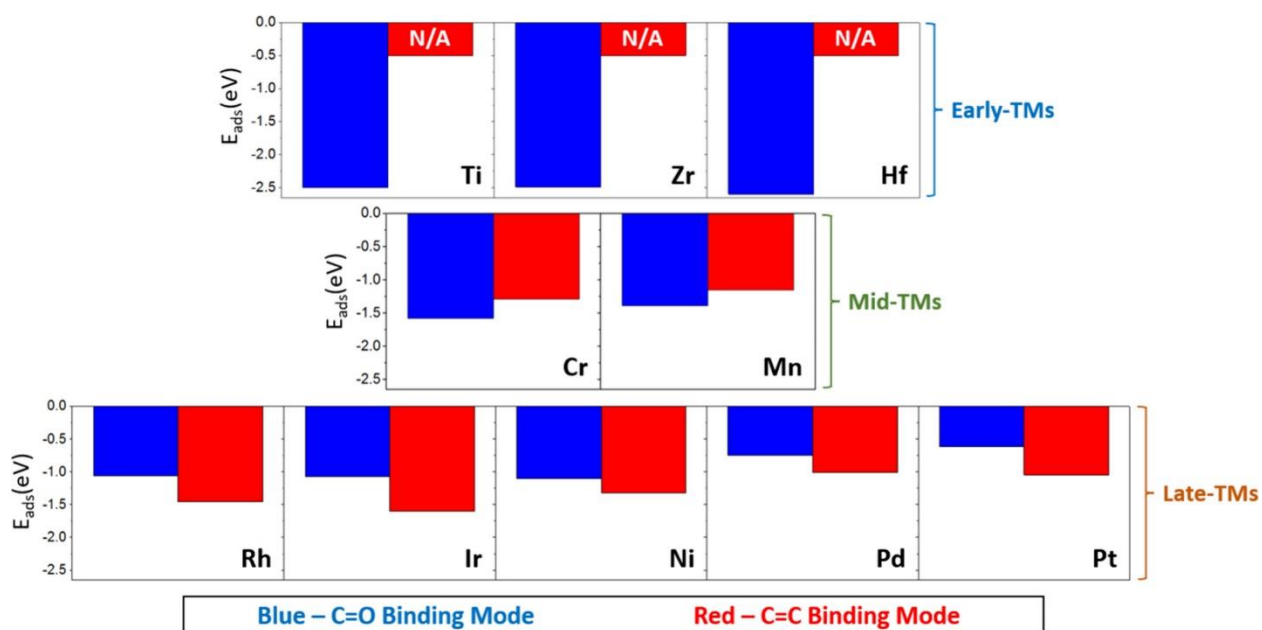


Figure 5.4. Adsorption electronic energies of acrolein on early-, mid-, and late-transition metals in Cu(111) with the C=O (blue, C=O binding mode) and C=C (red, C=C binding mode) bonds on top of the dopant atom. No adsorption energy is reported for the C=C binding mode on early transition metals, as this configuration is not a metastable state on them and transforms into the C=O binding

mode.

Energies of adsorption for acrolein, locating the C=O or the C=C bond on the dopant, were evaluated on the 10 previously mentioned alloy candidates as a preliminary assessment to determine if they are capable of selectively forming propenol (Figure 5.4). A former study suggested that the initial adsorption configuration of unsaturated aldehydes would dictate the selectivity of the reaction.<sup>121</sup> To put it differently, if the C=O binding mode is favored over the C=C binding mode, the subsequent hydrogenation of the C=O bond would also be more favorable. Early transition metal SAAs of Ti, Zr, and Hf in Cu(111) exhibit a notable inclination to adsorb acrolein through its oxygen atom in the C=O bond (C=O binding mode), with the rest of the molecule situated on the Cu surface. Indeed, these early transition metals are so oxophilic that the adsorption energies by the O atom are more negative than -2.45 eV, and no stable C=C binding mode was observed. Mid-transition metal SAAs of Cr and Mn in Cu(111) also show a preference for the C=O binding mode over the C=C binding mode, with energy differences of 0.29 and 0.24 eV, respectively. Similar to the early transition metals, it is mainly the O atom in the C=O bond that interacts with Cr and Mn for the C=O binding mode, and the rest of the acrolein molecule lies flat on the surface. In the case of the C=C binding mode, both carbon atoms in the C=C bond engage in interaction with the dopants, as indicated by the similar interatomic distances observed. However, the binding strength of acrolein on these mid-transition metals is considerably weaker than that on the early-transition metals, regardless of the binding modes. Lastly, the late-transition metals Rh, Ir, Ni, Pd, and Pt do not favor the C=O binding mode. As a matter of fact, the C=C binding mode on them is 0.22 to 0.53 eV more stable than the C=O binding mode. This initial finding suggests that early- and mid-transition metals in Cu(111) might be candidates for selective hydrogenation of acrolein to form propenol, but late-transition metals might not be suitable for this

purpose. Nonetheless, further investigation is required to validate this claim.

### 5.3.3 Early-Transition Metals in Cu(111)

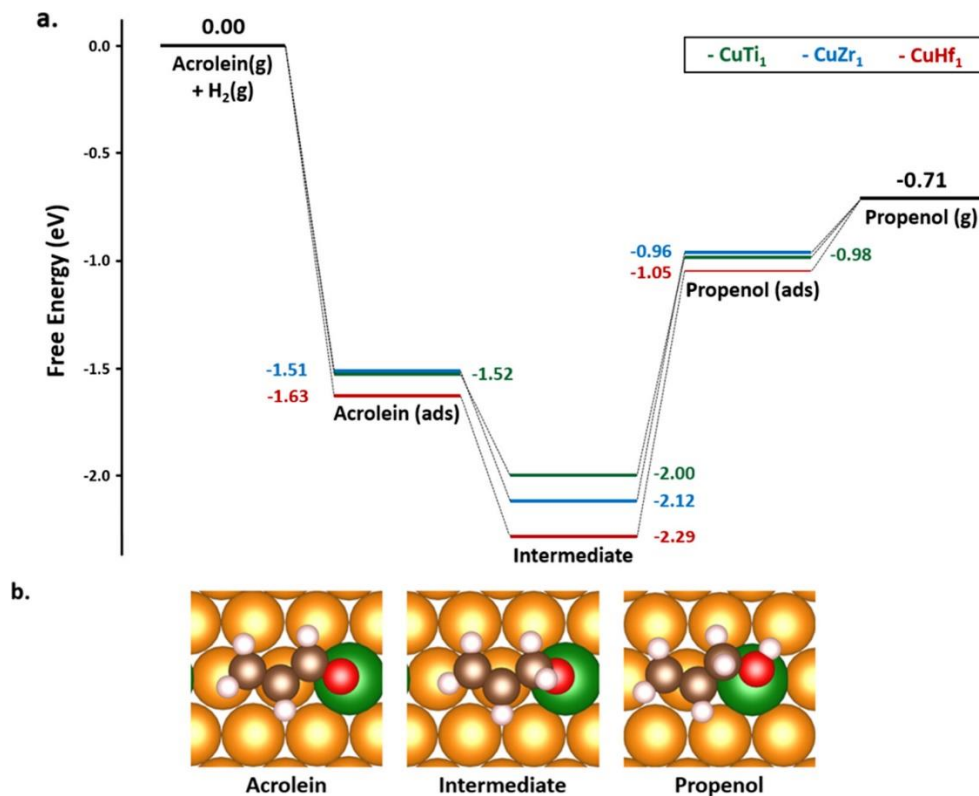


Figure 5.5. Free energy profile for acrolein hydrogenation on CuTi<sub>1</sub> (green), CuZr<sub>1</sub> (blue), and CuHf<sub>1</sub> (red). (b) Corresponding reaction configurations on CuTi<sub>1</sub>. Transition states are omitted in this study for simplicity. Reaction conditions are T = 375 K, P(acrolein) = 0.1 bar, P(H<sub>2</sub>) = 300 bar, and P(propenol) = P(propenal) = 0.01 bar.

Early transition metal single-atom alloys were first studied in detail for their enticing ability to bind only an acrolein molecule in the C=O binding mode. A simplified free energy profiles was constructed to compare the energy differences between each intermediate along the hydrogenation pathway for the three early transition metals Ti, Zr, and Hf (Figure 5.5; Figure D.1 for reaction configurations on CuZr<sub>1</sub> and CuHf<sub>1</sub>). It is demonstrated that acrolein binds to these surfaces very strongly, with the adsorption free energies being -1.52, -1.51, and -1.63 eV for CuTi<sub>1</sub>, CuZr<sub>1</sub>, and

CuHf<sub>1</sub>, respectively. This strong binding feature persists for the mono-hydrogenated intermediates, which are formed by hydrogenating the C atom in the C=O bond, and these states lie even lower in the free energy profile ( $G = -2.00$  to  $-2.29$  eV). The strong binding of acrolein and intermediates on the catalysts appears to be very alluring, as it is expected to significantly reduce the activation barriers for the formation of C-H bonds toward the intermediate. However, this strong binding renders the formation of adsorbed propenol highly endergonic (by 1.02 to 1.24 eV) and makes its desorption unfavorable under the studied conditions, by at least 0.25 eV. Hence, instead of being able to readily and selectively hydrogenate acrolein, early-transition metals in Cu(111) are likely to be poisoned by the mono-hydrogenated intermediates and become unreactive due to the unfavorable thermodynamics along the second half of the pathway. For selective hydrogenation, preference should be given to the binding of the C=O bond, but its adsorption should not be excessively strong, in accordance with the Sabatier principle.

### 5.3.4 Mid-Transition Metals in Cu(111)

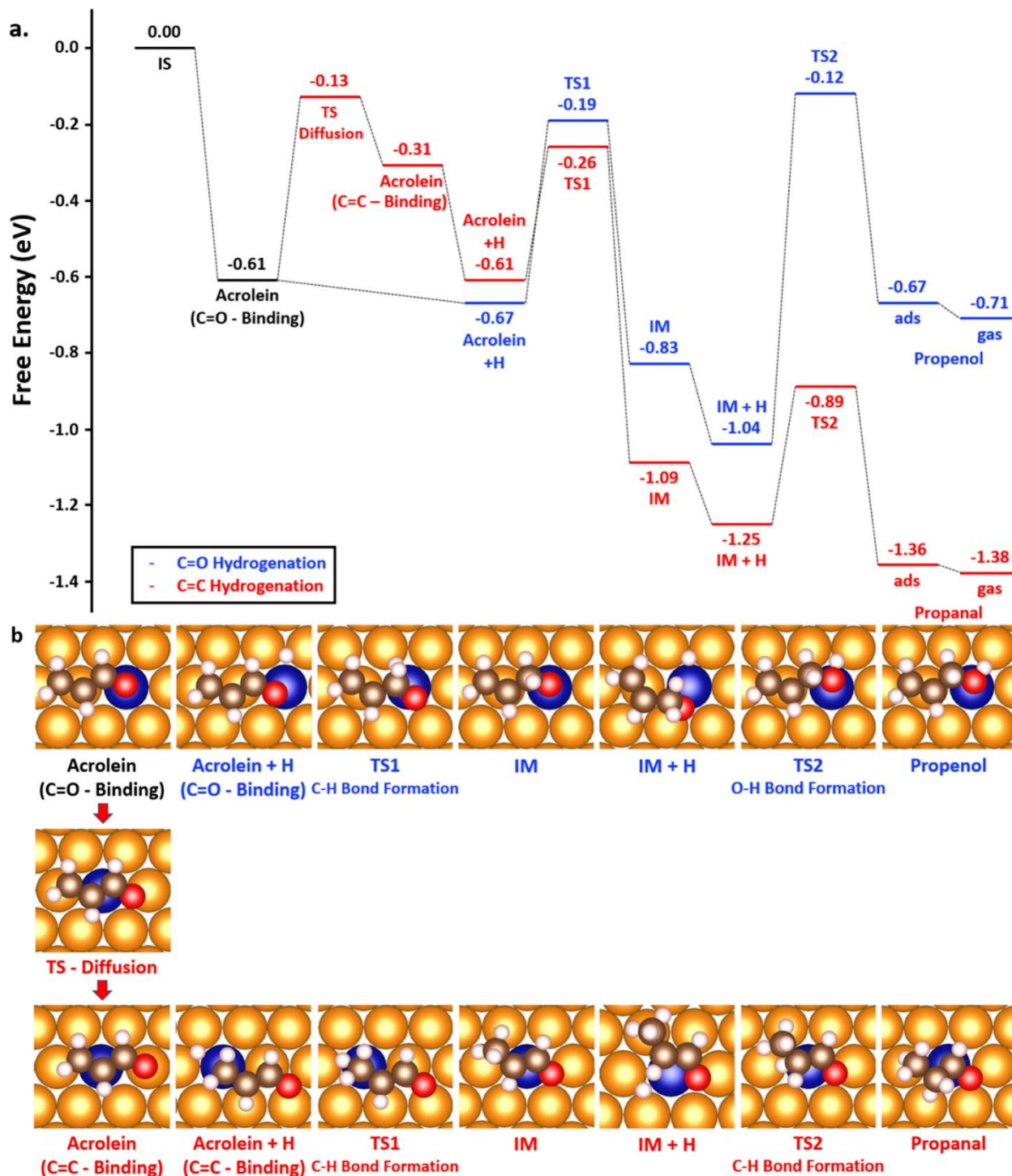


Figure 5.6. (a) Free energy profile for hydrogenation of the C=O bond (blue) and C=C bond (red) in acrolein on CuCr<sub>1</sub>. (b) Configurations of the corresponding reaction intermediates and transition

states along the energy profile. Reaction conditions are  $T = 375 \text{ K}$ ,  $P(\text{acrolein}) = 0.1 \text{ bar}$ ,  $P(\text{H}_2) = 300 \text{ bar}$ ,  $P(\text{propanal}) = 0.01 \text{ bar}$ , and  $P(\text{propenol}) = 0.01 \text{ bar}$ .

Mid-transition metals in Cu(111) might open up new opportunities for selective acrolein hydrogenation, as they favor the C=O binding mode and the binding strength is moderate. A detailed study of the reaction mechanism on  $\text{CuCr}_1$  was first carried out to ascertain the veracity of that assertion (Figure 5.6 and Figure D.2). The free energy profile for this reaction begins with the adsorption of acrolein in its most stable configuration, i.e. the C=O binding mode on the Cr dopant. The hydrogenation pathway of the C=O bond (Figure 5.6, blue pathway) then proceeds by drawing one H atom to its adsorption site (blue “acrolein + H”), followed by the transition state for C-H bond formation (blue “TS1”) to produce the mono-hydrogenated intermediate (blue “IM”). Once the mono-hydrogenated intermediate is formed, a second H atom is drawn to its adsorption site before going through the transition state for the formation of the O-H bond (blue “TS2”) and producing the desired product propenol. Similarly, the C=C bond hydrogenation pathway (Figure 5.6, red pathway) follows the same pattern. However, the acrolein molecule needs to first transform from the more stable C=O binding mode to the less stable C=C binding mode prior to the reaction, and the transition state for this transformation is labeled as “TS – Diffusion”.

It is important to highlight that the H atoms that are drawn to the reactant adsorption site are generated on a second active site or on the Cu(111) surface (which has been previously shown to be capable of performing  $\text{H}_2$  activation) due to the limitation imposed by the small ensemble size.<sup>130</sup> This  $\text{H}_2$  activation process on a second  $\text{CuCr}_1$  active site (Figure D.2) begins with the molecular adsorption, which is slightly exergonic in nature ( $\Delta G = -0.04 \text{ eV}$ ) under such a high pressure. Adsorbed  $\text{H}_2$  molecules subsequently split into two separated H atoms by going through the transition state for dissociation (TS-Dis in Figure D.2), and the obtained activation barrier is

moderate ( $\Delta G^\ddagger = 0.38$  eV). Following dissociation, the separated H atoms could migrate to the reactant adsorption site via the Cu surface. The activation barrier associated with the migration of the H atoms to the Cu domain is similar to that for H<sub>2</sub> dissociation, with the value being 0.37 eV. With these small activation barriers ( $\Delta G^\ddagger = 0.37 - 0.38$  eV), H<sub>2</sub> activation and H atom migration by spillover on the Cu could take place with ease on the CuCr<sub>1</sub> surface for acrolein hydrogenation. Eventually, it should be highlighted that H<sub>2</sub> activation on the Cu(111) surface encounters a somewhat higher barrier, with the value being 0.56 eV under the same studied conditions. Nevertheless, this pathway presents an alternative means to provide H atoms for the hydrogenation reaction.

As indicated in the free energy profile for acrolein hydrogenation on CuCr<sub>1</sub>, the initial adsorption of acrolein is moderate, with the free energy change being -0.61 eV for the C=O binding mode, which mainly occurs through a O-Cr interaction (Figure 5.6). Adsorption by the C=C bond is possible but is 0.3 eV less stable, which would correspond to a Boltzmann population of  $\sim 10^{-4}$ . However, this C=C binding mode is more prone to hydrogenation. First, hydrogen co-adsorption with the C=C binding mode is thermodynamically more favorable than that with the C=O binding mode, thereby minimizing the stability difference between the two co-adsorbed states to 0.06 eV. Second, the first hydrogenation at the C atom is easier for the C=C binding mode, as evidenced by the transition state free energy of -0.26 eV, versus -0.19 eV for the C=O binding mode. It is important to emphasize that hydrogenating the C atom in the C=O bond as the first step is more favorable than hydrogenating the O atom due to the oxophilic nature of Cr. Once the O atom is hydrogenated, the interaction between it and the active dopant will be diminished. This claim is justified by the higher adsorption energy of the mono-hydrogenated intermediate CH<sub>2</sub>CHCHOH than that of CH<sub>2</sub>CHCH<sub>2</sub>O, with the difference being 0.29 eV. In addition, a previous study finds

that in acetaldehyde hydrogenation on CuNi<sub>1</sub>, which is a less oxophilic element, the transition state energy for C-hydrogenation in the C=O bond is 0.68 eV lower than that for O-hydrogenation.<sup>131</sup> This difference is expected to be even larger on the more oxophilic Cr. Using this result as an analogy, the transition state for hydrogenating the O atom in the C=O bond of acrolein would also lie much higher in the energy profile than those of both the blue “TS1” and “TS2” in Figure 5.6. Hence, this pathway is less likely than the one detailed in this study.

In line with the transition states, the intermediate resulting from hydrogenating the C=C bond (-1.09 eV) also lies lower in the free energy profile compared to that from the C=O bond hydrogenation (-0.83 eV). This trend also holds true for the second transition states to hydrogenate the remaining O and C atoms; the transition state for the former is as high as -0.12 eV, whereas that for the latter is only -0.89 eV. The lower transition state energies seem to suggest that C=C bond hydrogenation is kinetically more favorable than C=O bond hydrogenation on CuCr<sub>1</sub>. However, the diffusion transition state to transform acrolein from its more stable C=O binding configuration to the less stable C=C binding configuration also lies high in the energy profile. In fact, this transition state has a free energy value of -0.13 eV, which is very similar to the transition state for the formation of the O-H bond (blue “TS2”, G = -0.12 eV). This marginal difference suggests that selective hydrogenation of acrolein on CuCr<sub>1</sub> remains probable. Moreover, while not depicted for simplicity in Figure 5.6, there exist transition states to bring H in proximity to reactants, or intermediates, and form the co-adsorption states. H atoms are readily available at the steady state on the Cu surface, as will be discussed in Microkinetic Modeling section, and the activation barrier to bring a H atom from the Cu surface to their adsorption sites is roughly 0.2 eV (Figure D.2 from H(Cr,Cu) to TS-M). Adding this barrier to the free energy of acrolein in the C=C binding mode yields a transition state energy of -0.11 eV, which is very close to that of the diffusion TS.

Consequently, it is anticipated that C=C hydrogenation on CuCr<sub>1</sub> is not preferred, and an enhanced selectivity could be expected from both the barrier for acrolein diffusion on the surface and the barrier to bring a H atom to the C=C-bound acrolein molecule. The discussion regarding the free energy profile is, however, qualitative, and a more comprehensive analysis is provided in the Microkinetic Modeling section. In the end, it is important to mention that the desorption of the two different products (propenol and propanal) is seen to be facile as demonstrated by the slightly exergonic nature of this process.

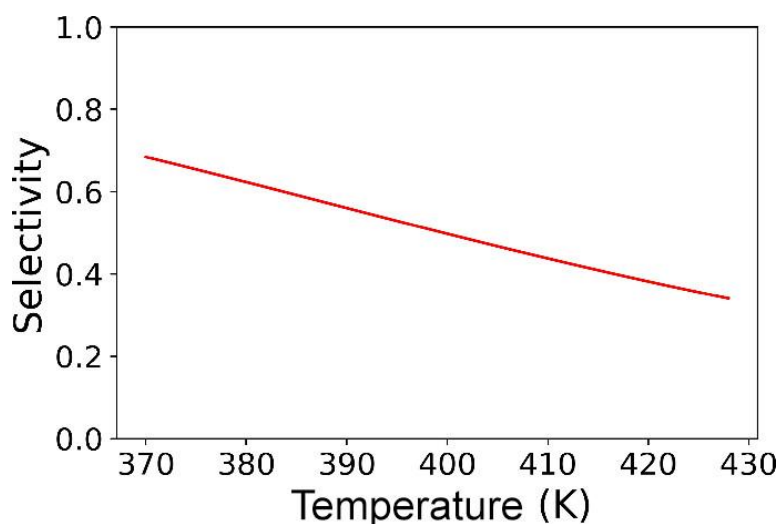


Figure 5.7. Selectivity for propenol formation on CuCr<sub>1</sub> as a function of temperature. Reaction conditions are P(acrolein) = 0.1 bar, P(H<sub>2</sub>) = 300 bar, P(propanal) = 0.01 bar, and P(propenol) = 0.01 bar.

Microkinetic modeling, which takes into consideration the collective impact of intermediate and transition state free energies in the profile, was conducted to further assess the selectivity for propenol formation on CuCr<sub>1</sub> (Figure 5.7). Briefly, the elementary steps considered in this microkinetic modeling include H<sub>2</sub> activation on both the Cu(111) and SAA surfaces, and acrolein hydrogenation on the SAA surface. A H atom is drawn to the acrolein/mono-hydrogenated intermediate adsorption site from another SAA ensemble or from the Cu(111) surface before every

bond-formation event (Table D.1). The results of microkinetic modeling indicate that at  $T = 370$  K, the selectivity achieved for propenol production is nearly as high as 70% (Figure 5.7). Additionally, DSC calculations (Figure D.6) from the kinetic modeling corroborate the analysis based on free energy, highlighting that the steps of acrolein diffusion and H-migration to the C=C binding molecule are most negatively selectivity-determining, whereas the O-H bond formation step (blue “TS2” in Figure 5.6) is positively selectivity-determining. It is important to clarify that in this context, selectivity refers specifically to the preference for propenol formation.

Although higher temperatures could enhance the reaction reactivity, the desired selectivity diminishes to below 40% when the temperature exceeds  $\sim 417$  K. The inverse correlation between selectivity and temperature is also mirrored in the DRC analysis (Figure D.7). Specifically, at lower temperature ( $T = 375$  K), the transition state for O-H bond formation (in the C=O hydrogenation pathway) exerts more control over the reaction rate when compared with the transition states for H-migration to the C=C binding acrolein and for acrolein diffusion (in the C=C hydrogenation pathway). However, this trend reverses when the temperature is higher ( $T = 475$  K). This outcome suggests a shift in the predominant pathway of the reaction, transitioning from the C=O hydrogenation pathway to the C=C hydrogenation pathway, when the temperature is increased.

It is recognized that higher temperatures stabilize all gaseous species due to a greater contribution of entropy to the free energy, consequently raising the relative free energies of the surface transition states. Note that, however, the increased entropic contribution of gas phase acrolein affects all three selectivity-determining transition states equally while that of gaseous  $H_2$  does not have an equal impact on them. To be more specific, the diffusion transition state energy does not depend on the entropy of  $H_2$  as this step does not need to involve any H atoms on the catalyst surface. The H-migration step to the C=C binding acrolein, on the other hand, requires the

introduction of one H atom to the catalyst surface, and it suffers from entropic penalty associated with half of a gaseous H<sub>2</sub> molecule. This penalty becomes even more pronounced for the O-H bond formation step as this step involves two surface H atoms (one is found in the mono-hydrogenated intermediate and the other one is to be attached to the same intermediate), and the entropy in one gaseous H<sub>2</sub> molecule is lost to achieve this. Therefore, at higher temperatures, there will be a greater increase in the free energy of the transition state for the formation of the O-H bond, rendering the C=O hydrogenation pathway less favorable and reducing the reaction selectivity. To mitigate this adverse effect of elevated temperature on selectivity, H<sub>2</sub> pressure, if possible, could be further increased to significantly bring the O-H bond formation transition state lower in energy while having a smaller impact on the H-migration step and none on the diffusion step. Eventually, it is worth noting that the substantial diffusion barrier can be viewed as an additional and promising approach to control selectivity, as its contribution is independent of reaction conditions.

While increased H<sub>2</sub> pressure may improve reaction selectivity, caution should be exercised with regard to surface poisoning. Microkinetic modeling indicates that, in addition to the Cu surface, above 97% of the dopant active sites on CuCr<sub>1</sub> are also covered by H atoms under the studied conditions (Figure D.8). This observation is consistent with the energy profiles, where the free energy of the “2H” state is -0.66 eV on CuCr<sub>1</sub> (Figure D.2) and that of acrolein is only -0.61 eV (Figure 5.6). Similar findings are also reflected in the DRC study in which the acrolein adsorption transition state is found to be the most rate-controlling (DRC ≈ 1), as most of the active sites are occupied by H atoms, and the “2H” state is found to have a DRC value of ~ -1 (Figure D.8). Despite the blocking of the active sites by the H atoms, a reasonable reaction rate of 0.03 s<sup>-1</sup> at ~383 K is still observed, with the selectivity being ~60%. Additionally, the dDsC-dispersion-corrected PBE functional is known to slightly overestimate the binding of H atoms.<sup>81</sup>

The true coverage of H in the experiments is expected to be lower. To further counter this site-blocking by the H atoms, the pressure of acrolein, along with the product partial pressures to maintain a ~10% conversion, could be increased. Increasing the acrolein pressure would lower its adsorption free energy (making adsorption more stable), such that it could displace some of the H atoms through competitive binding and enhance the reaction rate. Note that this action would not impact the calculated selectivity, as it does not alter the relative energy differences among the selectivity-determining transition states. Before closing up, it is worth mentioning that reaction intermediates adsorbed on active dopants in single-atom alloys do not experience lateral interactions, as they are inherently separated apart. Although the Cu surfaces are covered by H atoms, the lateral interaction between them and the reaction species on the dopants is negligible, as they are all small in size. Hence, the lateral interaction is not a concern in this study.

In addition to the exchange-correlation functional, DFT calculations are also prone to other errors arising from basis set limitations, treatment of core electrons, and numerical integrations, which collectively influence the accuracy of the computed results. Typically, the magnitude of the error is assumed to be around  $\pm 0.1$  eV. Consequently, two additional sets of microkinetic modeling were conducted. In these, the energy of the transition state for acrolein diffusion was raised, while the energy of the transition state for the formation of the O-H was reduced by 0.1 eV, aiming to investigate the potential changes in selectivity. These energy changes in the two transition states are shown to further improve the selectivity for propenol formation (Figure D.9). To be more specific, the selectivity is above 90% when the reaction temperature is lower than  $\sim 385$  K. Moreover, the hydrogenation reaction on CuCr<sub>1</sub> would remain selective (>50%) toward propenol at an elevated temperature ( $T = 477$  K) such that the reaction rate could also be enhanced. Since the H-migration step is more selectivity-determining than these two steps, lowering the activation

barrier for that specific process is predicted to exert an even stronger impact in enhancing the selectivity. Nevertheless, the inherent uncertainty in DFT calculations for each elementary step is not fully understood. It can only be suggested that there is a high probability of CuCr<sub>1</sub> being capable of performing selective acrolein hydrogenation. The same should also apply to another mid-transition metal CuMn<sub>1</sub>, on which the selectivity determining transition states in both hydrogenation pathways (“TS-Diffusion” and blue “TS1”) have similar free energy values (Figure D.3), despite that the H-migration transition state is slightly lower ( $G = 0.00$  eV) in this case and does not have a significant impact on the reaction selectivity (Figures D.3 and D.4).

Under reaction conditions, the surface structures of the CuCr<sub>1</sub> and CuMn<sub>1</sub> catalysts might be reconstructed by segregation. The initial stability assessment in Figure 5.3 was conducted on bare surfaces. With the presence of adsorbates, dopant segregation to the surface is further promoted as the energy decrease by adsorption on the dopant is greater than both the energy increase by segregation and the small energy decrease when the adsorption is on Cu(111). Specifically, for CuCr<sub>1</sub> the adsorption free energy of two H atoms on the Cr<sub>1</sub> ensemble is -0.66 eV while segregation is roughly quasi-thermoneutral and the adsorption free energy on Cu(111) is merely -0.36 eV. For CuMn<sub>1</sub>, segregation (a quasi-thermoneutral process) is also expected to be facilitated by the adsorption of the H atoms, despite that the coverage might be lower due to the smaller adsorption free energy of -0.55 eV (Figure D.4). While higher temperatures would indeed weaken the binding of adsorbates on the dopant, this elevated temperature regime is less relevant due to the lower selectivity observed. On the other hand, employing higher pressures of reactants would render their adsorption even more favorable, which would further promote dopant segregation. It is noted that the binding energy of adsorbates on dimers and even trimers is stronger than that on a monomer, which encourages the formation of larger surface aggregates in the presence of the

adsorbate. Nevertheless, this scenario could be effectively suppressed by controlling the amount of dopants that are placed in the less reactive metal host. Hence, by carefully managing the reaction conditions and tuning the dopant concentration, single-atom alloy surfaces are expected to remain unchanged throughout the reaction process.

It is noteworthy that the high selectivity of CuCr<sub>1</sub> for propenol production is not due to the ease of bond formation steps in the C=O hydrogenation pathway, but rather to the challenging steps of acrolein diffusion and H-migration. If one switches to a larger unsaturated aldehyde with a substituent attached to the C=C bond, the selectivity for unsaturated alcohol formation might not be necessarily dependent on these adsorbate diffusion steps. It is expected that the presence of a large substituent at the C=C bond would prevent this part of the molecule from coming close to the catalyst surface. Additionally, its presence would also destabilize the transition states for C=C bond hydrogenation due to steric hindrance and facilitate the unsaturated alcohol desorption. As a matter of fact, our DFT calculations show that AuFe<sub>1</sub> might not selectively hydrogenate acrolein to produce propenol because the highest transition state in the C=O hydrogenation pathway (blue “TS1”) exceeds that in the C=C hydrogenation pathway (red “TS1”) by 0.12 eV (Figure D.5). Moreover, C=C and C=O adsorption modes are very close in energy, and acrolein diffusion from one to the other is easy and not rate-limiting. Nevertheless, the trend in the transition state energy difference between red “TS1” and blue “TS1” in Figure D.5 can be effectively reversed if a methyl group is attached to the terminal C atom of acrolein (crotonaldehyde molecule), as shown by Spivey and Holewinski in their study on AuFe<sub>1</sub>.<sup>121</sup> In summary, reaction selectivity is influenced by various factors. The use of a diffusion barrier, alongside the well-known substituent effect, can be seen as a promising strategy to enhance selectivity in the hydrogenation of unsaturated aldehydes.

### 5.3.5 Late-Transition Metals in Cu(111)

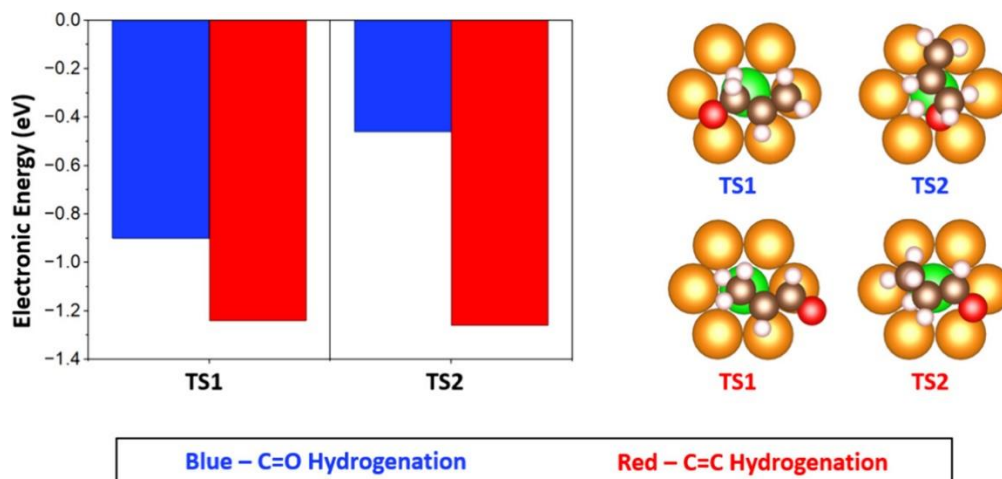


Figure 5.8. Electronic energies and the corresponding configurations of the transition states for C=O (blue) and C=C (red) hydrogenation on CuNi<sub>1</sub>.

The energies of the transition states for both hydrogenation pathways were computed on CuNi<sub>1</sub> to eliminate the possibility of late-transition metals (which favor the C=C binding mode) being able to selectively hydrogenate the C=O bond in acrolein (Figure 5.8). CuNi<sub>1</sub> was selected from the five late-transition metals due to its minimal adsorption energy difference (0.22 eV) between the two binding modes. Hence, Ni is the late-transition metal that could most possibly possess lower transition state energies for the C=O hydrogenation pathway than for the C=C hydrogenation pathway. Nevertheless, DFT calculations still indicate that the former pathway exhibits significantly higher transition state energies (Figure 5.8). Specifically, the first transition state for C=O bond hydrogenation is 0.34 eV higher than that for C=C bond hydrogenation and the difference in the second transition states is even as large as 1.20 eV. Therefore, CuNi<sub>1</sub> lacks the capability to selectively hydrogenate the C=O bond in acrolein. The same conclusion could also be safely extended to other late-transition metals with larger difference in adsorption energies between the two binding modes.

### 5.3.6 Chemical Bonding Analysis

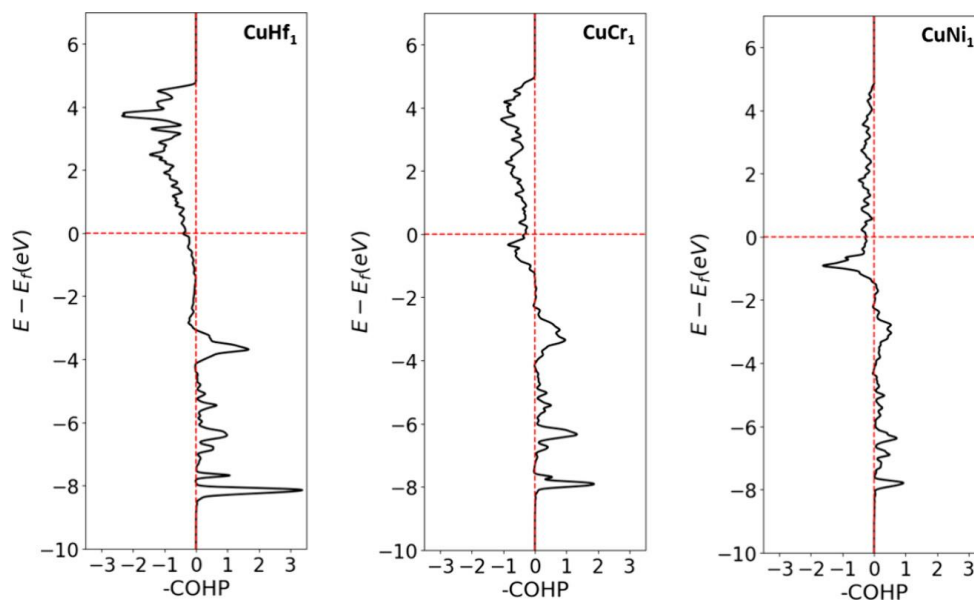


Figure 5.9. Crystal Orbital Hamilton Population (COHP) curves of the interactions between the O atom in acrolein and the three different dopant elements in Cu(111): Hf, Cr, and Ni.

A COHP analysis was carried out to understand the differences between the early- (Hf), mid- (Cr), and late-transition metals (Ni) in Cu(111) from a chemical bond perspective (Figure 5.9). Specifically, this study concentrates on the bonding strengths between the dopant atoms and the O atom in acrolein, as they determine which adsorption configuration is more favorable. In the case of the late-transition metal, Ni, it is seen that a significant portion of the antibonding orbitals with positive COHP values is below the Fermi level. This large occupancy of the antibonding orbitals weakens the bonding between Ni and O and helps explain the observation that the C=O binding mode is not favored on CuNi<sub>1</sub>. This claim is further supported by the small (absolute-value-wise) integrated COHP value of -1.07 between the two atoms. Moving to the mid-transition metal, Cr, COHP analysis demonstrates that a reduced portion of the antibonding orbitals are still populated when compared with Ni, as evidenced by both Figure 5.9 and its integrated COHP value of -2.72.

The same trend persists when one progresses to the early transition metal, Hf, which has an even smaller occupation of the antibonding orbitals and a greater integrated COHP value of -4.02. Not only are these findings highly aligned with the C=O binding strengths observed earlier, they also illustrate that the positions (relative to the Fermi level) of the antibonding orbitals between the dopants and the O atom in unsaturated aldehydes can be adjusted by dispersing different groups of transition metals in Cu(111). Hence, by carefully tuning its position, optimal reaction selectivity and reactivity could be attained simultaneously.

Before concluding, it is crucial to emphasize that an accurate description of the electronic structure requires to take into consideration the spin state on the dopant and itself affected by the presence of the adsorbate. Among the three categories of transition metals, both early- and late-transition metals in Cu(111) are found to be nonmagnetic, regardless of whether there is a surface intermediate on top or not. Mid-transition metals of Cr and Mn in Cu(111), however, exhibit magnetic moments, and these are preserved throughout the course of the reaction (Figure D.10). Nevertheless, this study properly addresses the spin states in the various systems investigated, providing insights into the promising catalysts (i.e. SAAs of mid-transition metals) for the selective hydrogenation of  $\alpha,\beta$ -unsaturated aldehydes.

## 5.4 Conclusion

Our theoretical study illustrates the pattern observed in Cu-based single-atom alloys for selective hydrogenation of  $\alpha,\beta$ -unsaturated aldehydes to produce unsaturated alcohols. The segregation and aggregation energies of a collection of transition metals in Cu(111) were first computed to assess the practicality of fabricating such catalysts in experiments. Out of these alloy combinations, early transition metals Ti, Zr, and Hf; mid-transition metals Cr and Mn; and late-transition metals Rh, Ir, Ni, Pd, and Pt in Cu(111) are found to be realizable. The two different

binding modes, namely C=O and C=C binding modes, of acrolein on these three categories of dopants were subsequently examined as a preliminary evaluation of their selectivity towards propenol formation. It is found that the early transition metal atoms in Cu(111) strongly favor the C=O binding mode of the acrolein molecule, with the magnitude of the adsorption free energies being greater than 1.5 eV. This tight interaction between the surface species and the catalyst surface is similarly maintained for the mono-hydrogenated intermediates, which have free energy values lower than -2.00 eV. While this characteristic may appear appealing since it could stabilize the transition states for bond formation, its strength is excessive, leading to subsequent hydrogenation and desorption steps that are highly endergonic in nature. Hence, acrolein hydrogenation cannot proceed on this type of SAAs.

Mid-transition metal atoms in Cu(111) are found to be the most promising for selective acrolein hydrogenation. These metals favor the C=O binding mode over the C=C binding mode, and the binding strength is moderate. DFT calculations and microkinetic modeling demonstrate that the selectivity for propenol formation on CuCr<sub>1</sub> is controlled by three elementary steps: (1) acrolein migration from the more stable C=O binding mode to the less stable C=C binding mode, (2) H-migration to the C=C binding acrolein, and (3) formation of the O-H bond from the mono-hydrogenated intermediate. To help enhance the selectivity, high H<sub>2</sub> pressure is required as it can lower down the free energies of the steps that involve the introduction of more H atoms on the catalyst surface (e.g. the O-H bond formation step), while acrolein diffusion step remains unaffected and the H-migration step less impacted. It is important to note that the inherent inaccuracies in DFT calculations might affect the computed selectivity. Therefore, one could only propose that it is highly probable that selective acrolein hydrogenation could be carried out on CuCr<sub>1</sub>. The same also holds true for another mid-transition metal, Mn, and they should be the first

systems to be investigated in experiments.

Lastly, late-transition metals in Cu(111) are unlikely to selectively hydrogenate acrolein. These metals exhibit a preference for the C=C binding mode over the C=O binding mode, thereby eliminating the need for molecular migration to produce the undesired product propanal. In addition, the transition states for propenol formation are found to be higher than those for propanal formation on CuNi<sub>1</sub>, which is the late-transition metal that has the smallest energy difference between the two different binding modes of acrolein. This result shows that CuNi<sub>1</sub> cannot selectively hydrogenate acrolein, let alone other late-transition metals, which possess even greater energy differences between the two binding modes. Nevertheless, unsaturated aldehydes with substituents attached to the C=C bond might possess higher selectivity as the presence of the substituents could destabilize the transition states in C=C bond hydrogenation and facilitate the desorption of the unsaturated alcohols.

The findings underline that while the simple descriptor of a preferred C=O adsorption mode of the unsaturated aldehydes is contributing, it is not solely sufficient to guarantee a high selectivity toward unsaturated alcohols. Rather, the magnitude of the migration barrier between the two binding modes is also crucial in inhibiting access to the generally more reactive hydrogenation of the C=C bond. The trends presented in this study offer important insights into the properties that a specific single-atom alloy catalyst should possess for the selective hydrogenation of various  $\alpha,\beta$ -unsaturated aldehydes. Dilute alloy catalysts appear as a versatile platform for adjusting the binding strength of intermediates and transition states, thereby allowing control over catalytic activity and selectivity.

# Chapter 6 Cu-Based Atom Alloys as Tunable Catalysts for Selective Propane Dehydrogenation

## 6.1 Introduction

Thanks to the breakthroughs in hydraulic fracturing technology, the extraction of shale gas condensates, which are abundant in propane, has seen a remarkable surge in scale.<sup>15</sup> Instead of burning the large amount of propane directly as a fuel, propane can be transformed into more value-added products like propylene. Propylene serves as a vital raw material in the production of crucial petrochemicals including polypropylene, propylene oxide, and acrylonitrile.<sup>132–134</sup> A large portion of the world's production of propylene currently relies on the conventional processes of pyrolysis and catalytic cracking of hydrocarbons. However, due to the swift depletion of fossil fuel resources, these conventional methods utilized for propylene generation are unable to satisfy the rising demands.<sup>15,135</sup> As a result, there is a pressing need to improve the propylene production technologies such that the generation rates could be enhanced.

Non-oxidative dehydrogenation of propane has drawn much attention lately as not only does it generate propylene, but it also yields the valuable H<sub>2</sub> which can be used as a clean energy source. In addition, the process does not directly form CO<sub>2</sub>. Pt-based catalysts have been widely used in the industry for this dehydrogenation reaction due to their high activity.<sup>136,137</sup> However, over-dehydrogenation and C-C bond cleavage frequently occur on the Pt-based catalysts under reaction conditions, resulting in diminished product selectivity as well as coking.<sup>14,15</sup> Besides, elevated temperatures during alkane dehydrogenation and regeneration processes often lead to significant sintering of Pt nanoparticles, primarily driven by the Ostwald ripening mechanism.<sup>138–140</sup> Furthermore, Pt also imposes an economical constraint on industry profitability due to its

expensive cost. These drawbacks necessitate the development of novel catalysts that could offer significant improvements from both a scientific and economic standpoint.

Single-atom alloys (SAA) are a promising class of catalytic materials to improve reaction selectivity and to reduce costs in chemical processes.<sup>41,55</sup> SAAs are often formed by atomically dispersing an active element, such as Pd and Pt, into a less active metal host, such as Cu, Ag, and Au.<sup>18–21,33</sup> The active elements often initiate the reaction mechanism, which is C-H bond cleavage in the case of propane dehydrogenation, while the less active metal host imparts the selectivity by isolating the active metal and modifying its electronic structure compared to the bulk case. Through diluting different active species in a metal host, the binding strength of reaction intermediates on the surface could be effectively adjusted, which could lead to a control of the reaction kinetics.<sup>45</sup> Depending on how much of the active species is incorporated, remaining in the dilute limit, the resulting active ensembles formed could span various sizes (monomer, dimer, trimer, etc.).<sup>49</sup> These different ensemble sizes dictate the number of active atoms that the reaction intermediates can interact with, and hence determine the binding strength. Small ensemble sizes are also important to limit side reactions of C-C bond formation and coking, since larger active elements are usually required for these coupling reactions.<sup>68</sup> In addition to the geometric contribution, isolated dopant atoms are also expected to have narrow d-states due to the weak orbital mixing between them and the metal host. The relative position of the d-states could also vary when different elements are dispersed in the less active metals.<sup>43</sup> This change in the electronic structures could hence effectively alter the interaction between the catalyst surfaces and the reaction intermediates. By carefully adjusting these two aspects of dilute alloys (i.e. geometric and electronic structures), an optimal catalyst could be achieved, striking a balance between reaction activity and selectivity.

Propane dehydrogenation is a highly endothermic reaction, with the standard enthalpy change being 124.3 kJ/mol.<sup>141</sup> Based on the Le Chatelier's principle, high temperatures are required to promote this endothermic process. Although pure Cu(111) is often prone to sintering (which would lead to catalyst deactivation) when the reaction is performed under high temperatures, the inclusion of active dopant elements such as Ni and Rh in it could provide enhanced sintering resistance, in addition to the improved reaction activity.<sup>54,55</sup> Nevertheless, under high reaction temperatures, alloy catalyst surface restructuring such as segregation (dopant atoms diffusing into the subsurface layers) and aggregation (dopant atoms grouping together to form a large surface active ensemble) should still be properly considered for optimal catalytic performance.

Previously, catalysts created by alloying Sn with Pt were shown to possess good selectivity in the reaction of propane dehydrogenation. Researchers proposed that the inclusion of Sn aids in breaking down larger Pt ensembles into smaller clusters, thereby removing the potential sites for coke formation.<sup>142-144</sup> Additionally, the electronic structure of Pt is also modified with the inclusion of Sn, and the electron transferred from Sn to Pt helps encourage the desorption of propylene and reduce the coke formation on the Pt sites.<sup>145,146</sup> Besides the Pt-Sn catalyst, the highly dilute Pt-Cu single atom alloy (SAA) catalyst has also been shown to achieve high propane dehydrogenation selectivity and anti-coke ability, which are attributed to the high barriers for C-C bond breaking and deep dehydrogenation of propene, in addition to the higher frequency of propene generation.<sup>41</sup> Another SAA catalyst of Rh-Cu also demonstrates high activity, selectivity, and coke-resistance in the propane dehydrogenation reaction. In the flow-reactor studies performed by Hannagan et al., not only is this catalyst seen to be more stable, but its activity also surpasses that of the Pt catalyst at low temperatures. Despite the sintering of the Cu nanoparticles at higher temperatures, the initial

propane dehydrogenation rates on Rh-Cu are still comparable to that on Pt-based catalysts.<sup>55</sup> Cu-based dilute alloys hence seem to be promising for propane dehydrogenation, and we aim to find from computations other alloy combinations that are even more efficient in this present work.

In this present study, we have utilized density functional theory (DFT) calculations and microkinetic modeling to unravel the underlying mechanisms that govern the propane dehydrogenation reaction on four different catalysts: CuHf<sub>1</sub>, CuIr<sub>1</sub>, CuRh<sub>1</sub>, and Pt (the latter two are used as references). By performing the degree of rate control analysis, we show that the rate-limiting step in the dehydrogenation is related to the first C-H bond cleavage on CuHf<sub>1</sub> and Pt, but to the H-migration on CuIr<sub>1</sub> and CuRh<sub>1</sub>. Among the alloy catalysts, the most reactive one is found to be CuHf<sub>1</sub> due to its strongest binding with the reaction intermediates and the transition states, leading to a lower effective barrier for C-H bond cleavage. In fact, this catalyst is calculated to be even more reactive than the conventional Pt catalyst on a per active site basis. Besides its reactivity, CuHf<sub>1</sub> also possesses high selectivity as further dehydrogenation beyond CH<sub>2</sub>CHCH<sub>2</sub> is not very likely. Following CuHf<sub>1</sub>, CuIr<sub>1</sub> and CuRh<sub>1</sub> are also found to be active and selective for propane dehydrogenation, despite showing a lower propylene formation rate than CuHf<sub>1</sub>. Not only do our results demonstrate novel potential alloy catalysts that have not been previously reported for propane dehydrogenation, but they also illustrate the important aspects that one should consider when developing other new catalysts for this reaction.

## 6.2 Methods

### 6.2.1 DFT Calculations

All density functional theory (DFT) calculations were performed using the Vienna ab initio simulation package (VASP).<sup>75,76</sup> Cu-based SAA surfaces for propane dehydrogenation were modeled using a four-layer slab and a (4 × 3) unit cell, with one of the surface Cu atoms replaced

by a dopant atom. For this unit cell size, a  $\Gamma$ -centered  $4 \times 5 \times 1$  K-points grid was used. During structural optimization, the bottom two layers were fixed in the Cu bulk position while the upper two layers and the surface adsorbates were allowed to relax until the convergence threshold of 0.02 eV/Å was reached. Based on the previous benchmarking on Pt(111), the exchange-correlation functional optPBE-vdW is shown to give the most accurate binding energies for alkane activation.<sup>81</sup> Hence, all calculations reported in this study were performed using the optPBE-vdW functional, along with a cutoff energy of 500 eV for the plane wave basis set.<sup>78–80</sup> Transition states were located using the climbing image nudged elastic band method (CI-NEB), the dimer method, and the quasi-Newton method.<sup>84,109,127,147</sup> Vibrational frequency calculations were also carried out. For the free energy calculations, small wavenumbers ( $< 50 \text{ cm}^{-1}$ ) and extra imaginary frequencies were shifted to  $50 \text{ cm}^{-1}$ , and vibrational degrees of freedom were included in the harmonic approximation. Crystal Orbital Hamilton Populations (COHP) analysis was conducted using Local Orbital Basis Suite Toward Electronic Structure Reconstruction (LOBSTER), and all structural configurations reported were visualized using VESTA.<sup>85,128</sup>

Free energy calculations for gaseous and surface species take into consideration zero-point energies and vibrational entropies. They were calculated using Eqs 6.1, 6.2, and 6.3:

$$G_{gas,linear} = E_{DFT} + E_{ZPE} + 3.5k_B T + \sum \frac{\epsilon_i}{\exp\left(\frac{\epsilon_i}{k_B T}\right) - 1} - T \left( S_{trans} + S_{rot} + S_{vib} - k_B \ln \frac{P}{P_0} \right) \quad (6.1)$$

$$G_{gas,nonlinear} = E_{DFT} + E_{ZPE} + 4k_B T + \sum \frac{\epsilon_i}{\exp\left(\frac{\epsilon_i}{k_B T}\right) - 1} - T \left( S_{trans} + S_{rot} + S_{vib} - k_B \ln \frac{P}{P_0} \right) \quad (6.2)$$

$$G_{surf} = E_{DFT} + E_{ZPE} + \sum \frac{\epsilon_i}{\exp\left(\frac{\epsilon_i}{k_B T}\right) - 1} - T S_{vib} \quad (6.3)$$

where  $E_{DFT}$  is the electronic energy given by DFT,  $E_{ZPE}$  is the zero-point energy,  $\epsilon_i$  is the vibrational energy,  $k_B$  is the Boltzmann's constant,  $T$  is the temperature,  $P$  is the pressure ( $P_0$  is the

reference pressure), and  $S_{trans}$ ,  $S_{rot}$ , and  $S_{vib}$  are the translational, rotational, and vibrational entropies, respectively.

An energy decomposition scheme was employed to understand the stabilization of the transition states for first C-H bond cleavages by splitting the binding strengths into two contributions: transition state deformation and catalyst-transition state interaction.<sup>148</sup> The deformation energy (Eq 6.4) for the former and interaction energy (Eq 6.5) for the latter were calculated as:

$$E_{def,TS} = E(TS') - E(C_3H_{8,g}) \quad (6.4)$$

$$E_{int,TS} = |E(TS - CuX_1) - E(TS') - E(CuX_1')| \quad (6.5)$$

where  $E(TS')$  is the energy of propane  $C_3H_8$  in the deformed geometry of the transition state in the gas phase,  $E(C_3H_{8,g})$  is the energy of the unconstrained propane molecule in the gas phase,  $E(TS - CuX_1)$  is the total energy of the unconstrained transition state on the catalyst surface, and  $E(CuX_1')$  is the energy of the frozen metal slab in the deformed geometry of the transition state “TS -  $CuX_1$ ”.

## 6.2.2 Microkinetic Modeling

Microkinetic simulations were performed to study the kinetic behavior of the proposed reaction mechanism (Appendix E.1) on the four catalysts using the energetics obtained from DFT. The rate constants for adsorption ( $k_{ads,i}$ ) and desorption ( $k_{des,i}$ ) were calculated using the collision theory (Eqs 6.6 and 6.7) and those for surface reactions ( $k_j$ ) by the transition state theory (Eq 6.8).<sup>87</sup>

$$k_{ads,i} = \frac{A_{st}}{\sqrt{2\pi m_i k_B T}} \quad (6.6)$$

$$k_{des,i} = k_{ads,i} P^o \exp\left(\frac{\Delta G_{ads,i}^o}{k_B T}\right) \quad (6.7)$$

$$k_j = \frac{k_B T}{h} \exp\left(-\frac{\Delta H^\ddagger}{k_B T}\right) \exp\left(\frac{\Delta S^\ddagger}{k_B}\right) \quad (6.8)$$

where  $A_{st}$  is the area of the adsorption site,  $m_i$  is the mass of the adsorbing species  $i$ ,  $k_B$  is the Boltzmann's constant,  $T$  is the temperature,  $P^o$  is the standard state pressure (1 bar),  $\Delta G_{ads,i}^o$  is the adsorption free energy of species  $i$  under standard state pressure,  $h$  is the Planck's constant, and  $\Delta H^\ddagger$  and  $\Delta S^\ddagger$  are respectively the enthalpy and entropy differences between the initial state and the transition state in elementary step  $j$ .

In the microkinetic simulations, the time-dependent coverages of surface species  $i$  were formulated as a combination of the elementary step rate equations  $r_j$ :

$$\frac{d\theta_i}{dt} = \sum_j \nu_{ij} r_j \quad (6.9)$$

where  $\theta_i$  is the coverage of surface species  $i$ ,  $\nu_{ij}$  is the stoichiometric coefficient of species  $i$  in elementary step  $j$ , and  $r_j$  is the rate equation for elementary step  $j$ . The catalyst surfaces were set to be bare initially. Steady-state coverages of surface species, which would be used in subsequent kinetic analysis, could be obtained by solving the set of ordinary differential equations.

The degree of rate control (DRC) analysis was employed to identify the rate-limiting steps in propane dehydrogenation over the four catalysts.<sup>92</sup> It is defined as the change in the overall reaction rate with respect to the change in the rate constant for one specific elementary step  $j$ , which could be reflected in the free energy of its transition state. Hence, the mathematical representation for DRC calculations is written as:

$$DRC = \left( \frac{\partial \ln(r)}{\partial \left( \frac{-G_j^{0,TS}}{k_B T} \right)} \right)_{G_{k \neq j}^{0,TS}, G^{0,IM}} \quad (6.10)$$

where  $r$  is the overall reaction rate, and  $G^{0,TS}$  and  $G^{0,IM}$  are respectively the standard state free energies of the transition states and the surface intermediates.

## 6.3 Results

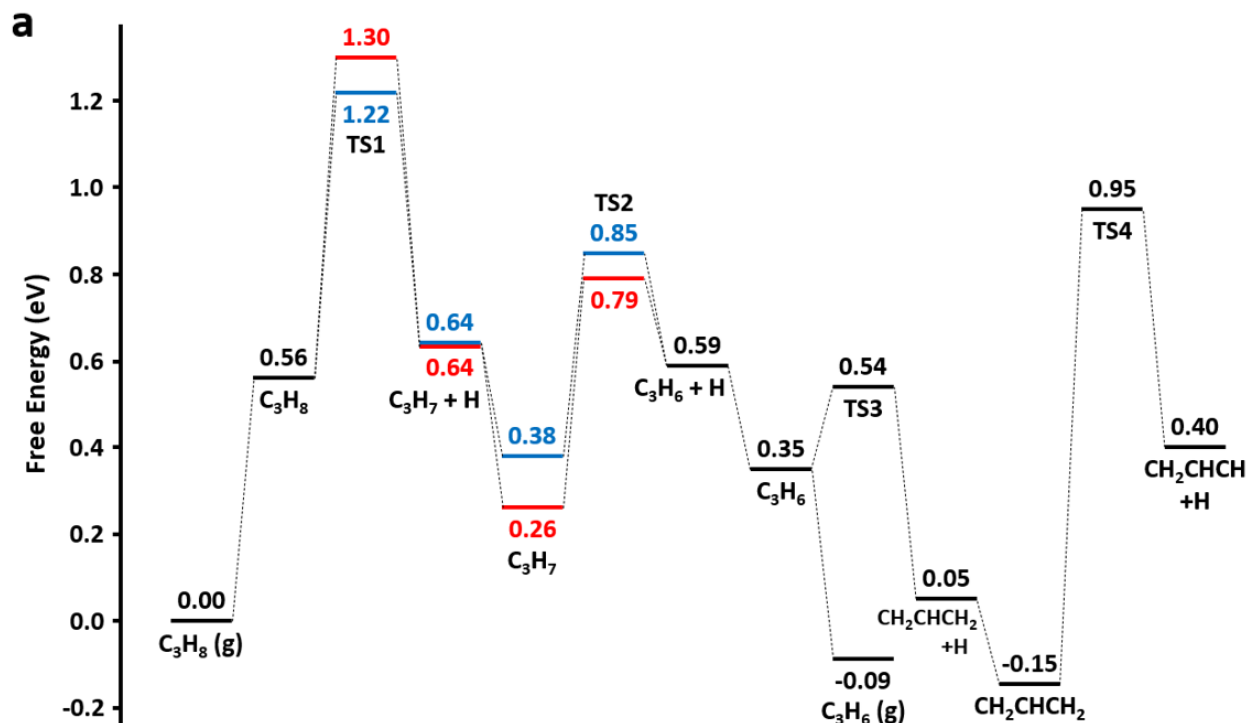
### 6.3.1 Dopant Segregation and Aggregation

In contrast to monometallic catalysts such as Pt, concern is often raised regarding the position of the active species in single-atom alloy catalysts. Segregation and aggregation energies are two important indicators that assess whether a single-atom alloy catalyst, with active species monomers embedded in the surface layer of the host, could be formed experimentally. The former is defined as the energy gain/loss when the dopant goes from subsurface Cu layer to the surface layer, and the latter is the energy difference when two isolated surface dopant atoms are brought together to form a dimer. Hence, negative segregation energy indicates that it is favorable for the dopants to stay in the surface layer, and positive aggregation energy suggests that the dopants would like to remain isolated. Earlier study finds that the segregation and aggregation energies for  $\text{CuHf}_1$  are 0.10 eV and 0.56 eV, respectively, and those for  $\text{CuIr}_1$  are 0.04 eV and 0.05 eV.<sup>45</sup> Although the segregation energies of these two catalysts are positive, which indicate unfavorable segregation to the surface, their magnitudes are small. The alloy catalysts can hence be treated under CO or O<sub>2</sub> pressures prior to the reaction to bring the dopants up to the surface, forming a low energy metastable state that is maintained throughout the course of the catalytic process. Segregation of Pd in Au(111) (the segregation energy of which is 0.31 eV), for example, has been previously shown to be facilitated in the presence of CO.<sup>46</sup> The same should also apply to  $\text{CuHf}_1$  and  $\text{CuIr}_1$  that exhibit even smaller segregation energy values.

Aggregation energies, on the other hand, are positive for both of the two alloy catalysts. The formation of larger dopant aggregates is therefore not thermodynamically favorable, and the

dopants should stay as isolated atoms in the surface layer. Nevertheless, it is important not to use high concentration of dopants when synthesizing the catalysts in experiments as it could force the dopant atoms together and form larger active ensembles. Prior to finalizing this part of the discussion, it should be noted that the successful synthesis of CuRh<sub>1</sub> has been previously reported in the literature.<sup>55</sup> Consequently, the provision of its segregation and aggregation energies is not necessary to ascertain its potential existence.

### 6.3.2 Propane Activation



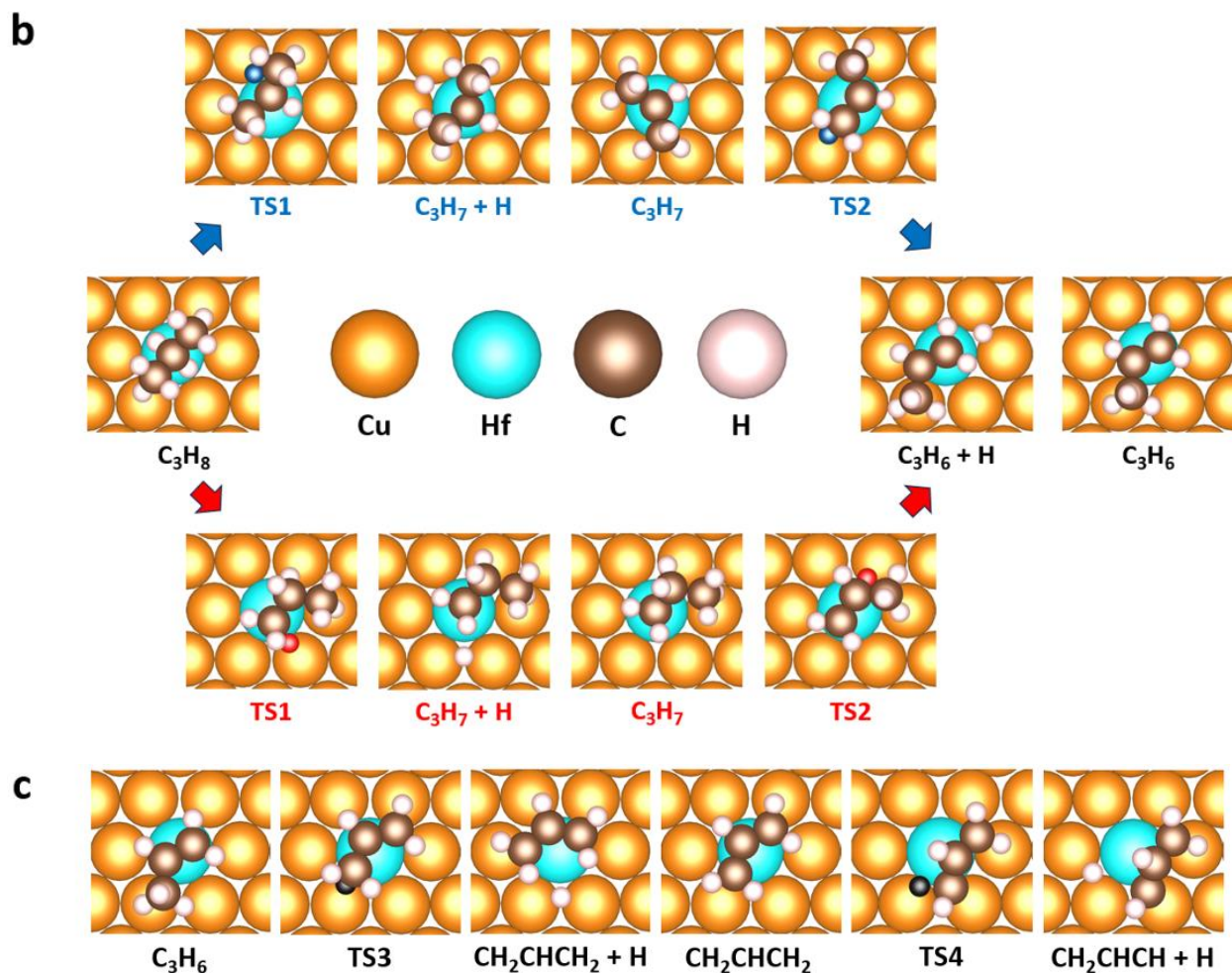


Figure 6.1. (a) Free energy profile and (b,c) corresponding adsorption configurations for propane dehydrogenation on  $\text{CuHf}_1$ . Side view of the transition states is provided in Figure E.1. Red and blue sections along the pathway indicate dehydrogenation at the terminal or central carbon atoms as the first step, respectively. For better visibility, the H atoms that are being detached in the transition states are colored in red or blue, accordingly, and in black for further dehydrogenation beyond propene. Reaction conditions are:  $T = 773 \text{ K}$ ,  $P(\text{C}_3\text{H}_8) = 0.64 \text{ bar}$ ,  $P(\text{H}_2) = 0.36 \text{ bar}$ , and  $P(\text{C}_3\text{H}_6) = 0.11 \text{ bar}$ .

Propane activation could take place by either cleaving the C-H bond at the terminal carbon atom first (Figure 6.1, red pathway) or at the central carbon atom first (Figure 6.1, blue pathway).

Free energy profiles for these reaction pathways were constructed for the single-atom alloy catalysts and the monometallic Pt catalyst to examine the differences among them (Figure 6.1, E.3, E.5, and E.6). On CuHf<sub>1</sub>, the free energy profile begins with the molecular adsorption of propane (C<sub>3</sub>H<sub>8</sub>) on the dopant, followed by the transition states for C-H bond cleavage to form either CH<sub>3</sub>CHCH<sub>3</sub> (blue pathway) or CH<sub>3</sub>CH<sub>2</sub>CH<sub>2</sub> (red pathway), which co-adsorb on the same active ensemble with the H atom detached (“C<sub>3</sub>H<sub>7</sub> + H” in Figure 6.1). For the presentation of the free energy profile, we assume that, before subsequent bond-breaking steps take place, this H atom will spill over on the Cu domain and recombine with another H atom either on the Cu surface directly or on a second active site, and effectively desorb as ½ H<sub>2</sub>(g). Although these processes (H-spillover and H-H recombination) are activated, they are not included in Figure 6.1 for simplicity, but they will be detailed in the following section. As will be confirmed by the following sections, this assumption does not affect the conclusion drawn from this free-energy-based analysis for CuHf<sub>1</sub>. After the H atom is removed, the propyl intermediate will follow the same dehydrogenation pattern to produce C<sub>3</sub>H<sub>6</sub>. Propylene formed on CuHf<sub>1</sub> could either desorb into the gas phase or stay on the surface for further reaction. Further reaction involves cleaving the C-H bond in the methyl group in propylene, generating an allyl intermediate CH<sub>2</sub>CHCH<sub>2</sub> on the catalyst surface. Eventually, the resulting CH<sub>2</sub>CHCH<sub>2</sub> will undergo additional dehydrogenation and terminate at CH<sub>2</sub>CHCH + H. Free energy profiles for other single-atom alloys and Pt(111) were constructed in a similar manner, although they stop at CH<sub>2</sub>CHCH<sub>2</sub>, and the reason of which will be discussed in the following section.

The free energy profile for propane dehydrogenation on CuHf<sub>1</sub> indicates that molecular adsorption of propane is not stable under the studied conditions, as demonstrated by the positive change in free energy ( $\Delta G = 0.56$  eV). Due to this unstable adsorption of propane, including this

initial step in either the free energy profile or the subsequent microkinetic modeling is not necessary, and this step was neglected for CuIr<sub>1</sub> and CuRh<sub>1</sub>. Following this molecular adsorption, the transition state to break the C-H bond at the central C atom (blue pathway) is seen to be more favorable than that at the terminal C atom (red pathway), as evidenced by the lower free energy value of 1.22 eV versus 1.30 eV. Nevertheless, the fact that these two transition states lie at the highest points in the entire free energy profile suggests that they are the most rate-limiting steps in this reaction, and blue TS1 would be even more rate-controlling than red TS1 as the former pathway is more favorable. Inconsistent with the first transition states, the intermediate formed by dehydrogenating the central C atom (blue C<sub>3</sub>H<sub>7</sub>; G = 0.38 eV) is less stable than that formed by terminal C dehydrogenation (red C<sub>3</sub>H<sub>7</sub>; G = 0.26 eV). The same persists into the second transition states for C-H bond cleavage to produce the desired product propylene. It is worth noting that although the red pathway is more favorable than the blue pathway in this second bond-breaking step, the transition state energies for these steps are much lower than those for the first ones. Hence, it will not reverse the qualitative suggestion that the blue pathway is more favorable.

Propylene formed on CuHf<sub>1</sub> could either desorb into the gas phase or stay on the catalyst surface for further dehydrogenation. It is seen that the activation barrier for additional C-H bond cleavage is considerably small (0.19 eV). This small activation barrier implies that this further dehydrogenation step to produce CH<sub>2</sub>CHCH<sub>2</sub>, which is remarkably stable on the catalyst surface (G = -0.15 eV; lower than that of gaseous propylene by 0.06 eV), is indeed very probable. However, dehydrogenation beyond CH<sub>2</sub>CHCH<sub>2</sub> is less likely as the forward activation barrier ( $\Delta G = 1.10$  eV) is 0.41 eV larger than the reverse barrier to produce propylene again. Additionally, since CH<sub>2</sub>CHCH<sub>2</sub> is more stable than either C<sub>3</sub>H<sub>6</sub> or CH<sub>2</sub>CHCH + H, the reaction is expected to be

trapped here instead of proceeding in either direction, populating the catalyst surface with  $\text{CH}_2\text{CHCH}_2$ .

### 6.3.3 H-H Recombination

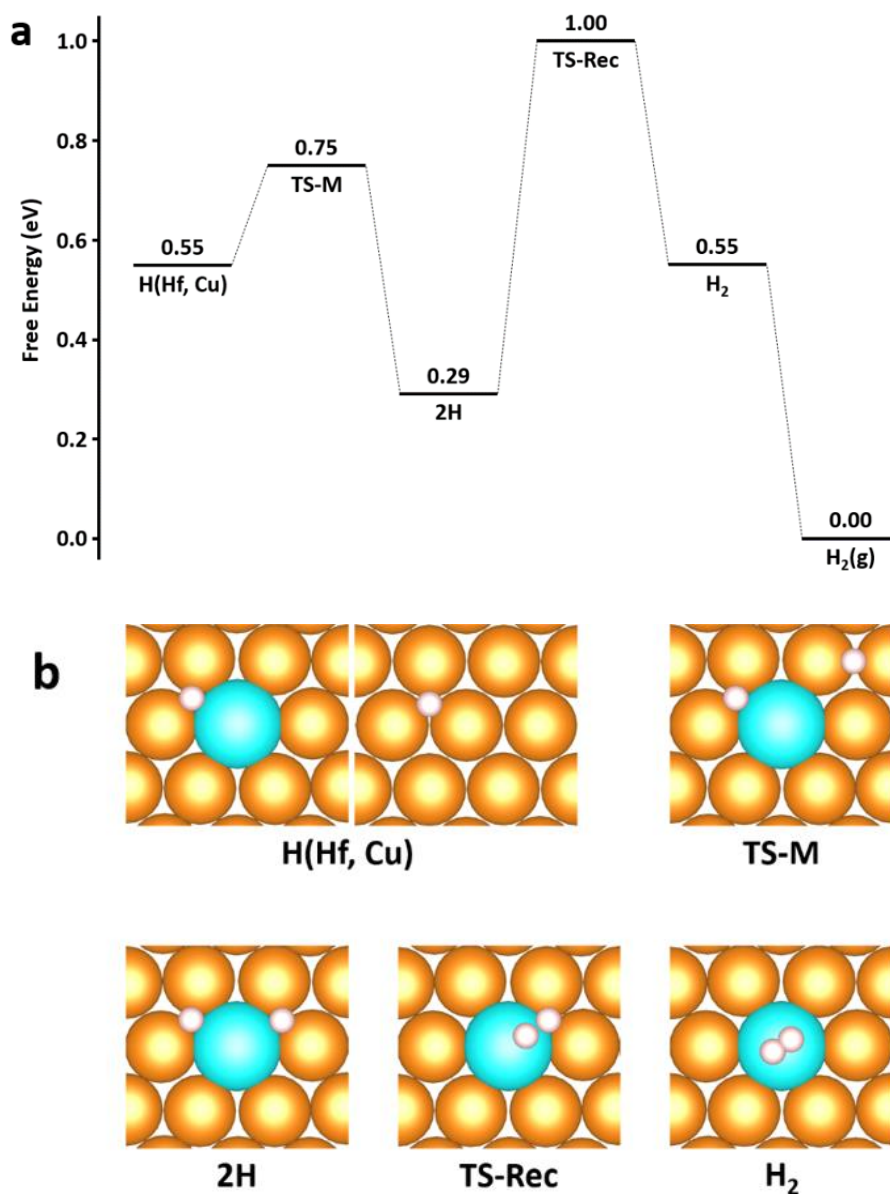


Figure 6.2. (a) Free energy profile and (b) corresponding adsorption configurations for H atoms recombination on  $\text{CuHf}_1$ . Reaction conditions are:  $T = 773 \text{ K}$  and  $P(\text{H}_2) = 0.36 \text{ bar}$ .

It is worth noting that, on single-atom alloys, the H atoms detached from propane and propyl will recombine on either a second active site or on Cu(111) before desorbing into the gas phase. The energy profile for such processes on CuHf<sub>1</sub> is shown in Figure 6.2. To achieve the recombination on a second CuHf<sub>1</sub> active site, it is needed to bring the H atoms already spilled over on the Cu domain to the single atom by overcoming a small migration barrier of ~ 0.20 eV. The same process was also assessed for the other two alloy catalysts (i.e. CuIr<sub>1</sub> and CuRh<sub>1</sub>), which reveals migration barriers of similar magnitudes to that observed on CuHf<sub>1</sub> (Figures E.2 and E.4). Once there are two H atoms on the same active ensemble (“2H” state in Figure 6.2, E.2, and E.4), recombination could take place by going through the associated transition state (“TS-Rec” in Figure 6.2 and E.4). In the case of CuHf<sub>1</sub>, this recombination process is considerably more difficult than those on CuRh<sub>1</sub> and CuIr<sub>1</sub> for its high transition state energy ( $G = 1.00$  eV) and large activation barrier of 0.71 eV. For CuRh<sub>1</sub>, on the other hand, the recombination transition state is at a comparable level to the molecular adsorption state of H<sub>2</sub>, making the activation barrier small and roughly equal to 0.1 eV (Figure E.4). Lastly, the binding of the H atoms on the CuIr<sub>1</sub> active sites is strong, with the adsorption free energy being -0.02 eV at the high reaction temperature (Figure E.2). This binding is so strong that no recombination transition state was found on the electronic energy surface and the two H atoms simply desorb as a gaseous H<sub>2</sub> molecule. Nevertheless, given the entropy change associated with adsorption/desorption processes, there should exist a free energy barrier in between gaseous H<sub>2</sub> and the “2H” state that we assume as negligible here. Before closing up, it should also be mentioned that the only barrier for H-H recombination on Pt(111) is the binding energy of the H atoms,<sup>149</sup> and the transition state energy and activation barrier for the same process on Cu(111) are 1.55 eV and 0.74 eV, respectively. Although these values are larger

than those on the active ensembles, Cu(111) could still serve as additional sites in the reaction mechanism to recombine the H atoms from propane activation.

### 6.3.4 Transition State Energy Comparison

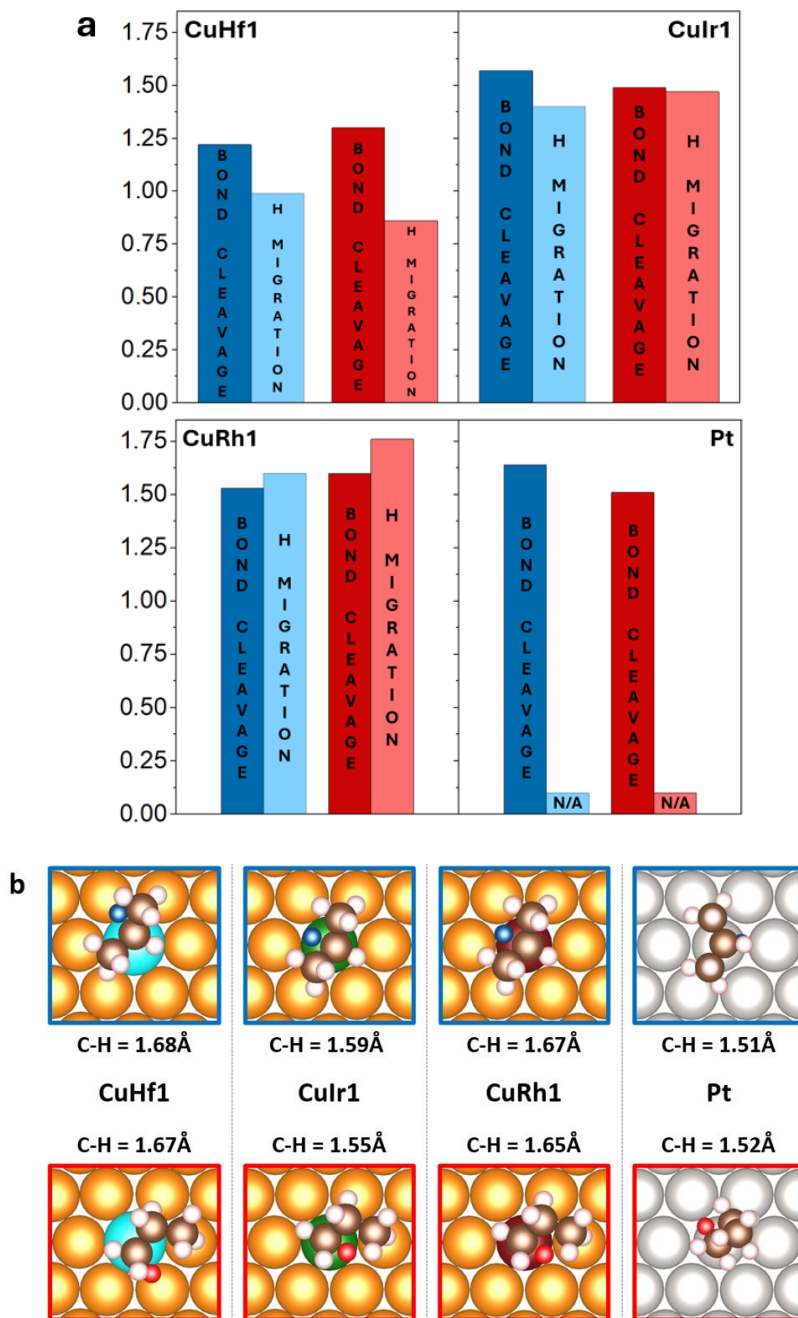


Figure 6.3. (a) Free energies of the transition states for the steps of initial C-H bond cleavage and subsequent H-migration away from the active ensembles. Note that H-migration steps are not

considered for Pt(111) due to the homogeneous nature of the surface. The free energies of the H-migration transition states were obtained by adding the activation barriers, which are the energy differences between “C<sub>3</sub>H<sub>7</sub> + TS-M (in the absence of the H residing on the active ensemble)” and “C<sub>3</sub>H<sub>7</sub> + H”, to “C<sub>3</sub>H<sub>7</sub> + H”. A schematic diagram for this process is provided in Figure E.7. (b) Corresponding adsorption configurations of the transition states for the initial C-H bond cleavage steps on the four catalyst surfaces, along with the lengths of the C-H bonds that are being cleaved listed. Side view of these transition states can be found in Figures E.1, E.3, E.5 and E.6. Blue and red colors for bars and frames represent the pathways in which the central or terminal carbon atoms of propane are dehydrogenated as the first step, respectively. The H atoms that are being detached are highlighted in blue or red accordingly. Reaction conditions are: T = 773 K, P(C<sub>3</sub>H<sub>8</sub>) = 0.64 bar, P(H<sub>2</sub>) = 0.36 bar, and P(C<sub>3</sub>H<sub>6</sub>) = 0.11 bar.

The complete propane dehydrogenation pathway was also studied in detail on CuIr<sub>1</sub>, CuRh<sub>1</sub>, and Pt(111) (Figures 6.3, E.3, E.5, and E.6), in addition to CuHf<sub>1</sub> (Figure 6.1). It is determined by the lower overall transition state free energies that CuRh<sub>1</sub> exhibits a preference for the production of propylene through CH<sub>3</sub>CHCH<sub>3</sub> (i.e. blue pathway), whereas CuIr<sub>1</sub> and Pt(111) opt for CH<sub>3</sub>CH<sub>2</sub>CH<sub>2</sub> (i.e. red pathway) for the same process (Figure 6.3). However, unlike CuHf<sub>1</sub>, propane activation is not the sole rate-limiting step on CuIr<sub>1</sub> and CuRh<sub>1</sub>. For CuIr<sub>1</sub>, the first C-H bond cleavage transition state in the red pathway is only 0.02 eV higher in free energy than the H-migration step towards the Cu domain (Figure 6.3). For CuRh<sub>1</sub>, the transition state for the spillover step in the blue pathway lies even higher in the energy profile than the bond cleavage step (Figure 6.3). These results strongly indicate that H-migration steps are also rate-controlling in the reaction mechanisms on the two single-atom alloys, which stands in stark contrast to the prevailing belief that alkane activation is only governed by the initial bond-cleavage step. It is noteworthy that the

change in the rate-limiting steps is most likely attributed to the stabilization of the dehydrogenated intermediates (i.e. “CH<sub>3</sub>CHCH<sub>3</sub> + H” and “CH<sub>3</sub>CH<sub>2</sub>CH<sub>2</sub> + H”). To be more specific, on CuHf<sub>1</sub>, the intermediate is stabilized (relative to the first bond cleavage transition state) to a greater extent than that on CuIr<sub>1</sub> and CuRh<sub>1</sub>, as evidenced by the free energy differences between the first bond cleavage transition states and the intermediate states ( $\Delta G = -0.58$  eV for CuHf<sub>1</sub>,  $\Delta G = -0.37$  eV for CuIr<sub>1</sub>, and  $\Delta G = -0.28$  eV for CuRh<sub>1</sub>). Additionally, the three alloy catalysts encounter similar activation barriers for the H-migration steps ( $\Delta G^\ddagger = 0.35 - 0.40$  eV; note that these barriers are lower when reaction intermediates are present due to repulsion, as opposed to situations where only one H atom is present or no species are present at all). These two aspects collectively lead to higher transition state energies for H-migration on CuIr<sub>1</sub> and CuRh<sub>1</sub>, consequently rendering them somewhat rate-controlling in the reaction network. To avoid proceeding through the rate-limiting H-migration steps, it might be possible to keep the H atoms on the active ensembles while cleaving the second C-H bonds in propyl. However, the transition states for these steps on CuIr<sub>1</sub> and CuRh<sub>1</sub> are demonstrated to possess even higher free energies than those for H-migration ( $> 0.11$  eV), suggesting that this pathway is less favorable and is not considered in this study (Figure E.8). In comparison, on the Pt(111) catalyst, H diffusion is easy and H-migration steps cannot govern the dehydrogenation rate.

In addition to the distinct rate-limiting steps, the highest transition state free energies for the more preferable pathway on CuIr<sub>1</sub>, CuRh<sub>1</sub>, and Pt(111) markedly exceed that observed for CuHf<sub>1</sub> (Figure 6.3). To clarify further, the free energy values range from 1.49 – 1.60 eV for these catalysts, versus 1.22 eV for CuHf<sub>1</sub>. These larger values could indicate that the corresponding reaction rates would be significantly lower when compared with CuHf<sub>1</sub>. Nevertheless, CuIr<sub>1</sub> and CuRh<sub>1</sub> encourage propylene desorption by imposing large activation barriers (Figures E.3 and E.5;

$\Delta G^\ddagger = 1.13$  eV for CuIr<sub>1</sub> and  $\Delta G^\ddagger = 0.89$  eV for CuRh<sub>1</sub>) for further dehydrogenation steps. Even if this additional bond cleavage step can take place, the resulting CH<sub>2</sub>CHCH<sub>2</sub> formed is not strongly bound, as indicated by the positive free energy changes of 0.46 – 0.50 eV for this intermediate state relative to gaseous propylene. Hence, propylene is not expected to undergo more dehydrogenation steps and these catalyst surfaces should not be populated by the intermediate CH<sub>2</sub>CHCH<sub>2</sub>. It is not straightforward from the pathways alone to decipher whether the activation barrier magnitude or the surface poisoning by intermediates will control the optimal propylene production rates on these SAA catalysts. The combined effect of these contributions will be thoroughly examined in the following microkinetic modeling section.

### 6.3.5 Microkinetic Simulation of Catalytic Activity and Selectivity

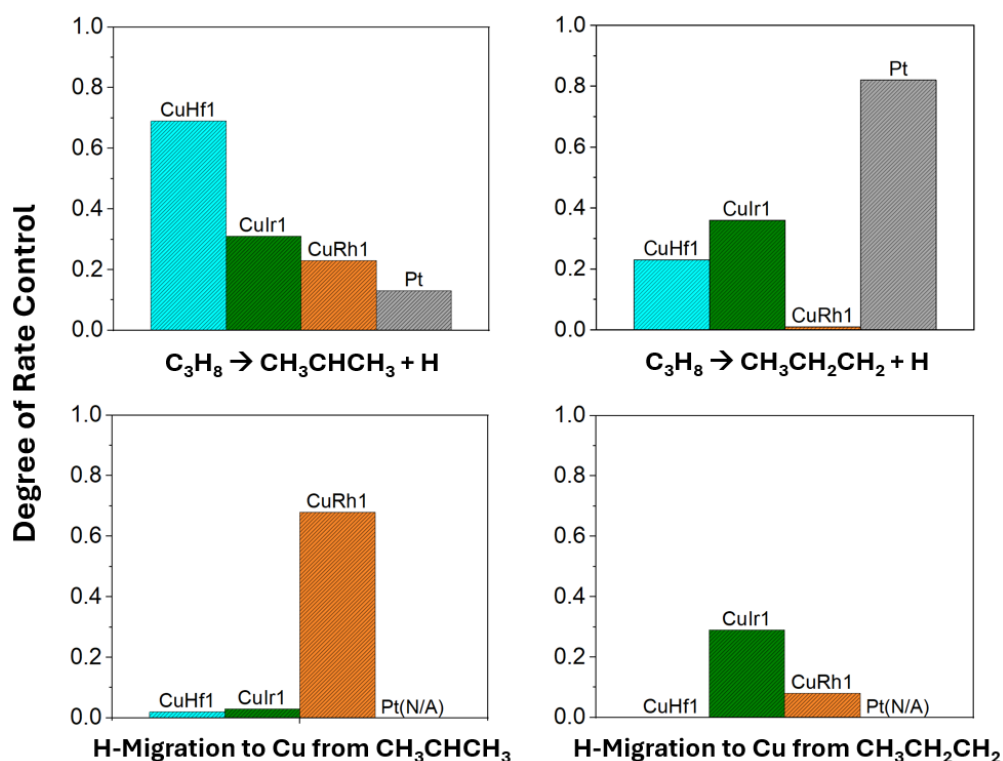
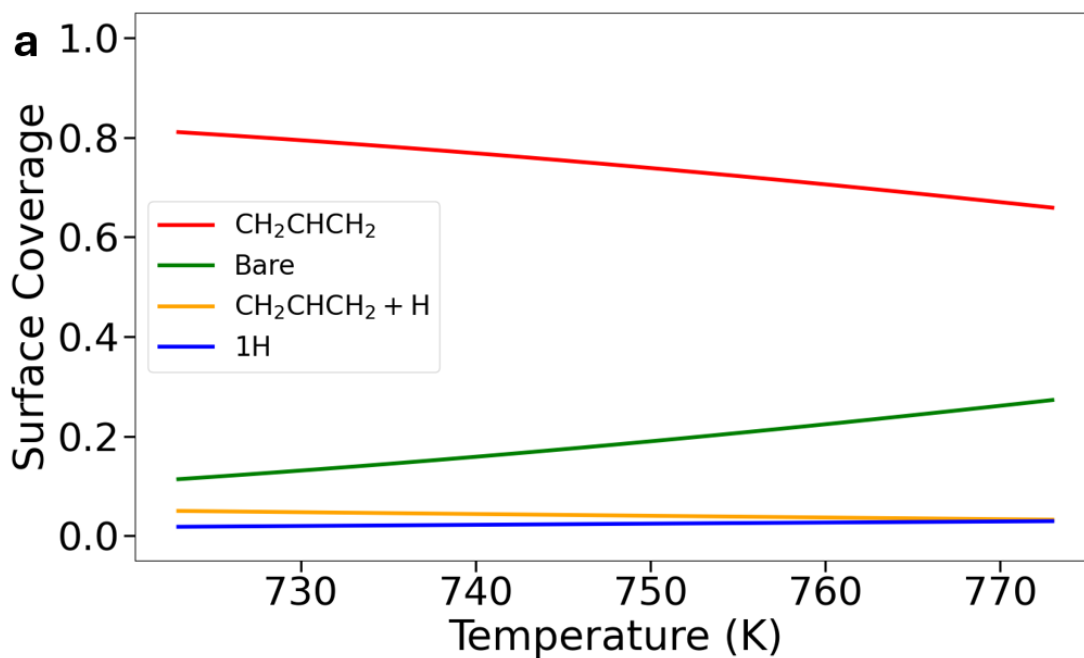


Figure 6.4. Degree of rate control of the transition states for the steps of initial C-H bond cleavage and subsequent H-migration away from the active ensembles. Note that H-migration steps are not

considered for Pt(111) due to the homogeneous nature of the surface. Reaction conditions are:  $T = 773$  K,  $P(\text{C}_3\text{H}_8) = 0.64$  bar,  $P(\text{H}_2) = 0.36$  bar, and  $P(\text{C}_3\text{H}_6) = 0.11$  bar.

Microkinetic modeling was performed to assess the combined effect of intermediate free energies and transition state free energies on the reaction rate. It also brings the two separate pathways of propane activation and H-H recombination together to provide a more comprehensive analysis of the activity of SAA catalysts. The details of the elementary steps considered in the reaction network can be found in Supplementary Information (Tables E.1-E.4). Briefly, the elementary steps include propane activation and dehydrogenation on the SAA surface (Propane Activation Section), and H-H migration and recombination on both the Cu(111) and SAA surfaces (H-H Recombination Section). Microkinetic modeling indicates that on  $\text{CuHf}_1$ , the transition states for dehydrogenating the central and terminal C atoms of propane are the most rate-controlling (Figure 6.4). Although both dehydrogenation pathways demonstrate a certain degree of rate control (i.e. reaction takes place through both pathways), the fact that dehydrogenating the central C atom of propane is more rate-controlling supports the free-energy-based analysis, where this pathway was shown to be more favorable and of primary importance. Similarly, reaction proceeds via both dehydrogenation pathways on  $\text{CuIr}_1$ , as evidenced by the degree of rate control exhibited by them. In this case, however, the pathway of dehydrogenating the terminal C atom of propane as an initial step is shown to be more favorable by the greater degree of rate control. More importantly, C-H bond cleavages are not the sole rate-limiting steps in alkane activation on  $\text{CuIr}_1$ . Rather, the step of moving the H atom away from  $\text{CH}_3\text{CH}_2\text{CH}_2$  also significantly controls the reaction rates. This situation starkly contrasts with extended active surfaces, on which the breaking of the C-H bonds is believed to be the only limiting factor for reaction rates. It is noted that the step of H-migration becomes even more prominent on  $\text{CuRh}_1$ , as this transition state is the most rate-limiting in the

reaction network, more rate-limiting than those for C-H bond cleavage (Figure 6.4). This observation is consistent with the free-energy-based assessment, where the free energy of this transition state is higher than that for dehydrogenating the central C atom of propane in the more favorable pathway (Figure 6.3). Eventually, the larger DRC value of the transition state for dehydrogenating the terminal C atom of propane on Pt(111) agrees well with the previous analysis that the reaction primarily proceeds through this pathway (Figures 6.3 and 6.4). Unlike the single-atom alloy catalysts, H-migration does not play a significant role in controlling the reaction rates on Pt(111) due to the homogeneous nature of the catalyst surface. These findings collectively suggest that in future research endeavors regarding alkane activation on single-atom alloys, attention should also be directed to H-migration, in addition to the ease of C-H bond activation.



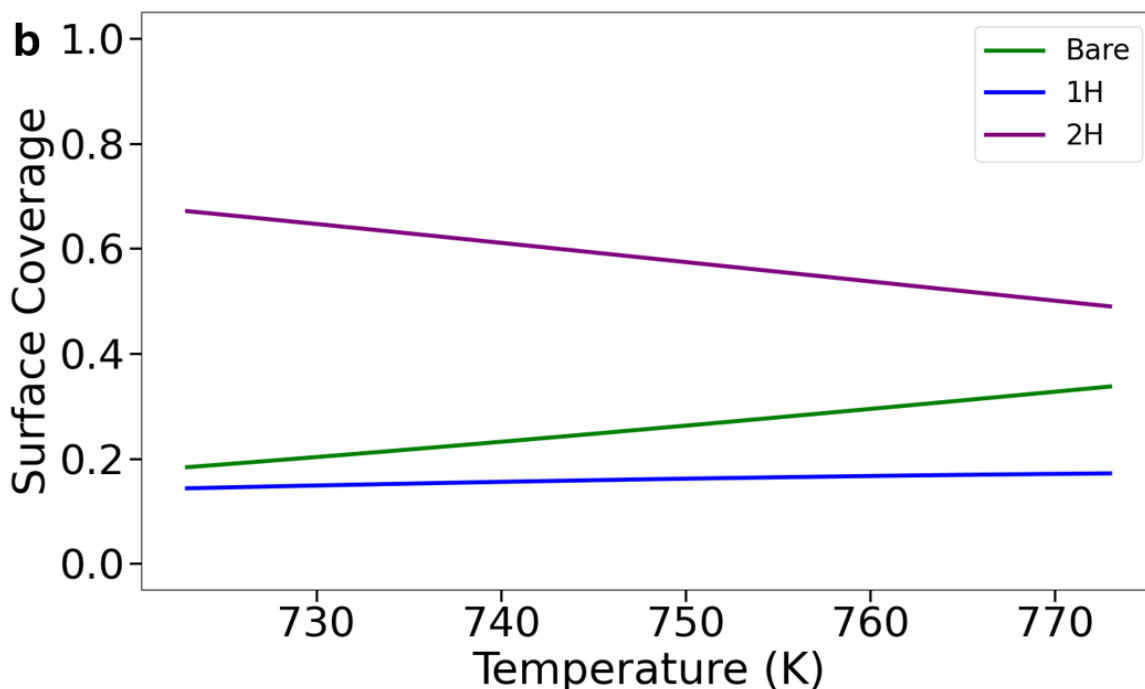


Figure 6.5. Steady-state surface coverage of reaction intermediates on (a) CuHf<sub>1</sub> and (b) CuIr<sub>1</sub> as a function of temperature. Reaction conditions are: P(C<sub>3</sub>H<sub>8</sub>) = 0.64 bar, P(H<sub>2</sub>) = 0.36 bar, and P(C<sub>3</sub>H<sub>6</sub>) = 0.11 bar.

The catalyst surfaces could be populated by reactants and intermediates during the course of the dehydrogenation reaction, which could lead to surface poisoning and catalyst deactivation. Results of kinetic modeling show that on CuHf<sub>1</sub>, most of the active sites are covered by CH<sub>2</sub>CHCH<sub>2</sub> due to its strong binding on the surface (Figures 6.1 and 6.5a; G = -0.15 eV), with the coverages being greater than 80 % at lower temperature and ~65 % at higher temperature. Despite this partial blocking of the active ensembles by the strongly bound CH<sub>2</sub>CHCH<sub>2</sub> intermediate, there are still some vacant sites (approximately 12 % to 28 %) available for reactions. Given that the free energies of the transition states for propane activation are considerably lower on CuHf<sub>1</sub>, it is expected that this catalyst could still efficiently produce propylene with only a fraction of active sites accessible. Unlike CuHf<sub>1</sub>, it is the H atoms (Figure 6.5b) that populate the surface of CuIr<sub>1</sub>,

for their strong adsorption on the active ensembles (Figure E.2;  $G = -0.02$  eV for the “2H” state). The coverage of these H atoms (“1H” and “2H”) accounts for ~65 % to 80 % of the total active sites, leaving only 20 – 35% of the sites bare for dehydrogenation. Although the amount of vacant active sites is similar on both  $\text{CuHf}_1$  and  $\text{CuIr}_1$ , propylene production rate should be lower on the latter due to the higher transition state free energy associated with the first C-H bond cleavage step. Eventually, it is seen that the surface of  $\text{CuRh}_1$  is mostly bare (Figure E.9), as there is no strongly bound reaction intermediate on it.

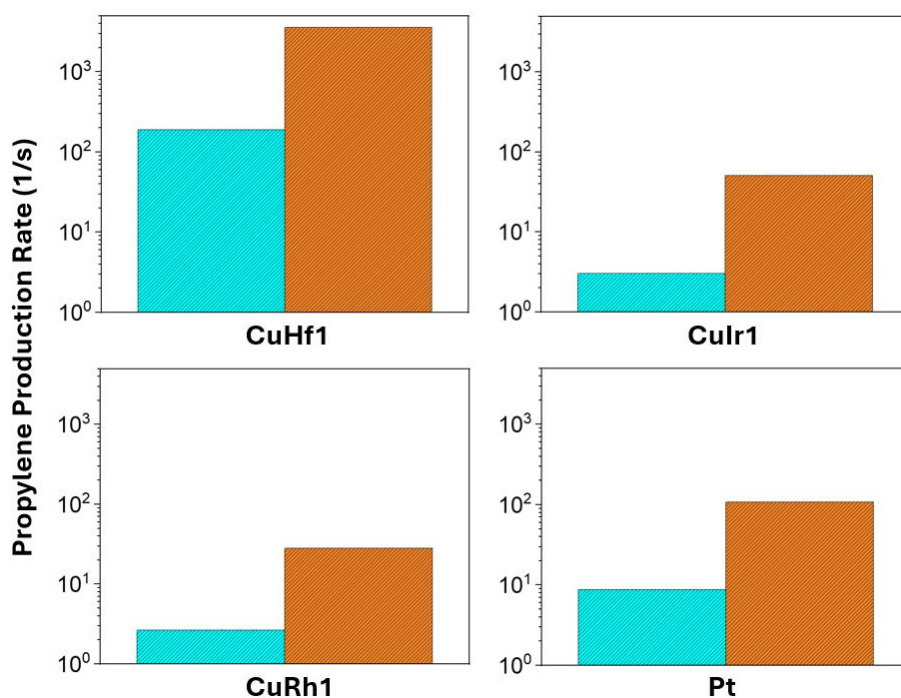


Figure 6.6. Steady-state rate of propylene production on the four catalyst surfaces. Blue represents the production rate at a lower temperature of 723 K and brown is at a higher temperature of 773 K. Pressures of reactants and products are:  $P(\text{C}_3\text{H}_8) = 0.64$  bar,  $P(\text{H}_2) = 0.36$  bar, and  $P(\text{C}_3\text{H}_6) = 0.11$  bar.

The rate of propylene production reflects the result of the interplay between activation barriers and surface poisoning. It is seen that  $\text{CuHf}_1$  is the most reactive catalyst ( $191 \text{ s}^{-1}$  at  $T =$

723 K;  $3576 \text{ s}^{-1}$  at  $T = 773 \text{ K}$ ) among the four for propylene production (Figure 6.6), although only a small portion of its active sites are available for dehydrogenation. More importantly, this single-atom alloy catalyst is markedly more reactive than Pt(111) ( $8.8 \text{ s}^{-1}$  at  $T = 723 \text{ K}$ ;  $108 \text{ s}^{-1}$  at  $T = 773 \text{ K}$ ) on a per active site basis, which suggests its potential to replace the currently-used Pt-based catalysts. CuIr<sub>1</sub> and CuRh<sub>1</sub>, on the other hand, demonstrate comparable propylene formation rates to Pt(111) ( $2.6 \text{ s}^{-1}$  at  $T = 723 \text{ K}$  and  $28.2 \text{ s}^{-1}$  at  $T = 773 \text{ K}$  for CuRh<sub>1</sub>;  $3.0 \text{ s}^{-1}$  at  $T = 723 \text{ K}$  and  $50.9 \text{ s}^{-1}$  at  $T = 773 \text{ K}$  for CuIr<sub>1</sub>), which are also significantly lower than that observed on CuHf<sub>1</sub>. These lower reaction rates are highly aligned with the higher transition state free energies as observed in Figure 6.3.

Single-atom alloy catalysts offer many advantages that conventional monometallic catalysts (e.g. Pt) do not possess. For example, the inherent geometric constraint (i.e. small ensemble size) of single-atom alloys prevents them from engaging in unwanted side reactions such as C-C bond breaking and deep-dehydrogenation, which would typically occur on extended active surfaces.<sup>14,15</sup> Such side reactions could lead to diverse serious issues, including carbon coking and subsequent catalyst deactivation. Moreover, even though propylene dehydrogenation could take place on CuHf<sub>1</sub>, the resulting CH<sub>2</sub>CHCH<sub>2</sub> intermediate cannot proceed even further to form CH<sub>2</sub>CHCH. Hence, deep dehydrogenation is not an issue on CuHf<sub>1</sub>, let alone other single-atom alloys which offer weaker stabilization to the surface species. Lastly and most importantly, CuHf<sub>1</sub> is much more reactive than the pure Pt catalyst on a per active site basis, and the other two SAA catalysts (CuIr<sub>1</sub> and CuRh<sub>1</sub>) also possess similar propylene production rates to Pt(111). Not only are these Cu-based alloy catalysts much cheaper than the monometallic Pt catalysts for the efficient use of precious metals, but they also attain similar catalytic reactivity and higher selectivity in our

modelling. Cu-based dilute alloys could therefore be seen as a versatile and efficient class of catalytic materials for the challenging alkane activation reactions.

### 6.3.6 Catalyst Stability under Reaction Conditions

Besides catalytic reactivity and selectivity, attention should also be drawn to the stability of the single-atom alloys under high temperature conditions in propane dehydrogenation. Often times, Cu catalysts suffer from sintering at high temperatures, which results in loss of reactivity.<sup>52,53</sup> However, several previous studies have revealed that this situation could be effectively suppressed when a highly dilute amount of dopant is introduced into Cu.<sup>54,55</sup> In addition to Cu sintering, concern is often raised regarding the surface restructuring (i.e. segregation and aggregation) of the single-atom alloy catalysts, especially in the presence of surface adsorbates and under reaction conditions. Microkinetic modeling indicates that the surfaces of CuHf<sub>1</sub> and CuIr<sub>1</sub> (Figure 6.5) are populated by CH<sub>2</sub>CHCH<sub>2</sub> and H atoms, respectively, even at high temperature. Due to the adsorbate-dopant bonds, the existence of these surface species can help stabilize the active dopants in the surface layer,<sup>47,48</sup> despite segregation is a slightly endothermic process for them in the case of the bare surface. Furthermore, one should still attain a significant propylene production rate on CuHf<sub>1</sub> even if the reaction temperature is lowered (note that the gaseous species pressures need to be changed accordingly to ensure that the reaction remains exergonic at the reduced temperature) due to the high reaction rates seen in Figure 6.6. This change in temperature could reduce the energy for the active dopant to diffuse back into the subsurface layer, in addition to minimizing Cu sintering. CuIr<sub>1</sub>, on the other hand, possesses similar segregation and aggregation energies as CuRh<sub>1</sub>. In a previous reactor study, it was observed that CuRh<sub>1</sub> remains stable for 50 hours during propane dehydrogenation at a reaction temperature of 623 K.<sup>55</sup> Since the strong binding of H atoms on CuIr<sub>1</sub>, which is not seen in the case of CuRh<sub>1</sub>,

could help position the active dopants in the surface layer, CuIr<sub>1</sub> is expected to demonstrate similar stability at an even higher temperature. As for aggregation, both CuHf<sub>1</sub> and CuIr<sub>1</sub> do not show a tendency to form large active ensembles on the surfaces based on the aggregation energies observed. This scenario of aggregation could be further restrained by strictly controlling the amount of dopant that one is going to put into Cu. Nevertheless, reactor studies are still required to ascertain the stability (and activity) of these alloy catalysts under alkane dehydrogenation conditions.

### 6.3.7 Origin of Catalytic Activity

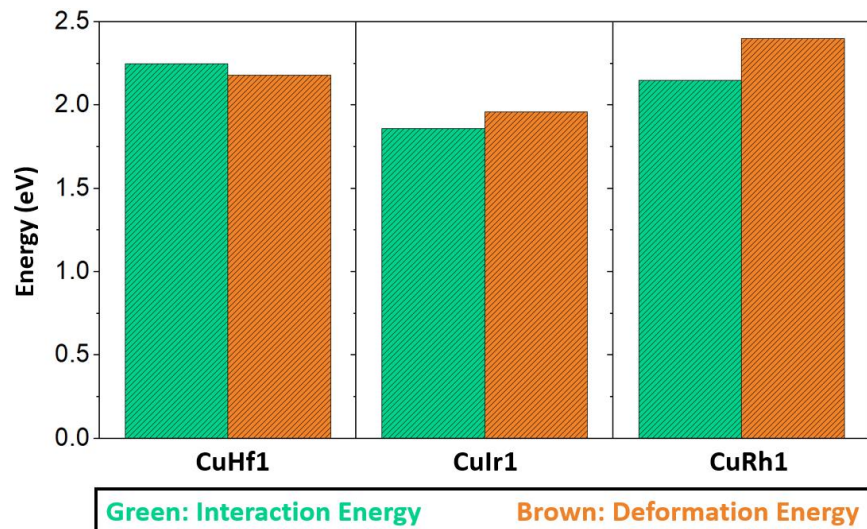


Figure 6.7. Energy of interaction (absolute value, green) between propane and the surface in the geometry of the transition states for initial C-H bond cleavage, and energy of deformation (brown) of propane in the same transition state geometry.

The catalytic activity of the three single-atom alloys is related to the free energies of the most rate-limiting transition states in the respective more favorable pathways. An energy decomposition scheme,<sup>148</sup> which focuses on the first C-H bond cleavage transition states, was employed to elucidate the magnitude difference. It is understood that on CuRh<sub>1</sub>, the transition state for H-migration is significantly more rate-controlling than that for C-H bond breaking.

Nevertheless, this study is still useful for the following reasons: (1) these C-H bond breaking transition states themselves play a significant role in controlling the reaction rates (Figure 6.4), and (2) the free energy of the “CH<sub>3</sub>CHCH<sub>3</sub> + H” state, which is the initial state for H-migration on CuRh<sub>1</sub>, is correlated to the C-H bond breaking transition state based on the Bronsted-Evans-Polanyi relation. To elaborate, the latter indicates that the high intermediate state of “CH<sub>3</sub>CHCH<sub>3</sub> + H”, which in turn results in the elevated H-migration transition state, can be reflected in the high C-H bond cleavage transition state. From our perspective, an analysis performed in this manner ensures a fair comparison across the single-atom alloy catalysts.

This energy decomposition scheme separates the electronic energy of the transition states into the contributions from the interaction energy between propane and the catalyst surfaces in the constrained geometry of the transition state, and from the distortion energy of propane in that same transition state geometry.<sup>148</sup> It is seen that the interaction energy in the structure of the transition states is the strongest for CuHf<sub>1</sub>, followed by CuRh<sub>1</sub>, and CuIr<sub>1</sub> (Figure 6.7). Additionally, CuHf<sub>1</sub> is also the only alloy catalyst among the three tested for which the deformation energy of the transition state is lower than the absolute value of the interaction energy. The strong interaction and the relatively small deformation of the transition state on CuHf<sub>1</sub> help explain the high reaction activity observed. Although the interaction between the surface species and CuRh<sub>1</sub> is much stronger than that with CuIr<sub>1</sub>, they exhibit rather similar catalytic activity. The reason behind this seeming contradiction is the deformation of the transition state on CuRh<sub>1</sub>, which is significantly larger than the interaction with the CuRh<sub>1</sub> surface. Hence, the positive effect linked with the interaction with CuRh<sub>1</sub> is cancelled out. Before wrapping up, it should be noted that the metal slabs are also deformed in the presence of the surface adsorbates. However, their deformation energy

magnitudes ( $\leq 0.15$  eV) and the differences among catalysts ( $\leq 0.04$  eV) are small, which make them less useful in the comparison of the transition state free energies.

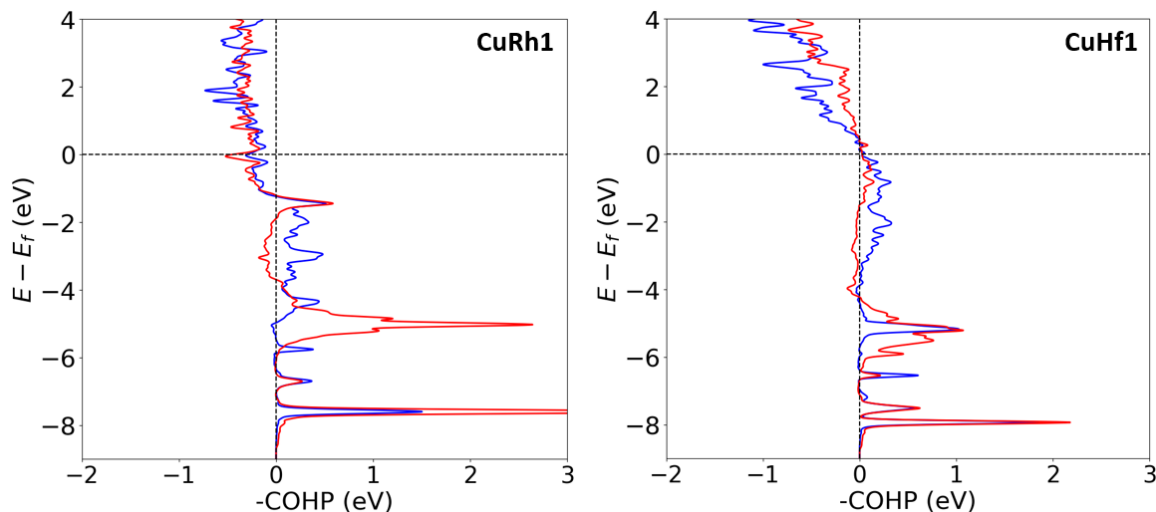


Figure 6.8. Crystal Orbital Hamilton Population (COHP) for the interactions between the dopants (Hf and Rh) alloyed in Cu(111) and the C (blue) or H (red) atoms in the transition states associated with the first C-H bond cleavage producing  $\text{CH}_3\text{CHCH}_3$ .

A COHP analysis was performed to understand the strong stabilization of the rate-limiting transition state on  $\text{CuHf}_1$  from a chemical bond perspective (Figure 6.8). Since the preferred pathway on  $\text{CuHf}_1$  and  $\text{CuRh}_1$  is the same (i.e. forming propylene via  $\text{CH}_3\text{CHCH}_3$ ), and the transition states for breaking the first C-H bond in propane adopt similar adsorption configurations on the two surfaces, a COHP curve was also constructed for  $\text{CuRh}_1$  to enable a comparison. It is worth noting that a portion of the antibonding orbitals (with negative -COHP values) between the Rh dopant and the two atoms (C and H) participating in the bond-breaking step is below the Fermi level (i.e. occupied). This filling of the anti-bonding orbital weakens the interaction between the transition state and the active dopant. Although the anti-bonding orbital between H and Rh is partially filled, the strong interaction seen for lower energy levels (around 8 eV and 5 eV below Fermi level) can compensate for this destabilization effect. Altogether, the energy integrated

ICOHP value for occupied states, characterizing the strength of the bond, is -1.56 between H and Rh and -1.41 between C and Rh. In contrast to CuRh<sub>1</sub>, the anti-bonding orbitals are seen to be above the Fermi level in almost their entirety for CuHf<sub>1</sub>, a strengthening factor for the bond between transition state and surface. The more electropositive character of Hf versus Rh pushes the d states at higher energy, and therefore also the antibonding combination with the adsorbate states. The total ICOHP between Hf and C is -2.16, much stronger than in the case of Rh. The ICOHP value between H and Hf, on the other hand, is -1.22; this interaction is somewhat weaker than the case of Rh, from the difference in lower bonding energy states. Altogether, the binding of the rate-limiting transition state as a whole is still stronger on the CuHf<sub>1</sub> surface, in line with the lower energy of the transition state and with the higher propylene production rate. This method of diluting different active elements into the Cu metal host can be subsequently seen as an effective approach to shift the position of the anti-bonding orbitals between transition state and surface relative to the Fermi level, and tune the reactivity for propane dehydrogenation.

## 6.4 Conclusion

DFT calculations and microkinetic modeling have been performed in a synergistic manner to explore dilute alloy catalysts with Cu as a host metal for the propane dehydrogenation reaction. In prior research, CuRh<sub>1</sub>, where Rh monomers are dispersed in Cu, has been recognized as an active and selective catalyst for that reaction.<sup>55</sup> Our present study extends this knowledge by showing that CuIr<sub>1</sub> also possesses comparable catalytic performance. Surprisingly, C-H bond breaking steps do not exclusively dictate the dehydrogenation rates on these two dilute alloys, contrary to what is typically observed on monometallic catalysts. In addition, the migration by spillover of H atoms away from the dehydrogenated intermediates also plays a pivotal role in controlling the reaction rates, and this is especially true for CuRh<sub>1</sub>. The possibility of dehydrogenating propyl in the

presence of the H atom at the active center was also explored to examine if the rate-limiting H-migration steps can be avoided. Nevertheless, this pathway is demonstrated to be less favorable. Hence, for propane dehydrogenation on single-atom alloys, the steps of species migration on the host metal, in addition to C-H bond activation, also warrant one's attention.

Besides CuIr<sub>1</sub>, CuHf<sub>1</sub> is also predicted to be capable of performing propane dehydrogenation to produce propylene. Compared to CuIr<sub>1</sub> and CuRh<sub>1</sub>, this catalyst is shown to possess a higher rate for propylene formation, despite the fact that some of the active sites are occupied by the dead-end over-dehydrogenated intermediate CH<sub>2</sub>CHCH<sub>2</sub>. More importantly, its calculated reactivity is even higher than that of the Pt catalyst on a per active site basis, making it an attractive candidate for experimental validation. Within expectation, the low free energy of the rate-limiting transition state and hence the high reaction rate on CuHf<sub>1</sub> is attributed to the significant interaction energy between the adsorbate and the surface, which is larger than the transition state deformation energy. COHP analysis further indicates that this strong interaction is a consequence of the depletion of the anti-bonding orbitals between Hf and the two atoms (C and H) participating in the bond-cleavage event of propane. The approach of shifting these anti-bonding orbitals above the Fermi level by dispersing different active elements into the Cu host could hence be used in the rational design of other alloy catalysts for reactive propane dehydrogenation.

Before concluding, it is emphasized that the reactivity of both CuHf<sub>1</sub> and CuIr<sub>1</sub> is not their sole advantageous attribute. Their intrinsic geometric configurations, characterized by isolated active atoms on the surface, play a pivotal role in mitigating undesired side reactions and inhibiting coke formation – a phenomenon which typically requires larger active ensembles. Consequently, these novel alloy catalysts exhibit remarkable stability and exceptional selectivity for propylene

formation. Single-atom alloys could therefore be seen as a promising class of catalytic materials for reactive and selective propane dehydrogenation, and they hold significant potential for advancing current industrial applications.

## Chapter 7 Conclusion

Through this dissertation, we performed DFT calculations in conjunction with microkinetic modeling techniques to explore the catalytic performance of highly dilute alloy catalysts in (de)hydrogenation reactions. In employing this comprehensive approach, not only did we establish the selective nature of these alloy catalysts, but we also elucidated the underlying mechanisms driving their selectivity. These outcomes contribute significantly to the comprehension of the catalytic behavior of the dilute alloy catalysts and broaden their potential applications in the scientific community.

We begin our concluding Chapter by revisiting the selective hydrogenation of alkynes to produce alkenes over the dilute Pd-in-Au alloy catalyst. In this work, our combined theoretical and experimental study shows that the sizable free energy barrier for H<sub>2</sub> dissociation on the surface of Pd<sub>1</sub>Au plays a major role in controlling the activity and selectivity of 1-hexyne hydrogenation. Specifically, our Gibbs free energy-based analysis and first-principles microkinetic simulations show that H<sub>2</sub> dissociation is the rate-limiting process for 1-hexyne hydrogenation on Pd<sub>1</sub>Au(111), while the C-H bond formation steps proceed with lower barriers. Somewhat more surprisingly, the sizable H<sub>2</sub> dissociation barrier also favorably impacts the selectivity for partial hydrogenation to 1-hexene because it slows down the undesired over-hydrogenation to hexane, as confirmed by our DSC analysis.

This major role of H<sub>2</sub> dissociation in the kinetic control of 1-hexyne hydrogenation on dilute Pd-in-Au catalysts markedly contrasts with previously studied extended Pd catalysts, on which the addition of atomic H to the adsorbed alkyne or alkenyl is accepted to be the rate-determining step, and the selectivity is controlled by competitive adsorption of alkyne and alkene. On Pd<sub>1</sub>Au, however, the selectivity is controlled instead by competition of hydrogenation rates of alkyne and

alkene, which does not depend on reaction conversion. Hence, the energetics and kinetics of the 1-hexyne hydrogenation mechanism over dilute Pd-in-Au alloy are distinct with respect to bulk Pd catalysts.

Another key property of dilute Pd-in-Au alloys is that the adsorption energy of hydrocarbon species is moderate, so that the coverage of Pd sites by these hydrocarbon intermediates is low, enabling access and activation of H<sub>2</sub> and preventing poisoning and coking of the catalysts. Once again, this is different from extended Pd catalysts, on which hydrocarbon species exhibit strong binding and have the potential to form coke at high coverage, thus deactivating the catalyst. The apparent activation enthalpies and reaction orders for dilute Pd-in-Au obtained from our microkinetic modeling align well with previous experiments, despite a temperature shift of approximately 60 K. This temperature variation is attributed to the slight overestimation of the adsorption energies of surface species when the xc-functional optPBE-vdW is used. In summary, this study remarkably illustrates that the enhanced selectivity of the dilute Pd-in-Au alloy catalyst arises from two key factors: the significant barrier for H<sub>2</sub> dissociation and the small barrier for C-H bond formation from 1-hexyne to 1-hexenyl (which is smaller than that for C-H bond formation from 1-hexene to 1-hexyl). The formation of dilute active species in a less active host metal can therefore be seen as a way to tune the binding energy of reactants, alter reaction profiles, and induce distinct kinetic behaviors for an optimal catalytic activity and selectivity. This concept of dilute alloy catalyst is hence a versatile approach to design highly selective heterogeneous catalysts.

Next, we shift our focus from 1-hexyne hydrogenation to 1-hexene hydrogenation/isomerization. By combining isotope-exchange experiments, DFT calculations, and microkinetic modeling, hexene isomerization and hydrogenation on a dilute Pd-in-Au alloy catalyst is shown to take place via the same Horiuti-Polanyi mechanism as on a monometallic Pd

surface. H<sub>2</sub> dissociation and H-spillover onto the Au host are also demonstrated to be the rate- and selectivity-limiting elementary steps in the reaction mechanism, which hinders the hydrogenation reaction. Once more, this is distinct from the common assumption that the enhanced alkene selectivity of Pd alloys originates from the weakening of the alkene adsorption energies. It is emphasized that hexene adsorption and H<sub>2</sub> dissociation cannot occur on the same Pd site, thus H-migration is a key step in hexene conversion on the dilute alloys. These results help shed light on the future design of more efficient alloy catalysts for alkyne and alkene hydrogenation.

Building upon our investigation of isolated Pd atoms on Au(111), we further examined larger Pd ensembles (Pd<sub>2</sub> and Pd<sub>3</sub>) to ascertain their potential for augmenting the hydrogenation rates of alkynes while preserving the desired selectivity. Regrettably, our findings suggest that they do not fulfill this objective. To be more specific, our DFT calculations reveal that isolated Pd atoms in Au(111) exhibit notably higher reactivity when compared to larger Pd ensembles (i.e. Pd<sub>2</sub> and Pd<sub>3</sub>) on the same Au surface. The diminished reactivity of Pd<sub>2</sub> and Pd<sub>3</sub> is attributed to surface poisoning by the strongly bound acetylene molecule, resulting in challenging and highly rate-limiting H<sub>2</sub> dissociation to provide H atoms for the reaction. Conversely, Pd<sub>1</sub> demonstrates a moderate binding strength for acetylene, allowing for the presence of vacant active sites for H-atom generation. Hence, in experiments, an optimum Pd concentration in Au should strike a balance between a high concentration of Pd monomers and a high segregation of Pd atoms to the surface. The Au<sub>0.96</sub>Pd<sub>0.04</sub> catalyst appears to achieve this balance; its higher Pd concentration compared to Au<sub>0.98</sub>Pd<sub>0.02</sub> promotes the segregation of Pd atoms to the surface, while the concentration is still low enough to inhibit the significant formation of larger Pd ensembles, as is the case in Au<sub>0.91</sub>Pd<sub>0.09</sub>.

Now we transition to another reaction: the selective hydrogenation of unsaturated aldehydes (acrolein) to produce unsaturated alcohols (propenol) on Cu-based dilute alloy catalysts. In this

work, the segregation and aggregation energies of a collection of transition metals in Cu(111) were first computed to assess the practicality of synthesizing such catalysts in experiments. Out of these alloy combinations, early transition metals Ti, Zr, and Hf; mid-transition metals Cr and Mn; and late-transition metals Rh, Ir, Ni, Pd, and Pt in Cu(111) are found to be realizable. The two different binding modes, namely C=O and C=C binding modes, of acrolein on these three categories of dopants were subsequently examined as a preliminary evaluation of their selectivity towards propenol formation. It is found that the early transition metal atoms in Cu(111) strongly favor the C=O binding mode of the acrolein molecule, with the magnitude of the adsorption free energies being greater than 1.5 eV. This tight interaction between the surface species and the catalyst surface is also preserved for the mono-hydrogenated intermediates, which have free energy values lower than -2.00 eV. Although this feature seems to be appealing as it could stabilize the transition states for bond formation, it is too strong such that subsequent hydrogenation and desorption steps are highly endergonic in nature. Hence, acrolein hydrogenation cannot proceed on this type of SAAs.

Mid-transition metal atoms in Cu(111) are found to be the most promising for selective acrolein hydrogenation. These metals favor the C=O binding mode over the C=C binding mode, and the binding strength is moderate. DFT calculations and microkinetic modeling demonstrate that the selectivity for propenol formation on CuCr<sub>1</sub> is controlled by three elementary steps: (1) acrolein migration from the more stable C=O binding mode to the less stable C=C binding mode, (2) H-migration to the C=C binding acrolein, and (3) formation of the O-H bond from the mono-hydrogenated intermediate. To help enhance the selectivity, high H<sub>2</sub> pressure is required as it can lower down the free energies of the steps that involve the introduction of more H atoms on the catalyst surface (e.g. the O-H bond formation step), while acrolein diffusion step remains unaffected and the H-migration step less impacted. It is important to note that the inherent

inaccuracies in DFT calculations might affect the computed selectivity. Therefore, one could only propose that it is highly probable that selective acrolein hydrogenation could be carried out on CuCr<sub>1</sub>. The same also holds true for another mid-transition metal, Mn, and they should be the first systems to be investigated in experiments.

Lastly, late-transition metals in Cu(111) are unlikely to selectively hydrogenate acrolein. These metals exhibit a preference for the C=C binding mode over the C=O binding mode, thereby eliminating the need for molecular migration to produce the undesired product propanal. In addition, the transition states for propenol formation are found to be higher than those for propanal formation on CuNi<sub>1</sub>, which is the late-transition metal that has the smallest energy difference between the two different binding modes of acrolein. This result shows that CuNi<sub>1</sub> cannot selectively hydrogenate acrolein, let alone other late-transition metals, which possess even greater energy differences between the two binding modes. Nevertheless, unsaturated aldehydes with substituents attached to the C=C bond might possess higher selectivity as the presence of the substituents could destabilize the transition states in C=C bond hydrogenation and facilitate the desorption of the unsaturated alcohols.

The findings underline that while the simple descriptor of a preferred C=O adsorption mode of the unsaturated aldehydes is contributing, it is not solely sufficient to guarantee a high selectivity toward unsaturated alcohols. Rather, the magnitude of the migration barrier between the two binding modes is also crucial in inhibiting access to the generally more reactive hydrogenation of the C=C bond. The trends presented in this study offer important insights into the properties that a specific single-atom alloy catalyst should possess for the selective hydrogenation of various  $\alpha,\beta$ -unsaturated aldehydes. Dilute alloy catalysts appear as a versatile platform for adjusting the binding strength of intermediates and transition states, thereby allowing control over catalytic

activity and selectivity.

In addition to the selective hydrogenation of acrolein, propane activation was also explored on the Cu-based dilute alloy catalysts. In prior research, CuRh<sub>1</sub> has been recognized as an active and selective catalyst for that reaction.<sup>55</sup> Our present study extends this knowledge by showing that CuIr<sub>1</sub> also possesses comparable catalytic performance. Surprisingly, contrary to what is typically observed on monometallic catalysts, C-H bond breaking steps are not the only rate-limiting steps in the reaction mechanisms on these two alloy catalysts. Rather, the migration by spillover of H atoms away from the dehydrogenated intermediates also plays a crucial role in determining the reaction rates, and this is especially true for CuRh<sub>1</sub>. To avoid proceeding through these rate-limiting H-migration steps, it might be possible to keep the H atoms on the same active ensemble while cleaving the second C-H bond in propyl. Nevertheless, this pathway is shown to be even less favorable. Hence, for propane dehydrogenation on single-atom alloys, the steps of species migration on the host metal, in addition to C-H bond activation, also warrant one's attention.

Besides CuIr<sub>1</sub>, CuHf<sub>1</sub> is also predicted to be capable of performing propane dehydrogenation to produce propylene. Compared to CuIr<sub>1</sub> and CuRh<sub>1</sub>, this catalyst is shown to possess a higher rate for propylene formation, despite the fact that some of the active sites are covered by the dead-end over-dehydrogenated intermediate CH<sub>2</sub>CHCH<sub>2</sub>. More importantly, its calculated reactivity is even higher than that of the Pt catalyst on a per active site basis, making it an attractive candidate for experimental validation. As confirmed by the chemical bonding analysis, the high propylene production rate is a consequence of the depletion of the anti-bonding orbitals between Hf and the two atoms (C and H) in the most rate-limiting transition state (i.e. first C-H bond cleavage in propane) in the reaction network, which results in the strong stabilization of this transition state and a lower activation barrier. The approach of shifting these anti-bonding orbitals above the Fermi

level by dispersing different active elements into the Cu host could hence be used in the rational design of other alloy catalysts for reactive propane dehydrogenation.

Eventually, it is emphasized that the reactivity of both CuHf<sub>1</sub> and CuIr<sub>1</sub> is not their sole advantageous attribute. Their intrinsic geometric configurations, characterized by isolated active atoms on the surface, play a pivotal role in mitigating undesired side reactions and inhibiting coke formation – a phenomenon which typically requires larger active ensembles. Consequently, these novel alloy catalysts exhibit remarkable stability and exceptional selectivity for propylene formation. Single-atom alloys could therefore be seen as a promising class of catalytic materials for reactive and selective propane dehydrogenation, and they hold significant potential for advancing current industrial applications.

In conclusion, our research endeavor has demonstrated the capability of single-atom alloy catalysts in achieving high selectivity in various (de)hydrogenation reactions. Through rigorous experimentation and analysis, we have shown that these catalysts offer opportunities for meticulous regulation and fine-tuning of reaction pathways, thereby enabling the engineering of them for the desired outcomes. As we move forward, the utilization of single-atom alloy catalysts holds great promise for advancing the field of catalysis, offering tailored solutions for diverse chemical transformations.

## Appendix A Supplementary Information for Chapter 2

### A.1 Supplementary Energetics and Adsorption Configurations

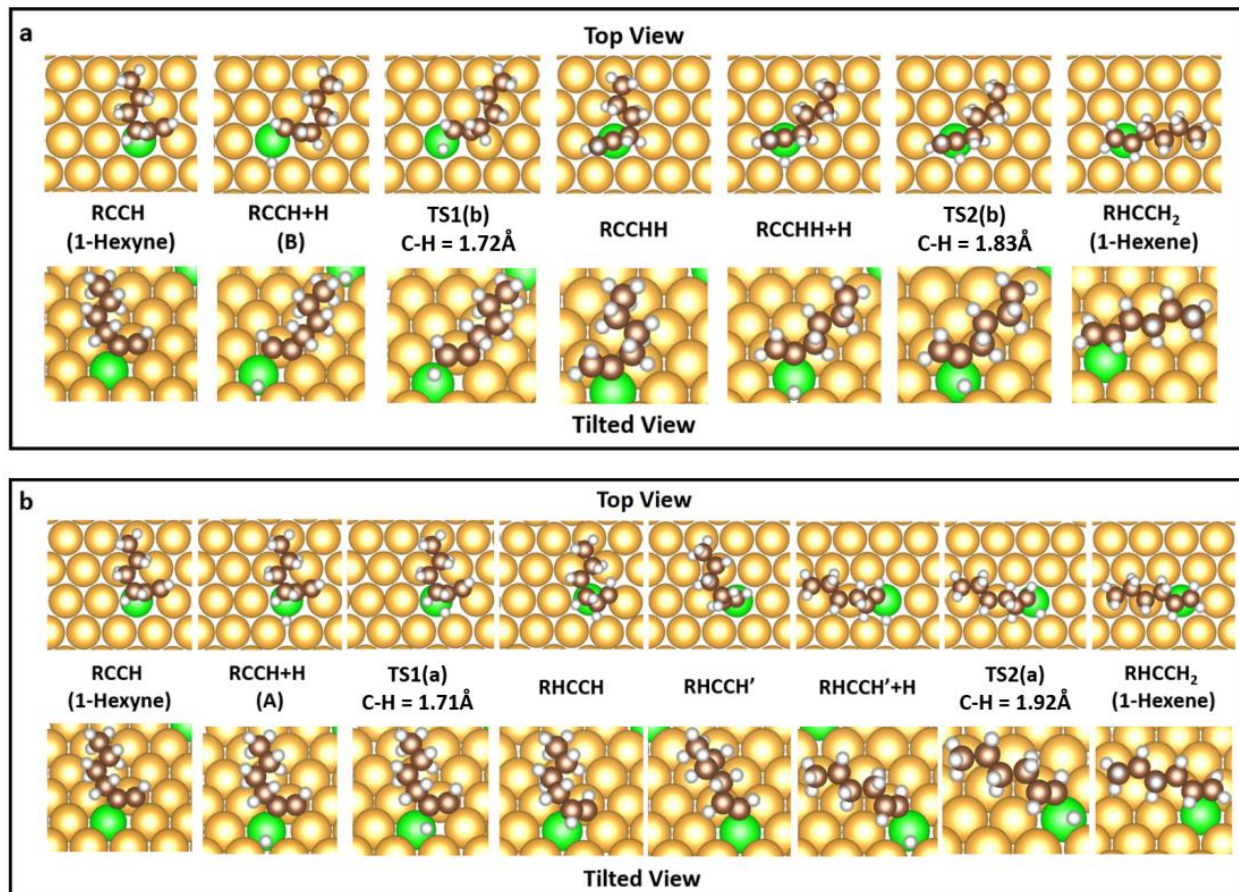


Figure A.1. Adsorption configuration of the carbonaceous intermediates on Pd<sub>1</sub>Au(111) for (a) the hydrogenation of the terminal carbon atom (C<sub>1</sub>) in the first reaction step, followed by the hydrogenation of the carbon atom attached to the butyl group (C<sub>2</sub>) and for (b) the hydrogenation of C<sub>2</sub> in the first step, followed by the hydrogenation of C<sub>1</sub>.

Table A.1. Free energy values for 1-hexene hydrogenation to form hexane. The same reference for 1-hexyne hydrogenation was used, i.e. 1-hexyne and H<sub>2</sub> in the gas phase. Conditions are: T = 363 K, P(H<sub>2</sub>) = 0.2 bar, P(C<sub>6</sub>H<sub>10</sub>) = 0.01 bar, P(C<sub>6</sub>H<sub>12</sub>) = P(C<sub>6</sub>H<sub>14</sub>) = 0.001 bar.

States	Free Energy (eV)
RHCCH <sub>2</sub> (1-Hexene)	-1.42
TS (H atom to RHCCH <sub>2</sub> )	-0.56
RHCCH <sub>2</sub> + H (To form 1-Hexyl)	-0.96
RHCCH <sub>2</sub> + H (To form 2-Hexyl)	-0.91
TS (To form 1-Hexyl)	-0.65
TS (To form 2-Hexyl)	-0.56
RH <sub>2</sub> CCH <sub>2</sub> (1-Hexyl)	-1.33
RHCCH <sub>3</sub> (2-Hexyl)	-1.29
TS (H atom to RH <sub>2</sub> CCH <sub>2</sub> )	-0.47
TS (H atom to RHCCH <sub>3</sub> )	-0.43
RH <sub>2</sub> CCH <sub>2</sub> + H	-0.95
RHCCH <sub>3</sub> + H	-0.95
TS (From RH <sub>2</sub> CCH <sub>2</sub> + H)	-0.74
TS (From RHCCH <sub>3</sub> + H)	-0.79
Hexane	-2.22
Hexane (g)	-2.56

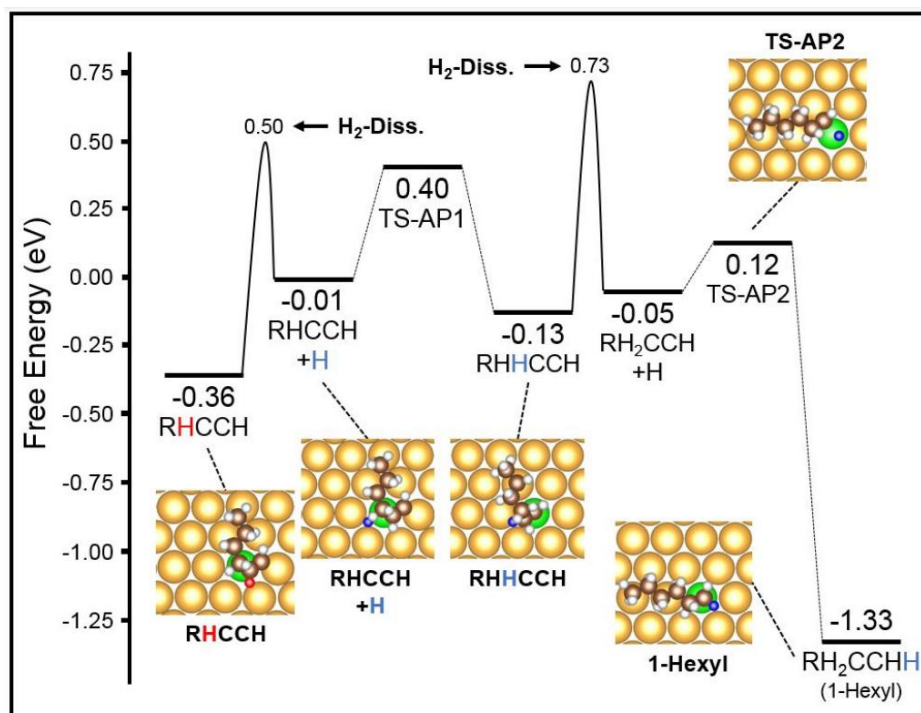
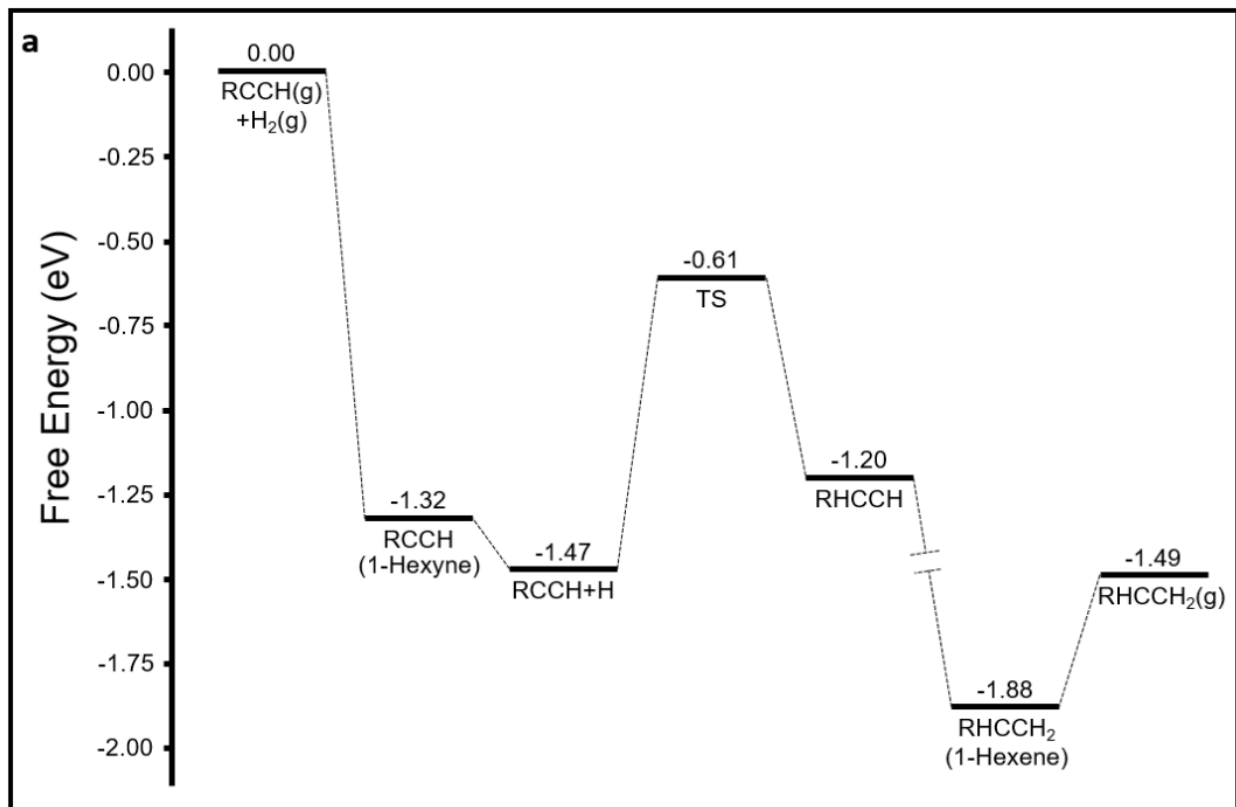


Figure A.2. Free energy diagram of 1-hexyl formation via 1-hexylidene on the Pd<sub>1</sub>Au(111) surface.

The C<sub>2</sub> atom was chosen in the first place for the over-hydrogenation as there is electron donation from the carbon chain to help stabilize the transition state. The barrier for the forward hydrogenation of 1-hexylidene (RHCCH) is 0.33 eV higher than the reverse barrier. In addition, this side-pathway has an overall free energy barrier (1.09 eV) that is at least 0.26 eV higher than that of the regular pathway to form 1-hexyl via 1-hexene (0.83 eV). Hence, this pathway is energetically unfavorable and is unlikely to deteriorate the selectivity for 1-hexene formation. Conditions are: T = 363 K, P(H<sub>2</sub>) = 0.2 bar, P(C<sub>6</sub>H<sub>10</sub>) = 0.01 bar, P(C<sub>6</sub>H<sub>12</sub>) = P(C<sub>6</sub>H<sub>14</sub>) = 0.001 bar.



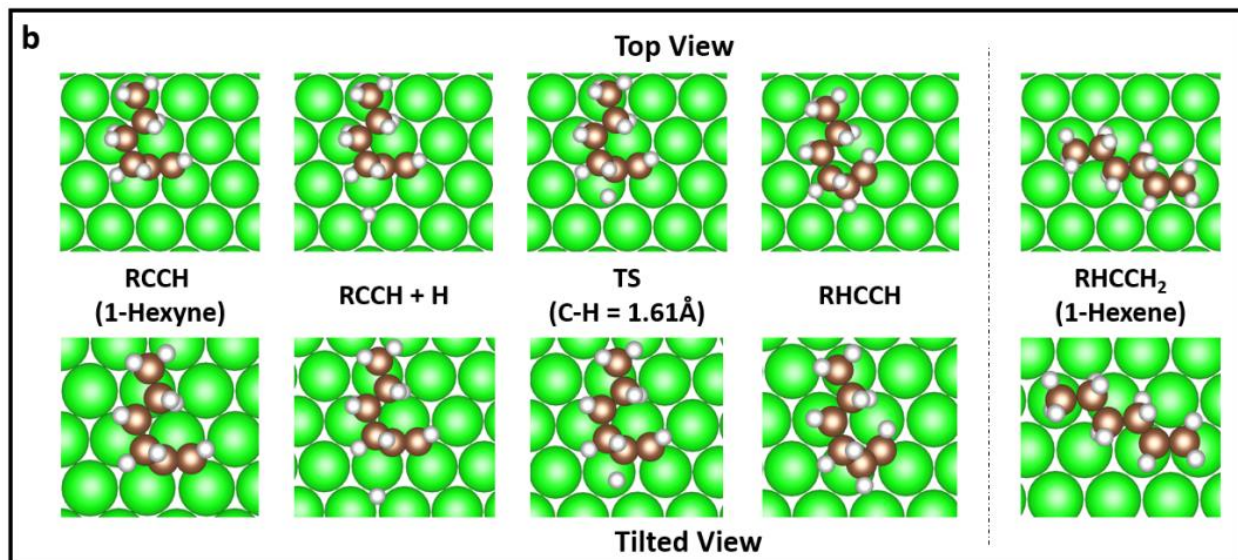


Figure A.3. (a) Free energy diagram and (b) the corresponding configurations of 1-hexyne hydrogenation to form 1-hexene on Pd(111). The butyl group attached to C≡C bond is abbreviated as R. For simplicity, only the first hydrogenation step is detailed. Reaction conditions are: T = 363 K, P(H<sub>2</sub>) = 0.2 bar, P(C<sub>6</sub>H<sub>10</sub>) = 0.01 bar, P(C<sub>6</sub>H<sub>12</sub>) = P(C<sub>6</sub>H<sub>14</sub>) = 0.001 bar. All species are chemisorbed, unless indicated by (g) for gas phase species.

## A.2 Detailed Description of the Microkinetic Model

Table A.2. Kinetic parameters, Gibbs free energies of reaction and activation derived from DFT-computed electronic energies evaluated at 363 K and standard pressure (1 bar). The n-butyl tail of gaseous and adsorbed C<sub>6</sub> species is denoted as “R”. Hydrogen atoms co-adsorbed with carbonaceous intermediates are indicated as (H).

#	Elementary step	$\Delta G^\circ$ (eV)	$\Delta G_{\text{fwd}}^{\ddagger}$ (eV)	$k^{\text{fwd}}$ (s <sup>-1</sup> )	$k^{\text{rev}}$ (s <sup>-1</sup> )
1	$\text{Pd}_1 + \text{H}_{2(\text{g})} \rightleftharpoons \text{H}_2 - \text{Pd}_1$	0.28	N/A	$6.92 \times 10^8$	$6.07 \times 10^{12}$
2	$\text{H}_2 - \text{Pd}_1 \rightleftharpoons \text{PdH}_2$	0.22	0.52	$4.02 \times 10^5$	$4.59 \times 10^8$
3	$\text{PdH}_2 + \text{Au} \rightleftharpoons \text{PdH}_1 + \text{H} - \text{Au}$	0.20	0.26	$1.77 \times 10^9$	$1.12 \times 10^{12}$
4	$\text{PdH}_1 + \text{Au} \rightleftharpoons \text{Pd} + \text{H} - \text{Au}$	0.23	0.28	$8.71 \times 10^8$	$1.18 \times 10^{12}$
5	$\text{Pd}_1 + \text{RCCH}_{(\text{g})} \rightleftharpoons \text{RCCH} - \text{Pd}_1$	-0.09	N/A	$1.08 \times 10^8$	$5.58 \times 10^6$

6	$\text{RCCH} - \text{Pd}_1 + \text{H} - \text{Au} \rightleftharpoons (\text{H})\text{RCCH} - \text{Pd}_1 + \text{Au}$	-0.14	0.06	$1.15 \times 10^{12}$	$1.16 \times 10^{10}$
7	$(\text{H})\text{RCCH} - \text{Pd}_1 \rightleftharpoons \text{RHCCH} - \text{Pd}_1$	-0.79	0.32	$2.80 \times 10^8$	$3.30 \times 10^{-3}$
8	$\text{RHCCH} - \text{Pd}_1 + \text{H} - \text{Au} \rightleftharpoons \text{RHCCH}(\text{H}) - \text{Pd}_1 + \text{Au}$	0.03	0.06	$1.15 \times 10^{12}$	$3.38 \times 10^{12}$
9	$\text{RHCCH}(\text{H}) - \text{Pd}_1 \rightleftharpoons \text{RHCCH}_2 - \text{Pd}_1$	-1.56	0.07	$9.33 \times 10^{11}$	$2.13 \times 10^{-10}$
10	$\text{Pd}_1 + \text{RHCCH}_{2(\text{g})} \rightleftharpoons \text{RHCCH}_2 - \text{Pd}_1$	-0.15	N/A	$1.07 \times 10^8$	$8.57 \times 10^5$
11	$\text{RCCH} - \text{Pd}_1 + \text{H} - \text{Au} \rightleftharpoons \text{RCCH}(\text{H}) - \text{Pd}_1 + \text{Au}$	-0.13	0.06	$1.15 \times 10^{12}$	$1.67 \times 10^{10}$
12	$\text{RCCH}(\text{H}) - \text{Pd}_1 \rightleftharpoons \text{RCCH}_2 - \text{Pd}_1$	-0.78	0.43	$7.36 \times 10^6$	$9.75 \times 10^{-5}$
13	$\text{RCCH}_2 - \text{Pd}_1 + \text{H} - \text{Au} \rightleftharpoons (\text{H})\text{RCCH}_2 - \text{Pd}_1 + \text{Au}$	-0.16	0.06	$1.15 \times 10^{12}$	$8.09 \times 10^9$
14	$(\text{H})\text{RCCH}_2 - \text{Pd}_1 \rightleftharpoons \text{RHCCH}_2 - \text{Pd}_1$	-1.39	0.13	$1.08 \times 10^{11}$	$6.38 \times 10^{-9}$
15	$\text{RHCCH}_2 - \text{Pd}_1 + \text{H} - \text{Au} \rightleftharpoons (\text{H})\text{RHCCH}_2 - \text{Pd}_1 + \text{Au}$	-0.03	0.06	$1.15 \times 10^{12}$	$4.95 \times 10^{11}$
16	$(\text{H})\text{RHCCH}_2 - \text{Pd}_1 \rightleftharpoons \text{RH}_2\text{CCH}_2 - \text{Pd}_1$	-0.37	0.31	$4.26 \times 10^8$	$3.24 \times 10^3$
17	$\text{RH}_2\text{CCH}_2 - \text{Pd}_1 + \text{H} - \text{Au} \rightleftharpoons \text{RH}_2\text{CCH}_2(\text{H}) - \text{Pd}_1 + \text{Au}$	-0.12	0.06	$1.15 \times 10^{12}$	$2.64 \times 10^{10}$
18	$\text{RH}_2\text{CCH}_3 - \text{Pd}_1 \rightleftharpoons \text{RH}_2\text{CCH}_3 - \text{Pd}_1$	-1.26	0.22	$7.81 \times 10^9$	$2.41 \times 10^{-8}$
19	$\text{Pd}_1 + \text{RH}_2\text{CCH}_{3(\text{g})} \rightleftharpoons \text{RH}_2\text{CCH}_3 - \text{Pd}_1$	0.12	N/A	$1.06 \times 10^8$	$5.53 \times 10^9$
20	$\text{RHCCH}_2 - \text{Pd}_1 + \text{H} - \text{Au} \rightleftharpoons \text{RHCCH}_2(\text{H}) - \text{Pd}_1 + \text{Au}$	0.02	0.06	$1.15 \times 10^{12}$	$2.17 \times 10^{12}$
21	$\text{RHCCH}_2(\text{H}) - \text{Pd}_1 \rightleftharpoons \text{RHCCH}_3 - \text{Pd}_1$	-0.38	0.35	$1.14 \times 10^8$	$6.18 \times 10^2$
22	$\text{RHCCH}_3 - \text{Pd}_1 + \text{H} - \text{Au} \rightleftharpoons (\text{H})\text{RHCCH}_3 - \text{Pd}_1 + \text{Au}$	-0.15	0.06	$1.15 \times 10^{12}$	$8.42 \times 10^9$
23	$(\text{H})\text{RHCCH}_3 - \text{Pd}_1 \rightleftharpoons \text{RH}_2\text{CCH}_3 - \text{Pd}_1$	-1.26	0.16	$4.43 \times 10^{10}$	$1.37 \times 10^{-7}$
24	$\text{RHCCH} - \text{Pd}_1 + \text{H} - \text{Au} \rightleftharpoons (\text{H})\text{RHCCH} - \text{Pd}_1 + \text{Au}$	-0.11	0.06	$1.15 \times 10^{12}$	$3.69 \times 10^{10}$
25	$(\text{H})\text{RHCCH} - \text{Pd}_1 \rightleftharpoons \text{RH}_2\text{CCH} - \text{Pd}_1$	-0.13	0.40	$2.09 \times 10^7$	$3.59 \times 10^5$
26	$\text{RH}_2\text{CCH} - \text{Pd}_1 + \text{H} - \text{Au} \rightleftharpoons \text{RH}_2\text{CCH}(\text{H}) - \text{Pd}_1 + \text{Au}$	-0.40	0.06	$1.15 \times 10^{12}$	$2.87 \times 10^6$
27	$\text{RH}_2\text{CCH}(\text{H}) - \text{Pd}_1 \rightleftharpoons \text{RH}_2\text{CCH}_2 - \text{Pd}_1$	-1.28	0.16	$4.04 \times 10^{10}$	$6.47 \times 10^{-8}$

To quantitatively compare the reaction mechanism proposed from theory, microkinetic models were constructed using reaction kinetic parameters computed from the DFT energetics. In total, 27 reactions were included in the overall microkinetic model, which can be classified into 6 groups (Table A.2). In the 1<sup>st</sup> group of reactions (Reactions 1-4), a molecule of H<sub>2</sub> is adsorbed and dissociated at a vacant Pd<sub>1</sub> site. The two dissociated H atoms can then individually exchange across the Au substrate for further reaction or recombination. In the 2<sup>nd</sup> (Reactions 5-10) and 3<sup>rd</sup> group (Reactions 11-14) of reactions, a molecule of 1-hexyne is adsorbed at a vacant Pd<sub>1</sub> site and hydrogenated to 1-hexene with H atoms exchanged across the Au substrate. The C<sub>2</sub> atom is

hydrogenated first in the 2<sup>nd</sup> group of reactions, while the C<sub>1</sub> atom is hydrogenated first in the 3<sup>rd</sup> group of reactions. The forward barrier for the exchange of H from the Au substrate to the C<sub>6</sub>-containing Pd<sub>1</sub> sites was assumed to be the average of the barriers for the exchange of H from the Au substrate to the bare Pd<sub>1</sub> site and Pd<sub>1</sub>H<sub>1</sub>. In the 4<sup>th</sup> (Reactions 15- 19) and the 5<sup>th</sup> group (Reactions 20-23) of reactions, an adsorbed 1-hexene molecule is hydrogenated to form n-hexane by exchanged H. These two groups are distinguished in the same way as in the hydrogenation of 1-hexyne to 1-hexene: the C<sub>2</sub> atom is hydrogenated first in the 4<sup>th</sup> group, while the C<sub>1</sub> atom is hydrogenated first in the 5<sup>th</sup> group. Finally, in the 6<sup>th</sup> group of reactions (Reactions 24-27), the 1-hexenyl intermediate is hydrogenated to the 1-hexylidene intermediate and then to the 1-hexyl intermediate by exchanged H.

### A.3 1-Hexyne hydrogenation reactivity and selectivity at higher conversion

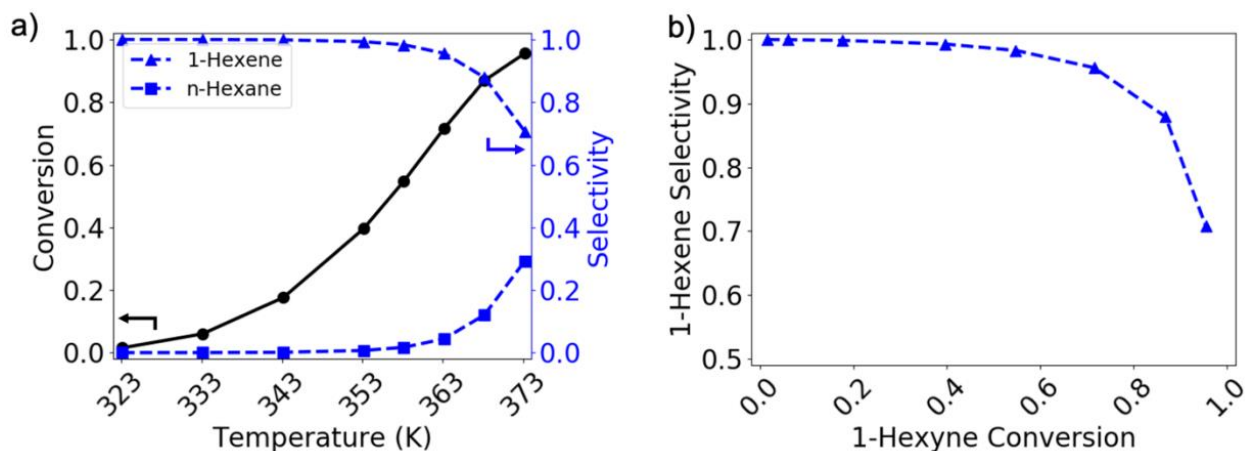


Figure A.4. Microkinetic simulations performed in the temperature range of 323-373 K at a constant inlet flow rate (50 SCCM, 20% H<sub>2</sub>, 1% 1-Hexyne, balance inert) and catalyst loading (20 mg). (a) 1-Hexyne conversion (black circles, full line), 1-hexene selectivity (blue triangles, dashed line), and 1-hexyne selectivity (blue squares, dashed line) as a function of reactor temperature. (b) 1-Hexene selectivity plotted against 1-hexyne conversion.

As a qualitative comparison to the steady state experiments of Luneau et al. at varying conversion and temperature, the reaction model (Table A.2) was embedded in an isothermal and isobaric plug-flow reactor (PFR), assumed to be operated at 1 bar. The reactant flow rate was set to 50 standard cubic centimeter per minute (SCCM, corresponding to  $T = 273.15$  K and  $P = 1$  atm), containing 20%  $H_2$ , 1% 1-Hexyne, and balance inert. The catalyst loading was set to 20 mg. The metal content of the catalyst was assumed to be 4.2 wt%. Each Pd-in-Au nanoparticle in the catalyst was assumed to be a sphere 4.9 nm in diameter, with 5% of all atoms in each particle being Pd. In the temperature range of 323 – 373 K, the conversion of 1-hexyne was found to rise from 1.5% to 95.5% (Figure A.4a). The selectivity of 1-hexene was found to be above 70% in this temperature range (Figure A.4b). The calculated relationship between selectivity and conversion agrees with the reported findings of Luneau et al.

#### A.4 Reaction Pathway Selectivity in 1-Hexyne Hydrogenation

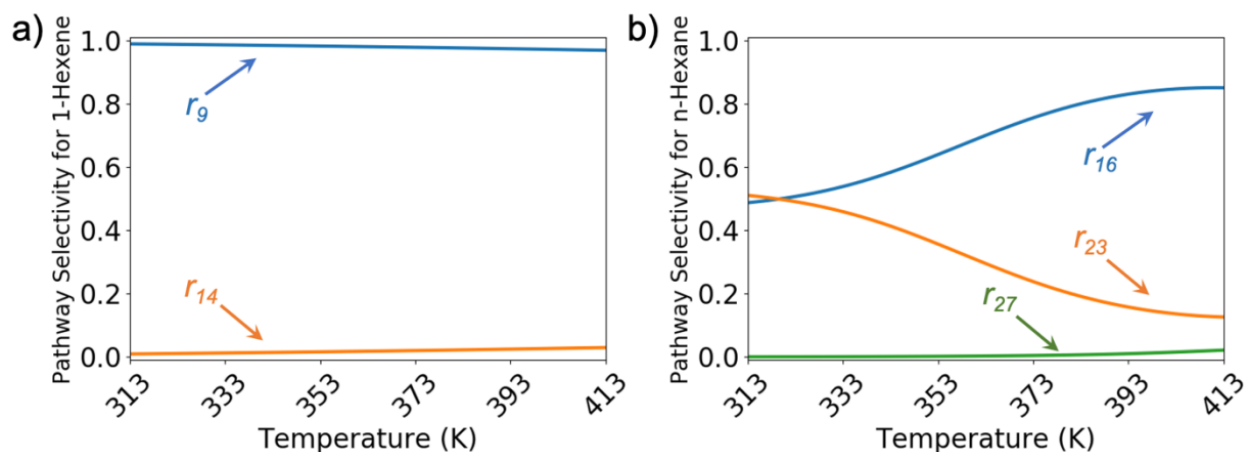


Figure A.5. Pathway selectivity for (a) the formation of 1-hexene through the hydrogenation of adsorbed 1-hexyne to 1-hexenyl ( $r_9$ , blue) and through the hydrogenation of adsorbed 1-hexyne to 2-hexenyl ( $r_{14}$ , orange), and (b) the formation of n-hexane through the hydrogenation of adsorbed 1-hexene to 1-hexyl ( $r_{16}$ , blue), through the hydrogenation of adsorbed 1-hexene to 1-hexyl ( $r_{23}$ ,

orange), and through the hydrogenation of 1-hexenyl to 1-hexylidene and then 1-hexyl ( $r_{27}$ , green).

### A.5 Degree of Rate Control of Intermediate States in the Reaction Network

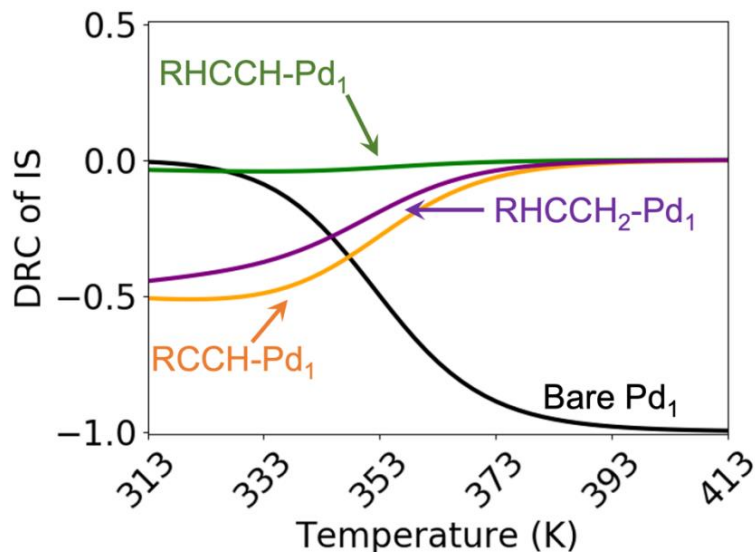


Figure A.6. The degrees of rate control of key intermediate states in the hydrogenation of 1-hexyne to 1-hexene. Adsorbed 1-hexyne (orange line) and 1-hexene (purple line) are the main rate-controlling intermediates until 353 K, largely mirroring the influence of temperature on coverages.

### A.6 Chemical Potentials

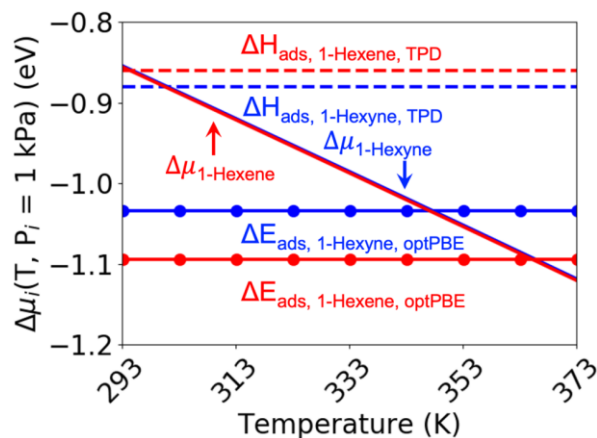


Figure A.7. The chemical potentials of 1-hexyne (blue) and 1-hexene (red) as functions of

temperature at fixed pressures (1 kPa for both 1-hexyne and 1-hexene), compared to their adsorption enthalpies measured by TPD (dashed lines) and their adsorption energies calculated by the optPBE XC functional (dots).

### A.7 Electronic Structure of Pd(111) and Pd<sub>1</sub>Au(111)

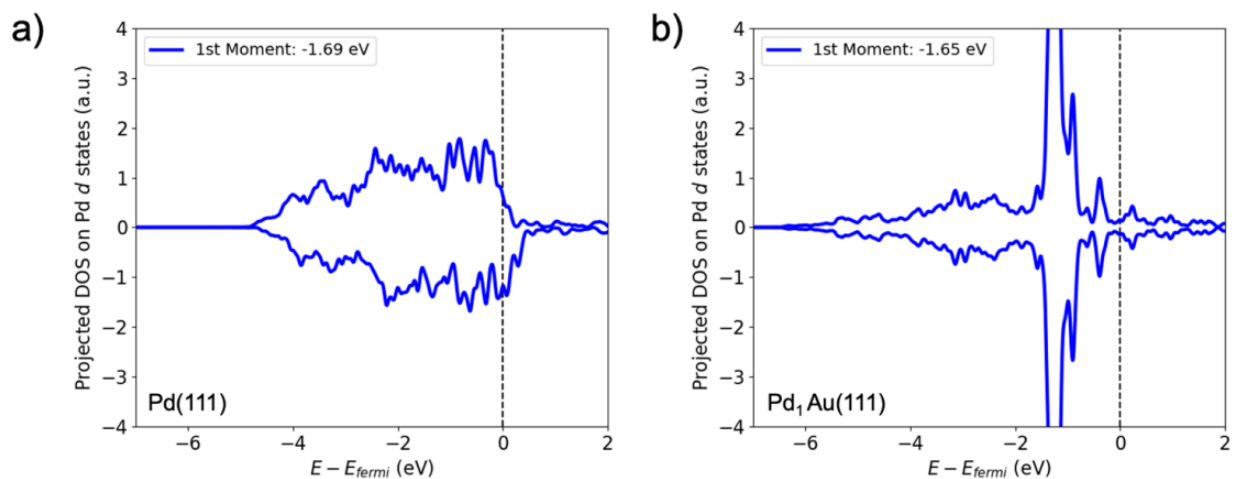


Figure A.8. Projected density of states (DOS) onto the Pd 4d orbitals of a single Pd atom on the surface of (a) Pd(111) and (b) Pd<sub>1</sub>Au(111). The first moment of the Pd 4d states (d band center) in two situations is not very different.

To qualitatively compare the electronic structure of bulk Pd and Pd<sub>1</sub>Au, we computed the projected DOS on both a single Pd atom on the surface of Pd(111) and one on the surface of Pd<sub>1</sub>Au(111) (Fig. A.8). These DOS calculations were performed in (3 · 3) cells, and the Brillouin zone integrations were performed over (9 · 9 · 1) Gamma point-centered k-point meshes. To obtain the first moment, the Pd 4d DOS was integrated from -7 eV to 2 eV relative to the Fermi level. We found that the Pd 4d band centers of the Pd atom in the two states to be very similar, at -1.69 eV for Pd(111) and -1.65 eV for Pd<sub>1</sub>Au(111); though, the shape of the Pd 4d bands are very different.

## Appendix B Supplementary Information for Chapter 3

### B.1 Experimental Results

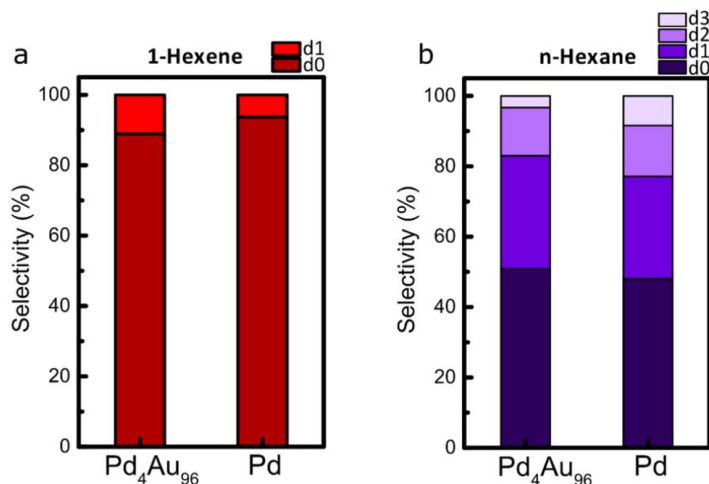


Figure B.1. Deuterium incorporation in the hexene isomers and n-hexane for the Pd<sub>4</sub>Au<sub>96</sub> and Pd catalysts. Product selectivity to (a) 1-hexene d<sub>0</sub> and d<sub>1</sub>, and (b) n-hexane d<sub>0</sub> – d<sub>3</sub>. The catalytic data were measured under steady-state conditions at 373 K (Pd<sub>4</sub>Au<sub>96</sub>) and 320 K (Pd) in 1 vol % 1-hexene and 20 vol % D<sub>2</sub> in Ar, with a total flow of 50 mL/min using a catalyst bed of 20 mg of 4.2 wt % Pd<sub>4</sub>Au<sub>96</sub> and 2 mg of 0.6 wt % Pd.

## B.2 Supplementary Adsorption Configurations

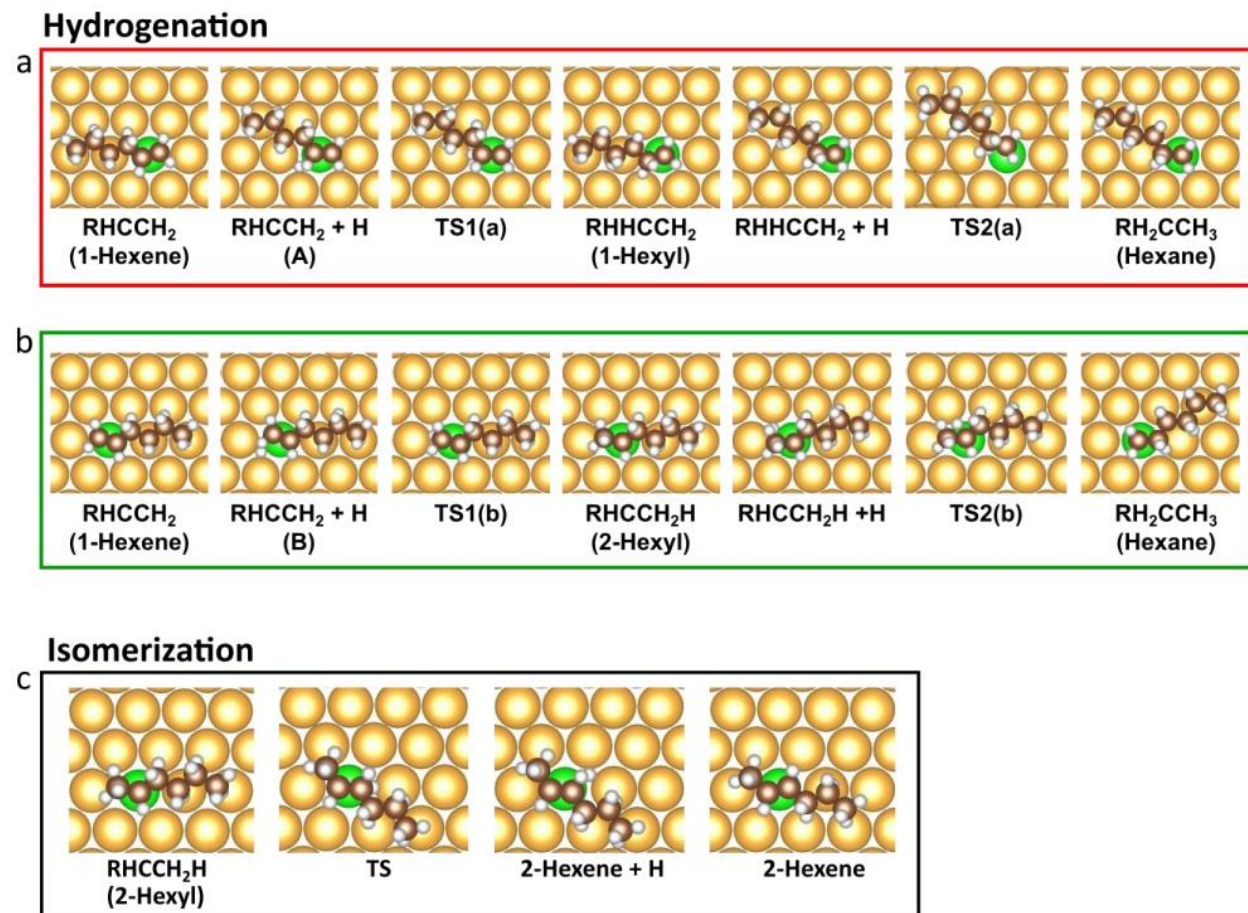


Figure B.2. Adsorption configurations of the reactant, the intermediates, and the products on Pd<sub>1</sub>Au(111) for the hydrogenation of 1-hexene to n-hexane via the 1-hexyl (a) and 2-hexyl (b) intermediates, and (c) isomerization of the 2-hexyl intermediate to 2-hexene.

## B.3 Detailed Description of Microkinetic Model

Table B.1. Kinetic rate constants, Gibbs free energies of reaction and of activation derived from DFT-computed electronic energies and evaluated at 373.15 K and standard pressure (1 bar). The n-propyl tail of gaseous and adsorbed C<sub>6</sub> species is denoted as “R”. Steps in bold indicated those not involving deuterium. No shift was applied to the barriers of H<sub>2</sub>/D<sub>2</sub>/HD dissociation or H/D spillover steps.

#	Elementary step	$\Delta G^\circ$ (eV)	$\Delta G_{\text{fwd}}^{\ddagger}$ (eV)	$k^{\text{fwd}}$ (s <sup>-1</sup> )	$k^{\text{rev}}$ (s <sup>-1</sup> )
1	$\text{Pd}_1 + \text{H}_{2(\text{g})} \rightleftharpoons \text{H}_2 - \text{Pd}_1$	0.30	N/A	6.82E+08	7.29E+12
2	$\text{H}_2 - \text{Pd}_1 \rightleftharpoons \text{PdH}_2$	0.22	0.52	6.48E+05	6.12E+08
3	$\text{PdH}_2 + \text{Au} \rightleftharpoons \text{PdH}_1 + \text{H} - \text{Au}$	0.20	0.26	2.27E+09	1.21E+12
4	$\text{PdH}_1 + \text{Au} \rightleftharpoons \text{Pd} + \text{H} - \text{Au}$	0.23	0.28	1.14E+09	1.27E+12
5	$\text{Pd}_1 + \text{D}_{2(\text{g})} \rightleftharpoons \text{D}_2 - \text{Pd}_1$	0.35	N/A	4.83E+08	2.91E+13
6	$\text{D}_2 - \text{Pd}_1 \rightleftharpoons \text{PdD}_2$	0.22	0.52	6.48E+05	6.12E+08
7	$\text{PdD}_2 + \text{Au} \rightleftharpoons \text{PdD}_1 + \text{D} - \text{Au}$	0.20	0.26	2.27E+09	1.21E+12
8	$\text{PdD}_1 + \text{Au} \rightleftharpoons \text{Pd} + \text{D} - \text{Au}$	0.23	0.28	1.14E+09	1.27E+12
9	$\text{Pd}_1 + \text{HD}_{(\text{g})} \rightleftharpoons \text{HD} - \text{Pd}_1$	0.35	N/A	5.57E+08	2.91E+13
10	$\text{HD} - \text{Pd}_1 \rightleftharpoons \text{PdHD}$	0.22	0.52	6.48E+05	6.12E+08
11	$\text{PdHD} + \text{Au} \rightleftharpoons \text{PdH}_1 + \text{D} - \text{Au}$	0.20	0.26	2.27E+09	1.21E+12
12	$\text{PdHD} + \text{Au} \rightleftharpoons \text{PdD}_1 + \text{H} - \text{Au}$	0.20	0.26	2.27E+09	1.21E+12
13	$\text{Pd}_1 + \text{RCH}_3\text{CHCH}_{2(\text{g})} \rightleftharpoons \text{RCH}_3\text{CHCH}_2 - \text{Pd}_1$	-0.12	N/A	1.06E+08	2.40E+06
14	$\text{RCH}_3\text{CHCH}_2 - \text{Pd}_1 + \text{H} - \text{Au}$ $\rightleftharpoons \text{RCH}_3\text{CHCH}_2 - \text{Pd}_1 - \text{H} + \text{Au}$	-0.03	0.06	1.24E+12	5.47E+11
15	$\text{RCH}_3\text{CHCH}_2 - \text{Pd}_1 - \text{H} \rightleftharpoons \text{RCH}_3\text{CH}_2\text{CH}_2 - \text{Pd}_1$	-0.37	0.31	5.69E+08	5.94E+03
16	$\text{RCH}_3\text{CH}_2\text{CH}_2 - \text{Pd}_1 + \text{H} - \text{Au}$ $\rightleftharpoons \text{RCH}_3\text{CH}_2\text{CH}_2 - \text{Pd}_1 - \text{H} + \text{Au}$	-0.12	0.06	1.24E+12	3.16E+10
17	$\text{RCH}_3\text{CH}_2\text{CH}_2 - \text{Pd}_1 - \text{H} \rightleftharpoons \text{RCH}_3\text{CH}_2\text{CH}_3 - \text{Pd}_1$	-1.26	0.22	9.65E+09	8.76E-08
18	$\text{RCH}_3\text{CH}_2\text{CH}_2 - \text{Pd}_1 + \text{D} - \text{Au}$ $\rightleftharpoons \text{RCH}_3\text{CH}_2\text{CH}_2 - \text{Pd}_1 - \text{D} + \text{Au}$	-0.12	0.06	1.24E+12	3.16E+10
19	$\text{RCH}_3\text{CH}_2\text{CH}_2 - \text{Pd}_1 - \text{D} \rightleftharpoons \text{RCH}_3\text{CH}_2\text{CH}_2\text{D} - \text{Pd}_1$	-1.26	0.22	9.65E+09	8.76E-08
20	$\text{Pd}_1 + \text{RCH}_3\text{CH}_2\text{CH}_{3(\text{g})} \rightleftharpoons \text{RCH}_3\text{CH}_2\text{CH}_3 - \text{Pd}_1$	0.15	N/A	1.04E+08	1.21E+10
21	$\text{Pd}_1 + \text{RCH}_3\text{CH}_2\text{CH}_2\text{D}_{(\text{g})} \rightleftharpoons \text{RCH}_3\text{CH}_2\text{CH}_2\text{D} - \text{Pd}_1$	0.18	N/A	1.04E+08	2.54E+10
22	$\text{RCH}_3\text{CHCH}_2 - \text{Pd}_1 + \text{H} - \text{Au}$ $\rightleftharpoons \text{RCH}_3\text{CHCH}_2 - \text{H} - \text{Pd}_1 + \text{Au}$	0.02	0.06	1.24E+12	2.31E+12
23	$\text{RCH}_3\text{CHCH}_2 - \text{H} - \text{Pd}_1 \rightleftharpoons \text{RCH}_3\text{CHCH}_3 - \text{Pd}_1$	-0.38	0.35	1.57E+08	1.18E+03
24	$\text{RCH}_3\text{CHCH}_3 - \text{Pd}_1 + \text{H} - \text{Au}$ $\rightleftharpoons \text{RCH}_3\text{CHCH}_3 - \text{Pd}_1 - \text{H} + \text{Au}$	-0.15	0.06	1.24E+12	1.04E+10
25	$\text{RCH}_3\text{CHCH}_3 - \text{Pd}_1 - \text{H} \rightleftharpoons \text{RCH}_3\text{CH}_2\text{CH}_3 - \text{Pd}_1$	-1.26	0.16	5.22E+10	4.73E-07
26	$\text{RCH}_3\text{CHCH}_3 - \text{Pd}_1 + \text{D} - \text{Au}$ $\rightleftharpoons \text{RCH}_3\text{CHCH}_3 - \text{Pd}_1 - \text{D} + \text{Au}$	-0.15	0.06	1.24E+12	1.04E+10

27	$\text{RCH}_3\text{CHCH}_3 - \text{Pd}_1 - \text{D} \rightleftharpoons \text{RCH}_3\text{CHDCH}_3 - \text{Pd}_1$	-1.26	0.16	5.22E+10	4.73E-07
28	$\text{RCH}_3\text{CHCH}_3 - \text{Pd}_1 \rightleftharpoons \text{RCH}_2\text{CHCH}_3 - \text{Pd}_1 - \text{H}$	<b>0.38</b>	<b>0.65</b>	<b>1.12E+04</b>	<b>1.69E+09</b>
29	$\text{RCH}_2\text{CHCH}_3 - \text{Pd}_1 - \text{H} + \text{Au}$ $\rightleftharpoons \text{RCH}_2\text{CHCH}_3 - \text{Pd}_1 + \text{H} - \text{Au}$	<b>0.07</b>	<b>0.13</b>	<b>1.44E+11</b>	<b>1.24E+12</b>
30	$\text{Pd}_1 + \text{RCH}_3\text{CHDCH}_3(\text{g}) \rightleftharpoons \text{RCH}_3\text{CHDCH}_3 - \text{Pd}_1$	0.18	N/A	1.04E+08	2.55E+10
31	$\text{Pd}_1 + \text{RCH}_2\text{CHCH}_3(\text{g}) \rightleftharpoons \text{RCH}_2\text{CHCH}_3 - \text{Pd}_1$	<b>0.17</b>	<b>N/A</b>	<b>1.06E+08</b>	<b>2.28E+10</b>
32	$\text{RCH}_3\text{CHCH}_2 - \text{Pd}_1 + \text{D} - \text{Au}$ $\rightleftharpoons \text{RCH}_3\text{CHCH}_2 - \text{Pd}_1 - \text{D} + \text{Au}$	-0.03	0.06	1.24E+12	5.47E+11
33	$\text{RCH}_3\text{CHCH}_2 - \text{Pd}_1 - \text{D} \rightleftharpoons \text{RCH}_3\text{CHDCH}_2 - \text{Pd}_1$	-0.37	0.31	5.69E+08	5.94E+03
34	$\text{RCH}_3\text{CHDCH}_2 - \text{Pd}_1 + \text{H} - \text{Au}$ $\rightleftharpoons \text{RCH}_3\text{CHDCH}_2 - \text{Pd}_1 - \text{H} + \text{Au}$	-0.12	0.06	1.24E+12	3.16E+10
35	$\text{RCH}_3\text{CHDCH}_2 - \text{Pd}_1 - \text{H} \rightleftharpoons \text{RCH}_3\text{CHDCH}_3 - \text{Pd}_1$	-1.26	0.22	9.65E+09	8.76E-08
36	$\text{RCH}_3\text{CHDCH}_2 - \text{Pd}_1 + \text{D} - \text{Au}$ $\rightleftharpoons \text{RCH}_3\text{CHDCH}_2 - \text{Pd}_1 - \text{D} + \text{Au}$	-0.12	0.06	1.24E+12	3.16E+10
37	$\text{RCH}_3\text{CHDCH}_2 - \text{Pd}_1 - \text{D} \rightleftharpoons \text{RCH}_3\text{CHDCH}_2\text{D} - \text{Pd}_1$	-1.26	0.22	9.65E+09	8.76E-08
38	$\text{RCH}_3\text{CHDCH}_2 - \text{Pd}_1 \rightleftharpoons \text{RCH}_3\text{CDCH}_2 - \text{Pd}_1 - \text{H}$	0.37	0.68	5.94E+03	5.69E+08
39	$\text{RCH}_3\text{CDCH}_2 - \text{Pd}_1 - \text{H} + \text{Au}$ $\rightleftharpoons \text{RCH}_3\text{CDCH}_2 - \text{Pd}_1 + \text{H} - \text{Au}$	0.03	0.09	5.47E+11	1.24E+12
40	$\text{RCH}_3\text{CHDCH}_2\text{D}(\text{g}) + \text{Pd}_1 \rightleftharpoons \text{RCH}_3\text{CHDCH}_2\text{D} - \text{Pd}_1$	0.18	N/A	1.03E+08	2.68E+10
41	$\text{RCH}_3\text{CDCH}_2(\text{g}) + \text{Pd}_1 \rightleftharpoons \text{RCH}_3\text{CHDCH}_2 - \text{Pd}_1$	-0.12	N/A	1.05E+08	2.52E+06
42	$\text{RCH}_3\text{CHCH}_2 - \text{Pd}_1 + \text{D} - \text{Au}$ $\rightleftharpoons \text{RCH}_3\text{CHCH}_2 - \text{D} - \text{Pd}_1 + \text{Au}$	0.02	0.06	1.24E+12	2.31E+12
43	$\text{RCH}_3\text{CHCH}_2 - \text{D} - \text{Pd}_1 \rightleftharpoons \text{RCH}_3\text{CHCH}_2\text{D} - \text{Pd}_1$	-0.38	0.35	1.57E+08	1.18E+03
44	$\text{RCH}_3\text{CHCH}_2\text{D} - \text{Pd}_1 + \text{H} - \text{Au}$ $\rightleftharpoons \text{RCH}_3\text{CHCH}_2\text{D} - \text{Pd}_1 - \text{H} + \text{Au}$	-0.15	0.06	1.24E+12	1.04E+10
45	$\text{RCH}_3\text{CHCH}_2\text{D} - \text{Pd}_1 - \text{H} \rightleftharpoons \text{RCH}_3\text{CH}_2\text{CH}_2\text{D} - \text{Pd}_1$	-1.26	0.16	5.22E+10	4.73E-07
46	$\text{RCH}_3\text{CHCH}_2\text{D} - \text{Pd}_1 + \text{D} - \text{Au}$ $\rightleftharpoons \text{RCH}_3\text{CHCH}_2\text{D} - \text{Pd}_1 - \text{D} + \text{Au}$	-0.15	0.06	1.24E+12	1.04E+10
47	$\text{RCH}_3\text{CHCH}_2\text{D} - \text{Pd}_1 - \text{D} \rightleftharpoons \text{RCH}_3\text{CHDCH}_2\text{D} - \text{Pd}_1$	-1.26	0.16	5.22E+10	4.73E-07
48	$\text{RCH}_3\text{CHCH}_2\text{D} - \text{Pd}_1 \rightleftharpoons \text{RCH}_2\text{CHCH}_2\text{D} - \text{Pd}_1 - \text{H}$	0.38	0.65	1.12E+04	1.69E+09
49	$\text{RCH}_2\text{CHCH}_2\text{D} - \text{Pd}_1 - \text{H} + \text{Au}$ $\rightleftharpoons \text{RCH}_2\text{CHCH}_2\text{D} - \text{Pd}_1 + \text{H} - \text{Au}$	0.07	0.13	1.44E+11	1.24E+12
50	$\text{RCH}_3\text{CHCH}_2\text{D} - \text{Pd}_1 \rightleftharpoons (\text{E}) \text{RCH}_2\text{CHCHD} - \text{H} - \text{Pd}_1$	0.38	0.73	1.18E+03	1.57E+08
51	$(\text{E}) \text{RCH}_2\text{CHCHD} - \text{H} - \text{Pd}_1 + \text{Au}$ $\rightleftharpoons (\text{E}) \text{RCH}_2\text{CHCHD} - \text{Pd}_1 + \text{H} - \text{Au}$	-0.02	0.04	2.31E+12	1.24E+12

52	$\text{RCH}_3\text{CHCH}_2\text{D} - \text{Pd}_1 \rightleftharpoons (\text{Z}) \text{RCH}_2\text{CHCHD} - \text{H} - \text{Pd}_1$	0.38	0.73	1.18E+03	1.57E+08
53	$(\text{Z}) \text{RCH}_2\text{CHCHD} - \text{H} - \text{Pd}_1 + \text{Au} \rightleftharpoons (\text{Z}) \text{RCH}_2\text{CHCHD} - \text{Pd}_1 + \text{H} - \text{Au}$	-0.02	0.04	2.31E+12	1.24E+12
54	$\text{RCH}_3\text{CDCH}_2(\text{g}) + \text{Pd}_1 \rightleftharpoons \text{RCH}_3\text{CDCH}_2 - \text{Pd}_1$	0.17	N/A	1.05E+08	2.40E+10
55	$(\text{E}) \text{RCH}_2\text{CHCHD}(\text{g}) + \text{Pd}_1 \rightleftharpoons (\text{E}) \text{RCH}_2\text{CHCHD} - \text{Pd}_1$	-0.12	N/A	1.05E+08	2.54E+06
56	$(\text{Z}) \text{RCH}_2\text{CHCHD}(\text{g}) + \text{Pd}_1 \rightleftharpoons (\text{Z}) \text{RCH}_2\text{CHCHD} - \text{Pd}_1$	-0.12	N/A	1.05E+08	2.55E+06

## B.4 Degree of Selectivity Control

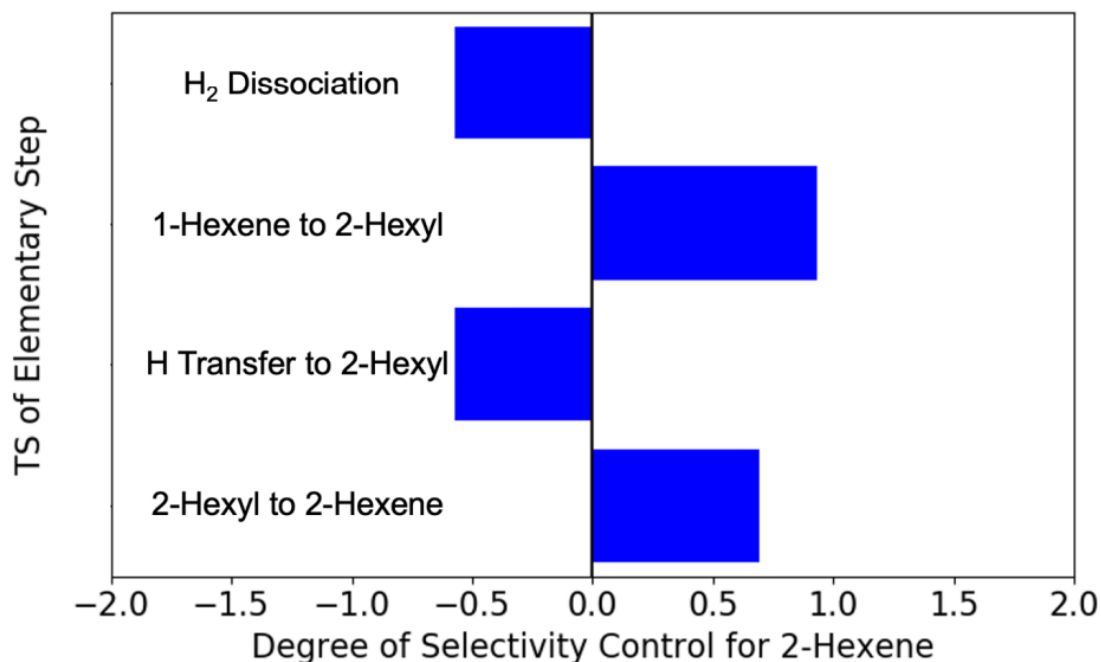


Figure B.3. Degree of selectivity control (DSC) of selected TS for 2-hexene formation evaluated at fixed partial pressures. DSC for 2-hexene formation evaluated at  $T = 373 \text{ K}$ ,  $P(\text{H}_2) = 0.2 \text{ bar}$ ,  $P(1\text{-hexene}) = 0.01 \text{ bar}$ , and  $P(2\text{-hexene}) = P(\text{n-hexane}) = 0.001 \text{ bar}$ . The TS of  $\text{H}_2$  dissociation (DSC = -0.57) and H spillover to 2-hexyl (DSC = -0.57) have the most negative impact on the selectivity of 2-hexene, while the TS of the hydrogenation of 1-hexene to 2-hexyl (DSC = 0.93) and the dehydrogenation of 2-hexyl to 2-hexene (DSC = 0.69) have the most positive impact on the selectivity of 2-hexene.

## B.5 Additional Microkinetic Simulations

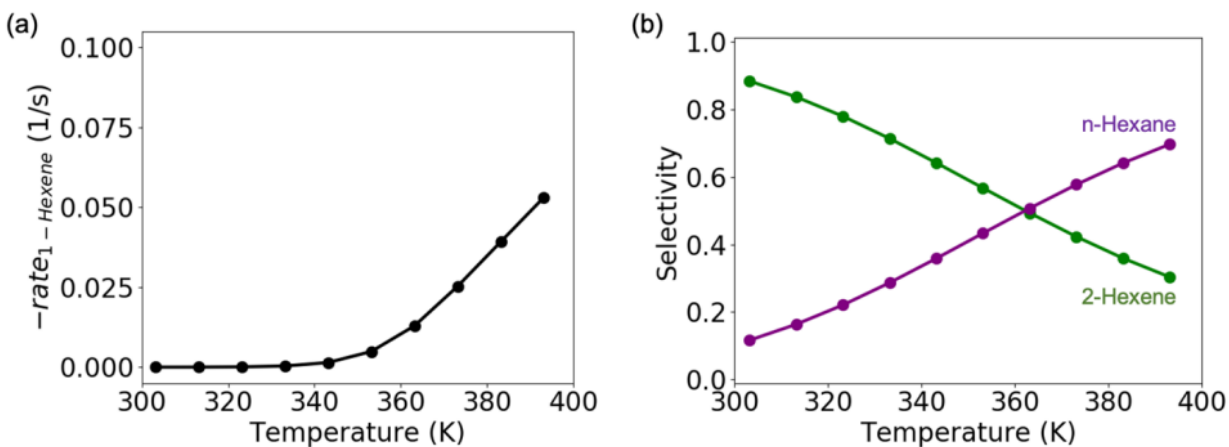


Figure B.4. 1-Hexene consumption rate and product selectivity evaluated at fixed partial pressures after increasing the barriers of  $\text{H}_2$  dissociation and H spillover by 0.1 eV. Microkinetic model of 1-hexene reaction with  $\text{H}_2$  evaluated at  $P(\text{H}_2) = 0.2$  bar,  $P(1\text{-hexene}) = 0.01$  bar, and  $P(2\text{-hexene}) = P(\text{n-hexane}) = 0.001$  bar. (a) Rate of 1-hexene consumption, (b) selectivity of 2-hexene and n-hexane.

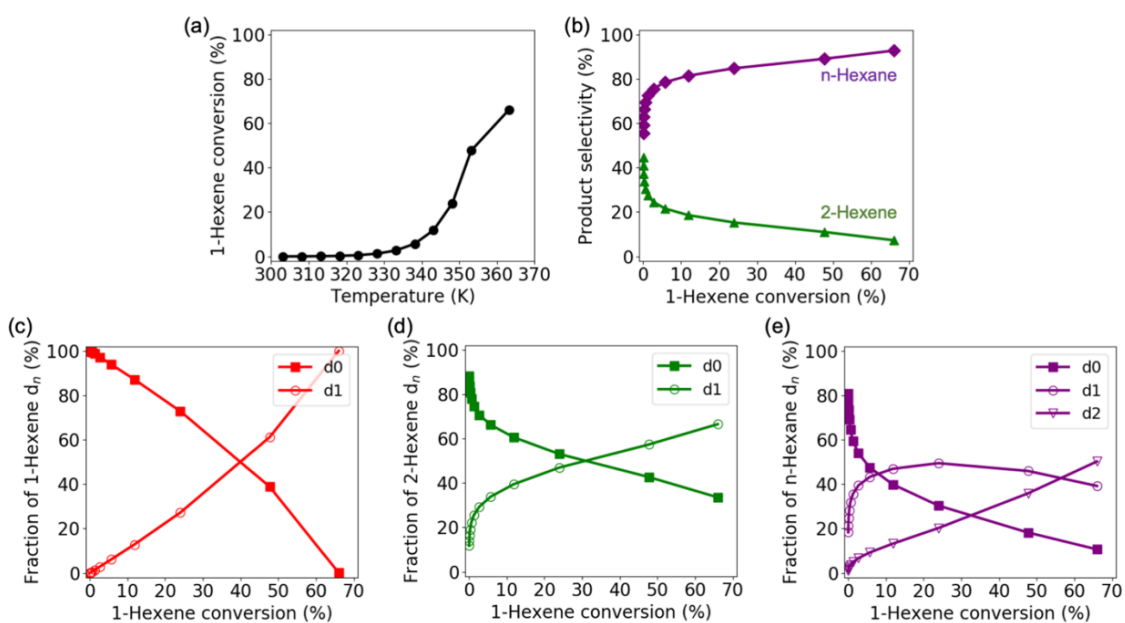


Figure B.5. Plug flow reactor (PFR) simulations of product and isotope selectivity of 1-hexene

deuteration and isomerization without shifts to the barrier of H<sub>2</sub> dissociation and spillover. (a) 1-Hexene conversion and (b) selectivity of 2-hexene and n-hexane as functions of reactor temperature. (c) 1-Hexene isotope distribution, (d) 2-hexene isotope distribution, and (e) n-hexane isotope distribution as functions of 1-hexene conversion.

## B.6 Binding Strengths of Carbonaceous Species

Table B.2. Adsorption Internal Energies of 1- and 2-Hexene on a Monometallic Pd(111) and Single Pd Atom on the Au(Pd<sub>1</sub>Au, 111) Surface. The values were computed using density functional theory (DFT) calculations.

	1-Hexene	2-Hexene
Pd <sub>1</sub> Au	-1.22 eV	-0.93 eV
Pd	-1.67 eV	-1.45 eV

## Appendix C Supplementary Information for Chapter 4

### C.1 Detailed Description of Microkinetic Model

Table C.1. Elementary steps included in the microkinetic simulation of acetylene hydrogenation on Pd<sub>1</sub> in Au(111). For microkinetic simulation of acetylene hydrogenation on Pd<sub>1</sub>, a total of 15 elementary steps were considered. Steps 1, 5, 10, and 15 represent the adsorption/desorption processes while the others are the surface reaction steps. Note that surface species are shown in brackets. [H – Pd<sub>1</sub>] and [C<sub>2</sub>H<sub>x</sub> – Pd<sub>1</sub>] stand for the H atom and the hydrocarbon intermediate binding to a Pd<sub>1</sub> active site while [H – Au] is that binding to the Au surface. [C<sub>2</sub>H<sub>x</sub>(H) – Pd<sub>1</sub>], on the other hand, corresponds to the co-adsorption of a H atom and a hydrocarbon intermediate C<sub>2</sub>H<sub>x</sub> on the same Pd<sub>1</sub> active site.

#	Elementary Step
1	$\text{H}_{2(\text{g})} + [\text{Pd}_1] \rightleftharpoons [\text{H}_2 - \text{Pd}_1]$
2	$[\text{H}_2 - \text{Pd}_1] \rightleftharpoons [\text{H} - \text{Pd}_1 - \text{H}]$
3	$[\text{H} - \text{Pd}_1 - \text{H}] + [\text{Au}] \rightleftharpoons [\text{H} - \text{Pd}_1] + [\text{H} - \text{Au}]$
4	$[\text{H} - \text{Pd}_1] + [\text{Au}] \rightleftharpoons [\text{H} - \text{Au}] + [\text{Pd}_1]$
5	$\text{C}_2\text{H}_{2(\text{g})} + [\text{Pd}_1] \rightleftharpoons [\text{C}_2\text{H}_2 - \text{Pd}_1]$
6	$[\text{C}_2\text{H}_2 - \text{Pd}_1] + [\text{H} - \text{Au}] \rightleftharpoons [\text{C}_2\text{H}_2(\text{H}) - \text{Pd}_1] + [\text{Au}]$
7	$[\text{C}_2\text{H}_2(\text{H}) - \text{Pd}_1] \rightleftharpoons [\text{C}_2\text{H}_3 - \text{Pd}_1]$
8	$[\text{C}_2\text{H}_3 - \text{Pd}_1] + [\text{H} - \text{Au}] \rightleftharpoons [\text{C}_2\text{H}_3(\text{H}) - \text{Pd}_1] + [\text{Au}]$
9	$[\text{C}_2\text{H}_3(\text{H}) - \text{Pd}_1] \rightleftharpoons [\text{C}_2\text{H}_4 - \text{Pd}_1]$
10	$\text{C}_2\text{H}_{4(\text{g})} + [\text{Pd}_1] \rightleftharpoons [\text{C}_2\text{H}_4 - \text{Pd}_1]$
11	$[\text{C}_2\text{H}_4 - \text{Pd}_1] + [\text{H} - \text{Au}] \rightleftharpoons [\text{C}_2\text{H}_4(\text{H}) - \text{Pd}_1] + [\text{Au}]$
12	$[\text{C}_2\text{H}_4(\text{H}) - \text{Pd}_1] \rightleftharpoons [\text{C}_2\text{H}_5 - \text{Pd}_1]$
13	$[\text{C}_2\text{H}_5 - \text{Pd}_1] + [\text{H} - \text{Au}] \rightleftharpoons [\text{C}_2\text{H}_5(\text{H}) - \text{Pd}_1] + [\text{Au}]$
14	$[\text{C}_2\text{H}_5(\text{H}) - \text{Pd}_1] \rightleftharpoons [\text{C}_2\text{H}_6 - \text{Pd}_1]$
15	$\text{C}_2\text{H}_{6(\text{g})} + [\text{Pd}_1] \rightleftharpoons [\text{C}_2\text{H}_6 - \text{Pd}_1]$

Table C.2. Elementary steps included in the microkinetic simulation of acetylene hydrogenation on Pd<sub>2</sub> in Au(111). A total of 15 elementary steps were considered in the microkinetic simulation of acetylene hydrogenation on Pd<sub>2</sub>. The notations used in Table C.2 are similar to those in Table C.1 except that the surface species are now binding to a Pd<sub>2</sub> ensemble. Note that one of the two H atoms formed after dissociation is doubly-coordinated to Pd while the remaining one is singly-coordinated. The former and the latter are shown as [H<sup>2</sup> – Pd<sub>2</sub>] and [H<sup>1</sup> – Pd<sub>2</sub>], respectively. [H<sup>2</sup> – Pd<sub>2</sub> – H<sup>1</sup>] represents the co-adsorption of the two H atoms on the same Pd<sub>2</sub> site. Note that [Pd<sub>2</sub>] represents a full dimer, not an individual Pd atom in the dimer.

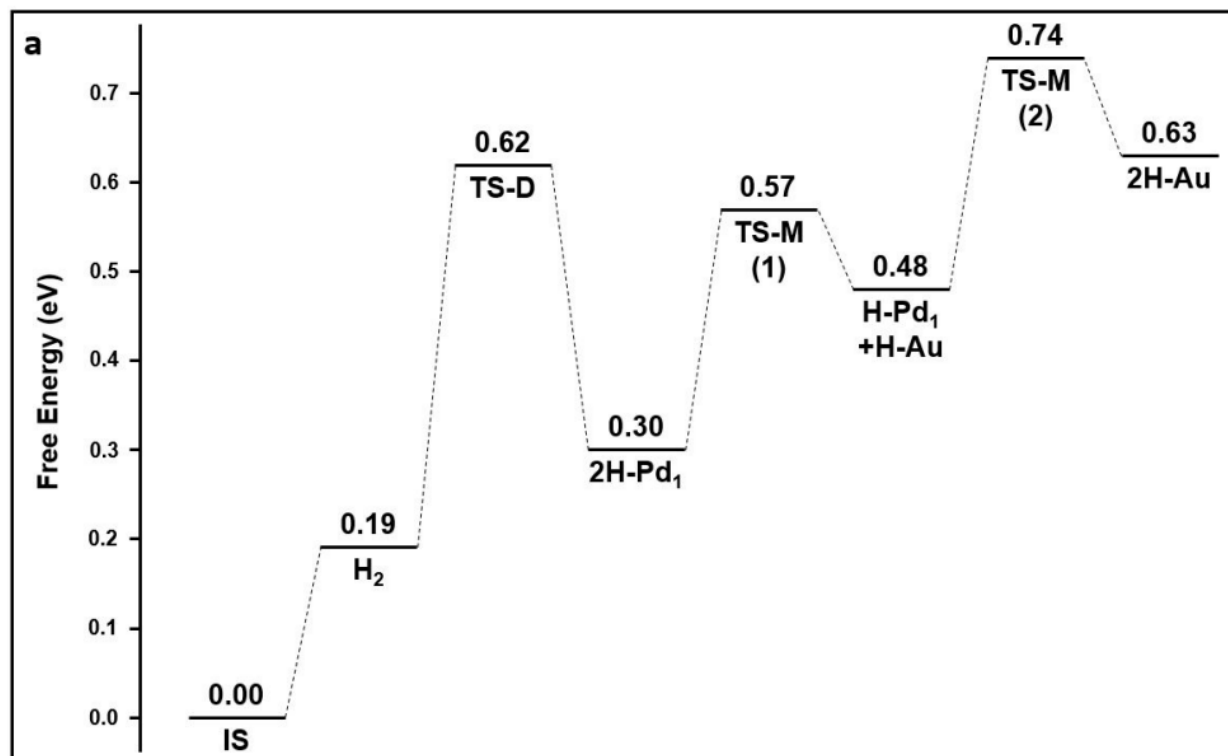
#	Elementary Step
1	$\text{H}_{2(\text{g})} + [\text{Pd}_2] \rightleftharpoons [\text{H}_2 - \text{Pd}_2]$
2	$[\text{H}_2 - \text{Pd}_2] \rightleftharpoons [\text{H}^2 - \text{Pd}_2 - \text{H}^1]$
3	$[\text{H}^2 - \text{Pd}_2 - \text{H}^1] + [\text{Au}] \rightleftharpoons [\text{H}^2 - \text{Pd}_2] + [\text{H} - \text{Au}]$
4	$[\text{H}^2 - \text{Pd}_2] + [\text{Au}] \rightleftharpoons [\text{H} - \text{Au}] + [\text{Pd}_2]$
5	$\text{C}_2\text{H}_{2(\text{g})} + [\text{Pd}_2] \rightleftharpoons [\text{C}_2\text{H}_2 - \text{Pd}_2]$
6	$[\text{C}_2\text{H}_2 - \text{Pd}_2] + [\text{H} - \text{Au}] \rightleftharpoons [\text{C}_2\text{H}_2(\text{H}) - \text{Pd}_2] + [\text{Au}]$
7	$[\text{C}_2\text{H}_2(\text{H}) - \text{Pd}_2] \rightleftharpoons [\text{C}_2\text{H}_3 - \text{Pd}_2]$
8	$[\text{C}_2\text{H}_3 - \text{Pd}_2] + [\text{H} - \text{Au}] \rightleftharpoons [\text{C}_2\text{H}_3(\text{H}) - \text{Pd}_2] + [\text{Au}]$
9	$[\text{C}_2\text{H}_3(\text{H}) - \text{Pd}_2] \rightleftharpoons [\text{C}_2\text{H}_4 - \text{Pd}_2]$
10	$\text{C}_2\text{H}_{4(\text{g})} + [\text{Pd}_2] \rightleftharpoons [\text{C}_2\text{H}_4 - \text{Pd}_2]$
11	$[\text{C}_2\text{H}_4 - \text{Pd}_2] + [\text{H} - \text{Au}] \rightleftharpoons [\text{C}_2\text{H}_4(\text{H}) - \text{Pd}_2] + [\text{Au}]$
12	$[\text{C}_2\text{H}_4(\text{H}) - \text{Pd}_2] \rightleftharpoons [\text{C}_2\text{H}_5 - \text{Pd}_2]$
13	$[\text{C}_2\text{H}_5 - \text{Pd}_2] + [\text{H} - \text{Au}] \rightleftharpoons [\text{C}_2\text{H}_5(\text{H}) - \text{Pd}_2] + [\text{Au}]$
14	$[\text{C}_2\text{H}_5(\text{H}) - \text{Pd}_2] \rightleftharpoons [\text{C}_2\text{H}_6 - \text{Pd}_2]$
15	$\text{C}_2\text{H}_{6(\text{g})} + [\text{Pd}_2] \rightleftharpoons [\text{C}_2\text{H}_6 - \text{Pd}_2]$

Table C.3. Elementary steps included in the microkinetic simulation of acetylene hydrogenation on Pd<sub>3</sub> in Au(111). A total of 34 elementary steps were considered for acetylene hydrogenation on Pd<sub>3</sub>. The notations used are similar to the ones used on Pd<sub>1</sub> and Pd<sub>2</sub>. [H – H – C<sub>2</sub>H<sub>2</sub> – Pd<sub>3</sub>] and [H – H – C<sub>2</sub>H<sub>4</sub> – Pd<sub>3</sub>] represent the co-adsorption of two H atoms with acetylene and ethylene on the same Pd<sub>3</sub> ensemble. [H – C<sub>2</sub>H<sub>2</sub> – Pd<sub>3</sub>]/[H – C<sub>2</sub>H<sub>3</sub> – Pd<sub>3</sub>] is also the co-adsorption of an H atom with C<sub>2</sub>H<sub>2</sub>/C<sub>2</sub>H<sub>3</sub>, but it adopts a different configuration from [C<sub>2</sub>H<sub>2</sub>(H) – Pd<sub>3</sub>]/[C<sub>2</sub>H<sub>3</sub>(H) – Pd<sub>3</sub>]. The abbreviations used in the step numbering are: R for the regular pathway, SP for the special pathway, NM for the no-migration pathway and C for the configurational transformation. Note that [Pd<sub>3</sub>] represents a full trimer, not an individual Pd atom in the trimer.

#	Elementary Step
R1	$\text{H}_{2(\text{g})} + [\text{Pd}_3] \rightleftharpoons [\text{H}_2 - \text{Pd}_3]$
R2	$[\text{H}_2 - \text{Pd}_3] \rightleftharpoons [\text{H}^3 - \text{Pd}_3 - \text{H}^1]$
R3	$[\text{H}^3 - \text{Pd}_3 - \text{H}^1] + [\text{Au}] \rightleftharpoons [\text{H}^3 - \text{Pd}_3] + [\text{H} - \text{Au}]$
R4	$[\text{H}^3 - \text{Pd}_3] + [\text{Au}] \rightleftharpoons [\text{H} - \text{Au}] + [\text{Pd}_3]$
R5	$\text{C}_2\text{H}_{2(\text{g})} + [\text{Pd}_3] \rightleftharpoons [\text{C}_2\text{H}_2 - \text{Pd}_3]$
R6	$[\text{C}_2\text{H}_2 - \text{Pd}_3] + [\text{H} - \text{Au}] \rightleftharpoons [\text{C}_2\text{H}_2(\text{H}) - \text{Pd}_3] + [\text{Au}]$
R7	$[\text{C}_2\text{H}_2(\text{H}) - \text{Pd}_3] \rightleftharpoons [\text{C}_2\text{H}_3 - \text{Pd}_3]$
R8	$[\text{C}_2\text{H}_3 - \text{Pd}_3] + [\text{H} - \text{Au}] \rightleftharpoons [\text{C}_2\text{H}_3(\text{H}) - \text{Pd}_3] + [\text{Au}]$
R9	$[\text{C}_2\text{H}_3(\text{H}) - \text{Pd}_3] \rightleftharpoons [\text{C}_2\text{H}_4 - \text{Pd}_3]$
R10	$\text{C}_2\text{H}_{4(\text{g})} + [\text{Pd}_3] \rightleftharpoons [\text{C}_2\text{H}_4 - \text{Pd}_3]$
R11	$[\text{C}_2\text{H}_4 - \text{Pd}_3] + [\text{H} - \text{Au}] \rightleftharpoons [\text{C}_2\text{H}_4(\text{H}) - \text{Pd}_3] + [\text{Au}]$
R12	$[\text{C}_2\text{H}_4(\text{H}) - \text{Pd}_3] \rightleftharpoons [\text{C}_2\text{H}_5 - \text{Pd}_3]$
R13	$[\text{C}_2\text{H}_5 - \text{Pd}_3] + [\text{H} - \text{Au}] \rightleftharpoons [\text{C}_2\text{H}_5(\text{H}) - \text{Pd}_3] + [\text{Au}]$
R14	$[\text{C}_2\text{H}_5(\text{H}) - \text{Pd}_3] \rightleftharpoons [\text{C}_2\text{H}_6 - \text{Pd}_3]$
R15	$\text{C}_2\text{H}_{6(\text{g})} + [\text{Pd}_3] \rightleftharpoons [\text{C}_2\text{H}_6 - \text{Pd}_3]$
SP1	$\text{C}_2\text{H}_{2(\text{g})} + [\text{H}^3 - \text{Pd}_3] \rightleftharpoons [\text{C}_2\text{H}_2(\text{H}) - \text{Pd}_3 - \text{SP}]$
SP2	$[\text{C}_2\text{H}_2(\text{H}) - \text{Pd}_3 - \text{SP}] \rightleftharpoons [\text{C}_2\text{H}_3 - \text{Pd}_3 - \text{SP}]$
SP3	$[\text{C}_2\text{H}_3 - \text{Pd}_3 - \text{SP}] + [\text{H} - \text{Au}] \rightleftharpoons [\text{H} - \text{C}_2\text{H}_3 - \text{Pd}_3] + [\text{Au}]$
SP4	$[\text{H} - \text{C}_2\text{H}_3 - \text{Pd}_3] \rightleftharpoons [\text{C}_2\text{H}_4 - \text{Pd}_3]$
SP5	$\text{C}_2\text{H}_{4(\text{g})} + [\text{H}^3 - \text{Pd}_3] \rightleftharpoons [\text{C}_2\text{H}_4(\text{H}) - \text{Pd}_3 - \text{SP}]$
SP6	$[\text{C}_2\text{H}_4(\text{H}) - \text{Pd}_3 - \text{SP}] \rightleftharpoons [\text{C}_2\text{H}_5 - \text{Pd}_3]$
NM1	$\text{H}_{2(\text{g})} + [\text{C}_2\text{H}_2 - \text{Pd}_3] \rightleftharpoons [\text{H}_2 - \text{C}_2\text{H}_2 - \text{Pd}_3]$
NM2	$[\text{H}_2 - \text{C}_2\text{H}_2 - \text{Pd}_3] \rightleftharpoons [\text{H} - \text{H} - \text{C}_2\text{H}_2 - \text{Pd}_3]$
NM3-1	$[\text{H} - \text{H} - \text{C}_2\text{H}_2 - \text{Pd}_3] \rightleftharpoons [\text{H} - \text{C}_2\text{H}_3 - \text{Pd}_3]$
NM3-2	$[\text{H} - \text{H} - \text{C}_2\text{H}_2 - \text{Pd}_3] + [\text{Au}] \rightleftharpoons [\text{H} - \text{C}_2\text{H}_2 - \text{Pd}_3] + [\text{H} - \text{Au}]$
NM4	$\text{H}_{2(\text{g})} + [\text{C}_2\text{H}_4 - \text{Pd}_3] \rightleftharpoons [\text{H}_2 - \text{C}_2\text{H}_4 - \text{Pd}_3]$
NM5	$[\text{H}_2 - \text{C}_2\text{H}_4 - \text{Pd}_3] \rightleftharpoons [\text{H} - \text{H} - \text{C}_2\text{H}_4 - \text{Pd}_3]$
NM6-1	$[\text{H} - \text{H} - \text{C}_2\text{H}_4 - \text{Pd}_3] \rightleftharpoons [\text{C}_2\text{H}_5(\text{H}) - \text{Pd}_3]$

NM6-2	$[H - H - C_2H_4 - Pd_3] + [Au] \rightleftharpoons [C_2H_4(H) - Pd_3] + [H - Au]$
C1	$[H - C_2H_3 - Pd_3] \rightleftharpoons [C_2H_3(H) - Pd_3]$
C2	$[C_2H_2(H) - Pd_3 - SP] \rightleftharpoons [C_2H_2(H) - Pd_3]$
C3	$[C_2H_3 - Pd_3 - SP] \rightleftharpoons [C_2H_3 - Pd_3]$
C4	$[C_2H_4(H) - Pd_3 - SP] \rightleftharpoons [C_2H_4(H) - Pd_3]$
C5	$[H - C_2H_2 - Pd_3] \rightleftharpoons [C_2H_2(H) - Pd_3]$

## C.2 Supplementary Energetics and Adsorption Configurations



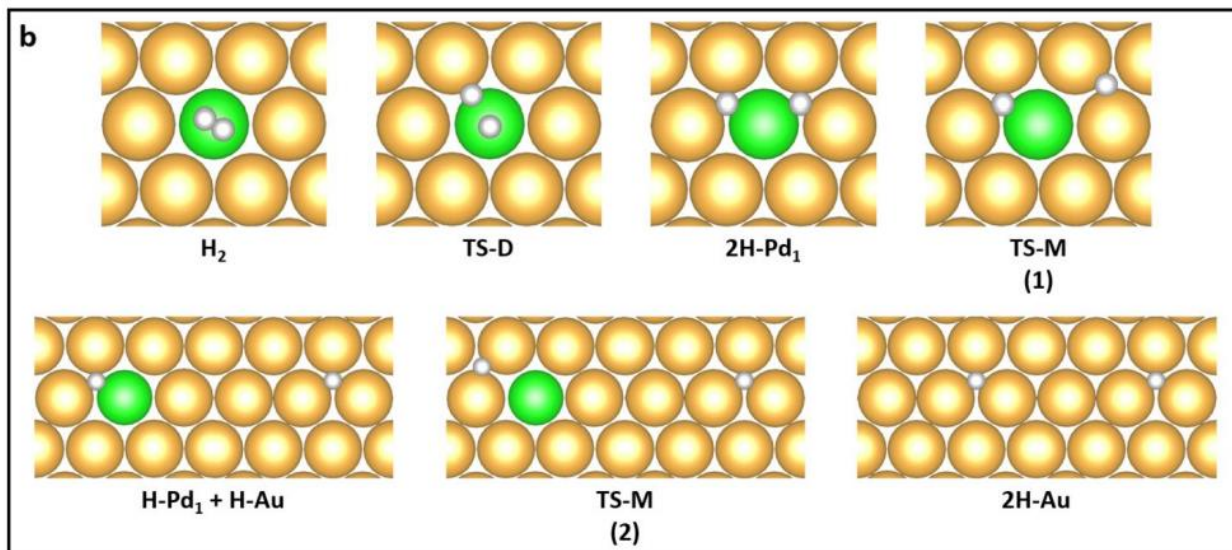
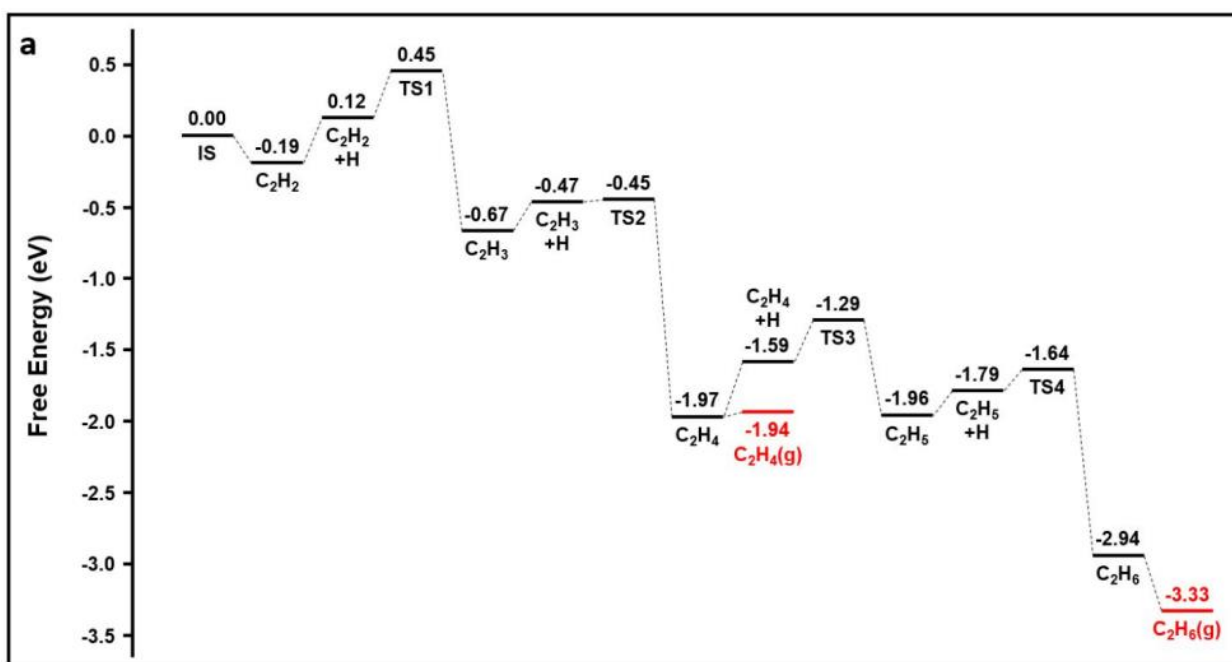


Figure C.1. (a) Free energy profile and (b) corresponding adsorption configurations of  $\text{H}_2$  dissociation and migration on  $\text{Pd}_1$  evaluated at  $T = 363$  K and under the standard-state pressures of the gaseous species. TS-D and TS-M stand for the transition states for dissociation and migration, respectively.  $\text{H-Pd}_1$  indicates that the H atom is singly-coordinated to Pd. Color codes: Green (Pd), Gold (Au), and White (H).



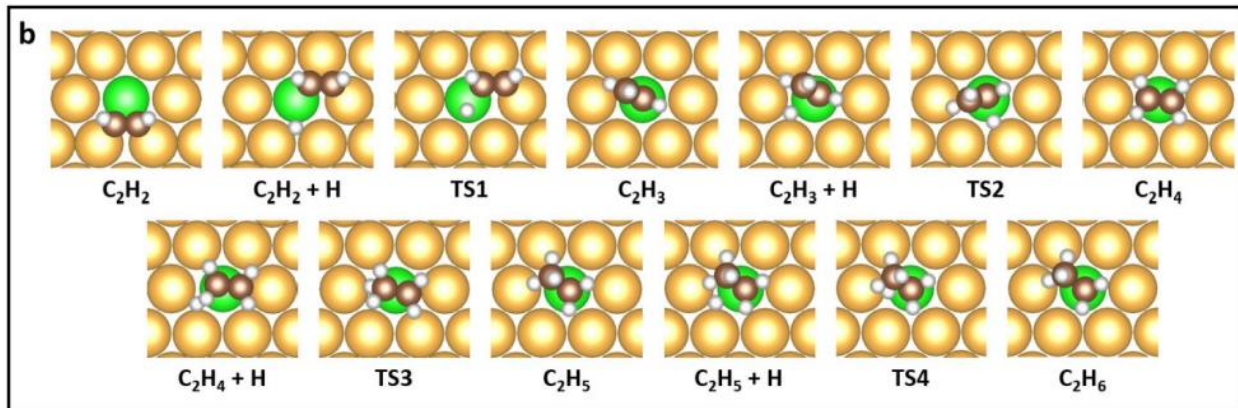
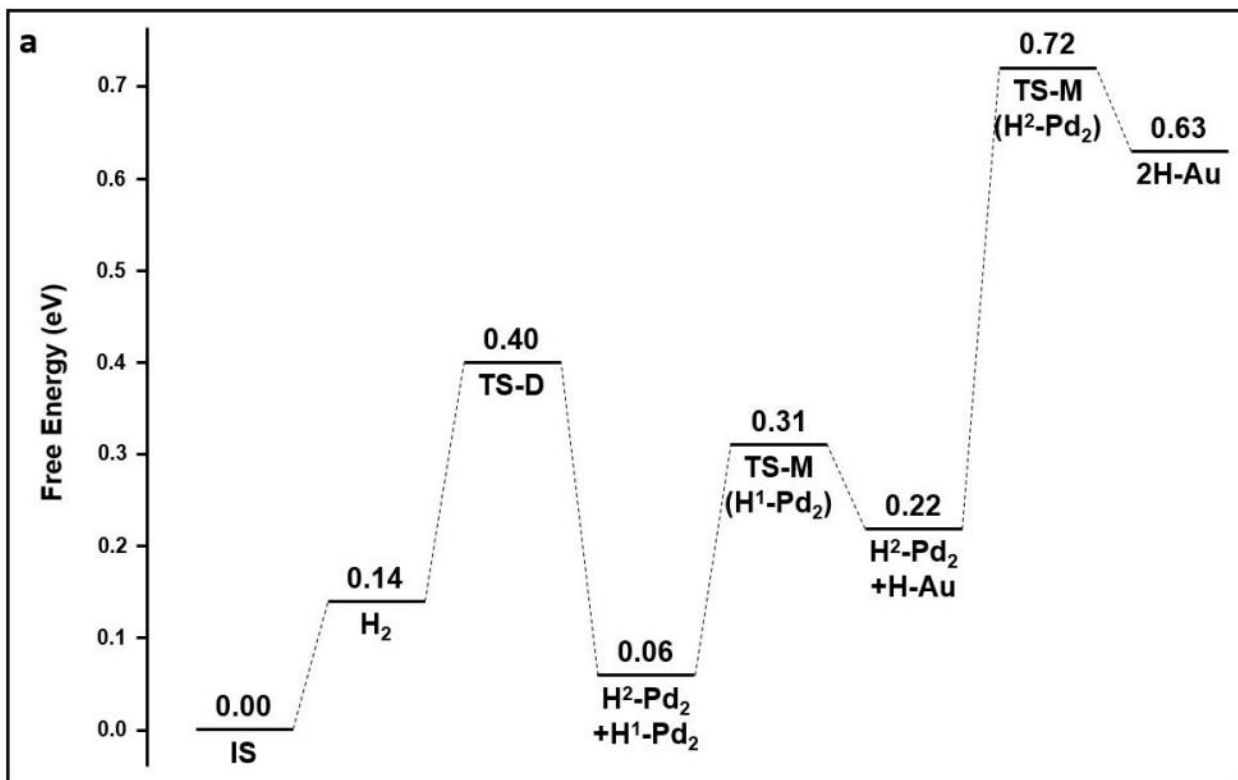


Figure C.2. (a) Free energy profile and (b) corresponding adsorption configurations of acetylene hydrogenation on Pd<sub>1</sub> evaluated at T = 363 K and under the standard-state pressures of the gaseous species. Color codes: Green (Pd), Gold (Au), Dark Brown (C), and White (H).



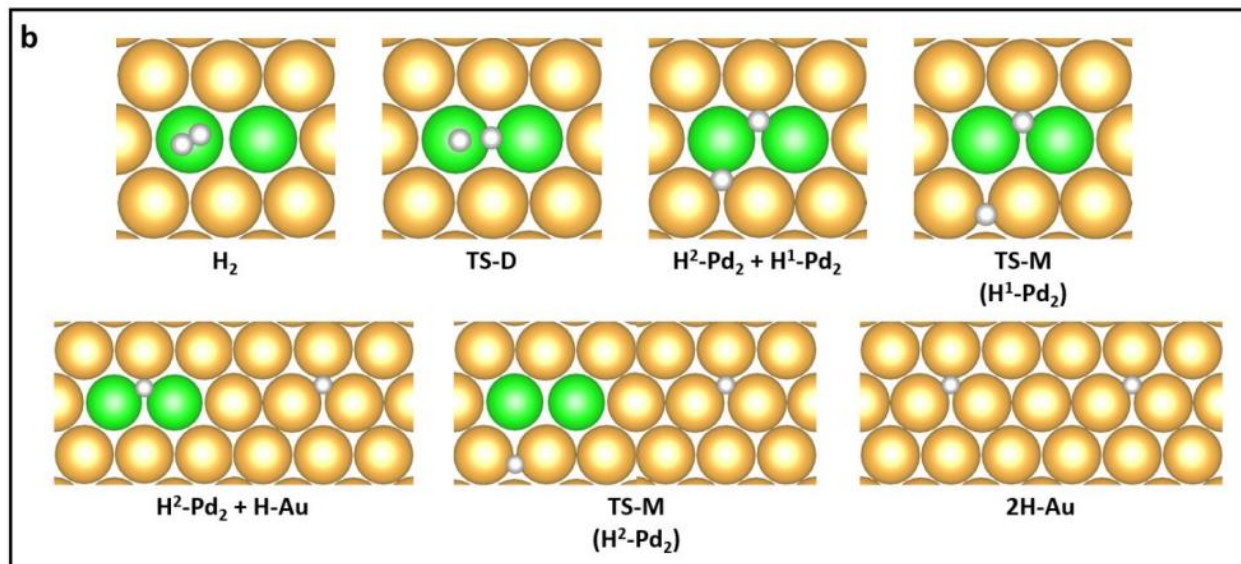
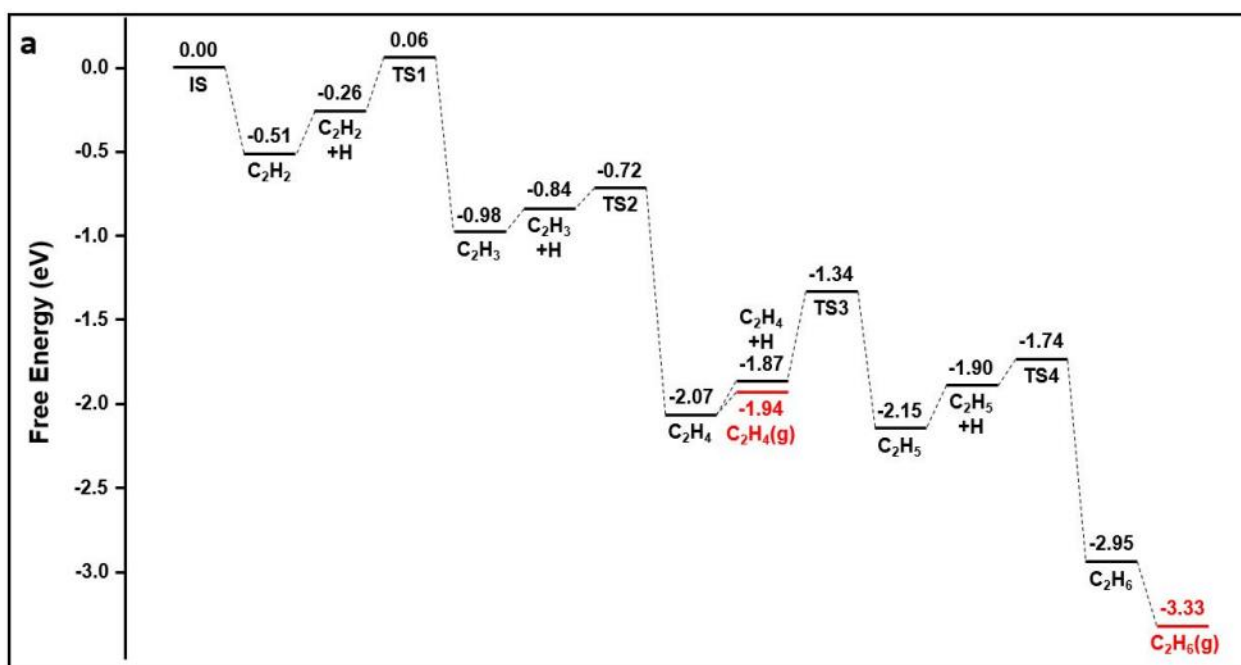


Figure C.3. (a) Free energy profile and (b) corresponding adsorption configurations of  $H_2$  dissociation and migration on  $Pd_2$  evaluated at  $T = 363$  K and under the standard-state pressures of the gaseous species. TS-D and TS-M stand for the transition states for dissociation and migration, respectively.  $H^2-Pd_2$  and  $H^1-Pd_2$  mean that the H atom is doubly and singly-coordinated to Pd. Color codes: Green (Pd), Gold (Au), and White (H).



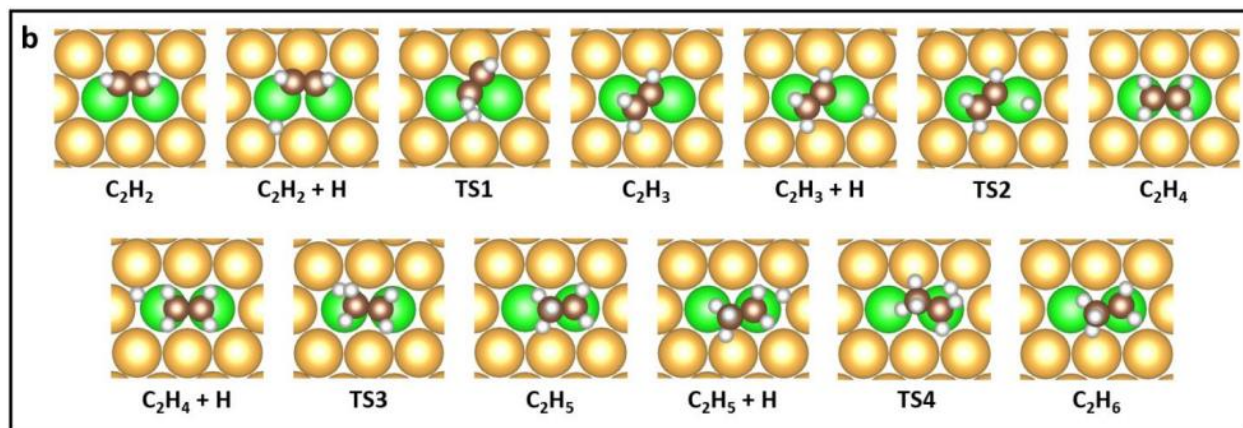
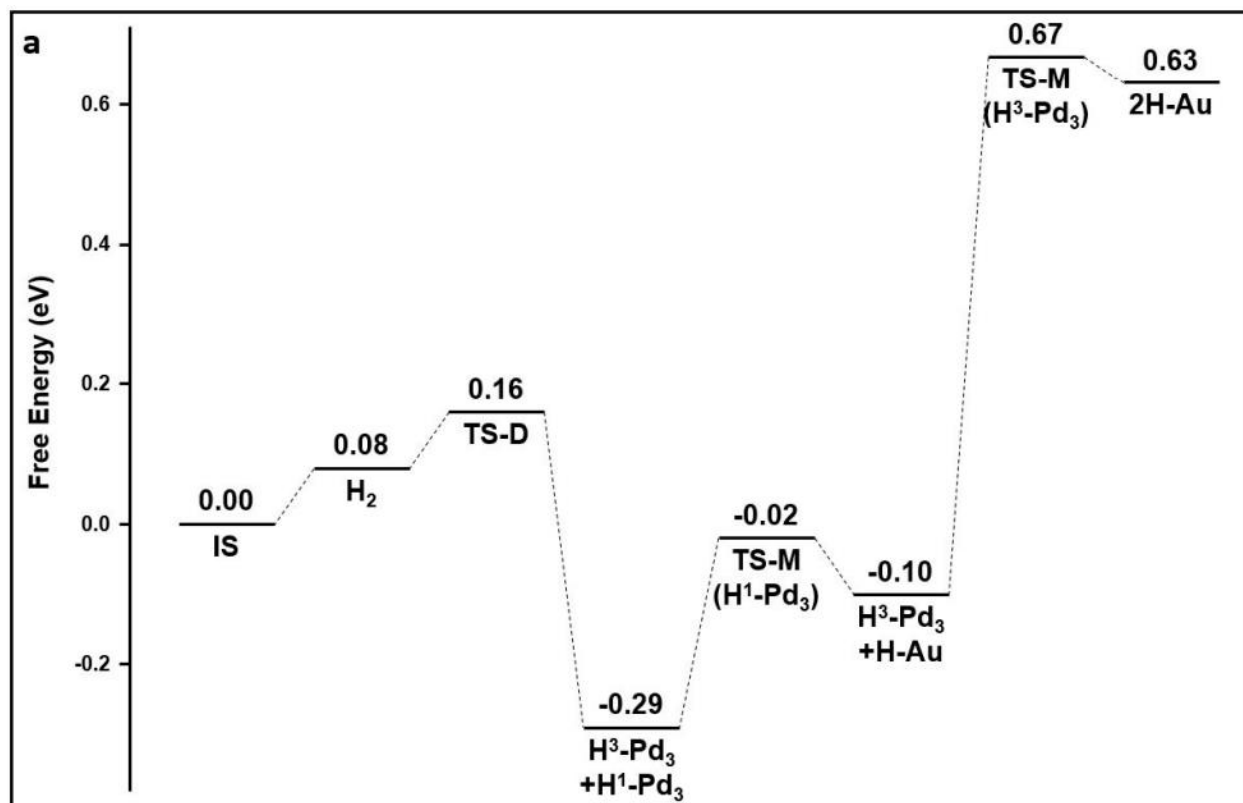


Figure C.4. (a) Free energy profile and (b) corresponding adsorption configurations of acetylene hydrogenation on Pd<sub>2</sub> evaluated at T = 363 K and under the standard-state pressures of gaseous species. Color codes: Green (Pd), Gold (Au), Dark Brown (C), and White (H).



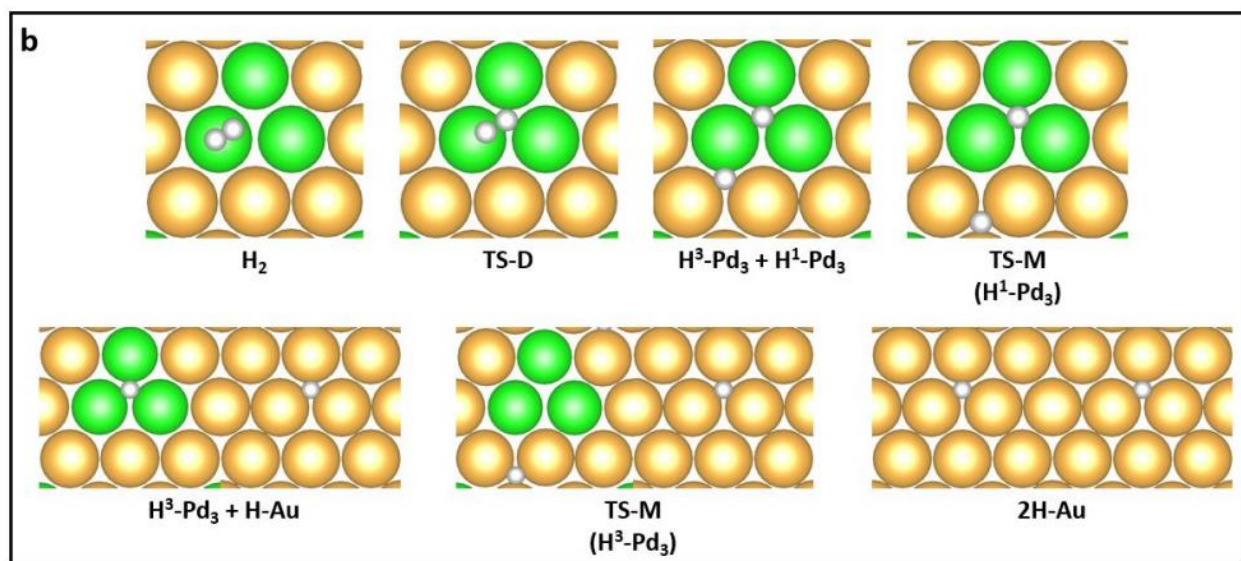


Figure C.5. (a) Free energy profile and (b) corresponding adsorption configurations of  $H_2$  dissociation and migration on  $Pd_3$  evaluated at  $T = 363$  K and under the standard-state pressures of gaseous species. TS-D and TS-M stand for the transition states for dissociation and migration, respectively.  $H^3\text{-Pd}_3$  and  $H^1\text{-Pd}_3$  mean that the H atom is triply and singly-coordinated to Pd. The migration barrier of the triply-coordinated H atom toward the Au site is large with the value being 0.77 eV. Color codes: Green (Pd), Gold (Au), and White (H).

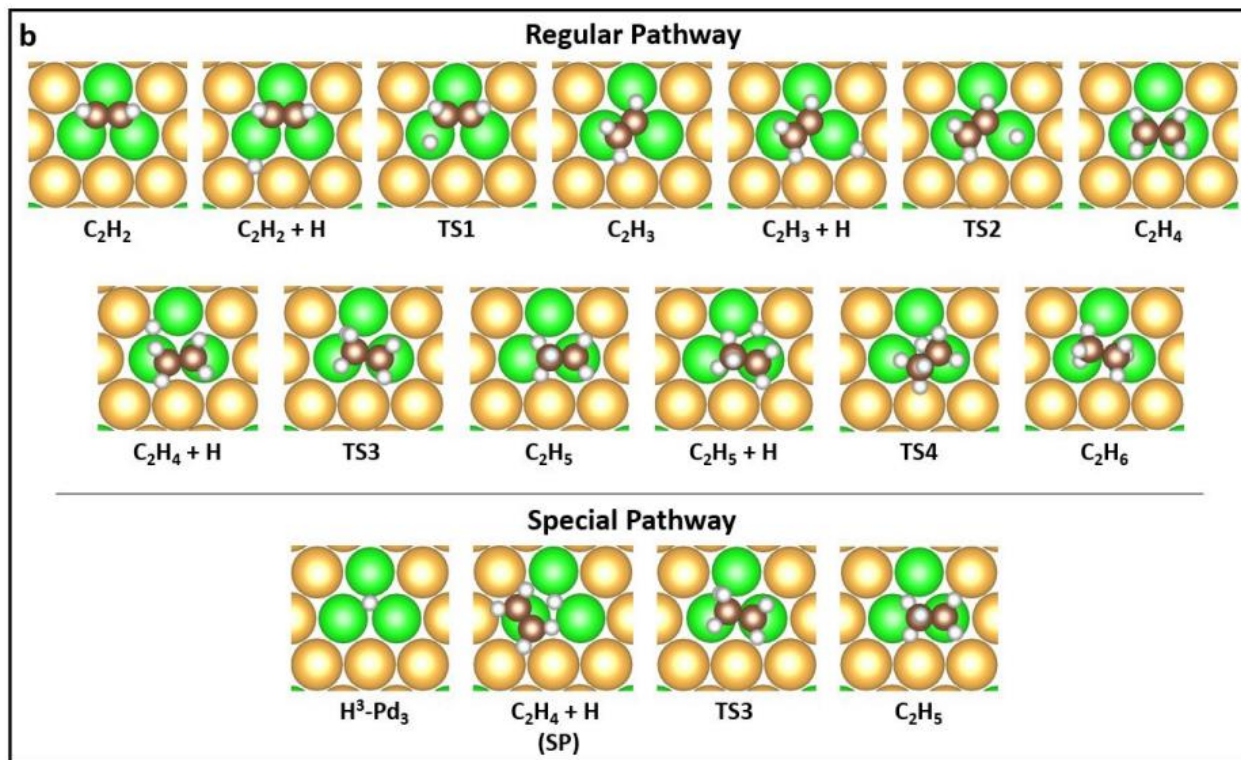
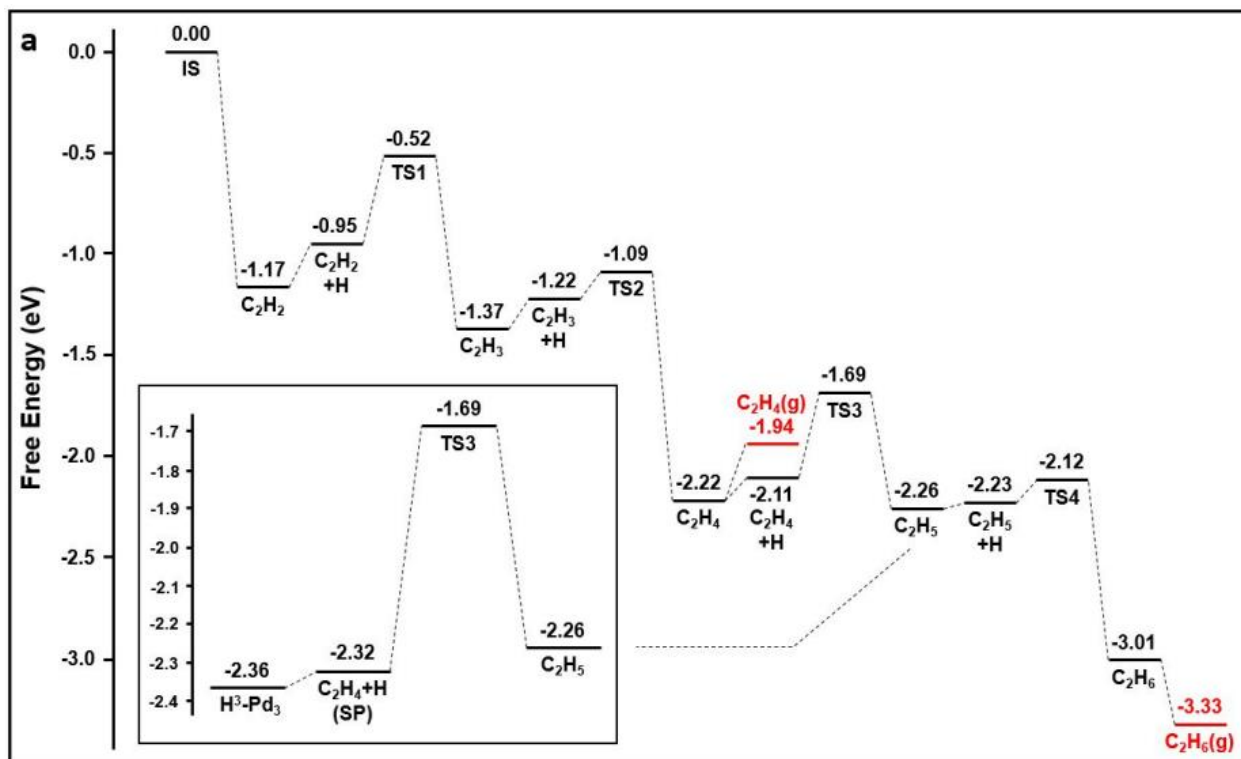
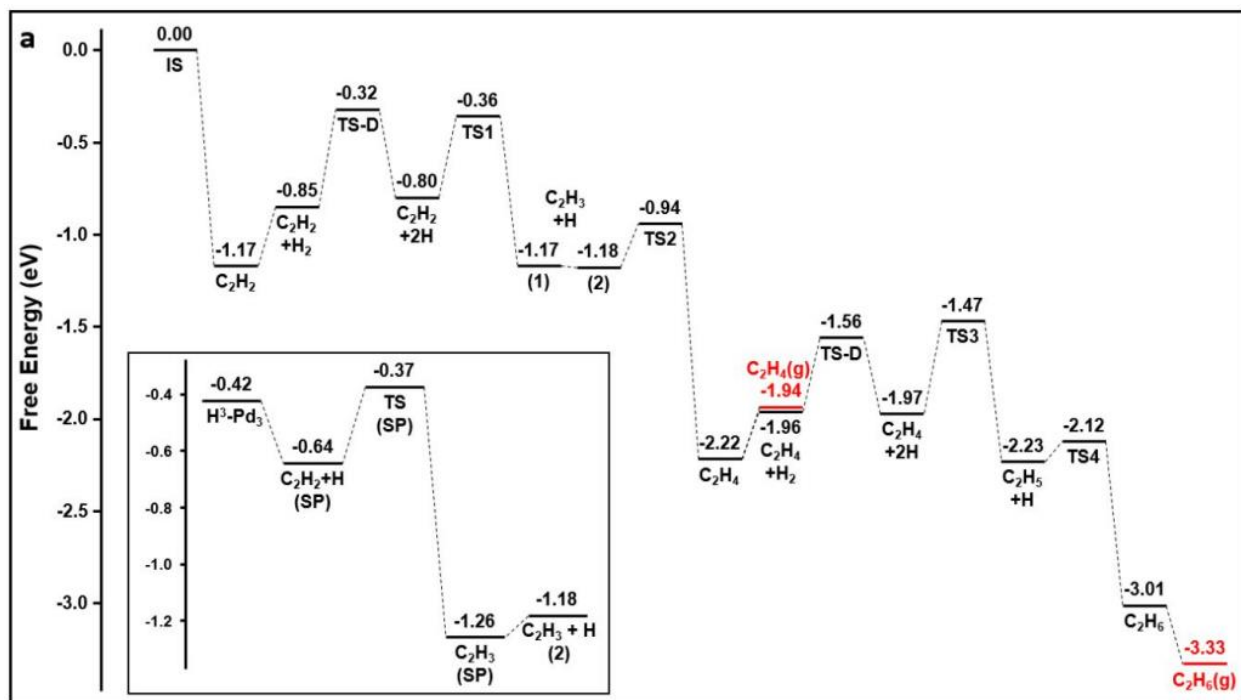


Figure C.6. (a) Free energy profile and (b) corresponding adsorption configurations of acetylene

hydrogenation on Pd<sub>3</sub> evaluated at T = 363 K and under the standard-state pressures of the gaseous species. The inset in (a) is the special pathway when an ethylene molecule adsorbs onto a Pd<sub>3</sub> ensemble in the presence of a triply-coordinated H atom. Subsequent hydrogenation would eventually lead this pathway to the C<sub>2</sub>H<sub>5</sub> state in the regular pathway. Color codes: Green (Pd), Gold (Au), Dark Brown (C), and White (H).



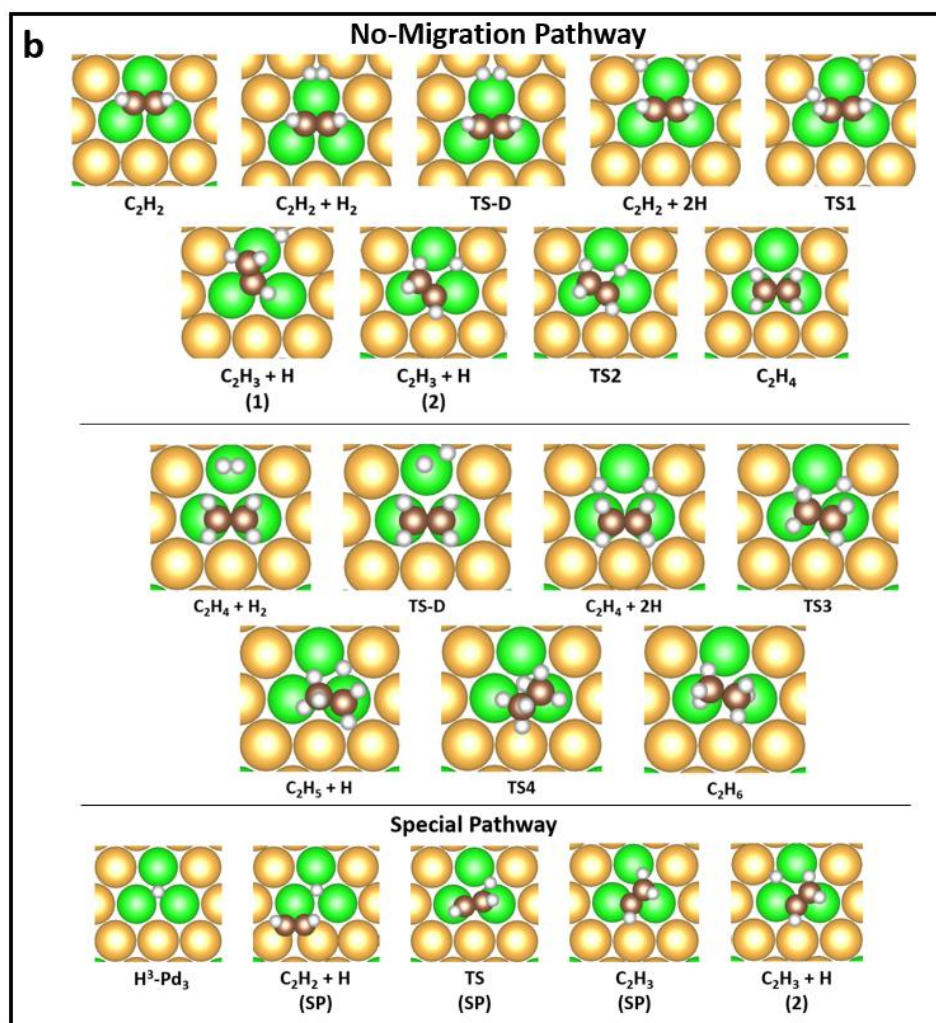


Figure C.7. (a) Free energy profile and (b) corresponding adsorption configurations of acetylene hydrogenation on Pd<sub>3</sub> evaluated at T = 363 K and under the standard-state pressures of gaseous species. This is the no-migration pathway which considers the dissociation of H<sub>2</sub> (transition state for dissociation is represented as TS-D) on the same Pd<sub>3</sub> ensemble on which an acetylene or ethylene molecule already resides. The inset shows the special pathway in which an acetylene molecule adsorbs onto a Pd<sub>3</sub> ensemble in the presence of a triply-coordinated H atom. This special pathway ultimately leads to the [C<sub>2</sub>H<sub>3</sub> + H (2)] state in the no-migration pathway. Color codes: Green (Pd), Gold (Au), Dark Brown (C), and White (H).

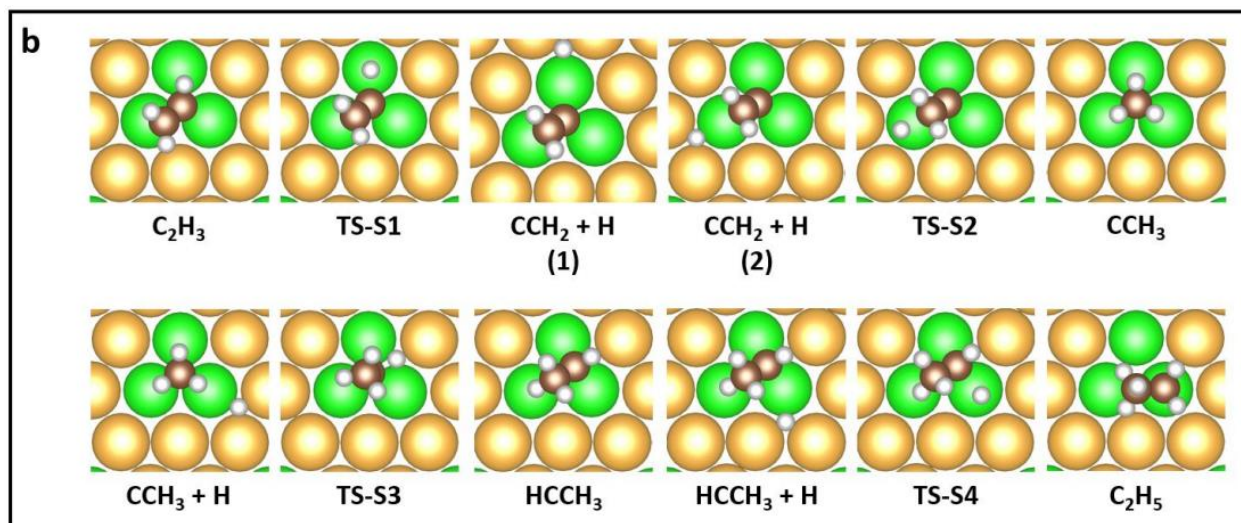
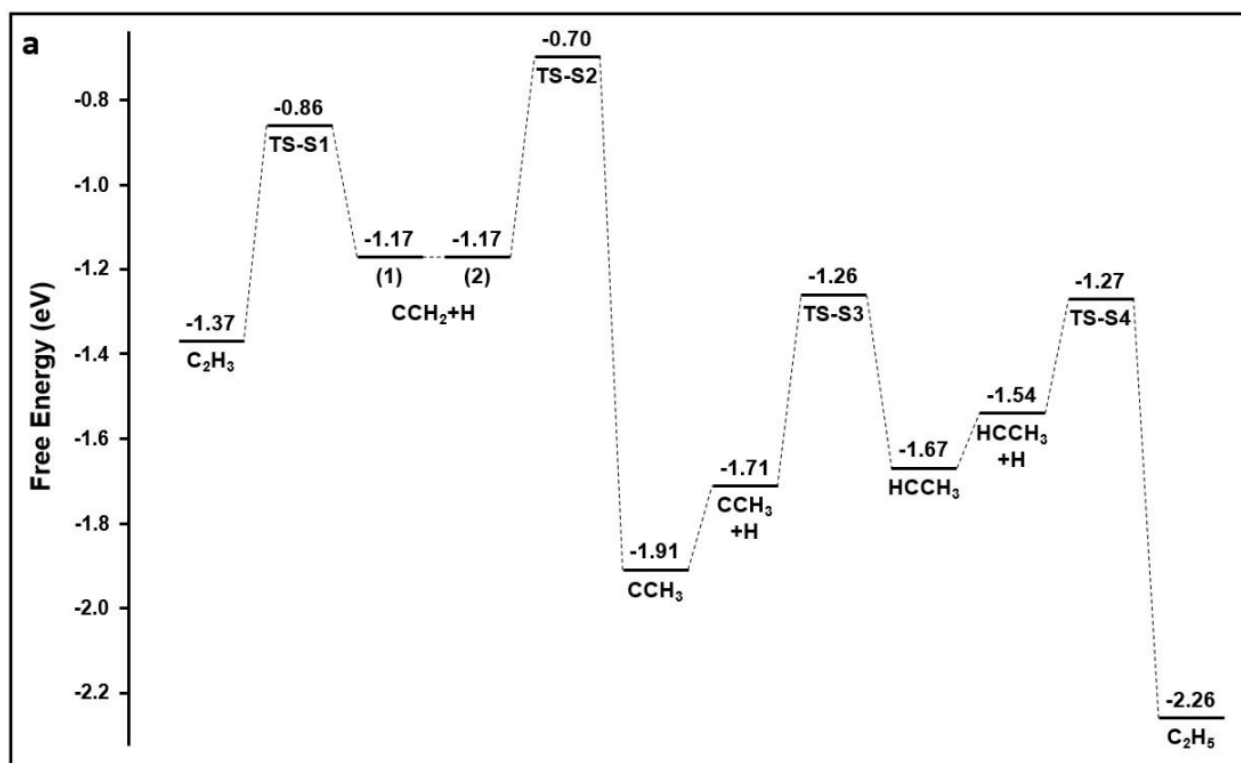


Figure C.8. (a) Free energy profile and (b) corresponding adsorption configurations of ethynyl hydrogenation to form ethyl via ethylidyne on  $Pd_3$  evaluated at  $T = 363$  K and under the standard-state pressures of gaseous species. Note that this reaction pathway was not included in the microkinetic modeling as it is significantly less favorable than the regular pathway to form  $C_2H_5$ .

### C.3 Catalyst Surface Coverage

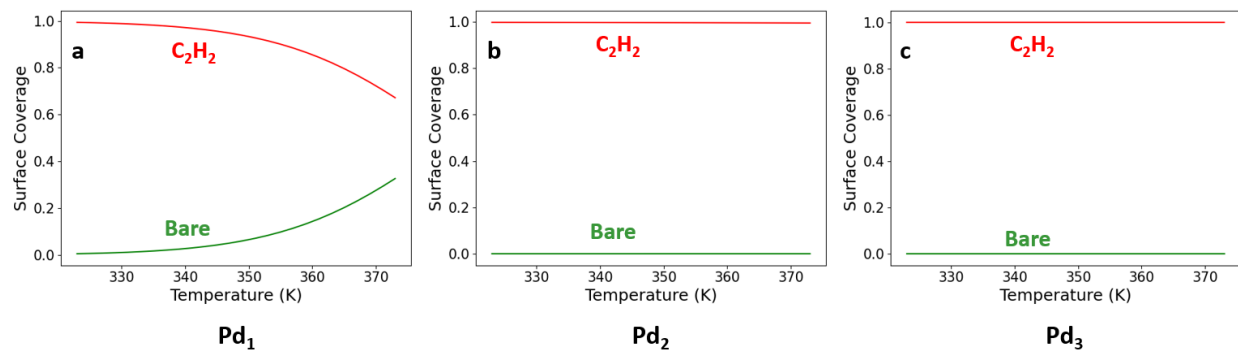


Figure C.9. Surface coverage of the active sites of the dilute Pd-in-Au alloy catalyst at steady states as a function of temperature. The study was performed under the following conditions:  $P(\text{H}_2) = 0.2$  bar,  $P(\text{C}_2\text{H}_2) = 0.01$  bar,  $P(\text{C}_2\text{H}_4) = 0.001$  bar and  $P(\text{C}_2\text{H}_6) = 0.001$  bar.

## C.4 Degree of Rate Control of Surface Intermediates and Apparent Activation Energies

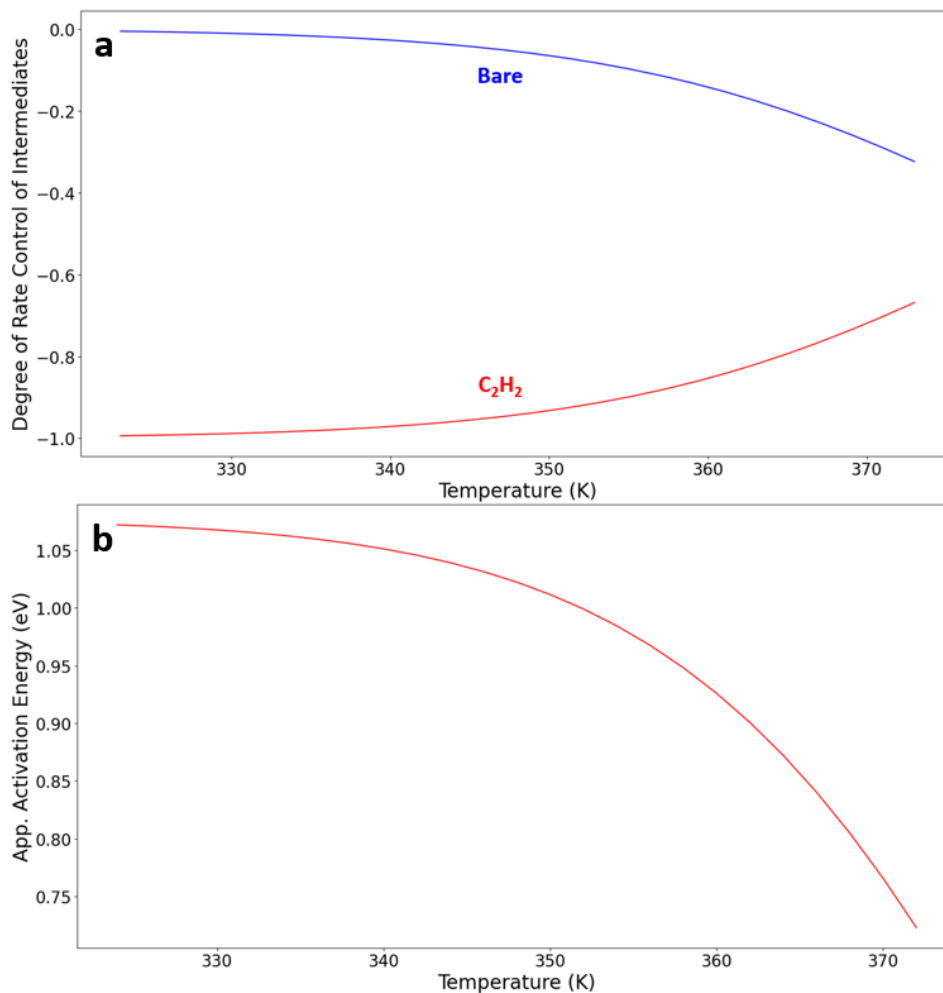


Figure C.10. (a) Degree of rate control of surface intermediates and (b) apparent activation energy for acetylene hydrogenation on Pd<sub>1</sub> calculated using microkinetic simulations. The calculations were performed at  $P(\text{C}_2\text{H}_2) = 0.01$  bar,  $P(\text{H}_2) = 0.2$  bar,  $P(\text{C}_2\text{H}_4) = 0.001$  bar, and  $P(\text{C}_2\text{H}_6) = 0.001$  bar.

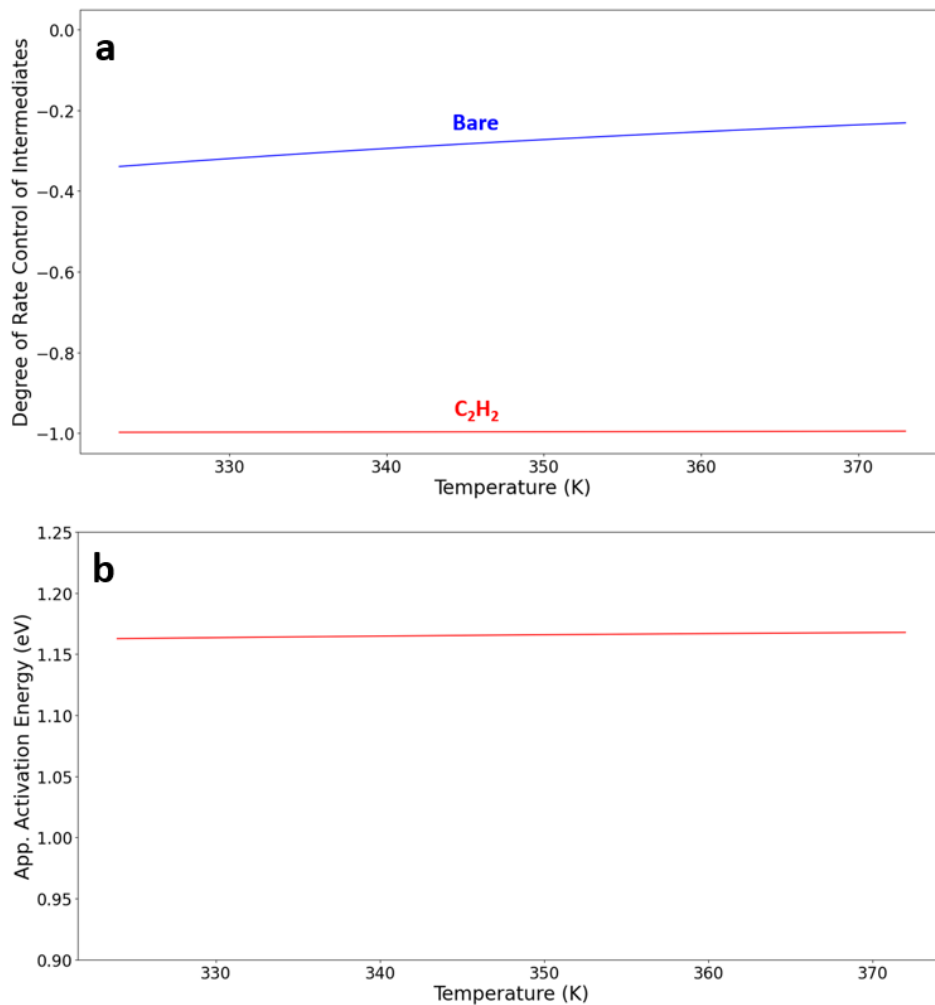


Figure C.11. (a) Degree of rate control of surface intermediates and (b) apparent activation energy for acetylene hydrogenation on Pd<sub>2</sub> calculated using microkinetic simulations. The calculations were performed at P(C<sub>2</sub>H<sub>2</sub>) = 0.01 bar, P(H<sub>2</sub>) = 0.2 bar, P(C<sub>2</sub>H<sub>4</sub>) = 0.001 bar, and P(C<sub>2</sub>H<sub>6</sub>) = 0.001 bar.

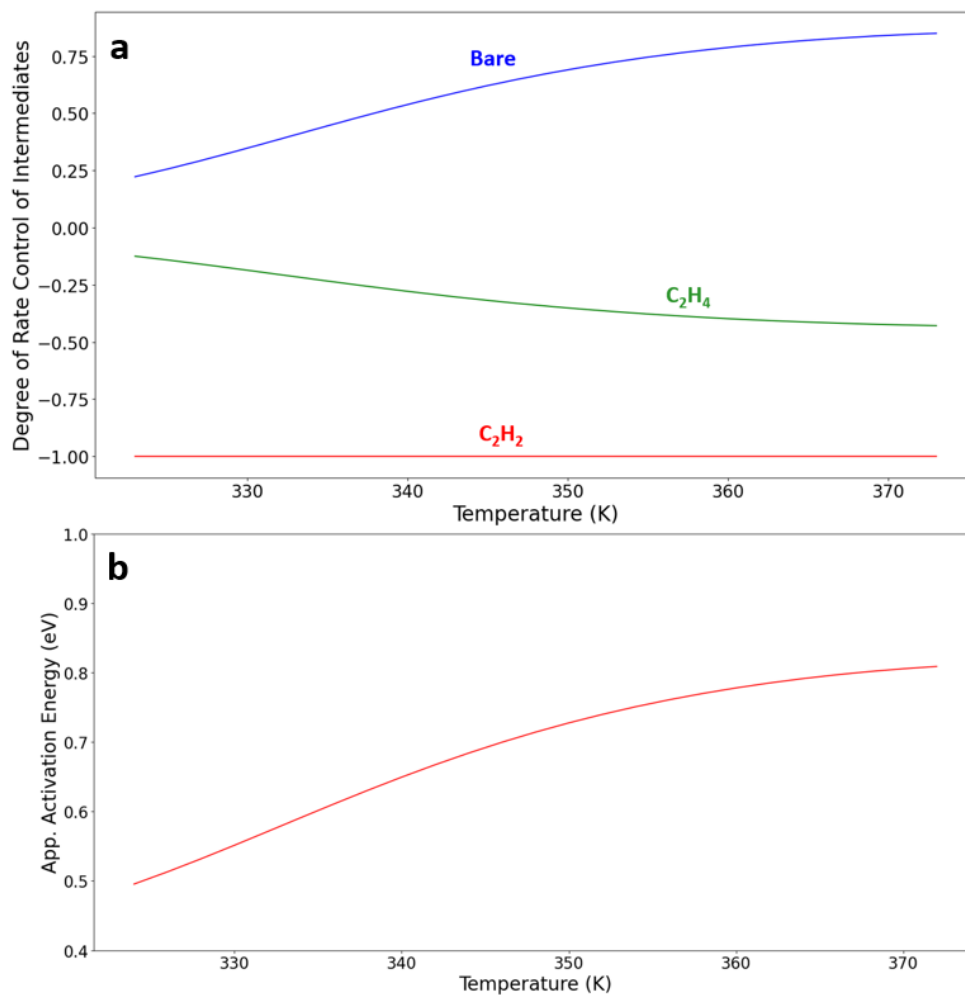


Figure C.12. (a) Degree of rate control of surface intermediates and (b) apparent activation energy for acetylene hydrogenation on Pd<sub>3</sub> calculated using microkinetic simulations. The calculations were performed at P(C<sub>2</sub>H<sub>2</sub>) = 0.01 bar, P(H<sub>2</sub>) = 0.2 bar, P(C<sub>2</sub>H<sub>4</sub>) = 0.001 bar, and P(C<sub>2</sub>H<sub>6</sub>) = 0.001 bar.

## C.5 Reaction Network of Acetylene Hydrogenation on Pd<sub>3</sub>

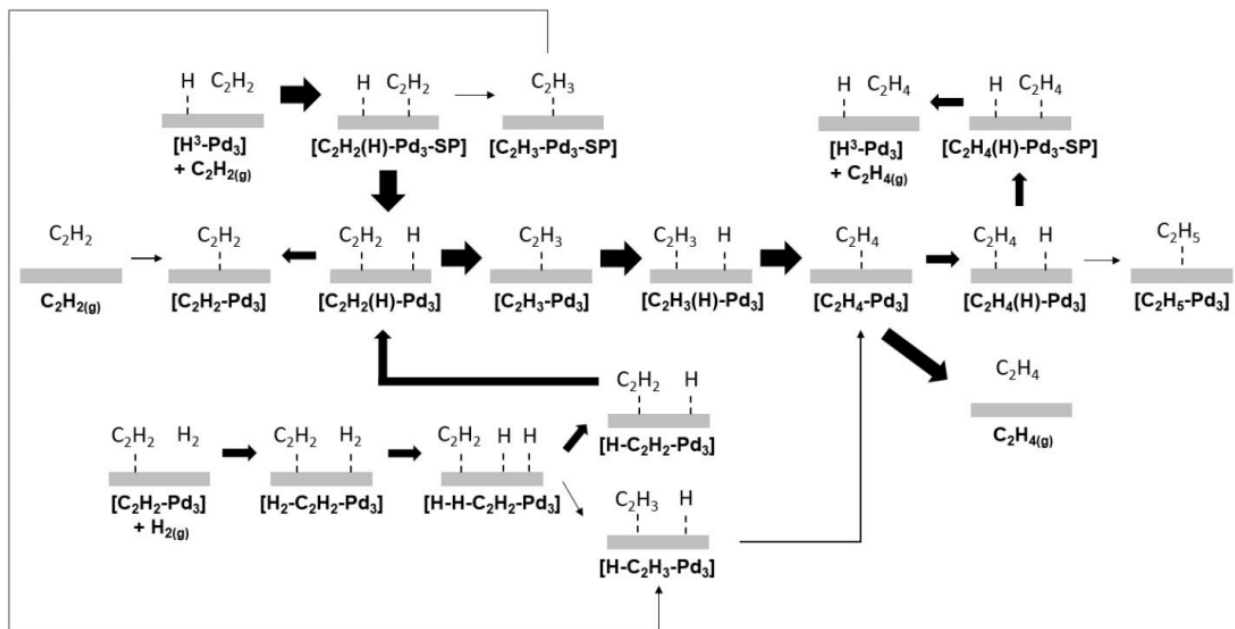


Figure C.13. Simplified reaction network of acetylene hydrogenation on Pd<sub>3</sub>, with the special pathway on top, regular pathway in the middle, and no-migration pathway at the bottom. The thickness of the arrows indicates the magnitude of the reaction rate of each elementary step. Elementary steps with negligible reaction rates are omitted from this reaction network.

## C.6 Ensemble Size Distribution in Pd-Au Catalyst

Table C.4. Probability of Finding Pd as Monomers, Dimers, and Trimers Based on the Binomial Distribution for the Surface Atoms, Assuming a Uniform Distribution of Pd

Sample	% of Pd as Monomers	% of Pd as Dimers	% of Pd as Trimers
Au <sub>0.98</sub> Pd <sub>0.02</sub>	88.6	10.8	0.6
Au <sub>0.96</sub> Pd <sub>0.04</sub>	78.4	19.6	2.0
Au <sub>0.91</sub> Pd <sub>0.09</sub>	56.8	33.6	8.4
Au <sub>0.75</sub> Pd <sub>0.25</sub>	17.8	35.6	29.6

## Appendix D Supplementary Information for Chapter 5

### D.1 Detailed Description of Microkinetic Model

Table D.1. Elementary steps considered in the microkinetic modeling of acrolein hydrogenation on CuCr<sub>1</sub>. Co-adsorption of a reaction intermediate with a H atom is denoted as [X(H) – Cr<sub>1</sub>] or [(H)X – Cr<sub>1</sub>], where X is the reaction intermediate. The suffixes “OB” and “PB” represent the C=O and C=C binding modes, respectively. A total of 17 elementary steps were considered, where step 1 is the dissociative adsorption of H<sub>2</sub> on Cu(111), steps 2 – 5 are H<sub>2</sub> activation on Cr<sub>1</sub> and subsequent migration towards the Cu surface, steps 6 – 11 represent the hydrogenation of the C=O bond in acrolein, and steps 12 – 17 illustrate the hydrogenation of the C=C bond in the same molecule.

#	Elementary Step
1	$\text{H}_{2(\text{g})} + 2[\text{Cu}] \rightleftharpoons 2[\text{H} - \text{Cu}]$
2	$\text{H}_{2(\text{g})} + [\text{Cr}_1] \rightleftharpoons [\text{H}_2 - \text{Cr}_1]$
3	$[\text{H}_2 - \text{Cr}_1] \rightleftharpoons [\text{H} - \text{Cr}_1 - \text{H}]$
4	$[\text{H} - \text{Cr}_1 - \text{H}] + [\text{Cu}] \rightleftharpoons [\text{H} - \text{Cr}_1] + [\text{H} - \text{Cu}]$
5	$[\text{H} - \text{Cr}_1] + [\text{Cu}] \rightleftharpoons [\text{H} - \text{Cu}] + [\text{Cr}_1]$
6	$\text{CH}_2\text{CHCHO}_{(\text{g})} + [\text{Cr}_1] \rightleftharpoons [\text{CH}_2\text{CHCHO} - \text{Cr}_1 - \text{OB}]$
7	$[\text{CH}_2\text{CHCHO} - \text{Cr}_1 - \text{OB}] + [\text{H} - \text{Cu}] \rightleftharpoons [\text{CH}_2\text{CHCHO}(\text{H}) - \text{Cr}_1 - \text{OB}] + [\text{Cu}]$
8	$[\text{CH}_2\text{CHCHO}(\text{H}) - \text{Cr}_1 - \text{OB}] \rightleftharpoons [\text{CH}_2\text{CHCH}_2\text{O} - \text{Cr}_1 - \text{OB}]$
9	$[\text{CH}_2\text{CHCH}_2\text{O} - \text{Cr}_1 - \text{OB}] + [\text{H} - \text{Cu}] \rightleftharpoons [\text{CH}_2\text{CHCH}_2\text{O}(\text{H}) - \text{Cr}_1 - \text{OB}] + [\text{Cu}]$
10	$[\text{CH}_2\text{CHCH}_2\text{O}(\text{H}) - \text{Cr}_1 - \text{OB}] \rightleftharpoons [\text{CH}_2\text{CHCH}_2\text{OH} - \text{Cr}_1 - \text{OB}]$
11	$\text{CH}_2\text{CHCH}_2\text{OH}_{(\text{g})} + [\text{Cr}_1] \rightleftharpoons [\text{CH}_2\text{CHCH}_2\text{OH} - \text{Cr}_1 - \text{OB}]$
12	$[\text{CH}_2\text{CHCHO} - \text{Cr}_1 - \text{OB}] \rightleftharpoons [\text{CH}_2\text{CHCHO} - \text{Cr}_1 - \text{PB}]$
13	$[\text{CH}_2\text{CHCHO} - \text{Cr}_1 - \text{PB}] + [\text{H} - \text{Cu}] \rightleftharpoons [(\text{H})\text{CH}_2\text{CHCHO} - \text{Cr}_1 - \text{PB}] + [\text{Cu}]$
14	$[(\text{H})\text{CH}_2\text{CHCHO} - \text{Cr}_1 - \text{PB}] \rightleftharpoons [\text{CH}_3\text{CHCHO} - \text{Cr}_1 - \text{PB}]$
15	$[\text{CH}_3\text{CHCHO} - \text{Cr}_1 - \text{PB}] + [\text{H} - \text{Cu}] \rightleftharpoons [(\text{H})\text{CH}_3\text{CHCHO} - \text{Cr}_1 - \text{PB}] + [\text{Cu}]$
16	$[(\text{H})\text{CH}_3\text{CHCHO} - \text{Cr}_1 - \text{PB}] \rightleftharpoons [\text{CH}_3\text{CH}_2\text{CHO} - \text{Cr}_1 - \text{PB}]$
17	$\text{CH}_3\text{CH}_2\text{CHO}_{(\text{g})} + [\text{Cr}_1] \rightleftharpoons [\text{CH}_3\text{CH}_2\text{CHO} - \text{Cr}_1 - \text{PB}]$

## D.2 Supplementary Energetics and Adsorption Configurations

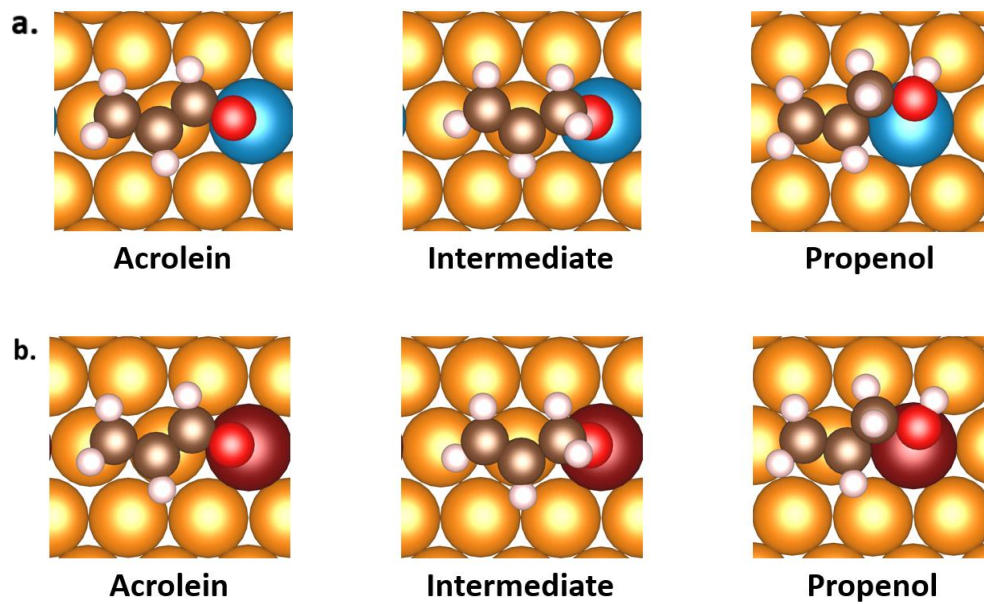


Figure D.1. Reaction configurations for acrolein hydrogenation on (a) CuZr<sub>1</sub> and (b) CuHf<sub>1</sub>.

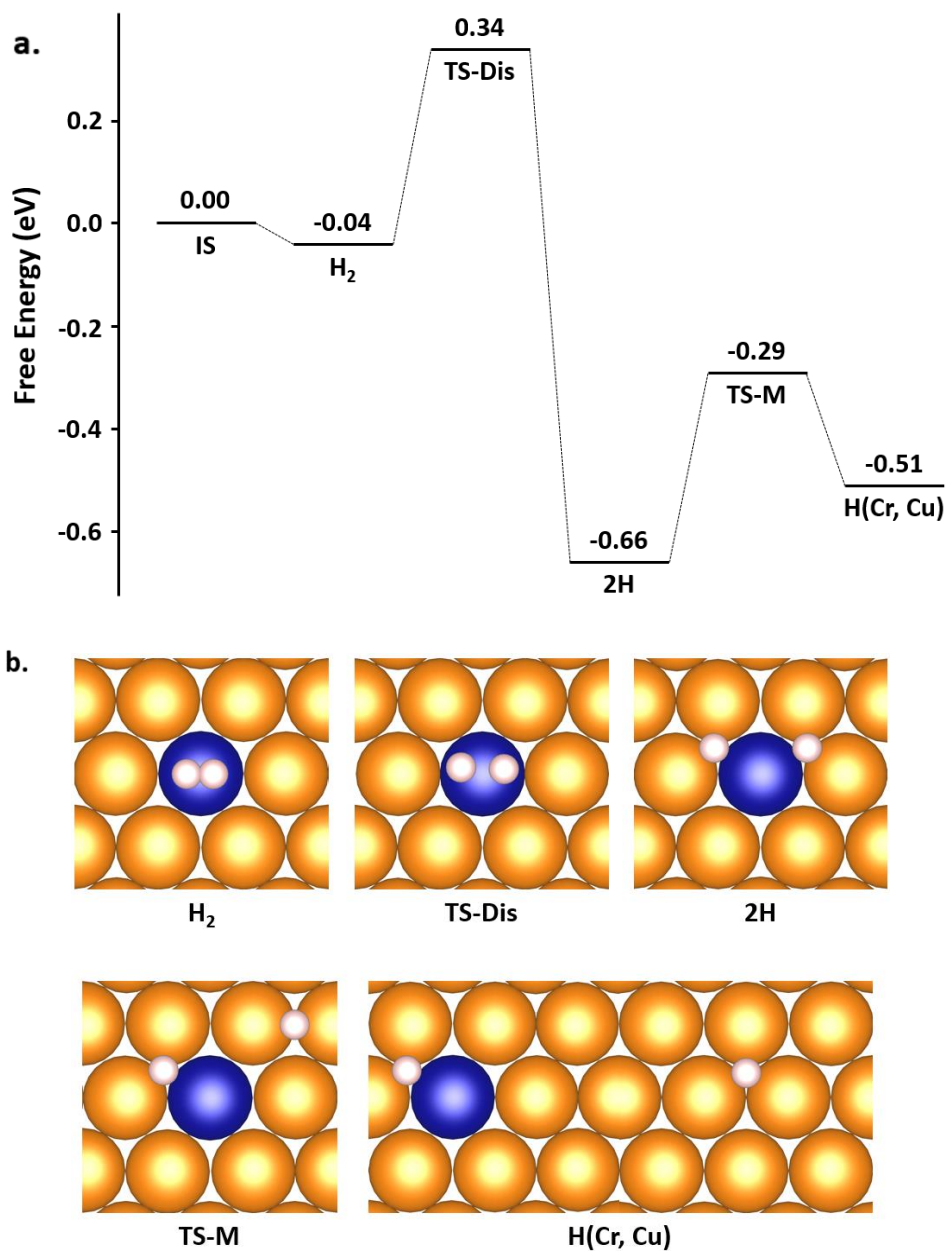


Figure D.2. (a) Free energy profile and (b) corresponding reaction configurations for H<sub>2</sub> activation on CuCr<sub>1</sub>. The notations used are defined as: H<sub>2</sub> – molecular adsorption of hydrogen, TS-Diss – transition state for dissociation, 2H – co-adsorption of two H atoms on the same Cr<sub>1</sub> ensemble, TS-M – transition state for migration of one H atom away from the Cr<sub>1</sub> ensemble, and H(Cr, Cu) – adsorption of one H atom on the Cr<sub>1</sub> ensemble and the other one on the Cu(111) surface. Reaction conditions are T = 375 K and P(H<sub>2</sub>) = 300 bar.

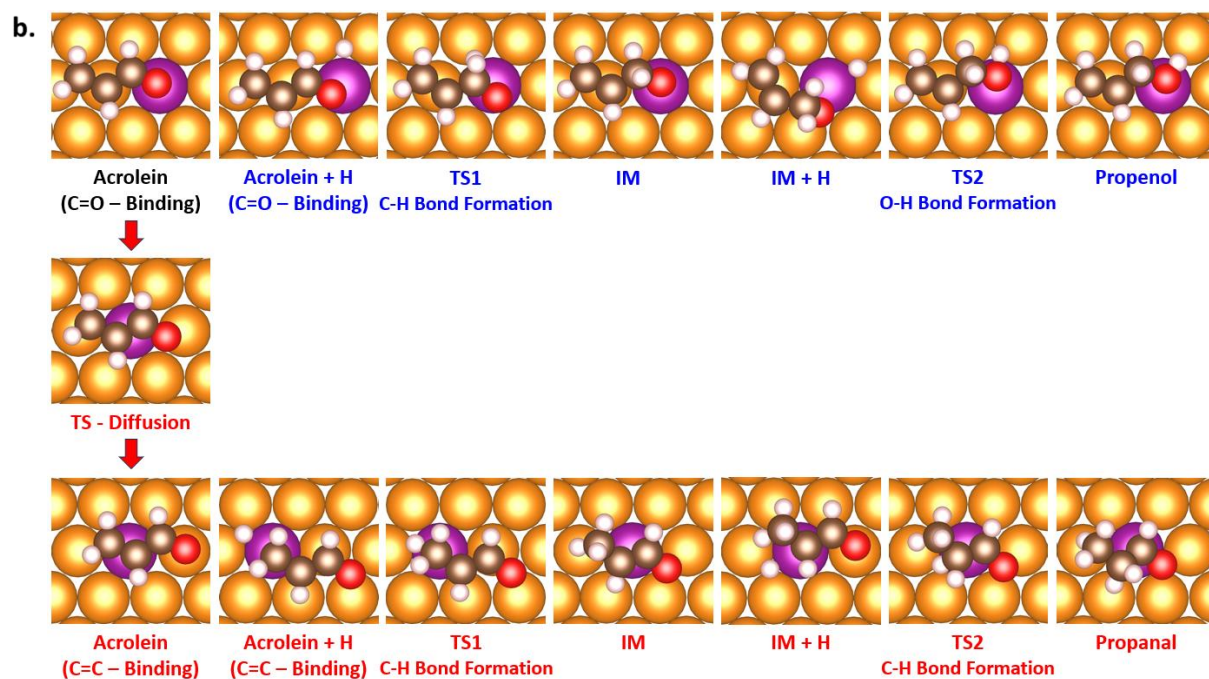
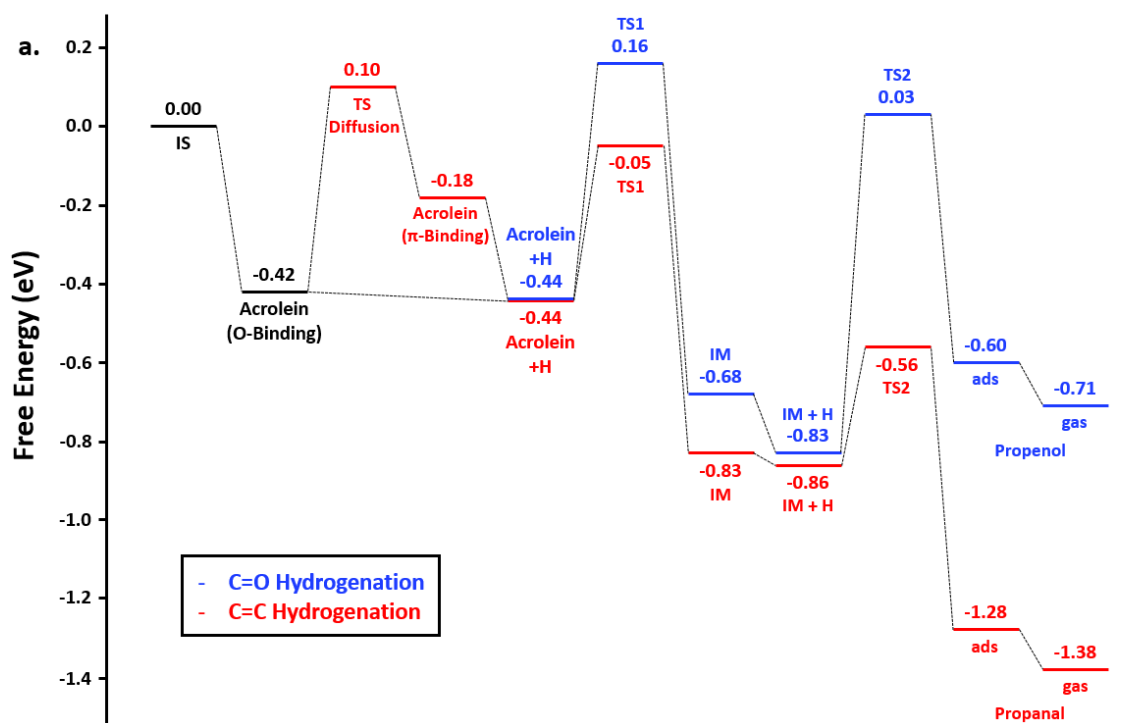


Figure D.3. (a) Free energy profile and (b) corresponding reaction configurations for hydrogenation of the C=O bond (blue) and C=C bond (red) in acrolein on CuMn<sub>1</sub>. Reaction conditions are T = 375 K, P(Acrolein) = 0.1 bar, P(H<sub>2</sub>) = 300 bar, P(Propanal) = P(Propenol) =

0.01 bar.

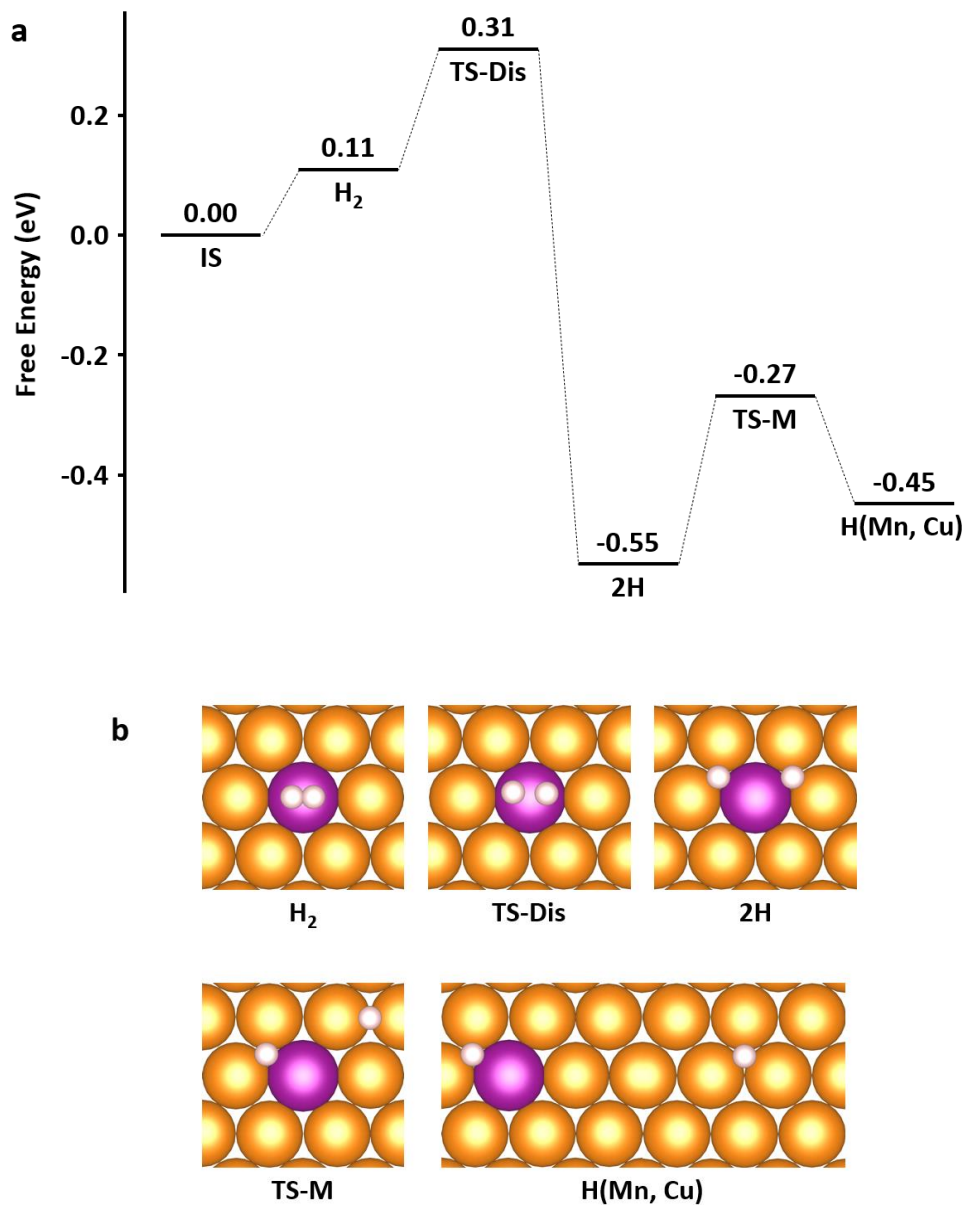


Figure D.4. (a) Free energy profile and (b) corresponding reaction configurations for H<sub>2</sub> activation on CuMn<sub>1</sub>. The notations used are defined as: H<sub>2</sub> – molecular adsorption of hydrogen, TS-Dis – transition state for dissociation, 2H – co-adsorption of two H atoms on the same Mn<sub>1</sub> ensemble, TS-M – transition state for migration of one H atom away from the Mn<sub>1</sub> ensemble, and H(Mn, Cu) – adsorption of one H atom on the Mn<sub>1</sub> ensemble and the other one on the Cu(111) surface.

Reaction conditions are  $T = 375$  K and  $P(\text{H}_2) = 300$  bar.

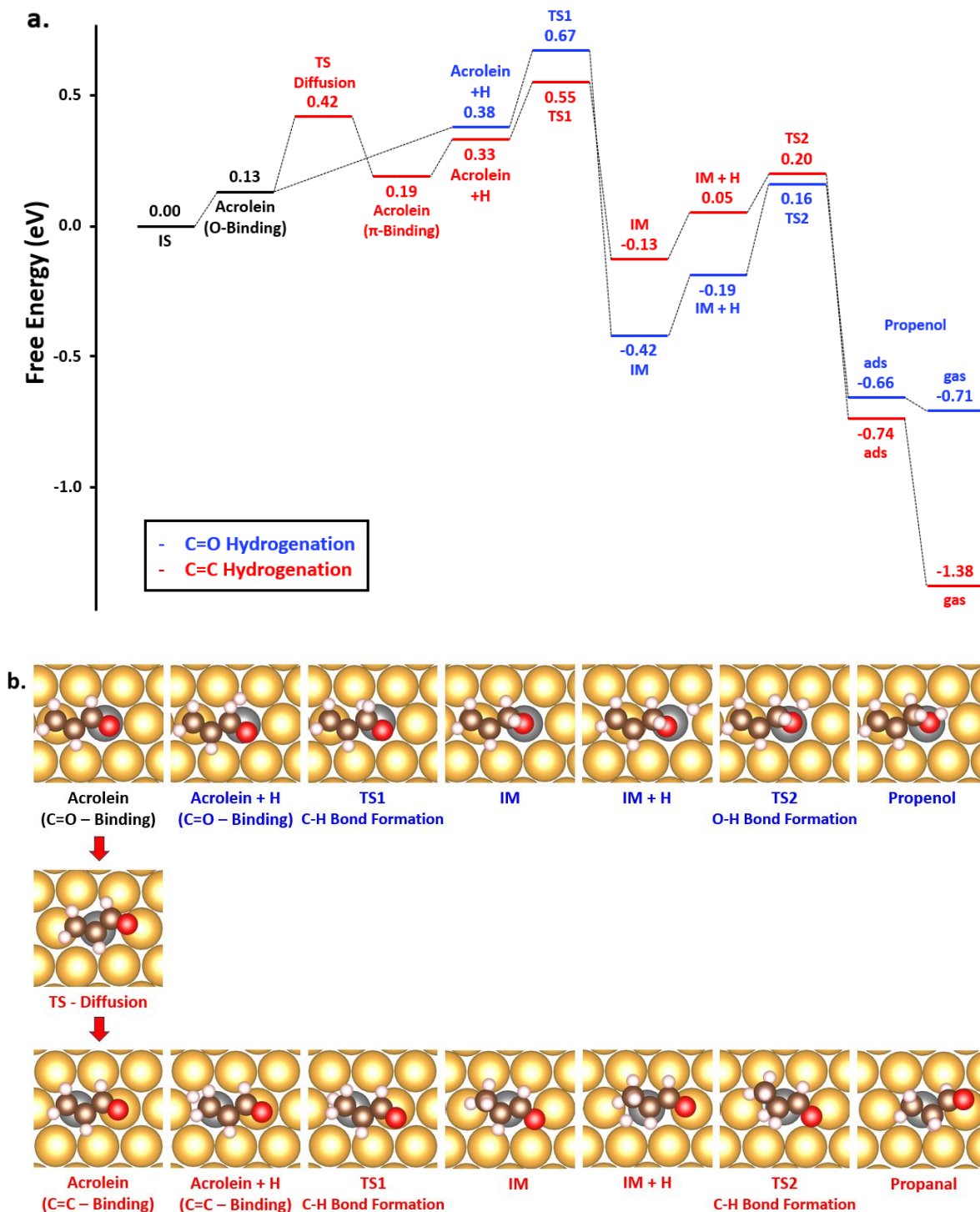


Figure D.5. (a) Free energy profile and (b) corresponding reaction configurations for hydrogenation of the C=O bond (blue) and C=C bond (red) in acrolein on AuFe<sub>1</sub>. Reaction

conditions are  $T = 375 \text{ K}$ ,  $P(\text{Acrolein}) = 0.1 \text{ bar}$ ,  $P(\text{H}_2) = 300 \text{ bar}$ ,  $P(\text{Propanal}) = P(\text{Propenol}) = 0.01 \text{ bar}$ .

### D.3 Degree of Rate and Selectivity Controls

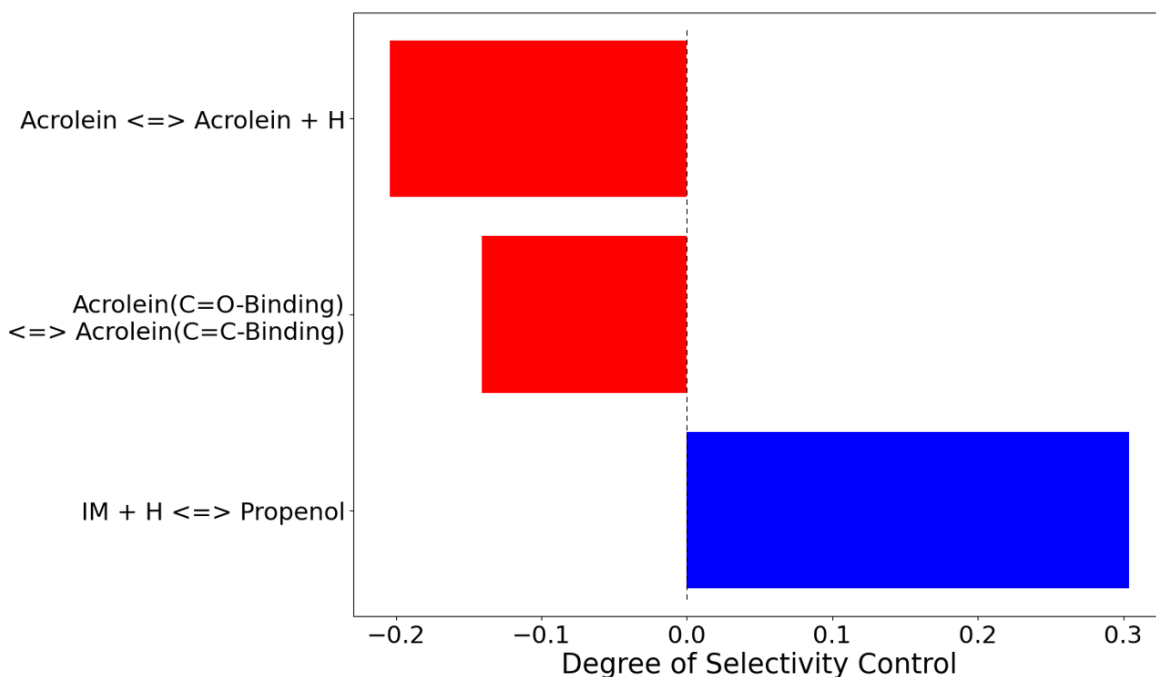


Figure D.6. Degree of selectivity control (DSC) of the transition states in the reaction network. For simplicity, only the transition states with significant DSC values are shown. Steps in the hydrogenation of the C=O bond and C=C bond of the acrolein molecule are represented in blue and red, respectively. Reaction conditions are:  $T = 375 \text{ K}$ ,  $P(\text{Acrolein}) = 0.1 \text{ bar}$ ,  $P(\text{H}_2) = 300 \text{ bar}$ ,  $P(\text{Propanal}) = 0.01 \text{ bar}$ , and  $P(\text{Propenol}) = 0.01 \text{ bar}$ .

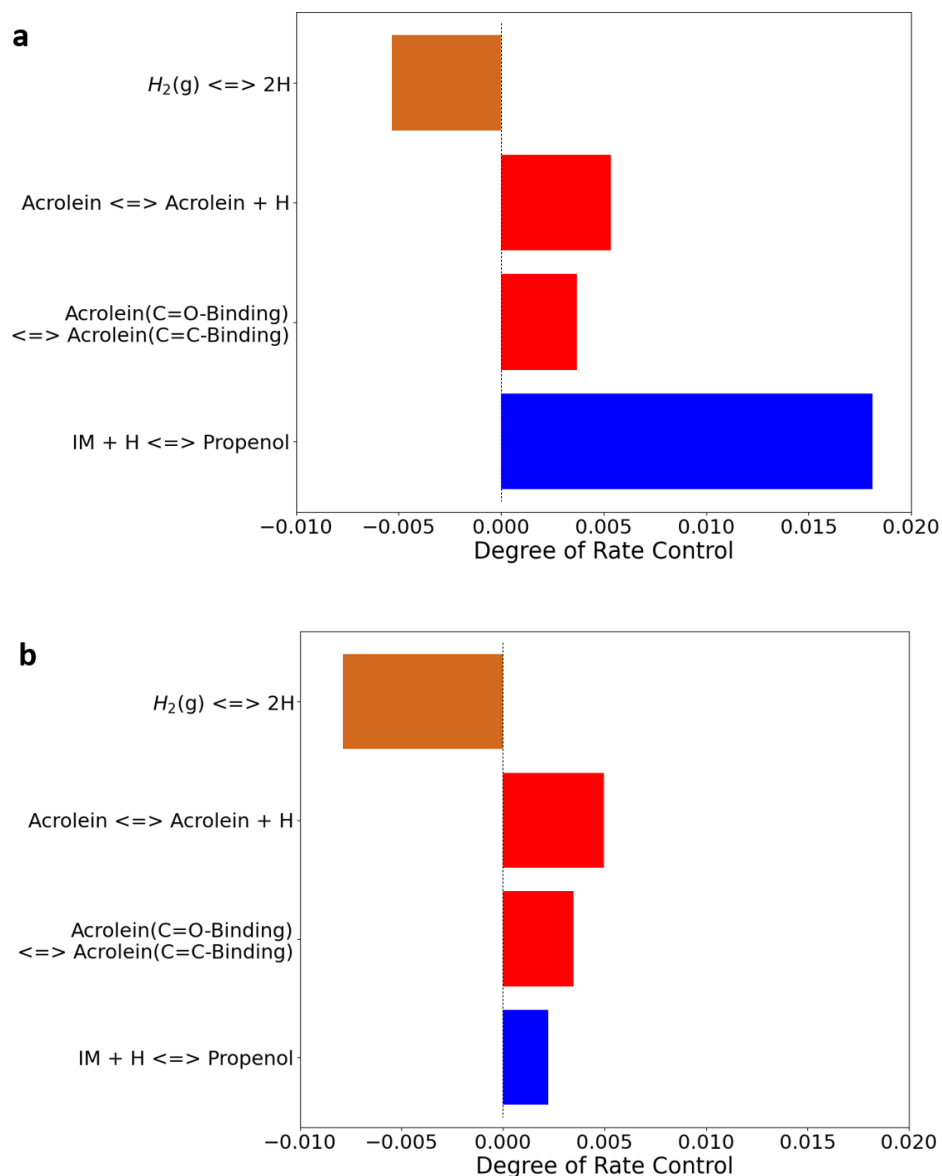


Figure D.7. Degree of rate control (DRC) of transition states at (a)  $T = 375$  K and (b)  $T = 475$  K on  $CuCr_1$ . Steps in the hydrogenation of the C=O bond and C=C bond of the acrolein molecule are represented in blue and red, respectively, whereas the step of  $H_2$  dissociation on  $Cu(111)$  is represented in brown. The most rate-controlling transition state under both conditions is acrolein adsorption, with the DRC values being close to 1 (0.98 at  $T = 375$  K and 1.00 at  $T = 475$  K). It is omitted in this study to demonstrate the differences between the other steps. Reaction conditions are:  $P(\text{Acrolein}) = 0.1$  bar,  $P(H_2) = 300$  bar,  $P(\text{Propanal}) = 0.01$  bar, and  $P(\text{Propenol}) = 0.01$  bar.

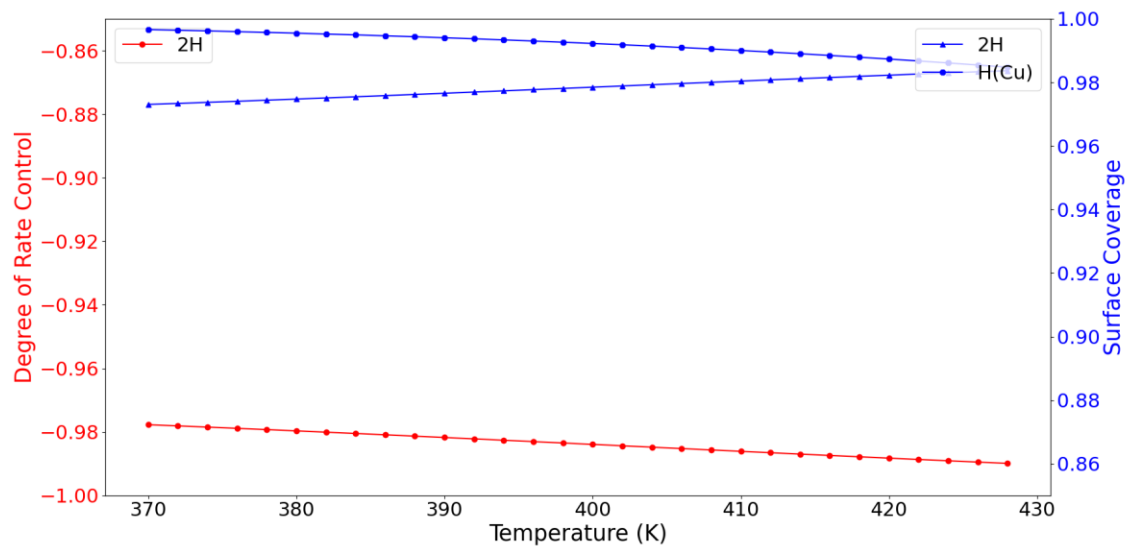


Figure D.8. Degree of rate control (DRC; red) of the “2H” state on the Cr active sites and the surface coverage (blue) of H atoms on the catalyst surface. “2H” corresponds to H-adsorption on the Cr active sites and H(Cu) corresponds to the adsorption on the Cu(111) surface. Surface coverage is normalized with respect to the total number of active sites and Cu sites. Reaction conditions are: P(Acrolein) = 0.1 bar, P(H<sub>2</sub>) = 300 bar, P(Propanal) = 0.01 bar, and P(Propenol) = 0.01 bar.

## D.4 Additional Microkinetic Simulations

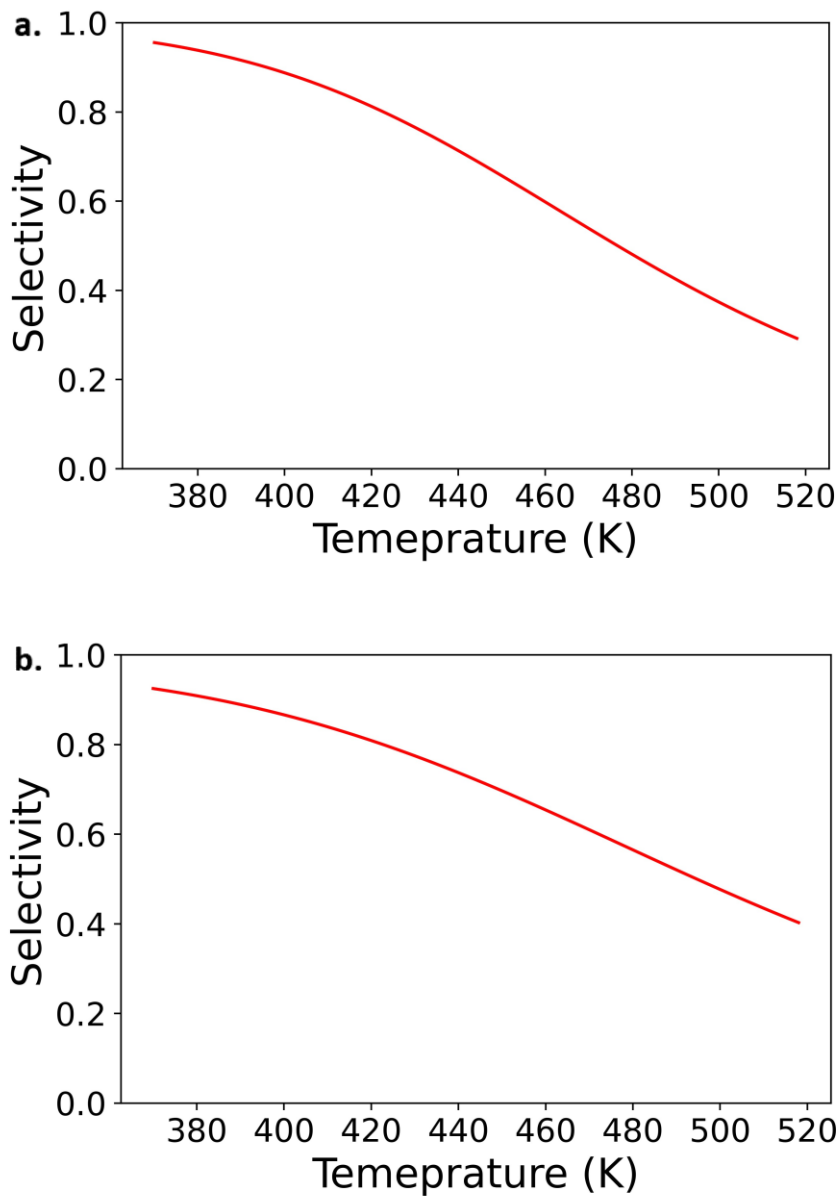


Figure D.9. Calculated selectivity for propenol formation on CuCr<sub>1</sub> after (a) increasing the diffusion transition state energy by 0.1 eV and (b) lowering the transition state energy for O-H bond formation by 0.1 eV. Reaction conditions are: P(Acrolein) = 0.1 bar, P(H<sub>2</sub>) = 300 bar, P(Propanal) = 0.01 bar, and P(Propenol) = 0.01 bar.

## D.5. Magnetization of Dopants in Cu(111)

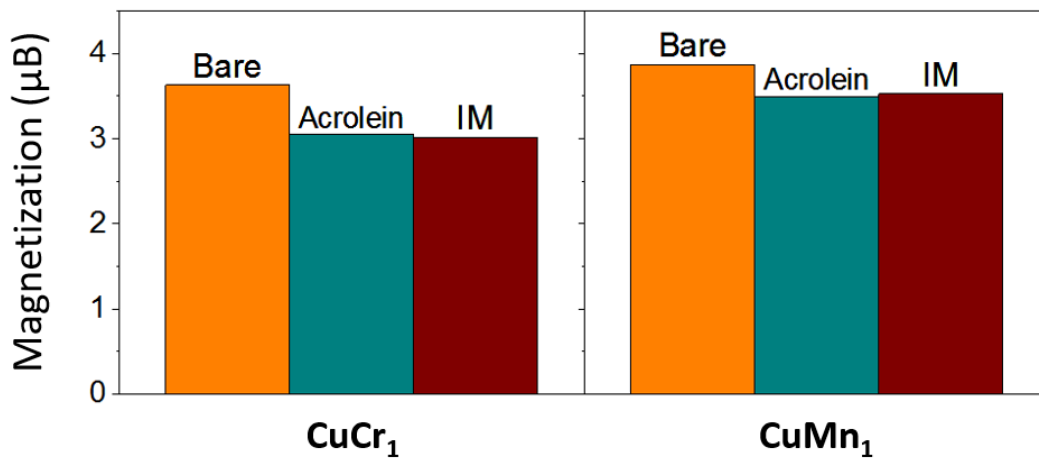


Figure D.10. Magnetization of the dopants (Cr and Mn) in Cu(111) when the surface is bare (orange), and in the presence of acrolein (teal) and mono-hydrogenated intermediate (maroon). Acrolein adopts the C=O binding configuration for this magnetization calculation, and the mono-hydrogenated intermediate reported here is the one formed after hydrogenating the C atom in the C=O bond.

## Appendix E Supplementary Information for Chapter 6

### E.1 Detailed Description of Microkinetic Model

Table E.1. Elementary steps considered in the microkinetic modeling of propane dehydrogenation on CuHf<sub>1</sub>. Co-adsorption of a reaction intermediate with a H atom is denoted as [X(H) – Hf<sub>1</sub>], where X is the reaction intermediate. A total of 17 elementary steps were considered, where step 1 is the recombination of H atoms on the Cu(111) surface, steps 2-5 are the same process on the active ensemble, step 6 is the adsorption of the propane molecule, steps 7-9 (dehydrogenate central C atom first) and 10-12 (dehydrogenate terminal C atom first) correspond to the two different pathways for propane activation, steps 13-14 are H-migration away from propylene adsorption site, followed by propylene desorption, and steps 15-17 are further dehydrogenation of propylene.

#	Elementary Step
1	$2[\text{H} - \text{Cu}] \rightleftharpoons \text{H}_{2(\text{g})} + 2[\text{Cu}]$
2	$[\text{H} - \text{Cu}] + [\text{Hf}_1] \rightleftharpoons [\text{H} - \text{Hf}_1] + [\text{Cu}]$
3	$[\text{H} - \text{Cu}] + [\text{H} - \text{Hf}_1] \rightleftharpoons [\text{H} - \text{Hf}_1 - \text{H}] + [\text{Cu}]$
4	$[\text{H} - \text{Hf}_1 - \text{H}] \rightleftharpoons [\text{H}_2 - \text{Hf}_1]$
5	$[\text{H}_2 - \text{Hf}_1] \rightleftharpoons \text{H}_{2(\text{g})} + [\text{Hf}_1]$
6	$\text{C}_3\text{H}_{8(\text{g})} + [\text{Hf}_1] \rightleftharpoons [\text{C}_3\text{H}_8 - \text{Hf}_1]$
7	$[\text{C}_3\text{H}_8 - \text{Hf}_1] \rightleftharpoons [\text{CH}_3\text{CHCH}_3(\text{H}) - \text{Hf}_1]$
8	$[\text{CH}_3\text{CHCH}_3(\text{H}) - \text{Hf}_1] + [\text{Cu}] \rightleftharpoons [\text{CH}_3\text{CHCH}_3 - \text{Hf}_1] + [\text{H} - \text{Cu}]$
9	$[\text{CH}_3\text{CHCH}_3 - \text{Hf}_1] \rightleftharpoons [\text{C}_3\text{H}_6(\text{H}) - \text{Hf}_1]$
10	$[\text{C}_3\text{H}_8 - \text{Hf}_1] \rightleftharpoons [\text{CH}_3\text{CH}_2\text{CH}_2(\text{H}) - \text{Hf}_1]$
11	$[\text{CH}_3\text{CH}_2\text{CH}_2(\text{H}) - \text{Hf}_1] + [\text{Cu}] \rightleftharpoons [\text{CH}_3\text{CH}_2\text{CH}_2 - \text{Hf}_1] + [\text{H} - \text{Cu}]$
12	$[\text{CH}_3\text{CH}_2\text{CH}_2 - \text{Hf}_1] \rightleftharpoons [\text{C}_3\text{H}_6(\text{H}) - \text{Hf}_1]$
13	$[\text{C}_3\text{H}_6(\text{H}) - \text{Hf}_1] + [\text{Cu}] \rightleftharpoons [\text{C}_3\text{H}_6 - \text{Hf}_1] + [\text{H} - \text{Cu}]$
14	$[\text{C}_3\text{H}_6 - \text{Hf}_1] \rightleftharpoons \text{C}_3\text{H}_{6(\text{g})} + [\text{Hf}_1]$
15	$[\text{C}_3\text{H}_6 - \text{Hf}_1] \rightleftharpoons [\text{CH}_2\text{CHCH}_2(\text{H}) - \text{Hf}_1]$
16	$[\text{CH}_2\text{CHCH}_2(\text{H}) - \text{Hf}_1] + [\text{Cu}] \rightleftharpoons [\text{CH}_2\text{CHCH}_2 - \text{Hf}_1] + [\text{H} - \text{Cu}]$
17	$[\text{CH}_2\text{CHCH}_2 - \text{Hf}_1] \rightleftharpoons [\text{CH}_2\text{CHCH}(\text{H}) - \text{Hf}_1]$

Table E.2. Elementary steps considered in the microkinetic modeling of propane dehydrogenation on CuIr<sub>1</sub>. Co-adsorption of a reaction intermediate with a H atom is denoted as [X(H) – Ir<sub>1</sub>], where X is the reaction intermediate. A total of 14 elementary steps were considered, where step 1 is the recombination of H atoms on the Cu(111) surface, steps 2-4 are the same process on the active ensemble, steps 5-7 (dehydrogenate central C atom first) and 8-10 (dehydrogenate terminal C atom first) correspond to the two different pathways for propane activation, steps 11-12 are H-migration away from propylene adsorption site, followed by propylene desorption, and steps 13-14 are further dehydrogenation of propylene.

#	Elementary Step
1	$2[\text{H} - \text{Cu}] \rightleftharpoons \text{H}_{2(\text{g})} + 2[\text{Cu}]$
2	$[\text{H} - \text{Cu}] + [\text{Ir}_1] \rightleftharpoons [\text{H} - \text{Ir}_1] + [\text{Cu}]$
3	$[\text{H} - \text{Cu}] + [\text{H} - \text{Ir}_1] \rightleftharpoons [\text{H} - \text{Ir}_1 - \text{H}] + [\text{Cu}]$
4	$[\text{H} - \text{Ir}_1 - \text{H}] \rightleftharpoons \text{H}_{2(\text{g})} + [\text{Ir}_1]$
5	$\text{C}_3\text{H}_{8(\text{g})} + [\text{Ir}_1] \rightleftharpoons [\text{CH}_3\text{CHCH}_3(\text{H}) - \text{Ir}_1]$
6	$[\text{CH}_3\text{CHCH}_3(\text{H}) - \text{Ir}_1] + [\text{Cu}] \rightleftharpoons [\text{CH}_3\text{CHCH}_3 - \text{Ir}_1] + [\text{H} - \text{Cu}]$
7	$[\text{CH}_3\text{CHCH}_3 - \text{Ir}_1] \rightleftharpoons [\text{C}_3\text{H}_6(\text{H}) - \text{Ir}_1]$
8	$\text{C}_3\text{H}_{8(\text{g})} + [\text{Ir}_1] \rightleftharpoons [\text{CH}_3\text{CH}_2\text{CH}_2(\text{H}) - \text{Ir}_1]$
9	$[\text{CH}_3\text{CH}_2\text{CH}_2(\text{H}) - \text{Ir}_1] + [\text{Cu}] \rightleftharpoons [\text{CH}_3\text{CH}_2\text{CH}_2 - \text{Ir}_1] + [\text{H} - \text{Cu}]$
10	$[\text{CH}_3\text{CH}_2\text{CH}_2 - \text{Ir}_1] \rightleftharpoons [\text{C}_3\text{H}_6(\text{H}) - \text{Ir}_1]$
11	$[\text{C}_3\text{H}_6(\text{H}) - \text{Ir}_1] + [\text{Cu}] \rightleftharpoons [\text{C}_3\text{H}_6 - \text{Ir}_1] + [\text{H} - \text{Cu}]$
12	$[\text{C}_3\text{H}_6 - \text{Ir}_1] \rightleftharpoons \text{C}_3\text{H}_{6(\text{g})} + [\text{Ir}_1]$
13	$[\text{C}_3\text{H}_6 - \text{Ir}_1] \rightleftharpoons [\text{CH}_2\text{CHCH}_2(\text{H}) - \text{Ir}_1]$
14	$[\text{CH}_2\text{CHCH}_2(\text{H}) - \text{Ir}_1] + [\text{Cu}] \rightleftharpoons [\text{CH}_2\text{CHCH}_2 - \text{Ir}_1] + [\text{H} - \text{Cu}]$

Table E.3. Elementary steps considered in the microkinetic modeling of propane dehydrogenation on CuRh<sub>1</sub>. Co-adsorption of a reaction intermediate with a H atom is denoted as [X(H) – Rh<sub>1</sub>], where X is the reaction intermediate. A total of 15 elementary steps were considered, where step 1 is the recombination of H atoms on the Cu(111) surface, steps 2-5 are the same process on the active ensemble, steps 6-8 (dehydrogenate central C atom first) and 9-11 (dehydrogenate terminal C atom first) correspond to the two different pathways for propane activation, steps 12-13 are H-migration away from propylene adsorption site, followed by propylene desorption, and steps 14-15 are further dehydrogenation of propylene.

#	Elementary Step
1	$2[\text{H} - \text{Cu}] \rightleftharpoons \text{H}_{2(\text{g})} + 2[\text{Cu}]$
2	$[\text{H} - \text{Cu}] + [\text{Rh}_1] \rightleftharpoons [\text{H} - \text{Rh}_1] + [\text{Cu}]$
3	$[\text{H} - \text{Cu}] + [\text{H} - \text{Rh}_1] \rightleftharpoons [\text{H} - \text{Rh}_1 - \text{H}] + [\text{Cu}]$
4	$[\text{H} - \text{Rh}_1 - \text{H}] \rightleftharpoons [\text{H}_2 - \text{Rh}_1]$
5	$[\text{H}_2 - \text{Rh}_1] \rightleftharpoons \text{H}_{2(\text{g})} + [\text{Rh}_1]$
6	$\text{C}_3\text{H}_{8(\text{g})} + [\text{Rh}_1] \rightleftharpoons [\text{CH}_3\text{CHCH}_3(\text{H}) - \text{Rh}_1]$
7	$[\text{CH}_3\text{CHCH}_3(\text{H}) - \text{Rh}_1] + [\text{Cu}] \rightleftharpoons [\text{CH}_3\text{CHCH}_3 - \text{Rh}_1] + [\text{H} - \text{Cu}]$
8	$[\text{CH}_3\text{CHCH}_3 - \text{Rh}_1] \rightleftharpoons [\text{C}_3\text{H}_6(\text{H}) - \text{Rh}_1]$
9	$\text{C}_3\text{H}_{8(\text{g})} + [\text{Rh}_1] \rightleftharpoons [\text{CH}_3\text{CH}_2\text{CH}_2(\text{H}) - \text{Rh}_1]$
10	$[\text{CH}_3\text{CH}_2\text{CH}_2(\text{H}) - \text{Rh}_1] + [\text{Cu}] \rightleftharpoons [\text{CH}_3\text{CH}_2\text{CH}_2 - \text{Rh}_1] + [\text{H} - \text{Cu}]$
11	$[\text{CH}_3\text{CH}_2\text{CH}_2 - \text{Rh}_1] \rightleftharpoons [\text{C}_3\text{H}_6(\text{H}) - \text{Rh}_1]$
12	$[\text{C}_3\text{H}_6(\text{H}) - \text{Rh}_1] + [\text{Cu}] \rightleftharpoons [\text{C}_3\text{H}_6 - \text{Rh}_1] + [\text{H} - \text{Cu}]$
13	$[\text{C}_3\text{H}_6 - \text{Rh}_1] \rightleftharpoons \text{C}_3\text{H}_{6(\text{g})} + [\text{Rh}_1]$
14	$[\text{C}_3\text{H}_6 - \text{Rh}_1] \rightleftharpoons [\text{CH}_2\text{CHCH}_2(\text{H}) - \text{Rh}_1]$
15	$[\text{CH}_2\text{CHCH}_2(\text{H}) - \text{Rh}_1] + [\text{Cu}] \rightleftharpoons [\text{CH}_2\text{CHCH}_2 - \text{Rh}_1] + [\text{H} - \text{Cu}]$

Table E.4. Elementary steps considered in the microkinetic modeling of propane dehydrogenation on Pt(111). A total of 8 elementary steps were considered, where step 1 is the recombination of H atoms on the Pt(111) surface, step 2 is the adsorption of the propane molecule, steps 3-4 (dehydrogenate central C atom first) and 5-6 (dehydrogenate terminal C atom first) correspond to the two different pathways for propane activation, step 7 is propylene desorption, and step 8 is the further dehydrogenation of propylene.

#	Elementary Step
1	$2[\text{H} - \text{Pt}] \rightleftharpoons \text{H}_{2(\text{g})} + 2[\text{Pt}]$
2	$\text{C}_3\text{H}_{8(\text{g})} + [\text{Pt}] \rightleftharpoons [\text{C}_3\text{H}_8 - \text{Pt}]$
3	$[\text{C}_3\text{H}_8 - \text{Pt}] + [\text{Pt}] \rightleftharpoons [\text{CH}_3\text{CHCH}_3 - \text{Pt}] + [\text{H} - \text{Pt}]$
4	$[\text{CH}_3\text{CHCH}_3 - \text{Pt}] + [\text{Pt}] \rightleftharpoons [\text{C}_3\text{H}_6 - \text{Pt}] + [\text{H} - \text{Pt}]$
5	$[\text{C}_3\text{H}_8 - \text{Pt}] + [\text{Pt}] \rightleftharpoons [\text{CH}_3\text{CH}_2\text{CH}_2 - \text{Pt}] + [\text{H} - \text{Pt}]$
6	$[\text{CH}_3\text{CH}_2\text{CH}_2 - \text{Pt}] + [\text{Pt}] \rightleftharpoons [\text{C}_3\text{H}_6 - \text{Pt}] + [\text{H} - \text{Pt}]$
7	$[\text{C}_3\text{H}_6 - \text{Pt}] \rightleftharpoons \text{C}_3\text{H}_{6(\text{g})} + [\text{Pt}]$
8	$[\text{C}_3\text{H}_6 - \text{Pt}] + [\text{Pt}] \rightleftharpoons [\text{CH}_2\text{CHCH}_2 - \text{Pt}] + [\text{H} - \text{Pt}]$

## E.2 Supplementary Energetics and Adsorption Configurations

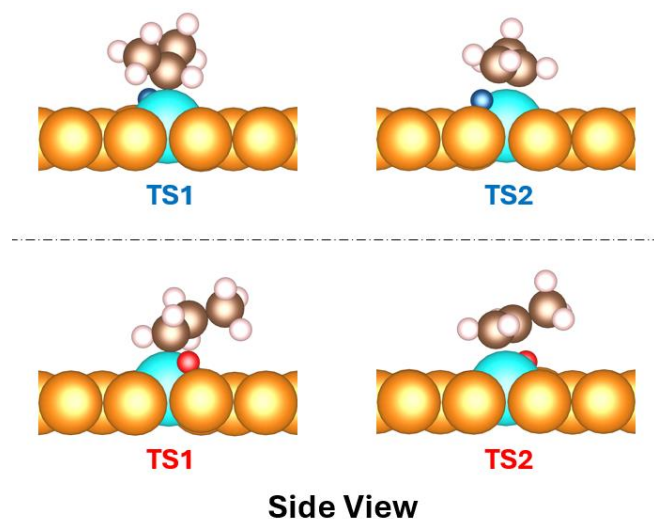


Figure E.1. Side view of the adsorption configurations of the transition states for C-H bond cleavage on CuHf<sub>1</sub>. The H atoms that are being detached are colored in blue and red.

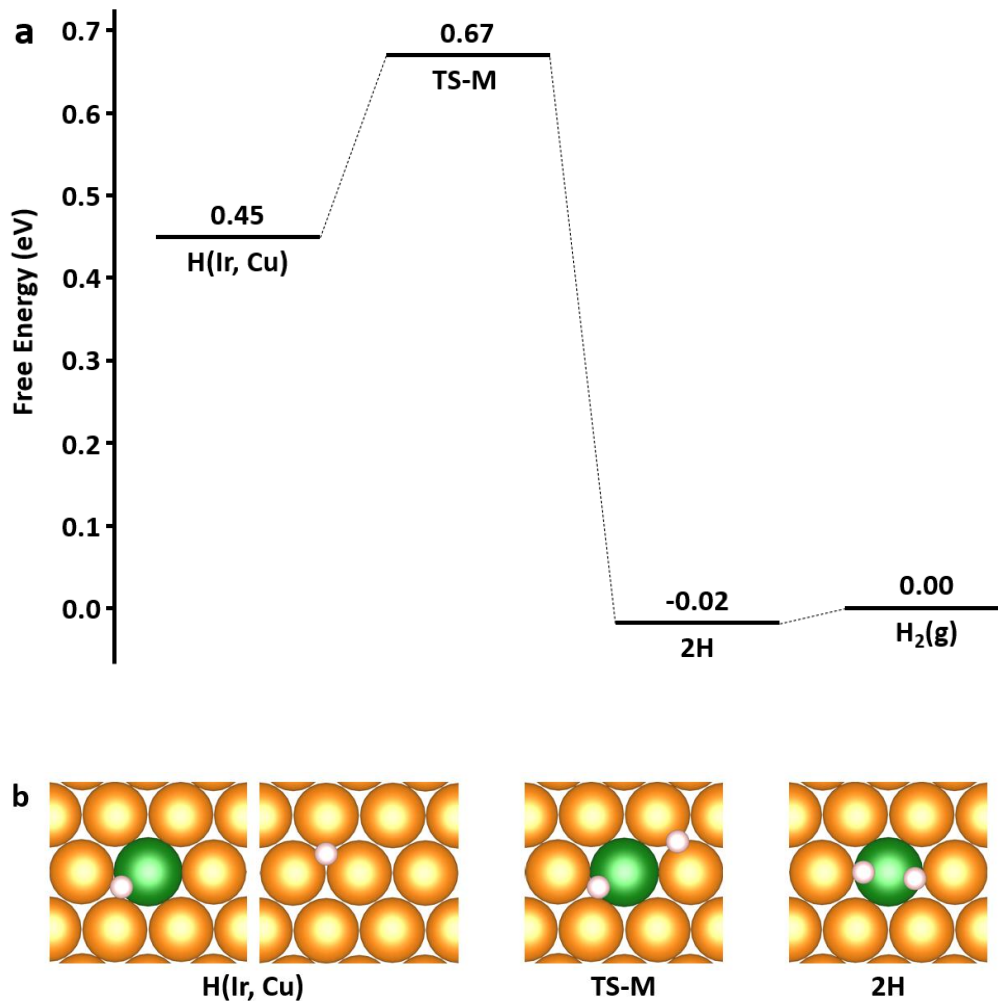
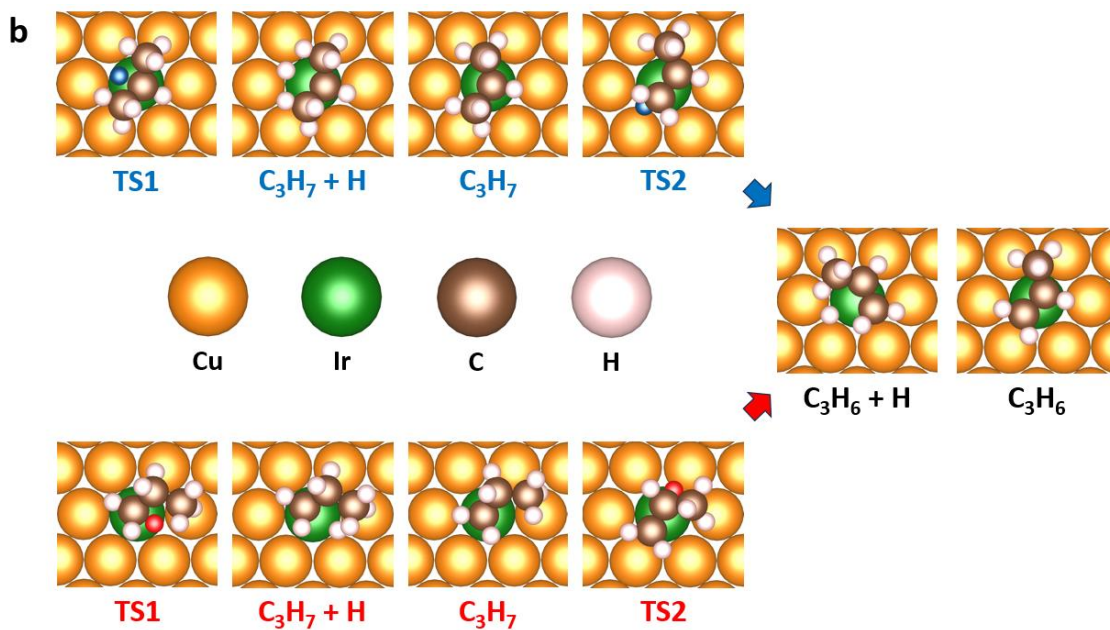
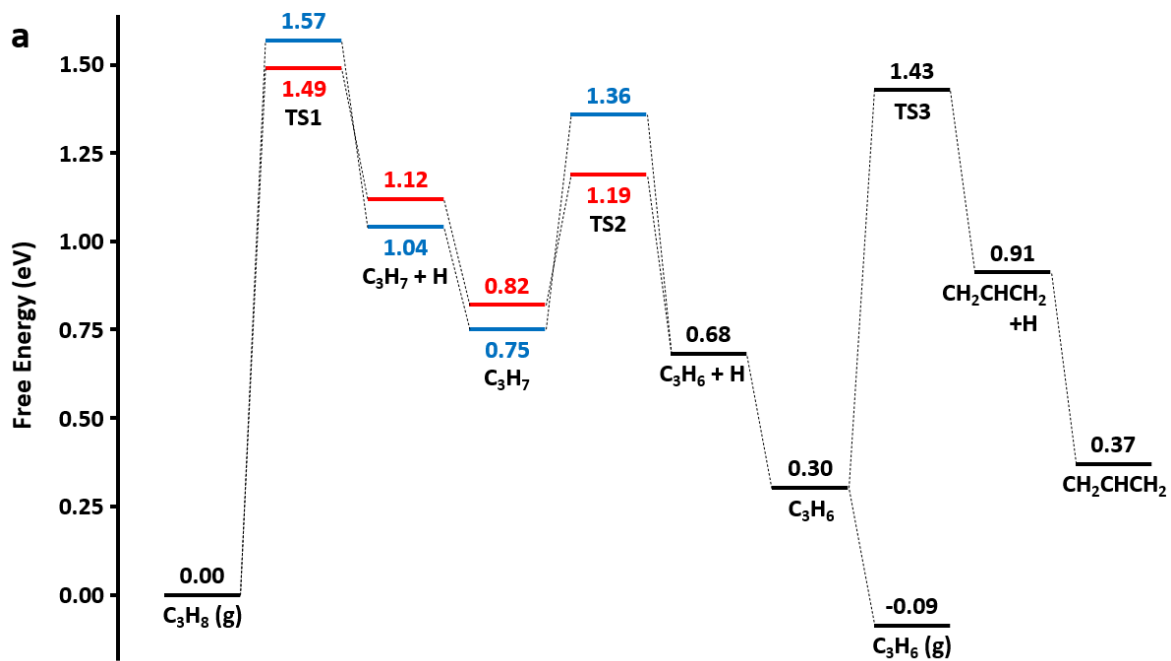


Figure E.2. (a) Free energy profile and (b) corresponding adsorption configurations for H atoms recombination on CuIr<sub>1</sub>. Reaction conditions are: T = 773 K, P(H<sub>2</sub>) = 0.36 bar.



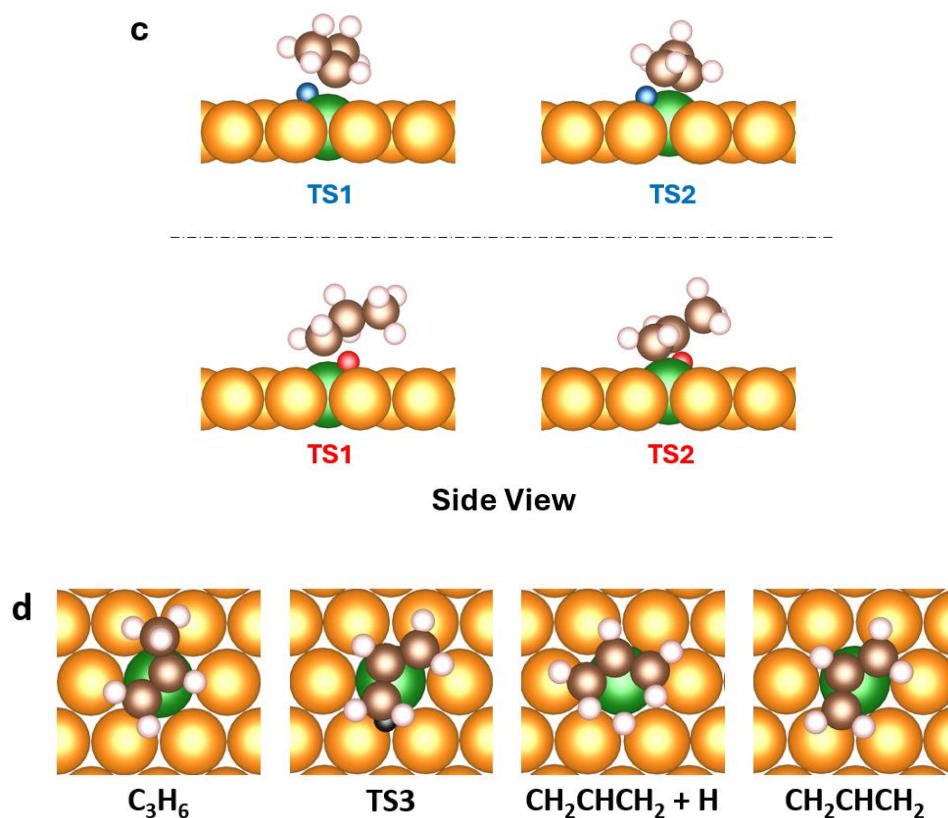


Figure E.3. (a) Free energy profile and (b,c,d) corresponding adsorption configurations for propane dehydrogenation on CuIr<sub>1</sub>. A side view is specifically provided in (c) for transition states to facilitate the visualization of the C-H bonds that are being cleaved. Red and blue sections along the pathway indicate dehydrogenation at the terminal or central carbon atoms as the first step, respectively. H atoms that are being detached in the transition states are colored in red or blue, accordingly, and in black for further dehydrogenation beyond propene. Reaction conditions are: T = 773 K, P(C<sub>3</sub>H<sub>8</sub>) = 0.64 bar, P(H<sub>2</sub>) = 0.36 bar, and P(C<sub>3</sub>H<sub>6</sub>) = 0.11 bar.

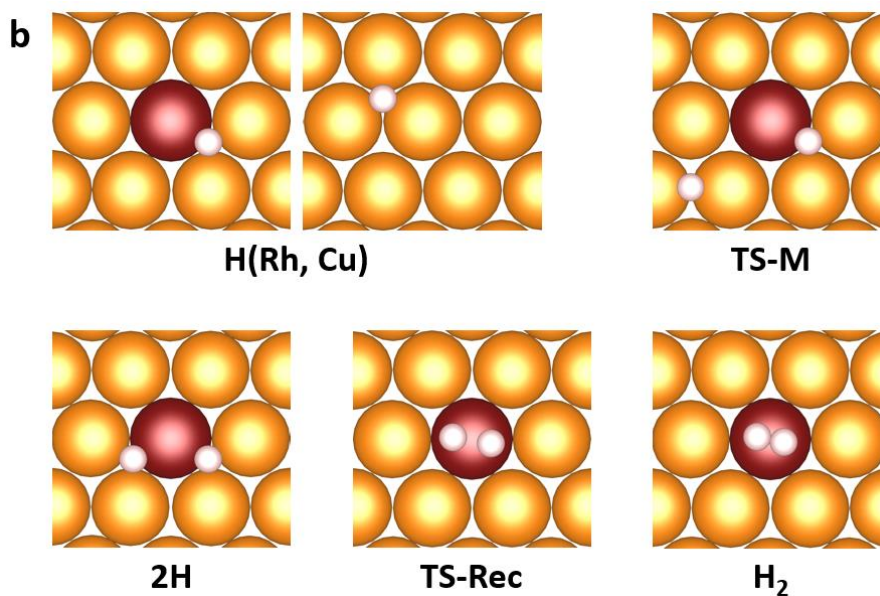
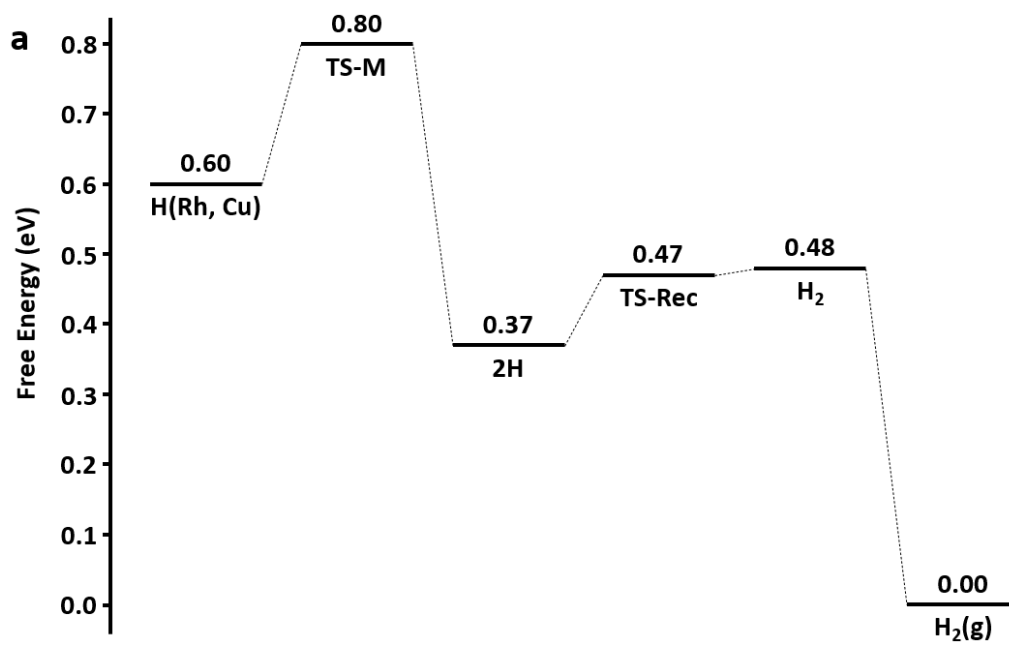
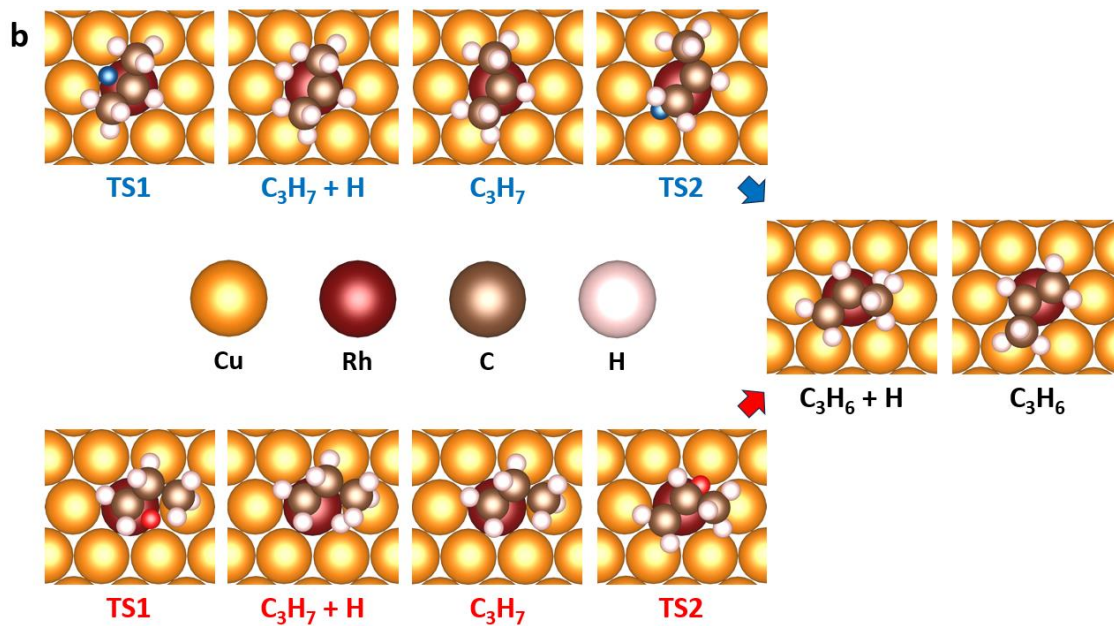
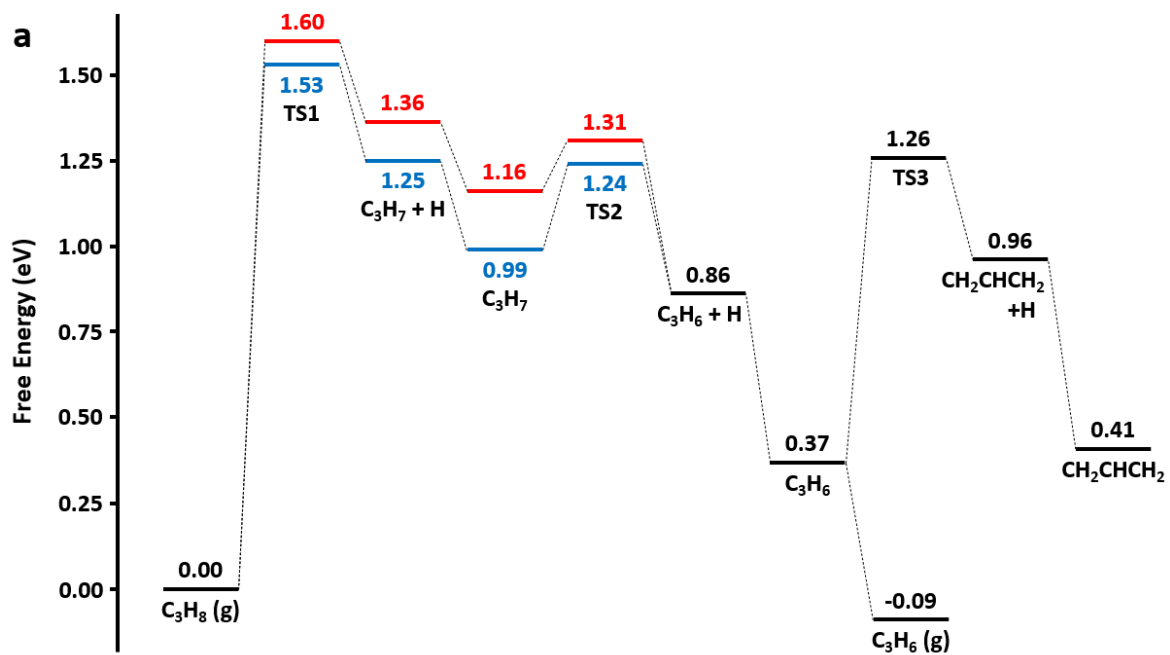


Figure E.4. (a) Free energy profile and (b) corresponding adsorption configurations for H atoms recombination on CuRh<sub>1</sub>. Reaction conditions are: T = 773 K, P(H<sub>2</sub>) = 0.36 bar.



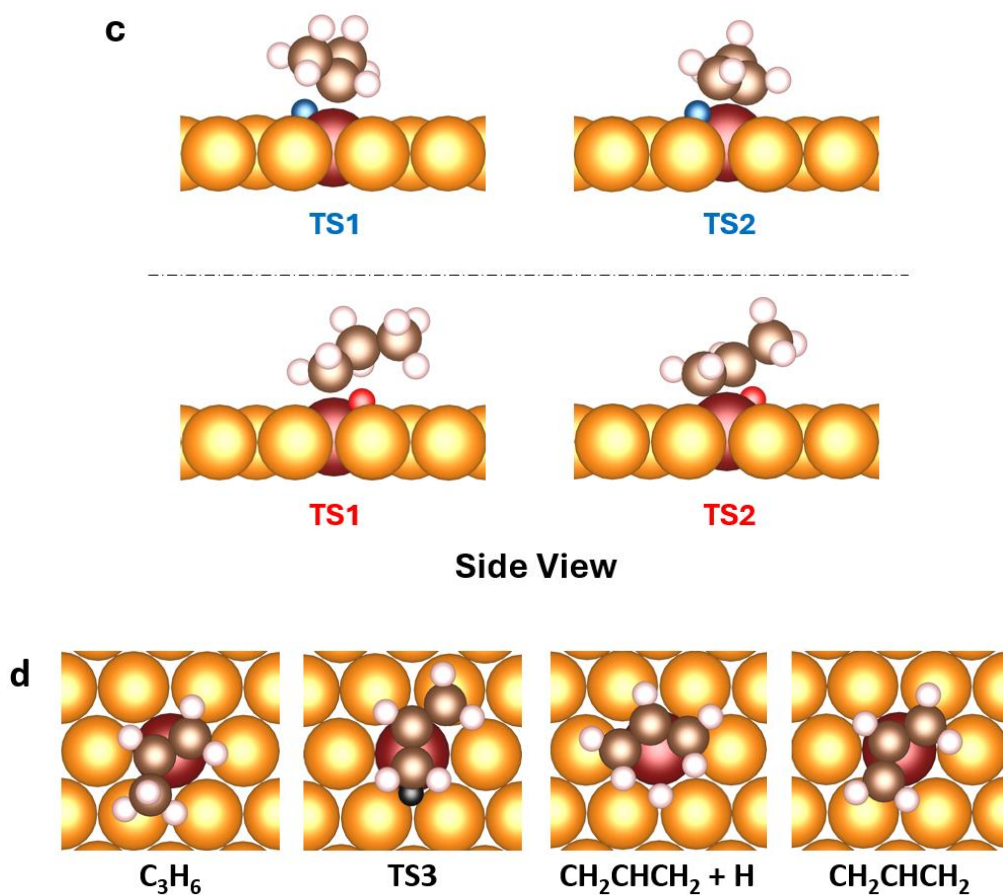
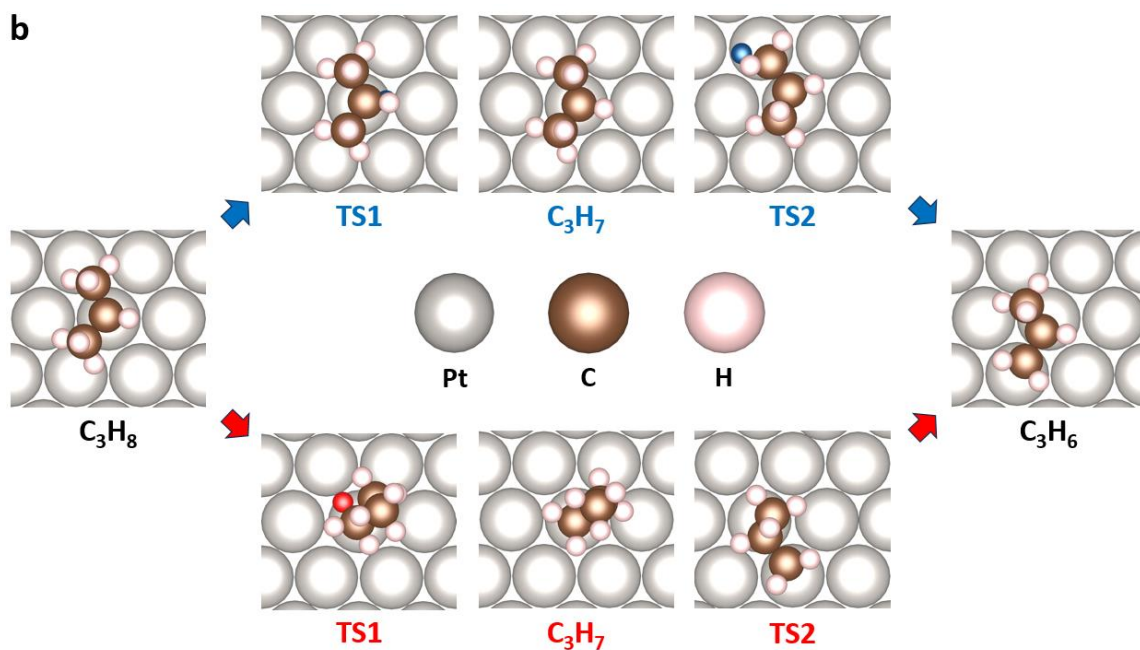
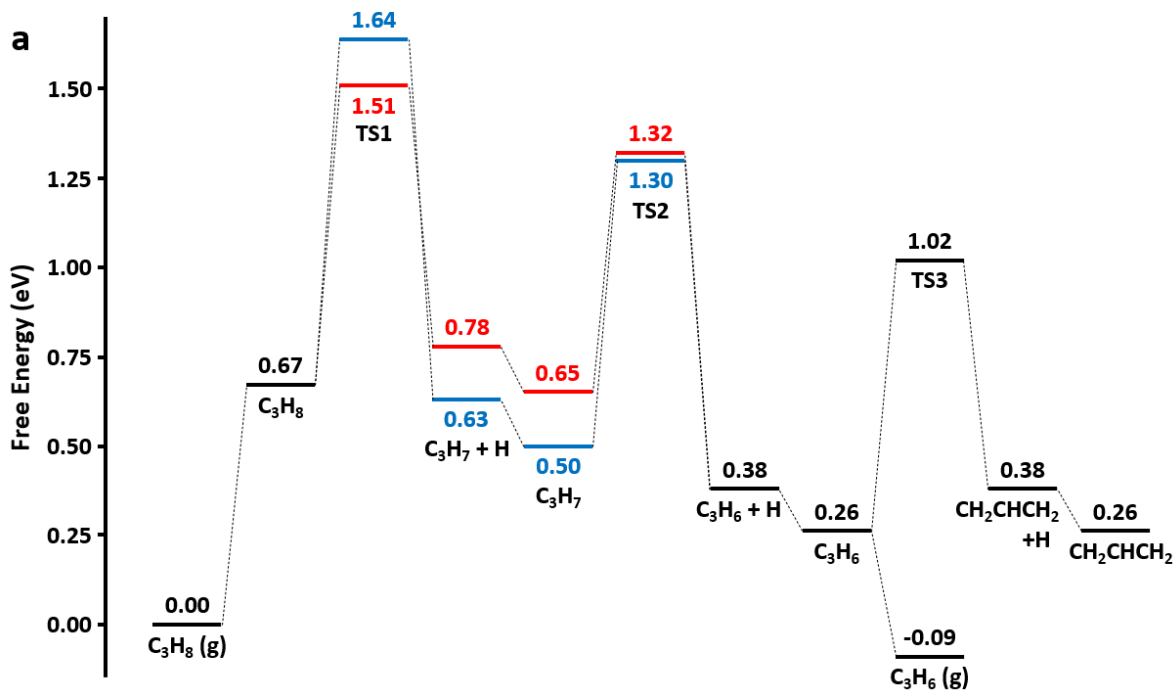


Figure E.5. (a) Free energy profile and (b,c,d) corresponding adsorption configurations for propane dehydrogenation on CuRh<sub>1</sub>. A side view is specifically provided in (c) for transition states to facilitate the visualization of the C-H bonds that are being cleaved. Red and blue sections along the pathway indicate dehydrogenation at the terminal or central carbon atoms as the first step, respectively. H atoms that are being detached in the transition states are colored in red or blue, accordingly, and in black for further dehydrogenation beyond propene. Reaction conditions are: T = 773 K, P(C<sub>3</sub>H<sub>8</sub>) = 0.64 bar, P(H<sub>2</sub>) = 0.36 bar, and P(C<sub>3</sub>H<sub>6</sub>) = 0.11 bar.



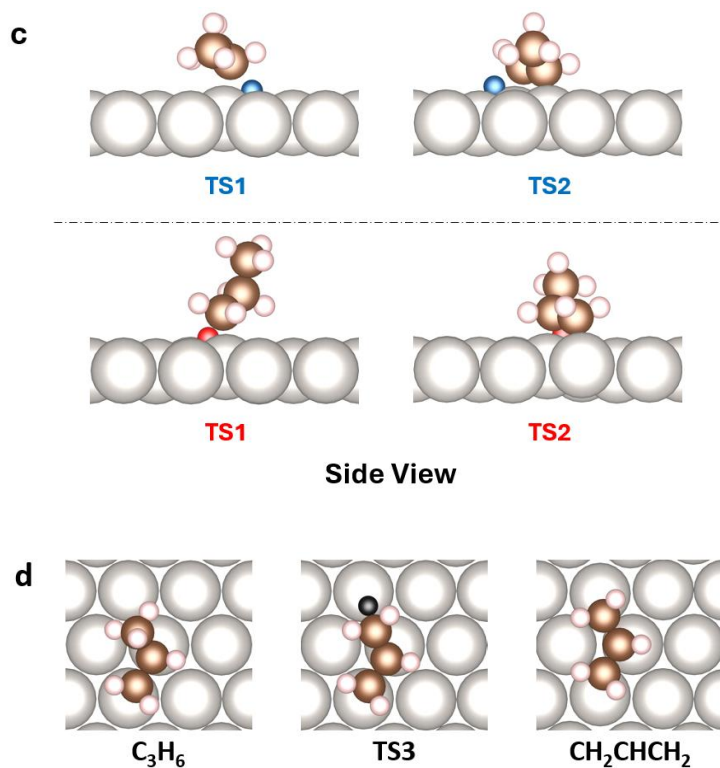


Figure E.6. (a) Free energy profile and (b,c,d) corresponding adsorption configurations for propane dehydrogenation on Pt(111). A side view is specifically provided in (c) for transition states to facilitate the visualization of the C-H bonds that are being cleaved. Red and blue sections along the pathway indicate dehydrogenation at the terminal or central carbon atoms as the first step, respectively. H atoms that are being detached in the transition states are colored in red or blue, accordingly, and in black for further dehydrogenation beyond propene. Reaction conditions are:  $T = 773$  K,  $P(\text{C}_3\text{H}_8) = 0.64$  bar,  $P(\text{H}_2) = 0.36$  bar, and  $P(\text{C}_3\text{H}_6) = 0.11$  bar.

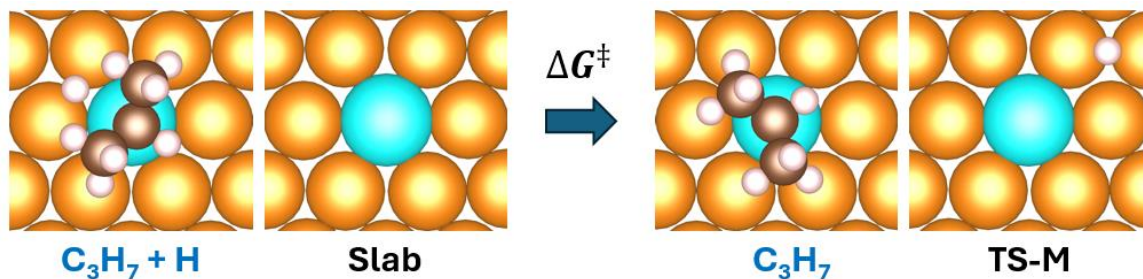


Figure E.7. A schematic representation of the calculation of activation barriers for H-migration away from the mono-dehydrogenated intermediate. Note that a bare slab is needed to balance the number of atoms in the calculation.

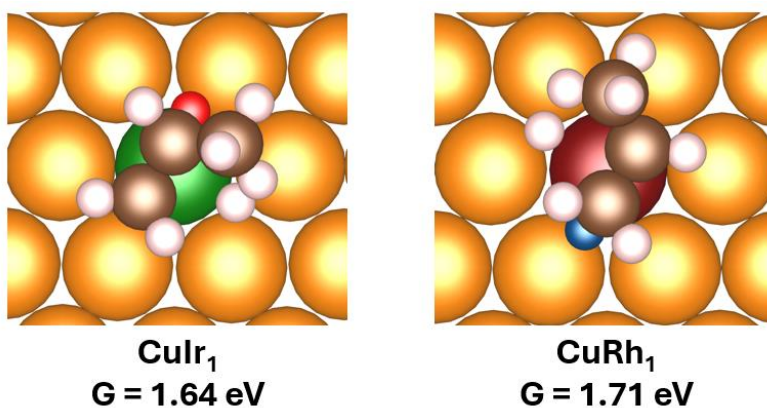


Figure E.8. Free energies relative to gaseous propane and corresponding adsorption configurations of the transition states for dehydrogenating propyls in the presence of an H atom. The H atoms that are being detached are marked in red and blue. Reaction conditions are:  $T = 773 \text{ K}$ ,  $P(\text{C}_3\text{H}_8) = 0.64 \text{ bar}$ ,  $P(\text{H}_2) = 0.36 \text{ bar}$ , and  $P(\text{C}_3\text{H}_6) = 0.11 \text{ bar}$ .

### E.3 Additional Microkinetic Simulations

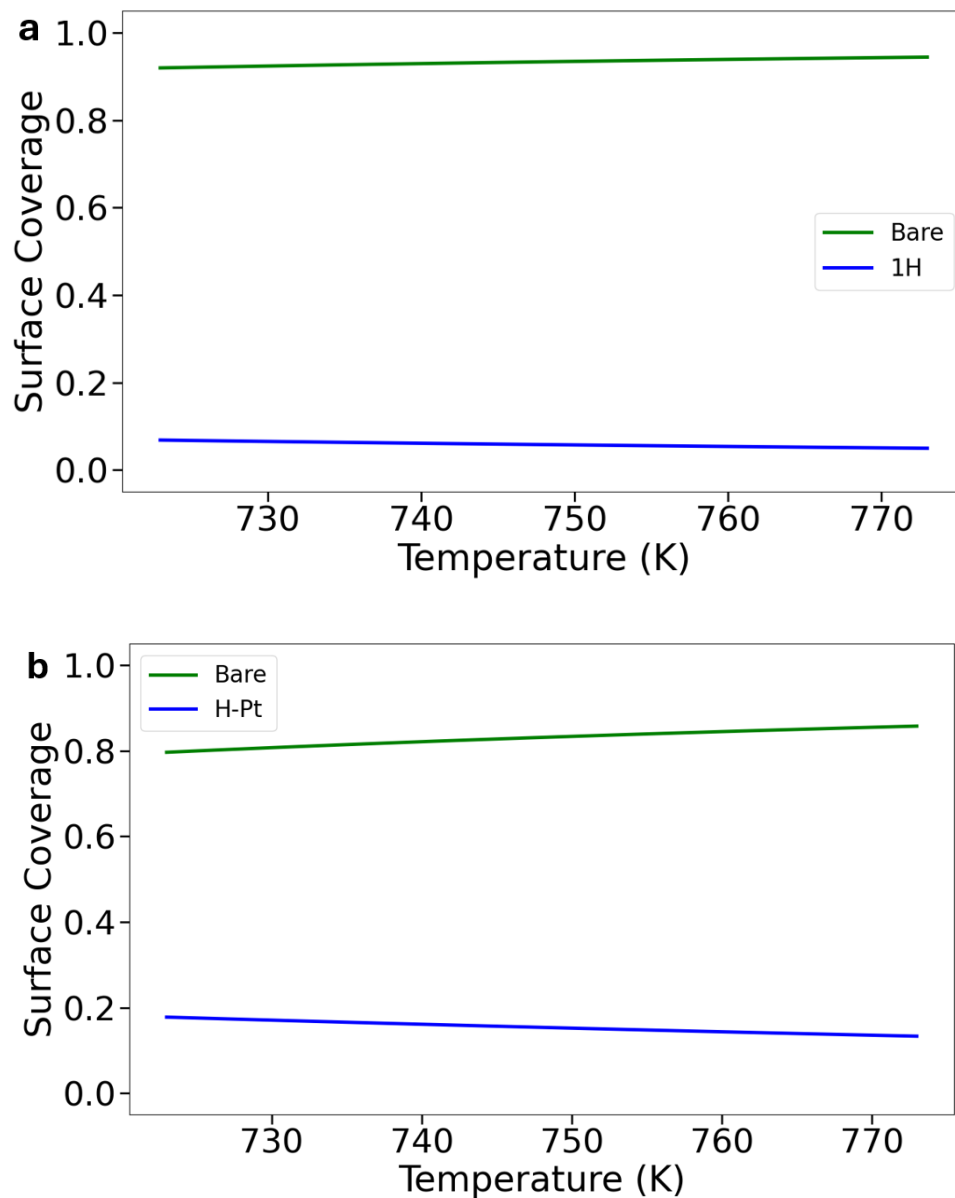


Figure E.9. Steady-state surface coverage of reaction intermediates on (a) CuRh<sub>1</sub> and (b) Pt(111) as a function of temperature. Reaction conditions are:  $P(\text{C}_3\text{H}_8) = 0.64$  bar,  $P(\text{H}_2) = 0.36$  bar, and  $P(\text{C}_3\text{H}_6) = 0.11$  bar.

## Bibliography

- (1) Corti, C. W.; Holliday, R. J.; Thompson, D. T. Commercial Aspects of Gold Catalysis. *Appl Catal A Gen* **2005**, *291* (1–2), 253–261.
- (2) Blaser, H.-U. Heterogeneous Catalysis for Fine Chemicals Production. *Catal Today* **2000**, *60* (3–4), 161–165.
- (3) Marcinkowski, M. D.; Liu, J.; Murphy, C. J.; Liriano, M. L.; Wasio, N. A.; Lucci, F. R.; Flytzani-Stephanopoulos, M.; Sykes, E. C. H. Selective Formic Acid Dehydrogenation on Pt-Cu Single-Atom Alloys. *ACS Catal* **2017**, *7* (1), 413–420.
- (4) Marcinkowski, M. D.; Darby, M. T.; Liu, J.; Wimble, J. M.; Lucci, F. R.; Lee, S.; Michaelides, A.; Flytzani-Stephanopoulos, M.; Stamatakis, M.; Sykes, E. C. H. Pt/Cu Single-Atom Alloys as Coke-Resistant Catalysts for Efficient C-H Activation. *Nat Chem* **2018**, *10* (3), 325–332.
- (5) Lucci, F. R.; Liu, J.; Marcinkowski, M. D.; Yang, M.; Allard, L. F.; Flytzani-Stephanopoulos, M.; Sykes, E. C. H. Selective Hydrogenation of 1,3-Butadiene on Platinum–Copper Alloys at the Single-Atom Limit. *Nat Commun* **2015**, *6* (1), 8550.
- (6) Kumar, A. Ethanol Decomposition and Dehydrogenation for Hydrogen Production: A Review of Heterogeneous Catalysts. *Ind Eng Chem Res* **2021**, *60* (46), 16561–16576.
- (7) Hughes, A. E.; Haque, N.; Northey, S. A.; Giddey, S. Platinum Group Metals: A Review of Resources, Production and Usage with a Focus on Catalysts. *Resources* **2021**, *10* (9), 93.
- (8) Jha, M. K.; Lee, J.; Kim, M.; Jeong, J.; Kim, B.-S.; Kumar, V. Hydrometallurgical Recovery/Recycling of Platinum by the Leaching of Spent Catalysts: A Review. *Hydrometallurgy* **2013**, *133*, 23–32.

- (9) Kettler, P. B. Platinum Group Metals in Catalysis: Fabrication of Catalysts and Catalyst Precursors. *Org Process Res Dev* **2003**, *7* (3), 342–354.
- (10) Hartley, F. R.; Bond, G. C.; Trimm, D. L.; Steinmetz, G. R.; Zoeller, J. R.; Parkins, A. W.; Knifton, J. F.; Chipperfield, J. R.; Gore, E. S.; Davies, J. A.; Eagle, C. T.; Balko, E. N.; Mills, A.; Anderson, G. K.; Jardine, F. H.; Levason, W.; Kozlowski, H.; Pettit, L. D.; McAuliffe, C. A.; Sharma, H. I.; Tinker, N. D.; Gurney, P. D.; Seymour, R. J. *Chemistry of the Platinum Group Metals Recent Developments*; Hartley, Frank. R., Ed.; Elsevier Science Publishers B.V., 1991.
- (11) Clark, H. C.; Manzer, L. E. Reactions of ( $\pi$ -1,5-Cyclooctadiene) Organoplatinum(II) Compounds and the Synthesis of Perfluoroalkylplatinum Complexes. *J Organomet Chem* **1973**, *59*, 411–428.
- (12) Hayashi, Y.; Isobe, K.; Nakamura, Y.; Okeya, S. Chloride-Bridged Methylpalladium(II) Dimers. Preparation, Carbonylation and Bridge-Splitting Reactions with Tertiary Phosphines. *J Organomet Chem* **1986**, *310* (1), 127–134.
- (13) Brune, H. A.; Stapp, B.; Schmidtberg, G. Synthesen 2,4-Dinitro-substituierter Bis(Phenyl)Platin(II)-Verbindungen. *Chem Ber* **1986**, *119* (6), 1845–1856.
- (14) Yang, M.-L.; Zhu, Y.-A.; Fan, C.; Sui, Z.-J.; Chen, D.; Zhou, X.-G. DFT Study of Propane Dehydrogenation on Pt Catalyst: Effects of Step Sites. *Physical Chemistry Chemical Physics* **2011**, *13* (8), 3257.
- (15) Chen, S.; Chang, X.; Sun, G.; Zhang, T.; Xu, Y.; Wang, Y.; Pei, C.; Gong, J. Propane Dehydrogenation: Catalyst Development, New Chemistry, and Emerging Technologies. *Chem Soc Rev* **2021**, *50* (5), 3315–3354.

- (16) Schwab, F.; Weidler, N.; Lucas, M.; Claus, P. Highly Cis-Selective and Lead-Free Hydrogenation of 2-Hexyne by a Supported Pd Catalyst with an Ionic-Liquid Layer. *Chemical Communications* **2014**, *50* (72), 10406–10408.
- (17) Lindlar, H. Ein Neuer Katalysator Für Selektive Hydrierungen. *Helv Chim Acta* **1952**, *35*, 446–450.
- (18) Hannagan, R. T.; Giannakakis, G.; Flytzani-Stephanopoulos, M.; Sykes, E. C. H. Single-Atom Alloy Catalysis. *Chem Rev* **2020**, *120* (21), 12044–12088.
- (19) Han, J.; Lu, J.; Wang, M.; Wang, Y.; Wang, F. Single Atom Alloy Preparation and Applications in Heterogeneous Catalysis. *Chin J Chem* **2019**, *37* (9), 977–988.
- (20) Giannakakis, G.; Flytzani-Stephanopoulos, M.; Sykes, E. C. H. Single-Atom Alloys as a Reductionist Approach to the Rational Design of Heterogeneous Catalysts. *Acc Chem Res* **2019**, *52* (1), 237–247.
- (21) Darby, M. T.; Stamatakis, M.; Michaelides, A.; Sykes, E. C. H. Lonely Atoms with Special Gifts: Breaking Linear Scaling Relationships in Heterogeneous Catalysis with Single-Atom Alloys. *Journal of Physical Chemistry Letters* **2018**, *9* (18), 5636–5646.
- (22) Lee, J. D.; Miller, J. B.; Shneidman, A. V.; Sun, L.; Weaver, J. F.; Aizenberg, J.; Biener, J.; Boscoboinik, J. A.; Foucher, A. C.; Frenkel, A. I.; van der Hoeven, J. E. S.; Kozinsky, B.; Marcella, N.; Montemore, M. M.; Ngan, H. T.; O'Connor, C. R.; Owen, C. J.; Stacchiola, D. J.; Stach, E. A.; Madix, R. J.; Sautet, P.; Friend, C. M. Dilute Alloys Based on Au, Ag, or Cu for Efficient Catalysis: From Synthesis to Active Sites. *Chem Rev* **2022**, *122* (9), 8758–8808.

- (23) Seemala, B.; Cai, C. M.; Kumar, R.; Wyman, C. E.; Christopher, P. Effects of Cu–Ni Bimetallic Catalyst Composition and Support on Activity, Selectivity, and Stability for Furfural Conversion to 2-Methylfuran. *ACS Sustain Chem Eng* **2018**, *6* (2), 2152–2161.
- (24) Seemala, B.; Cai, C. M.; Wyman, C. E.; Christopher, P. Support Induced Control of Surface Composition in Cu–Ni/TiO<sub>2</sub> Catalysts Enables High Yield Co-Conversion of HMF and Furfural to Methylated Furans. *ACS Catal* **2017**, *7* (6), 4070–4082.
- (25) Yang, C.; Miao, Z.; Zhang, F.; Li, L.; Liu, Y.; Wang, A.; Zhang, T. Hydrogenolysis of Methyl Glycolate to Ethanol over a Pt–Cu/SiO<sub>2</sub> Single-Atom Alloy Catalyst: A Further Step from Cellulose to Ethanol. *Green Chemistry* **2018**, *20* (9), 2142–2150.
- (26) Evans, E. J.; Li, H.; Yu, W.-Y.; Mullen, G. M.; Henkelman, G.; Mullins, C. B. Mechanistic Insights on Ethanol Dehydrogenation on Pd–Au Model Catalysts: A Combined Experimental and DFT Study. *Physical Chemistry Chemical Physics* **2017**, *19* (45), 30578–30589.
- (27) Li, H.; Evans, E. J.; Mullins, C. B.; Henkelman, G. Ethanol Decomposition on Pd–Au Alloy Catalysts. *The Journal of Physical Chemistry C* **2018**, *122* (38), 22024–22032.
- (28) Yu, W.-Y.; Mullen, G. M.; Flaherty, D. W.; Mullins, C. B. Selective Hydrogen Production from Formic Acid Decomposition on Pd–Au Bimetallic Surfaces. *J Am Chem Soc* **2014**, *136* (31), 11070–11078.
- (29) Ngan, H. T.; Yan, G.; van der Hoeven, J. E. S.; Madix, R. J.; Friend, C. M.; Sautet, P. Hydrogen Dissociation Controls 1-Hexyne Selective Hydrogenation on Dilute Pd-in-Au Catalysts. *ACS Catal* **2022**, *12* (21), 13321–13333.
- (30) Campbell, C. T. Bimetallic Surface Chemistry. *Annu Rev Phys Chem* **1990**, *41* (1), 775–837.

- (31) Sinfelt, J. H. Catalysis by Alloys and Bimetallic Clusters. *Acc Chem Res* **1977**, *10* (1), 15–20.
- (32) Yi, C.-W.; Luo, K.; Wei, T.; Goodman, D. W. The Composition and Structure of Pd–Au Surfaces. *J Phys Chem B* **2005**, *109* (39), 18535–18540.
- (33) Kyriakou, G.; Boucher, M. B.; Jewell, A. D.; Lewis, E. A.; Lawton, T. J.; Baber, A. E.; Tierney, H. L.; Flytzani-Stephanopoulos, M.; Sykes, E. C. H. Isolated Metal Atom Geometries as a Strategy for Selective Heterogeneous Hydrogenations. *Science (1979)* **2012**, *335* (6073), 1209–1212.
- (34) Wrasman, C. J.; Boubnov, A.; Riscoe, A. R.; Hoffman, A. S.; Bare, S. R.; Cargnello, M. Synthesis of Colloidal Pd/Au Dilute Alloy Nanocrystals and Their Potential for Selective Catalytic Oxidations. *J Am Chem Soc* **2018**, *140* (40), 12930–12939.
- (35) Cao, Y.; Chen, B.; Guerrero-Sánchez, J.; Lee, I.; Zhou, X.; Takeuchi, N.; Zaera, F. Controlling Selectivity in Unsaturated Aldehyde Hydrogenation Using Single-Site Alloy Catalysts. *ACS Catal* **2019**, *9* (10), 9150–9157.
- (36) Liu, L.; Corma, A. Metal Catalysts for Heterogeneous Catalysis: From Single Atoms to Nanoclusters and Nanoparticles. *Chem Rev* **2018**, *118* (10), 4981–5079.
- (37) Sankar, M.; Dimitratos, N.; Miedziak, P. J.; Wells, P. P.; Kiely, C. J.; Hutchings, G. J. Designing Bimetallic Catalysts for a Green and Sustainable Future. *Chem Soc Rev* **2012**, *41* (24), 8099.
- (38) Wang, A.; Li, J.; Zhang, T. Heterogeneous Single-Atom Catalysis. *Nat Rev Chem* **2018**, *2* (6), 65–81.
- (39) Tierney, H. L.; Baber, A. E.; Kitchin, J. R.; Sykes, E. C. H. Hydrogen Dissociation and Spillover on Individual Isolated Palladium Atoms. *Phys Rev Lett* **2009**, *103* (24), 246102.

- (40) Sun, G.; Zhao, Z.-J.; Mu, R.; Zha, S.; Li, L.; Chen, S.; Zang, K.; Luo, J.; Li, Z.; Purdy, S. C.; Kropf, A. J.; Miller, J. T.; Zeng, L.; Gong, J. Breaking the Scaling Relationship via Thermally Stable Pt/Cu Single Atom Alloys for Catalytic Dehydrogenation. *Nat Commun* **2018**, *9* (1), 4454.
- (41) Sun, S.; Sun, G.; Pei, C.; Zhao, Z.-J.; Gong, J. Origin of Performances of Pt/Cu Single-Atom Alloy Catalysts for Propane Dehydrogenation. *The Journal of Physical Chemistry C* **2021**, *125* (34), 18708–18716.
- (42) Giannakakis, G.; Kress, P.; Duanmu, K.; Ngan, H. T.; Yan, G.; Hoffman, A. S.; Qi, Z.; Trimpalis, A.; Annamalai, L.; Ouyang, M.; Liu, J.; Eagan, N.; Biener, J.; Sokaras, D.; Flytzani-Stephanopoulos, M.; Bare, S. R.; Sautet, P.; Sykes, E. C. H. Mechanistic and Electronic Insights into a Working NiAu Single-Atom Alloy Ethanol Dehydrogenation Catalyst. *J Am Chem Soc* **2021**, *143* (51), 21567–21579.
- (43) Thirumalai, H.; Kitchin, J. R. Investigating the Reactivity of Single Atom Alloys Using Density Functional Theory. *Top Catal* **2018**, *61* (5–6), 462–474.
- (44) Greiner, M. T.; Jones, T. E.; Beeg, S.; Zwiener, L.; Scherzer, M.; Girgsdies, F.; Piccinin, S.; Armbrüster, M.; Knop-Gericke, A.; Schlögl, R. Free-Atom-like d States in Single-Atom Alloy Catalysts. *Nat Chem* **2018**, *10* (10), 1008–1015.
- (45) Ngan, H. T.; Sautet, P. Tuning the Hydrogenation Selectivity of an Unsaturated Aldehyde via Single-Atom Alloy Catalysts. *J Am Chem Soc* **2024**, *146* (4), 2556–2567.
- (46) Zhou, C.; Ngan, H. T.; Lim, J. S.; Darbari, Z.; Lewandowski, A.; Stacchiola, D. J.; Kozinsky, B.; Sautet, P.; Boscoboinik, J. A. Dynamical Study of Adsorbate-Induced Restructuring Kinetics in Bimetallic Catalysts Using the PdAu(111) Model System. *J Am Chem Soc* **2022**, *144* (33), 15132–15142.

- (47) Fu, Q.; Luo, Y. Catalytic Activity of Single Transition-Metal Atom Doped in Cu(111) Surface for Heterogeneous Hydrogenation. *The Journal of Physical Chemistry C* **2013**, *117* (28), 14618–14624.
- (48) Darby, M. T.; Sykes, E. C. H.; Michaelides, A.; Stamatakis, M. Carbon Monoxide Poisoning Resistance and Structural Stability of Single Atom Alloys. *Top Catal* **2018**, *61* (5–6), 428–438.
- (49) Foucher, A. C.; Ngan, H. T.; Shirman, T.; Filie, A.; Duanmu, K.; Aizenberg, M.; Madix, R. J.; Friend, C. M.; Aizenberg, J.; Sautet, P.; Stach, E. A. Influence of Pd Concentration in Au-Pd Nanoparticles for the Hydrogenation of Alkynes. *ACS Appl. Nano Mater.* **2023**, *6* (24), 22927–22938.
- (50) Chang, F.-W.; Yang, H.-C.; Roselin, L. S.; Kuo, W.-Y. Ethanol Dehydrogenation over Copper Catalysts on Rice Husk Ash Prepared by Ion Exchange. *Appl Catal A Gen* **2006**, *304*, 30–39.
- (51) Tu, Y.-J.; Chen, Y.-W. Effects of Alkali Metal Oxide Additives on Cu/SiO<sub>2</sub> Catalyst in the Dehydrogenation of Ethanol. *Ind Eng Chem Res* **2001**, *40* (25), 5889–5893.
- (52) Twigg, M. V.; Spencer, M. S. Deactivation of Supported Copper Metal Catalysts for Hydrogenation Reactions. *Appl Catal A Gen* **2001**, *212* (1–2), 161–174.
- (53) Twigg, M. V.; Spencer, M. S. Deactivation of Copper Metal Catalysts for Methanol Decomposition, Methanol Steam Reforming and Methanol Synthesis. *Top Catal* **2003**, *22*, 191–203.
- (54) Shan, J.; Janvelyan, N.; Li, H.; Liu, J.; Egle, T. M.; Ye, J.; Biener, M. M.; Biener, J.; Friend, C. M.; Flytzani-Stephanopoulos, M. Selective Non-Oxidative Dehydrogenation of Ethanol

- to Acetaldehyde and Hydrogen on Highly Dilute NiCu Alloys. *Appl Catal B* **2017**, *205*, 541–550.
- (55) Hannagan, R. T.; Giannakakis, G.; Réocreux, R.; Schumann, J.; Finzel, J.; Wang, Y.; Michaelides, A.; Deshlahra, P.; Christopher, P.; Flytzani-Stephanopoulos, M.; Stamatakis, M.; Sykes, E. C. H. First-Principles Design of a Single-Atom–Alloy Propane Dehydrogenation Catalyst. *Science (1979)* **2021**, *372* (6549), 1444–1447.
- (56) Shi, J.; Ngan, H. T.; Sautet, P.; Weaver, J. F. High Selectivity and Activity of Ti-Cu(111) Dilute Alloys for the Deoxygenation of Ethanol to Ethylene. *ACS Catal* **2023**, *13* (17), 11244–11255.
- (57) van der Hoeven, J. E. S.; Ngan, H. T.; Yan, G.; Aizenberg, J.; Madix, R. J.; Sautet, P.; Friend, C. M. Unraveling 1-Hexene Hydrogenation over Dilute Pd-in-Au Alloys. *The Journal of Physical Chemistry C* **2022**, *126* (37), 15710–15723.
- (58) Wang, T.; Cui, X.; Winther, K. T.; Abild-Pedersen, F.; Bligaard, T.; Nørskov, J. K. Theory-Aided Discovery of Metallic Catalysts for Selective Propane Dehydrogenation to Propylene. *ACS Catal.* **2021**, *11* (10), 6290–6297.
- (59) Zhang, L.; Zhou, M.; Wang, A.; Zhang, T. Selective Hydrogenation over Supported Metal Catalysts: From Nanoparticles to Single Atoms. *Chem Rev* **2020**, *120* (2), 683–733.
- (60) Cárdenas-Lizana, F.; Keane, M. A. The Development of Gold Catalysts for Use in Hydrogenation Reactions. *J Mater Sci* **2013**, *48* (2), 543–564.
- (61) Studt, F.; Abild-Pedersen, F.; Bligaard, T.; Sorensen, R. Z.; Christensen, C. H.; Nørskov, J. K. Identification of Non-Precious Metal Alloy Catalysts for Selective Hydrogenation of Acetylene. *Science (1979)* **2008**, *320* (5881), 1320–1322.

- (62) Sheth, P. A.; Neurock, M.; Smith, C. M. A First-Principles Analysis of Acetylene Hydrogenation over Pd(111). *Journal of Physical Chemistry B* **2003**, *107* (9), 2009–2017.
- (63) Mei, D.; Sheth, P. A.; Neurock, M.; Smith, C. M. First-Principles-Based Kinetic Monte Carlo Simulation of the Selective Hydrogenation of Acetylene over Pd(111). *J Catal* **2006**, *242* (1), 1–15.
- (64) Luneau, M.; Shirman, T.; Foucher, A. C.; Duanmu, K.; Verbart, D. M. A.; Sautet, P.; Stach, E. A.; Aizenberg, J.; Madix, R. J.; Friend, C. M. Achieving High Selectivity for Alkyne Hydrogenation at High Conversions with Compositionally Optimized PdAu Nanoparticle Catalysts in Raspberry Colloid-Templated SiO<sub>2</sub>. *ACS Catal* **2020**, *10* (1), 441–450.
- (65) Zaera, F. The Surface Chemistry of Metal-Based Hydrogenation Catalysis. *ACS Catal* **2017**, *7* (8), 4947–4967.
- (66) Yuan, D.; Gong, X.; Wu, R. Atomic Configurations of Pd Atoms in PdAu(111) Bimetallic Surfaces Investigated Using the First-Principles Pseudopotential Plane Wave Approach. *Phys Rev B* **2007**, *75* (8), 085428.
- (67) Fung, V.; Hu, G.; Sumpter, B. Electronic Band Contraction Induced Low Temperature Methane Activation on Metal Alloys. *J Mater Chem A Mater* **2020**, *8* (12), 6057–6066.
- (68) Vignola, E.; Steinmann, S. N.; Al Farra, A.; Vandegehuchte, B. D.; Curulla, D.; Sautet, P. Evaluating the Risk of C–C Bond Formation during Selective Hydrogenation of Acetylene on Palladium. *ACS Catal* **2018**, *8* (3), 1662–1671.
- (69) Liu, J.; Shan, J.; Lucci, F. R.; Cao, S.; Sykes, E. C. H.; Flytzani-Stephanopoulos, M. Palladium-Gold Single Atom Alloy Catalysts for Liquid Phase Selective Hydrogenation of 1-Hexyne. *Catal Sci Technol* **2017**, *7* (19), 4276–4284.

- (70) Boucher, M. B.; Zugic, B.; Cladaras, G.; Kammert, J.; Marcinkowski, M. D.; Lawton, T. J.; Sykes, E. C. H.; Flytzani-Stephanopoulos, M. Single Atom Alloy Surface Analogs in Pd<sub>0.18</sub>Cu<sub>0.15</sub> Nanoparticles for Selective Hydrogenation Reactions. *Physical Chemistry Chemical Physics* **2013**, *15* (29), 12187–12196.
- (71) Pei, G. X.; Liu, X. Y.; Wang, A.; Li, L.; Huang, Y.; Zhang, T.; Lee, J. W.; Jang, B. W. L.; Mou, C.-Y. Promotional Effect of Pd Single Atoms on Au Nanoparticles Supported on Silica for the Selective Hydrogenation of Acetylene in Excess Ethylene. *New Journal of Chemistry* **2014**, *38* (5), 2043.
- (72) Pei, G. X.; Liu, X. Y.; Yang, X.; Zhang, L.; Wang, A.; Li, L.; Wang, H.; Wang, X.; Zhang, T. Performance of Cu-Alloyed Pd Single-Atom Catalyst for Semihydrogenation of Acetylene under Simulated Front-End Conditions. *ACS Catal* **2017**, *7* (2), 1491–1500.
- (73) Xie, W.; Xu, J.; Ding, Y.; Hu, P. Quantitative Studies of the Key Aspects in Selective Acetylene Hydrogenation on Pd(111) by Microkinetic Modeling with Coverage Effects and Molecular Dynamics. *ACS Catal* **2021**, *11* (7), 4094–4106.
- (74) Liu, J.; Uhlman, M. B.; Montemore, M. M.; Trimpalis, A.; Giannakakis, G.; Shan, J.; Cao, S.; Hannagan, R. T.; Sykes, E. C. H.; Flytzani-Stephanopoulos, M. Integrated Catalysis-Surface Science-Theory Approach to Understand Selectivity in the Hydrogenation of 1-Hexyne to 1-Hexene on PdAu Single-Atom Alloy Catalysts. *ACS Catal* **2019**, *9* (9), 8757–8765.
- (75) Kresse, G.; Hafner, J. Ab Initio Molecular Dynamics for Liquid Metals. *Phys Rev B* **1993**, *47* (1), 558–561.

- (76) Kresse, G.; Hafner, J. Ab Initio Molecular-Dynamics Simulation of the Liquid-Metalamorphous- Semiconductor Transition in Germanium. *Phys Rev B* **1994**, *49* (20), 14251–14269.
- (77) Monkhorst, H. J.; Pack, J. D. Special Points for Brillouin-Zone Integrations. *Phys Rev B Condens Matter Mater Phys* **1976**, *13*, 5188–5192.
- (78) Dion, M.; Rydberg, H.; Schröder, E.; Langreth, D. C.; Lundqvist, B. I. Van Der Waals Density Functional for General Geometries. *Phys Rev Lett* **2004**, *92* (24), 246401.
- (79) Román-Pérez, G.; Soler, J. M. Efficient Implementation of a van Der Waals Density Functional: Application to Double-Wall Carbon Nanotubes. *Phys Rev Lett* **2009**, *103* (9), 096102.
- (80) Klimeš, J.; Bowler, D. R.; Michaelides, A. Chemical Accuracy for the van Der Waals Density Functional. *Journal of Physics: Condensed Matter* **2010**, *22* (2), 022201.
- (81) Gautier, S.; Steinmann, S. N.; Michel, C.; Fleurat-Lessard, P.; Sautet, P. Molecular Adsorption at Pt(111). How Accurate Are DFT Functionals? *Physical Chemistry Chemical Physics* **2015**, *17* (43), 28921–28930.
- (82) Koeleman, B. J. J.; de Zwart, S. T.; Boers, A. L.; Poelsema, B.; Verhey, L. K. Adsorption Study of Hydrogen on a Stepped Pt (997) Surface Using Low Energy Recoil Scattering. *Nuclear Instruments and Methods in Physics Research* **1983**, *218* (1–3), 225–229.
- (83) Norton, P. R.; Davies, J. A.; Jackman, T. E. Absolute Coverage and Isosteric Heat of Adsorption of Deuterium on Pt(111) Studied by Nuclear Microanalysis. *Surface Science Letters* **1982**, *121* (1), A364.

- (84) Henkelman, G.; Jónsson, H. A Dimer Method for Finding Saddle Points on High Dimensional Potential Surfaces Using Only First Derivatives. *Journal of Chemical Physics* **1999**, *111* (15), 7010–7022.
- (85) Momma, K.; Izumi, F. VESTA 3 for Three-Dimensional Visualization of Crystal, Volumetric and Morphology Data. *J Appl Crystallogr* **2011**, *44*, 1272-1276.
- (86) Marcella, N.; Lim, J. S.; Płonka, A. M.; Yan, G.; Owen, C. J.; van der Hoeven, J. E. S.; Foucher, A. C.; Ngan, H. T.; Torrisi, S. B.; Marinkovic, N. S.; Stach, E. A.; Weaver, J. F.; Aizenberg, J.; Sautet, P.; Kozinsky, B.; Frenkel, A. I. Decoding Reactive Structures in Dilute Alloy Catalysts. *Nat Commun* **2022**, *13* (1), 832.
- (87) Gokhale, A. A.; Kandoi, S.; Greeley, J. P.; Mavrikakis, M.; Dumesic, J. A. Molecular-Level Descriptions of Surface Chemistry in Kinetic Models Using Density Functional Theory. *Chem Eng Sci* **2004**, *59* (22–23), 4679–4691.
- (88) Cortright, R. D.; Dumesic, J. A. Kinetics of Heterogeneous Catalytic Reactions: Analysis of Reaction Schemes. *Advances in Catalysis* **2001**, *46*, 161–264.
- (89) Wang, T.; Ibañez, J.; Wang, K.; Fang, L.; Sabbe, M.; Michel, C.; Paul, S.; Pera-Titus, M.; Sautet, P. Rational Design of Selective Metal Catalysts for Alcohol Amination with Ammonia. *Nat Catal* **2019**, *2* (9), 773–779.
- (90) van der Hoeven, J. E. S.; Ngan, H. T.; Taylor, A.; Eagan, N. M.; Aizenberg, J.; Sautet, P.; Madix, R. J.; Friend, C. M. Entropic Control of HD Exchange Rates over Dilute Pd-in-Au Alloy Nanoparticle Catalysts. *ACS Catal* **2021**, *11* (12), 6971–6981.
- (91) Dumesic, J. A. Analyses of Reaction Schemes Using De Donder Relations. *J Catal* **1999**, *185* (2), 496–505.

- (92) Campbell, C. T. The Degree of Rate Control: A Powerful Tool for Catalysis Research. *ACS Catal* **2017**, *7* (4), 2770–2779.
- (93) Mao, Z.; Campbell, C. T. Apparent Activation Energies in Complex Reaction Mechanisms: A Simple Relationship via Degrees of Rate Control. *ACS Catal* **2019**, *9* (10), 9465–9473.
- (94) Canduela-Rodriguez, G.; Sabbe, M. K.; Reyniers, M.-F.; Joly, J.-F.; Marin, G. B. Thermodynamic Study of Benzene and Hydrogen Coadsorption on Pd(111). *Phys. Chem. Chem. Phys.* **2014**, *16* (43), 23754–23768.
- (95) Darby, M. T.; Réocreux, R.; Sykes, E. Charles. H.; Michaelides, A.; Stamatakis, M. Elucidating the Stability and Reactivity of Surface Intermediates on Single-Atom Alloy Catalysts. *ACS Catal* **2018**, *8* (6), 5038–5050.
- (96) Li, H.; Chai, W.; Henkelman, G. Selectivity for Ethanol Partial Oxidation: The Unique Chemistry of Single-Atom Alloy Catalysts on Au, Ag, and Cu(111). *J Mater Chem A Mater* **2019**, *7* (41), 23868–23877.
- (97) Hammer, B.; Norskov, J. K. Why Gold Is the Noblest of All the Metals. *Nature* **1995**, *376* (6537), 238–240.
- (98) Xin, H.; Vojvodic, A.; Voss, J.; Nørskov, J. K.; Abild-Pedersen, F. Effects of d -Band Shape on the Surface Reactivity of Transition-Metal Alloys. *Phys Rev B Condens Matter Mater Phys* **2014**, *89* (11), 115114.
- (99) van der Hoeven, J. E. S.; Jelic, J.; Olthof, L. A.; Totarella, G.; van Dijk-Moes, R. J. A.; Krafft, J. M.; Louis, C.; Studt, F.; van Blaaderen, A.; de Jongh, P. E. Unlocking Synergy in Bimetallic Catalysts by Core–Shell Design. *Nat Mater* **2021**, 1–5.

- (100) Kolli, N. El; Delannoy, L.; Louis, C. Bimetallic Au–Pd Catalysts for Selective Hydrogenation of Butadiene: Influence of the Preparation Method on Catalytic Properties. *J Catal* **2013**, *297*, 79–92.
- (101) Rassolov, A. V.; Bragina, G. O.; Baeva, G. N.; Mashkovsky, I. S.; Stakheev, A. Yu. Alumina-Supported Palladium–Silver Bimetallic Catalysts with Single-Atom Pd1 Sites in the Liquid-Phase Hydrogenation of Substituted Alkynes. *Kinetics and Catalysis* **2020**, *61* (6), 869–878.
- (102) Pei, G. X.; Liu, X. Y.; Wang, A.; Lee, A. F.; Isaacs, M. A.; Li, L.; Pan, X.; Yang, X.; Wang, X.; Tai, Z.; Wilson, K.; Zhang, T. Ag Alloyed Pd Single-Atom Catalysts for Efficient Selective Hydrogenation of Acetylene to Ethylene in Excess Ethylene. *ACS Catal* **2015**, *5* (6), 3717–3725.
- (103) McCue, A. J.; Baker, R. T.; Anderson, J. A. Acetylene Hydrogenation over Structured Au–Pd Catalysts. *Faraday Discuss* **2016**, *188* (0), 499–523.
- (104) Choudhary, T. V.; Sivadinarayana, C.; Datye, A. K.; Kumar, D.; Goodman, D. W. Acetylene Hydrogenation on Au-Based Catalysts. *Catal Letters* **2003**, *86* (1–3), 1–8.
- (105) Luneau, M.; Guan, E.; Chen, W.; Foucher, A. C.; Marcella, N.; Shirman, T.; Verbart, D. M. A.; Aizenberg, J.; Aizenberg, M.; Stach, E. A.; Madix, R. J.; Frenkel, A. I.; Friend, C. M. Enhancing Catalytic Performance of Dilute Metal Alloy Nanomaterials. *Commun Chem* **2020**, *3* (1), 1–9.
- (106) Guan, E.; Foucher, A. C.; Marcella, N.; Shirman, T.; Luneau, M.; Head, A. R.; Verbart, D. M. A.; Aizenberg, J.; Friend, C. M.; Stacchiola, D.; Stach, E. A.; Frenkel, A. I. New Role of Pd Hydride as a Sensor of Surface Pd Distributions in Pd–Au Catalysts. *ChemCatChem* **2020**, *12* (3), 717–721.

- (107) Steinmann, S. N.; Corminboeuf, C. Comprehensive Benchmarking of a Density-Dependent Dispersion Correction. *J Chem Theory Comput* **2011**, *7* (11), 3567–3577.
- (108) Perdew, J. P.; Burke, K.; Ernzerhof, M. Generalized Gradient Approximation Made Simple. *Phys Rev Lett* **1996**, *77* (18), 3865–3868.
- (109) Henkelman, G.; Uberuaga, B. P.; Jónsson, H. Climbing Image Nudged Elastic Band Method for Finding Saddle Points and Minimum Energy Paths. *Journal of Chemical Physics* **2000**, *113* (22), 9901-9904.
- (110) Dostert, K.-H.; O'Brien, C. P.; Ivars-Barceló, F.; Schauermaun, S.; Freund, H.-J. Spectators Control Selectivity in Surface Chemistry: Acrolein Partial Hydrogenation Over Pd. *J Am Chem Soc* **2015**, *137* (42), 13496–13502.
- (111) Mohr, C.; Claus, P. Hydrogenation Properties of Supported Nanosized Gold Particles. *Sci Prog* **2001**, *84* (4), 311–334.
- (112) Marinelli, T. B. L. W.; Nabuurs, S.; Ponc, V. Activity and Selectivity in the Reactions of Substituted  $\alpha,\beta$ -Unsaturated Aldehydes. *J Catal* **1995**, *151* (2), 431–438.
- (113) Hoang-Van, C.; Zegaoui, O. Studies of High Surface Area Pt/MoO<sub>3</sub> and Pt/WO<sub>3</sub> Catalysts for Selective Hydrogenation Reactions. II. Reactions of Acrolein and Allyl Alcohol. *Appl Catal A Gen* **1997**, *164* (1–2), 91–103.
- (114) Györfy, N.; Paál, Z. Acrolein Hydrogenation on PdPt Powder Catalysts Prepared by Colloid Synthesis. *J Mol Catal A Chem* **2008**, *295* (1–2), 24–28.
- (115) Loffreda, D.; Delbecq, F.; Vigné, F.; Sautet, P. Chemo-Regioselectivity in Heterogeneous Catalysis: Competitive Routes for CO and CC Hydrogenations from a Theoretical Approach. *J Am Chem Soc* **2006**, *128* (4), 1316–1323.

- (116) Laref, S.; Delbecq, F.; Loffreda, D. Theoretical Elucidation of the Selectivity Changes for the Hydrogenation of Unsaturated Aldehydes on Pt(111). *J Catal* **2009**, *265* (1), 35–42.
- (117) Reyes, P.; Aguirre, M. C.; Fierro, J. L. G.; Santori, G.; Ferretti, O. Hydrogenation of Crotonaldehyde on Rh-Sn/SiO<sub>2</sub> Catalysts Prepared by Reaction of Tetrabutyltin on Prereduced Rh/SiO<sub>2</sub> Precursors. *J Mol Catal A Chem* **2002**, *184* (1–2), 431–441.
- (118) Zhao, J.; Ni, J.; Xu, J.; Xu, J.; Cen, J.; Li, X. Ir Promotion of TiO<sub>2</sub> Supported Au Catalysts for Selective Hydrogenation of Cinnamaldehyde. *Catal Commun* **2014**, *54*, 72–76.
- (119) Aich, P.; Wei, H.; Basan, B.; Kropf, A. J.; Schweitzer, N. M.; Marshall, C. L.; Miller, J. T.; Meyer, R. Single-Atom Alloy Pd–Ag Catalyst for Selective Hydrogenation of Acrolein. *The Journal of Physical Chemistry C* **2015**, *119* (32), 18140–18148.
- (120) Luneau, M.; Lim, J. S.; Patel, D. A.; Sykes, E. C. H.; Friend, C. M.; Sautet, P. Guidelines to Achieving High Selectivity for the Hydrogenation of  $\alpha,\beta$ -Unsaturated Aldehydes with Bimetallic and Dilute Alloy Catalysts: A Review. *Chem Rev* **2020**, *120* (23), 12834–12872.
- (121) Spivey, T. D.; Holewinski, A. Selective Interactions between Free-Atom-like d -States in Single-Atom Alloy Catalysts and Near-Frontier Molecular Orbitals. *J Am Chem Soc* **2021**, *143* (31), 11897–11902.
- (122) Muir, M.; Molina, D. L.; Islam, A.; Abdel-Rahman, M. K.; Trenary, M. Selective Hydrogenation of Acrolein on a Pd/Ag(111) Single-Atom Alloy Surface. *The Journal of Physical Chemistry C* **2020**, *124* (44), 24271–24278.
- (123) Delbecq, F.; Sautet, P. Influence of Sn Additives on the Selectivity of Hydrogenation of  $\alpha$ - $\beta$ -Unsaturated Aldehydes with Pt Catalysts: A Density Functional Study of Molecular Adsorption. *J Catal* **2003**, *220* (1), 115–126.

- (124) Methfessel, M.; Paxton, A. T. High-Precision Sampling for Brillouin-Zone Integration in Metals. *Phys Rev B* **1989**, *40* (6), 3616–3621.
- (125) Blöchl, P. E. Projector Augmented-Wave Method. *Phys Rev B* **1994**, *50* (24), 17953–17979.
- (126) Joubert, D. From Ultrasoft Pseudopotentials to the Projector Augmented-Wave Method. *Phys Rev B Condens Matter Mater Phys* **1999**, *59* (3), 1758–1775.
- (127) Henkelman, G.; Jónsson, H. Improved Tangent Estimate in the Nudged Elastic Band Method for Finding Minimum Energy Paths and Saddle Points. *J Chem Phys* **2000**, *113* (22), 9978–9985.
- (128) Maintz, S.; Deringer, V. L.; Tchougréeff, A. L.; Dronskowski, R. LOBSTER: A Tool to Extract Chemical Bonding from Plane-Wave Based DFT. *J Comput Chem* **2016**, *37* (11), 1030–1035.
- (129) Shi, J.; Owen, C. J.; Ngan, H. T.; Qin, S.; Mehar, V.; Sautet, P.; Weaver, J. F. Formation of a Ti–Cu(111) Single Atom Alloy: Structure and CO Binding. *J Chem Phys* **2021**, *154* (23), 234703.
- (130) Lee, J. D.; Qi, Z.; Foucher, A. C.; Ngan, H. T.; Dennis, K.; Cui, J.; Sadykov, I. I.; Crumlin, E. J.; Sautet, P.; Stach, E. A.; Friend, C. M.; Madix, R. J.; Biener, J. Facilitating Hydrogen Dissociation over Dilute Nanoporous Ti–Cu Catalysts. *J Am Chem Soc* **2022**, *144* (37), 16778-16791.
- (131) Patel, D. A.; Giannakakis, G.; Yan, G.; Ngan, H. T.; Yu, P.; Hannagan, R. T.; Kress, P. L.; Shan, J.; Deshlahra, P.; Sautet, P.; Sykes, E. C. H. Mechanistic Insights into Nonoxidative Ethanol Dehydrogenation on NiCu Single-Atom Alloys. *ACS Catal* **2023**, *13* (7), 4290–4303.

- (132) Ren, Y.; Zhang, F.; Hua, W.; Yue, Y.; Gao, Z. ZnO Supported on High Silica HZSM-5 as New Catalysts for Dehydrogenation of Propane to Propene in the Presence of CO<sub>2</sub>. *Catal Today* **2009**, *148* (3–4), 316–322.
- (133) Baek, J.; Yun, H. J.; Yun, D.; Choi, Y.; Yi, J. Preparation of Highly Dispersed Chromium Oxide Catalysts Supported on Mesoporous Silica for the Oxidative Dehydrogenation of Propane Using CO<sub>2</sub>: Insight into the Nature of Catalytically Active Chromium Sites. *ACS Catal* **2012**, *2* (9), 1893–1903.
- (134) Azzam, K. G.; Jacobs, G.; Shafer, W. D.; Davis, B. H. Dehydrogenation of Propane over Pt/KL Catalyst: Investigating the Role of L-Zeolite Structure on Catalyst Performance Using Isotope Labeling. *Appl Catal A Gen* **2010**, *390* (1–2), 264–270.
- (135) Lavrenov, A. V.; Saifulina, L. F.; Buluchevskii, E. A.; Bogdanets, E. N. Propylene Production Technology: Today and Tomorrow. *Catal Ind* **2015**, *7* (3), 175–187.
- (136) Bhasin, M. M.; McCain, J. H.; Vora, B. V.; Imai, T.; Pujadó, P. R. Dehydrogenation and Oxydehydrogenation of Paraffins to Olefins. *Appl Catal A Gen* **2001**, *221* (1–2), 397–419.
- (137) Sokolov, S.; Stoyanova, M.; Rodemerck, U.; Linke, D.; Kondratenko, E. V. Comparative Study of Propane Dehydrogenation over V-, Cr-, and Pt-Based Catalysts: Time on-Stream Behavior and Origins of Deactivation. *J Catal* **2012**, *293*, 67–75.
- (138) Im, J.; Choi, M. Physicochemical Stabilization of Pt against Sintering for a Dehydrogenation Catalyst with High Activity, Selectivity, and Durability. *ACS Catal* **2016**, *6* (5), 2819–2826.
- (139) Zhu, J.; Yang, M.-L.; Yu, Y.; Zhu, Y.-A.; Sui, Z.-J.; Zhou, X.-G.; Holmen, A.; Chen, D. Size-Dependent Reaction Mechanism and Kinetics for Propane Dehydrogenation over Pt Catalysts. *ACS Catal* **2015**, *5* (11), 6310–6319.

- (140) Wang, L.; Wang, L.; Meng, X.; Xiao, F. New Strategies for the Preparation of Sinter-Resistant Metal-Nanoparticle-Based Catalysts. *Advanced Materials* **2019**, *31* (50).
- (141) Sattler, J. J. H. B.; Ruiz-Martinez, J.; Santillan-Jimenez, E.; Weckhuysen, B. M. Catalytic Dehydrogenation of Light Alkanes on Metals and Metal Oxides. *Chem Rev* **2014**, *114* (20), 10613–10653.
- (142) Zhang, J.; Deng, Y.; Cai, X.; Chen, Y.; Peng, M.; Jia, Z.; Jiang, Z.; Ren, P.; Yao, S.; Xie, J.; Xiao, D.; Wen, X.; Wang, N.; Liu, H.; Ma, D. Tin-Assisted Fully Exposed Platinum Clusters Stabilized on Defect-Rich Graphene for Dehydrogenation Reaction. *ACS Catal* **2019**, *9* (7), 5998–6005.
- (143) Zhang, Y.; Zhou, Y.; Shi, J.; Zhou, S.; Sheng, X.; Zhang, Z.; Xiang, S. Comparative Study of Bimetallic Pt-Sn Catalysts Supported on Different Supports for Propane Dehydrogenation. *J Mol Catal A Chem* **2014**, *381*, 138–147.
- (144) Zhu, Y.; An, Z.; He, J. Single-Atom and Small-Cluster Pt Induced by Sn (IV) Sites Confined in an LDH Lattice for Catalytic Reforming. *J Catal* **2016**, *341*, 44–54.
- (145) Batzill, M.; Beck, D. E.; Koel, B. E. Electronic Contrast in Scanning Tunneling Microscopy of Sn–Pt(111) Surface Alloys. *Surf Sci* **2000**, *466* (1–3), L821–L826.
- (146) Santhosh Kumar, M.; Chen, D.; Holmen, A.; Walmsley, J. C. Dehydrogenation of Propane over Pt-SBA-15 and Pt-Sn-SBA-15: Effect of Sn on the Dispersion of Pt and Catalytic Behavior. *Catal Today* **2009**, *142* (1–2), 17–23.
- (147) Pulay, P. Convergence Acceleration of Iterative Sequences. the Case of Scf Iteration. *Chem Phys Lett* **1980**, *73* (2), 393–398.

- (148) VALERO, M.; RAYBAUD, P.; SAUTET, P. Interplay between Molecular Adsorption and Metal–Support Interaction for Small Supported Metal Clusters: CO and C<sub>2</sub>H<sub>4</sub> Adsorption on Pd<sub>4</sub>/ΓPd<sub>4</sub>/γ-Al<sub>2</sub>O<sub>3</sub>. *J Catal* **2007**, *247* (2), 339–355.
- (149) Hanh, T. T. T.; Takimoto, Y.; Sugino, O. First-Principles Thermodynamic Description of Hydrogen Electroadsorption on the Pt(111) Surface. *Surf Sci* **2014**, *625*, 104–111.